T.J. van Melis

Tolerable wave overtopping during construction of a breakwater

TUDelft Boskalis

Tolerable wave overtopping during construction of a breakwater

by

T.J. van Melis

in partial fulfilment of the requirements for the degree of

Master of Science
in Civil Engineering

at the Delft University of Technology,
to be defended publicly on Thursday September 26, 2019 at 12:00 PM.

Thesis committee:	Dr. ir. B. Hofland,	TU Delft
	Dr. ir. A. Antonini,	TU Delft
	Dr. ir. J.D. Bricker,	TU Delft
	Ir. B.C. Mous,	Royal Boskalis Westminster N.V.
Date	18-9-2019	

An electronic version of this thesis is available at http://repository.tudelft.nl/.

Cover picture: A breakwater under construction in Cotonou, Benin.

TUDelft **Boskalis**

Abstract

Wave overtopping is an important aspect for the design of rubble mound breakwaters. Acceptable overtopping limits are usually based on the mean overtopping discharge or the maximum overtopping volume (EurOtop, 2018). For temporary situations, such as breakwaters under construction, overtopping limits are not clearly defined. This complicates the choice for a working crest level, where the safety of staff and equipment on the partially constructed breakwater is the main concern.

In this study, OpenFOAM in combination with the waves2foam toolbox (Jacobsen et al., 2012) is used to model wave overtopping over a breakwater under construction to identify the flow characteristics (i.e. the flow depth and velocity) caused by overtopping waves. The aim of the study is to provide a method to define a safe working level for rubble mound breakwaters under construction, based on the tolerable flow depth and velocity. The safety of the staff and equipment is expressed in limit functions. The method of Sandoval (2016) is applied to define the limit function for workers safety on the breakwater under construction (based on combinations of flow depth and velocity). The safety of the hydraulic excavators is mainly based on the overtopping flow depth, e.g. the flow depth should not exceed the cabin-level.

2D physical model test results on a partially constructed breakwater are processed in order to obtain benchmark data to validate the numerical model. Once the numerical model was validated, a numerical test program was set up that varied the wave height, wave steepness and the relative freeboard, in order to investigate the dependence of the overtopped flow depth and velocity on the varied conditions. A JONSWAP spectrum was used to simulate 8 different wave fields of 250 waves. On the crest of the numerical breakwater, the flow depth and velocity are measured by means of equally spaced gauges and probes in order to describe the flow behavior.

Overtopping events due to the irregular wave train are statistically analysed in terms of flow depth and velocity. The empirical 2% exceedance values are considered as design parameters as these can be compared to existing literature on impermeable and smooth dikes, to highlight the effects of the partially finished and permeable structure.

Empirical relations between the investigated parameters and the overtopping flow depth and velocity on the core crest edge of the breakwater are presented. It is found that the maximum flow depth reduces exponentially over the crest. The reduction appears less strong when saturation of the crest material starts to play a role. The flow velocity increases over the crest for the cases with larger initial flow depths and/or flow detachment from the breakwater crest edge, in contrast to the formulas for dike cross sections. This latter phenomenon was explained by the acceleration caused by the redirection of the flow on the breakwater crest. From the numerical results, two distinct areas of the unconstructed breakwater crest can be identified: a "transition zone" where the flow is detached from the breakwater crest and a "flow zone" with attached flow where the limit functions are valid.

Based on the numerical findings, empirical guidance is given for the land-based workability of breakwaters under construction. It is shown how the newly developed empirical formulas can be applied in practice to determine a safe working level. It is noted that the maximum overtopping flow depth and flow velocity do not necessarily occur at the same moment. A method is introduced that shows how the safety can be assessed using a combinational number for the flow depth and flow velocity (based on numerical modelling) and the stability limit for people. It is shown how a safe working level can be found based on exceedance values of safety limits.

Preface

This thesis is the last step in obtaining a Master of Science degree in Hydraulic Engineering, with a specialisation in Coastal Engineering, at the Delft University of Technology.

The finalization of this thesis marks the finalization of my life as a student. I experienced the past 6 years as an awesome trip that started in Wageningen and ended in Delft, but showed me the whole world while making friendships for life along the way.

This thesis could not have been possible without the great help of my thesis committee: Alessandro, Bas, Bart & Jeremy. Your input was indispensable and taught me more than any lecture I've ever had. A special thanks goes to Bart, who was always ready for a chat over a cup of coffee and showed me around in the world of Boskalis.

Finally, I would like to thank my mother Marianne, my father Emiel, my brother Jurren, my sister Eline and my girlfriend Fenna. Thank you guys for always having my back.

T.J. van Melis
Rotterdam, September 2019

Contents

1 Introduction

When waves run up or break on the face of a coastal structure, this can cause water to pass over the crest of the structure. This phenomenon is called wave overtopping and it is an important aspect of designing coastal structures. Wave overtopping can cause a continuous flow over the structure ('green water') and/or a non-continuous splash over the structure ('white water'). Wave overtopping is characterised as highly irregular, both in space and time.

Overtopping has been investigated thoroughly for different structures, armour units, hydraulic conditions and (to a lesser extent) wind conditions. Extensive research results on overtopping have been collected in the EurOtop manual (van der Meer et al., 2018), which offers an obvious starting point for follow up research and engineering practice. In engineering practice, tolerable overtopping limits are set for wave overtopping over coastal structures. These limits are often expressed in a discharge (in m^3/s per m) or volume (in m^3/m) and are mostly based on professional experience. The limits depend on: 1) the use of the defence structure itself; 2) the use of land (or water) behind the structure; 3) standards and administrative practice; and 4) the economic and social basis for funding the structure (van der Meer et al., 2018). Using these limits, the structure can be dimensioned.

The overtopping limits are usually applied in combination with prevailing design conditions to design the final structure. The EurOtop manual however does not discuss limits for rubble mound breakwaters which are under construction. During construction the conditions are often less extreme, but the crest level is also lower than in the final design. It might also be that larger overtopping events are accepted for some time, considering the possibility to evacuate.

During the construction of rubble mound breakwaters, significant wave overtopping can occur depending on (amongst others) the selected crest level and the wave conditions. Choosing the appropriate crest level for construction with land-based equipment is important in order to minimize downtime and to avoid unsafe situations on the one hand, and to reduce rock volumes, costs and construction time on the other hand. When a lower working level can be chosen, especially the construction costs can be significantly reduced. The determination of the working level is often an arbitrary task. Depending on the various construction phases, different tolerable overtopping limits might apply.

The required working level for land-based equipment on rubble mound breakwaters is currently determined by rules of thumb solely based on engineering practice. Tolerable overtopping limits should be determined and traced back to hydraulic and structural input parameters. This should enable the determination of a safe working level and a more reliable workability analysis.

This research was initiated by Hydronamic, the inhouse engineering company of Royal Boskalis Westminster (a large marine contractor). Hydronamic is often involved in the design of breakwaters and their intermediate construction stages.

1.1 Scope

This research considers rubble mound breakwaters that are under construction and the safety of hydraulic excavators and personnel against wave overtopping.

1.1.1 Rubble mound Breakwaters

Breakwaters are most commonly used to reduce the wave action on the lee side of the breakwater. They are often built near ports or offshore mooring places for vessels. Rubble mound breakwaters consist of layers of loose material, sometimes in combination with a geotextile. This means that the breakwater is permeable to some extent. The breakwater is built up in layers, from a core made up out of fine materials

(usually quarry run), to filter layers following Terzaghi's filter rules (on permeability, general stability and internal stability), up to the final armour layer that is designed to resist the wave impact. The final armour layer can consist of rock or concrete elements specifically designed to withstand wave induced forces.

A distinction should be made between statically stable breakwaters, dynamically stable breakwaters, and berm breakwaters. Statically stable breakwaters are designed so they allow for little damage (displacement) under design conditions. Dynamically stable breakwaters reshape under the influence of wave action, but often move back to an equilibrium position after a disturbance has occurred. Berm breakwaters are somewhere in between the 2 former types, as they cannot withstand all wave conditions but they are over dimensioned for most wave conditions. Berm breakwaters are allowed to reshape within tolerable limits.

In this research, statically stable rubble mound breakwaters under construction are discussed. These breakwaters usually have a slope between 1:2 – 3:4, the gentle bound given by rock, the steep bound by the more technologically advanced concrete armour units.

1.1.2 Safety

To define the normative wave overtopping safety limit, it is required to distinguish between the following situations where wave overtopping threatens a specific safety aspect of a breakwater under construction:

1. **Safety of the breakwater**: the risk that the structural integrity of the breakwater is affected by overtopping during various construction phases. During the construction of a breakwater, adverse weather conditions can affect the partly built structure. Safety against this is often incorporated by 1) doing model tests with partly built breakwaters; 2) performing most of the construction works outside the storm season; 3) applying armour layers on top of vulnerable underlayers as soon as possible; and 4) applying temporary protection layers when adverse weather is expected.
2. **Safety of the Operational Site Staff**: the risk that an accident takes place caused by wave overtopping that results in an injury to the personnel directly involved in constructing the breakwater. The staff includes personnel working on foot and personnel controlling the land-based equipment. There can also be a risk that the staff feels unsafe and stops working, which causes downtime.
3. **Safety of the land-based equipment**: the risk that damage occurs to the land-based equipment due to wave overtopping. The land-based equipment that is typically used during the construction of breakwaters includes hydraulic excavators, wire cranes, rigid body dump trucks, articulated dump trucks (ADT's), bulldozers and wheel loaders.

In this research, the safety of the operational site staff (both on foot and in a hydraulic excavator), and the safety of hydraulic excavators are investigated. The focus is thus (besides the staff) on one specific type of vehicle, the hydraulic excavator. This is done for two reasons: 1) hydraulic excavators are used throughout most stages of the construction of a breakwater and are therefore expected to have a key influence on the downtime and 2) unlike dump trucks, bulldozers and wheel loaders, hydraulic excavators move slowly and evacuations when adverse weather is expected are more cumbersome. Hydraulic excavators are involved in the construction process during dumping, reshaping (trimming) and precise armour unit placement. To specify in more detail what is investigated, different failure types are listed:

1. **Failure of the Operational Site Staff**:
    a. Staff on foot: personnel loses balance due to wave overtopping. Endoh and Takahashi (Endoh and Takahashi, 1995) distinguish between two failure mechanisms, being 1) 'tumbling' (the moment created by the current forces around the feet is greater than the

moment produced by the persons' weight) and 2) 'slipping' (the current force is greater than the friction force between the shoes and the ground).

b. Staff controlling the hydraulic excavator: personnel in vehicle loses accuracy (e.g. through loss of vision) or a safe feeling. However, at this point the personnel should always be able to leave the excavator by foot. The failure mechanism of staff on foot is therefore always normative over this failure mechanism. During many different stages in the building process people can be present on the crest of the breakwater, e.g. for fuel supply, small maintenance or for giving instructions. The same failure mechanisms as for failure mechanism 1a are therefore applicable for staff in the hydraulic excavator.

2. **Failure of the Hydraulic Excavator**:
   a. Hydraulic excavator gets damaged and requires (costly and time-consuming) repairs. The damage occurs mostly to the electronics or engine of the hydraulic excavator. This failure is expected when green water overtopping causes flooding of the cabin (and so problems to the electrical system) and/or water inflow into the engine's air intake system. In general it can be said that when green water overtopping reaches above the tracks of the hydraulic excavator, damage is likely to occur.
   b. Hydraulic excavator loses stability either 1) direct: wave overtopping destabilizes the vehicle by exerting a force or moment on the vehicle that causes it to slip or tumble, or 2) indirect: wave overtopping causes erosion of the breakwater that causes the moment resisting tumbling to become too small. Instability of the hydraulic excavator is a very rare event.

When the failures listed above are reached, safety limits have been exceeded. Enhanced decision making for preliminary (design) measures or downtime analysis is possible when the failure mechanisms are known. All failures can cause downtime, but failure 2a and 2b also result in damage to the hydraulic excavators. Failure 1a and 1b are denoted as the staff-based failure. Work should be stopped before this failure is reached, causing downtime but preventing injuries. Failure 2a and 2b are denoted as the equipment-based failure. Hydraulic excavators should be removed from the breakwater before this failure is reached, causing downtime but preventing damage.

As mentioned, failure mechanism 1a is normative for the staff-based failure. Similarly, failure mechanism 2a is normative for the equipment-based failure. Damage can already occur to the excavator without it completely losing its stability. In this study damage due to loose stones is ignored as the structure is considered stable. Therefore, in this thesis, failure mechanisms 1a and 2a are analysed (Table 1).

Safety of	Subpart	Failure Mechanisms	Qualification
Operational Site Staff	On foot	Loss of stability caused by destabilising combination of flow velocity and depth	Staff-based failure
Land-Based Equipment	Hydraulic Excavator	Damage to electronics and/or engine caused by green water overtopping reaching the height of sensitive equipment	Equipment-based failure

Table 1: Failure mechanisms studied in this thesis

1.2 Problem statement

Overtopping limits, expressed in discharges and volumes, are based on experience and appear to be sufficiently safe for the final design of rubble mound breakwaters. However, limits during construction are not directly available. The discharge and volume methods are not derived from aspects that describe the instantaneous loads caused by wave overtopping. Instantaneous loads are the flow depth and flow velocity over a breakwater caused by an overtopping wave. Limits based on instantaneous overtopping loads for the safety of both hydraulic excavators and the staff on rubble mound breakwaters under construction are more intuitive and transparent to use as compared to the discharge or volume method.

Currently, no clear method is available to define the safe working level based on these instantaneous loads.

The problem is therefore the lack of in depth knowledge on the instantaneous loads caused by wave overtopping over breakwaters and how this causes safety problems to the staff and the hydraulic excavators during construction phases.

1.3 Objective

The goal of this thesis is to create a method that can determine the safe working level (with respect to wave overtopping) for the staff and the hydraulic excavators constructing a rubble mound breakwater. As this method is to be used in a preliminary design stage, it should be able to give this information without any physical modelling. The method should be based on a description of the relevant processes and should take into account the hydraulic conditions as well as the characteristics of a typical cross-section of a rubble mound breakwater under construction.

1.4 Research Questions

The objective is divided into 4 research questions. The main research question is given as:

Can a calculation methodology be developed to determine the safe working crest level of a breakwater under construction?

This question is divided into the following sub-questions:

1. *What knowledge is available on quantifying overtopping phenomena?*
2. *What are the limits for safe operation and which parameters are expected to influence these limits?*
3. *How can the parameters be tested that are expected to influence the limits for safe operations?*
4. *What hydraulic and structural parameters have an influence on the limits for safe operations?*

1.5 Methodology and thesis outline

An overview of the methodology and where in the report it is treated is given by Figure 1. Here the methodology is described per research question.

1. *What knowledge is available on quantifying overtopping phenomena?*
This sub question answers how overtopping can be quantified and how overtopping limits are defined in the available literature. This should give insight into how overtopping is analysed in engineering practice and what parameters are likely to be important in determining a safe working level.

2. *What are the limits for safe operation and which parameters are expected to influence these limits?*
When overtopping is well understood, it is important to link the overtopping phenomena to the staff-based failure and the equipment-based failure. For the staff-based failure, some literature is already available. To find out how the equipment-based failure works (so when hydraulic excavators are damaged), unstructured interviews with experienced project engineers are used. Literature is used to form hypotheses that consider relations between the limits for safe operations and the parameters that are expected to influence the limits.

3. *How can the parameters be tested that are expected to influence the limits for safe operations?*
To test the hypotheses, multiple methods are available. These are studied and a specific numerical model is chosen (OpenFOAM in combination with OceanWave3D) which is validated using a wave flume experiment. In the wave flume experiment, measurements were performed on overtopping flows over an unfinished breakwater. In the validation, these measurements are compared to measurements performed

4

in the numerical version of the physical experiment. The numerical model is optimized based on this comparison. A test program is set up that can test the hypotheses. The settings of this test program are used to run simulations and perform measurements with the validated numerical model. Due to the large computation time of the numerical model it is not efficient to simulate 1000 waves. A sufficiently large number of waves is modelled to overcome some of this inherent uncertainty, so a reliable exceedance analysis can be performed.

4. *What hydraulic and structural parameters have an influence on the limits for safe operations?*

Based on the results from the model, it is checked what parameters are most important in determining the safe working limit. This is done by studying the correlations between the varied parameters in the test program and the limiting parameters (the instantaneous loads) to find empirical relations. These empirical relations are useful as they give insight into which parameters are important to vary and to measure to test various wave climates and structural configurations for their safety against overtopping. If this question can be answered based on the previous sub-questions, the main research question is answered.
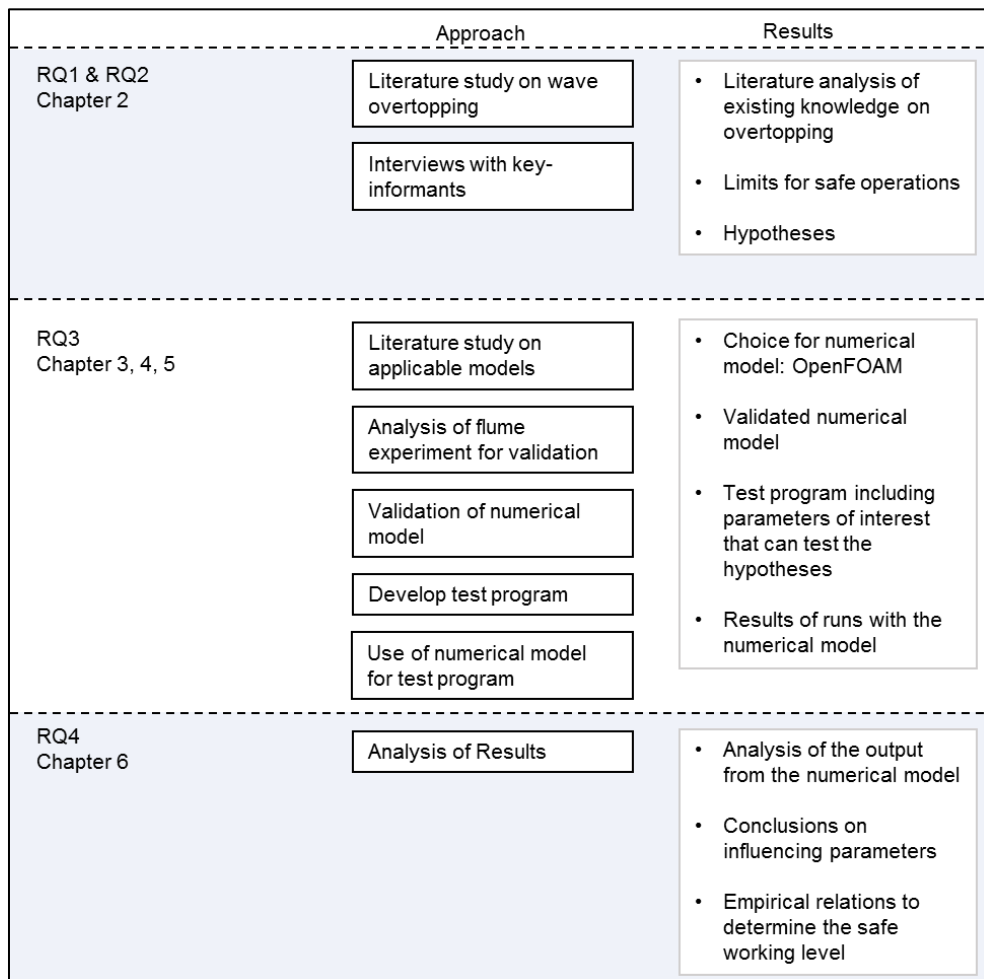

Figure 1: Methodology and thesis outline

2 Quantifying Overtopping

In this chapter, the main quantifiable characteristics of overtopping are discussed. The first section (section 2.1) discusses the current use of overtopping limits and questions what theory is required to determine the limits for staff-based failure and equipment-based failure.

Section 2.2 gives a brief overview of the parameters and formulas that are listed for the design of rubble mound structures in the latest EurOtop overtopping manual (van der Meer et al., 2018). Section 2.3 elaborates on this by analysing literature that considers the flow velocity and flow depths that are caused by overtopping flows over dikes. It is investigated what assumptions are made and what parameters influence the overtopping process.

As section 2.3 doesn't include research on breakwaters, research is gathered in section 2.4 on the reduction of the mean overtopping discharge over the crest of a rubble mound structure. Practically no theory exists yet on the flow velocity and flow depth over a breakwater crest as caused by overtopping flows. Section 2.5 summarizes the main findings of chapter 2 and gives hypotheses on what parameters are expected to influence the instantaneous loads on the breakwater crest.

2.1 Overtopping Limits

Designs for breakwaters are always adapted to prevent various failure mechanisms from happening. These failure mechanisms cause the structure to lose its functionality. The failure mechanisms can be of a soil mechanical nature, like global instability or settlement, or can be directly caused by external forces, for instance by ship collision or wave overtopping. Wave overtopping causes fast rushing water to flow over the breakwater and this can cause problems on top of and behind the breakwater.

An often used parameter to quantify overtopping is the mean overtopping discharge q. The mean overtopping discharge q is given in $[l/s \, per \, m]$ (meters width along the breakwater crest) and is calculated by gathering the cumulative volume of overtopped water during a specified testing phase (e.g. a storm duration) and dividing this volume by the measurement duration and the width of the measuring chute. The water collection takes place on the crest freeboard (R_c) or the armour freeboard (A_c). The first studies on overtopping strongly focussed on this mean overtopping discharge and the general limits for acceptable discharge that have been determined are still widely in use today.

The tolerable overtopping discharge is for instance discussed by Franco et al., who mention that tolerable overtopping (for humans) doesn't just depend on technical parameters but also on the psychology, age and clothes of a person (Franco, de Gerloni, and van der Meer, 1994). It is also described how the admissible overtopping discharge is a parameter that was introduced by Japanese guidelines, which are based on expert opinions of overtopping over prototypes. The paper also mentions a parameter that is used more and more nowadays, the overtopping volume per wave V in $[l/m \, per \, m]$. Franco et al. mention this parameter as they expect it to describe loads on a caisson crest wall better. At present, the overtopping volume is incorporated into design limits for various coastal structures. Franco even tested the stability of persons under overtopping by personally standing under a large water jet that simulated the overtopping volumes that were found during model tests.

More research has focussed on the maximum overtopping volume, as the overtopping discharge is not always a good measure to quantitatively analyse tolerable overtopping. This is because a mean overtopping discharge can be caused by many small waves, which can be harmless, or by a few large waves, which can inflict great damage. Therefore the calculation of safe limits is based more and more on the determination of the maximum overtopping volume V_{max}. The V_{max} gives the overtopping volume caused by the largest overtopping event. Table 2 shows overtopping limits for people and vehicles,

expressed in q and V, as collected in the EurOtop. These limits are given by professional experience, however some research has also been done to find relations between the stability of persons and certain overtopping conditions (see e.g. Geeraerts et al., 2004). The given quantities in Table 2 should be interpreted as an order of magnitude.

Hazard type and reason	Mean discharge q (l/s per m)	Max volume V_{max} (l per m)
People at structures with possible violent overtopping, mostly vertical structures	No access for any predicted overtopping	No access for any predicted overtopping
People at seawall / dike crest. Clear view of the sea.		
H_{m0} = 3 m	0.3	600
H_{m0} = 2 m	1	600
H_{m0} = 1 m	10-20	600
H_{m0} < 0.5 m	No limit	No limit
Cars on seawall / dike crest, or railway close behind crest		
H_{m0} = 3 m	<5	2000
H_{m0} = 2 m	10-20	2000
H_{m0} = 1 m	<75	2000
Highways and roads, fast traffic	Close before debris in spray becomes dangerous	Close before debris in spray becomes dangerous

Table 2: Overtopping limits for people and transport vehicles (Table 3.3 in the EurOtop Manual)

Especially the approach where tolerable limits are based on the V_{max} has been more clearly incorporated into the 2018 edition of the EurOtop manual compared to its 2007 predecessor. However, when it comes to the flow characteristics of overtopping waves, the information available in the manual is rather brief and solely applicable for dikes. This is partly because no generally accepted theory is available at present. Nevertheless, overtopping flow is very relevant for this study as it is the actual overtopping flow that causes instability to personnel and damage to the hydraulic excavator. Overtopping flow comprises both the flow velocity and the flow depth (the instantaneous loads) and the duration of the overtopping that is caused by a single overtopping event.

The stability of the staff depends on the flow velocity and flow depth over the crest (Endoh and Takahashi, 1995; Sandoval, 2015). One can reason that due to the friction on the crest the flow velocity reduces and that due to the permeability of the crest the flow depth reduces. As friction has more effect in shallow water, these two effects could strengthen each other. Then it is important to realize that the width of the crest could influence the failure types, as the flow could be less strong further away from the seaward crest edge (if the seaward crest is where the maximum flow velocities and depths can be found).

The evolution of the flow depth over the width of the crest is also relevant as it is reasoned that the flow depth (or the height that a continuous sheet of water reaches) can cause damage to hydraulic excavators. To mitigate the damage, (temporal) heightening or broadening of (a part of) the breakwater can be considered. This would require some extra material and stone-handling, but the downtime can be reduced. It is then possible to position the hydraulic excavators further away from the seaward crest edge. For instance special safe-havens can be used for this which are now often used to allow the passing of two vehicles.

This research therefore tries to find how the flow over the breakwater caused by overtopping waves can be characterised. For this it is required to find out what parameters have an influence on the flow velocity

and flow depth over the crest when a wave overtops. This research also wants to add to the knowledge of how an overtopping wave develops over the crest of a breakwater.

Both staff-based failure and equipment-based failure are currently reached because more significant overtopping occurs than expected. Especially damage to the hydraulic excavators occurs when the 'point of no return' is reached during construction. By this it is meant that for instance a weather forecast is not taken seriously enough (because often it is too conservative) and when the critical overtopping occurs it is already too late to take measures (like taking the excavator of the breakwater). An important consideration is then how you should deal with a storm prediction model. Knowing what waves you can expect and what kind of instantaneous loads these will cause should enhance this decision making.

2.1.1 Current practice: determination of the working level

This section as well as the characterization of the limit function for the hydraulic excavator is based on conversations with 4 project engineers (3 of which were consulted in person, 1 over the phone).

Currently, the working level is often based on the experience of project engineers. When presented with a design for a breakwater, the crest is checked for its width. The width is of importance as the breakwater should be accessible for the hydraulic excavators. The crest level should be low enough so the reach of the excavators is sufficient for the task at hand (e.g. the excavator should be able to reach the toe of the breakwater). When this criterion is met, the safety of the working level can be assessed.

For the calculation of the working level, different methods exist and no formal procedure is followed. Some engineers prefer to use the EurOtop manual guidelines (the limits for people) and include some extra safety as there are no specific guidelines for unfinished breakwaters. A main difference with finished breakwaters is that the risk is present that high swell waves erode the sides of the breakwater, resulting in instability of the crest and different overtopping patterns. In possible future studies where the erosion of the unfinished breakwater is researched, it is considered that knowledge on the instantaneous flow characteristics is required for various stability analyses.

The safe working level is mostly chosen to give conditions that are considered 'safe enough' to work. Evacuation of the breakwater occurs mostly 'on the spot'. Certain conditions occur that give the feeling that the working conditions are insufficiently safe and the breakwater is cleared. Rules of thumb are often used to determine the working level. One of such 'engineering tricks' is determining the working level by summing the expected high water and the significant wave height (H_s). What wave height is chosen (the one occurring during storms, or the weekly significant wave height and for what return period) is up to choice and depends also on the required working period.

It is important to note that downtime occurs when the staff starts feeling unsafe with working on the breakwater. As this is difficult to quantify (also because no downtime reports are available) it is chosen to look at the safety of people using stability relations.

2.1.2 Instantaneous loads: research on stability of people

Sandoval (Sandoval, 2015) combines theory on overtopping flow over dikes with theory on human stability in fluvial flow to investigate the human stability of people under overtopping flow. This is done by slightly adapting the stability theory developed by Endo and Takahashi (Endoh and Takahashi, 1995) through introducing the effect of buoyancy to the failure modes. The failure modes described are friction and moment instability. Friction instability describes the situation that the drag force caused by the overtopping flow is larger than the friction resistance of the person in the flow. Moment instability describes the situation that the moment created by the flow is larger than the person's resisting moment.

The study is based on finding stability curves that give either a stable or unstable combination of flow depth and flow speed, as visualised by Figure 2, left. Test data was gathered from tests that researched the stability in fluvial flows, as tests in flows similar to wave overtopping flows were not available. Although

these flows distinguish themselves from fluvial flows by being non-stationary and highly turbulent, Sandoval showed from video footage found online that green water overtopping (without falling jets) caused instability that fitted well onto the stability curves from the tests for fluvial flows. It was found that 70% of the data was located properly in the unstable zone of the graph, when the graph is adjusted for the effect of buoyancy. Considering the assumptions made, this is a very reasonable result. From the development of these stability graphs, and linking the flows to wave climates using the theory discussed in section 2.3, Sandoval found that the limits for 'trained staff' are realistic as given in the EurOtop 2007 edition (Pullen *et al.*, 2007).

A main finding was that overtopping flows cause instability at low water depths combined with high velocities. The graph on the right side of Figure 2 shows the graphs for the two failure modes (both the ones proposed by Endo and Takahasi and the ones corrected for buoyancy) and data from the test and video analyses. The found limit functions are elaborated in section 2.1.4. It is clear that the friction instability occurs in shallow and rapid flowing waters, whereas the moment instability is normative in deep and slow flowing waters. It is clear that overtopping flows mostly cause friction instability.
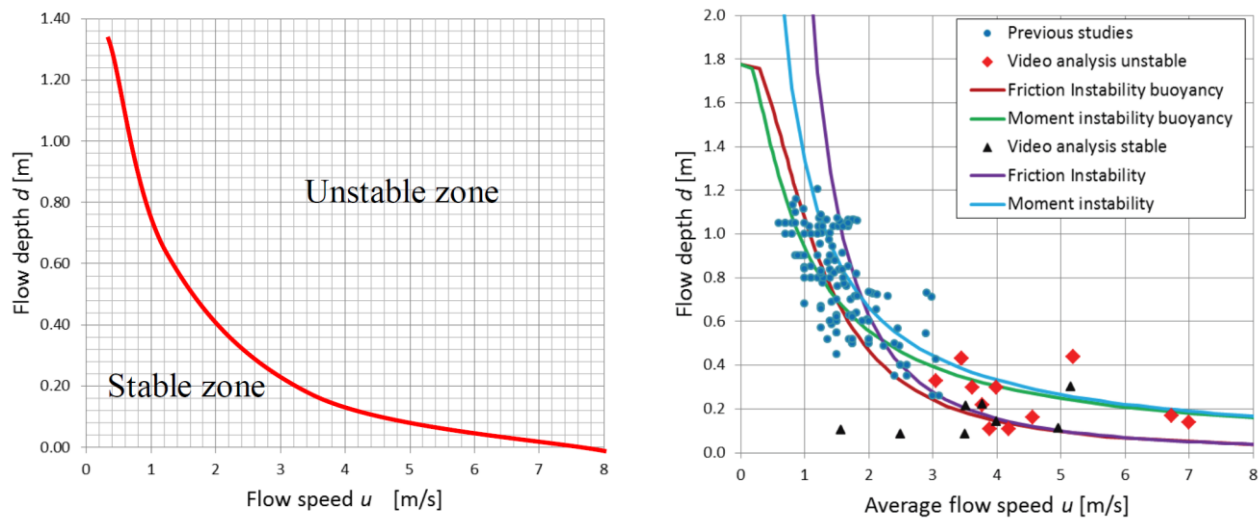
Figure 2: left) stability curve, right) stability curves for various failure modes and data from tests and videos (Sandoval, 2016)

2.1.3 Instantaneous loads: the safety of hydraulic excavators

In rare cases, it can occur that the hydraulic excavator gets damaged due to large overtopping events. Based on discussions with key-informants, it is concluded that significant damage occurs mostly to the electronics or engine of the hydraulic excavator. This failure is expected when green water overtopping causes flooding of the cabin (and so problems to the electrical system) and/or water inflow into the engine's air intake system. In general it can be said that when green water overtopping reaches above the tracks of the hydraulic excavator, damage is likely to occur.

2.1.4 Limit functions

For hydraulic excavators, the critical limit can be given by a certain maximum overtopping flow depth. The limit functions for people use the stability relations described by Sandoval. These limit functions are used in this research as the safety limits for the staff on the breakwaters. In the results from Sandoval's video analysis, which are also shown in Figure 2, some simplifications were made:

1. The subject's weight and height is based on national averages;
2. It is assumed that the flow speed is distributed uniformly over the height of the water column;
3. The speed of the flow is taken from the front velocity of the wave tongue;

4. To incorporate the effect of buoyancy, the body mass of the subject is distributed equally over the subject's height;
5. The standing position of the subject is facing the flow, standing straight up (see Figure 3). This position assumption is conservative, the subject is not expecting the flow impact.
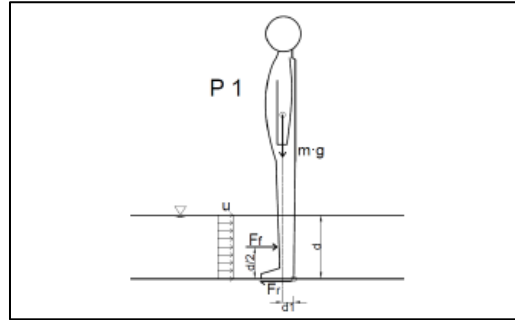
Figure 3: subject standing in front of the flow (Sandoval, 2016)

From this method, the limit functions for friction and moment instability can be generated. Filling in the drag force of the flow (as a function of velocity, depth, shape of the submerged body and the drag coefficient) and the resistance force of the person (as a function of weight and friction coefficient, incorporating the effect of buoyancy) the friction instability function is obtained. The effect of buoyancy is incorporated by assuming that a person's body volume is distributed evenly over its length. For friction instability, the following function is then derived:

$$F_f - F_r = C_d \frac{\rho}{2} u^2 B d - \mu(mg - V_d \rho g) = 0 \quad for \ 0 < d < h_p \tag{1}$$

Where:

F_f	=	Flow force	$[N]$
F_r	=	Resistance force	$[N]$
d	=	Water depth	$[d]$
h_p	=	Subject's height	$[m]$

Drag coefficient, according to Endoh and Takahashi:

C_d =

$$C_d = 1.1 \left(1 - \frac{L_f}{h_p}\right) \quad for \ \theta = 0°$$

$$C_d = 1.1 \left(1 + \frac{L_f}{h_p}\right) \quad for \ \theta = 45°, 90°$$

$[-]$

		L_f = Width between feet	$[m]$
		θ = Angle of the subject facing the flow	$[°]$
ρ	=	Water density (for seawater $1025 \ kg/m^3$)	$[kg/m^3]$
u	=	Average flow velocity	$[m/s]$
B	=	Average diameter of subject's legs	$[m]$
μ	=	Coefficient of friction between shoe sole and ground	$[-]$
m	=	Subject's mass	$[kg]$

Submerged volume of the body as a function of d:

V_d =

$$V_d = \frac{md}{\rho_o h_p}$$

$[m^3]$

ρ_o = density of the human body ($\approx 1062 \ kg/m^3$) $[kg/m^3]$

When the flow depth exceeds a person's height, it is reasoned that a person will not be able to offer any resistance against overtopping flow. The relationship between u & d for the friction instability becomes:

11

$$u = \sqrt{C_F m}\sqrt{1/d}\sqrt{(1 - \frac{d\rho}{\rho_o h_p})} \quad with \ C_F = \frac{2g\mu}{\rho C_d B} \tag{2}$$

A similar approach was adopted for moment instability, where a lever arm (d_1) is incorporated:

$$M_r - M_f = F_r d_1 - F_f \frac{d}{2} = 0 \tag{3}$$

$$u = \frac{C_M}{d}\sqrt{m}\sqrt{(1 - \frac{d\rho}{\rho_o h_p})} \quad with \ C_M = \sqrt{\frac{gd_1}{\rho C_d B}} \tag{4}$$

Where:

d_1 =   Lever arm, between centre of gravity and pivot point (Figure 3) $[m]$

The drag coefficient for a person directly facing the flow is used ($\theta = 0°$). For the coefficient of friction between a shoe sole and the ground (μ) a value was selected for a shoe with a rubber sole on rough concrete, $\mu = 0.95$ (Endoh and Takahashi, 1995). It should be noted that the material on top of the crest is composed of a rock grading, however no values are available for such an interface. The rough concrete is considered to be the most similar to a rock grading.

2.2 EurOtop manual: Parameters and theory

For finding out what parameters influence the overtopping process, the EurOtop manual forms a great source of information about research considering overtopping. The empirical relations given by this manual are widely accepted and used. This section briefly describes the main formulas that are applicable for breakwaters. Various parameters are used which are elaborated first. For a more detailed description, one is referred to the Eurotop manual (Van der Meer *et al.*, 2018). Figure 4 gives an overview of most parameters that are described below.
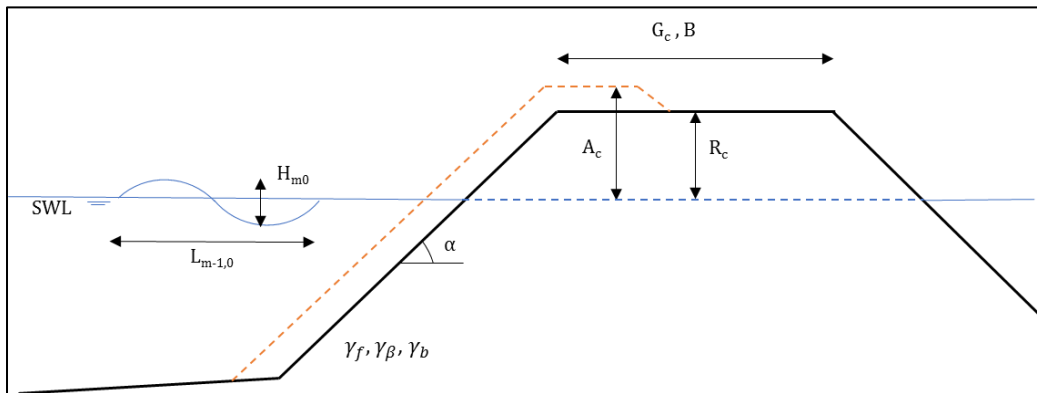
Figure 4: Basic structural and hydraulic parameters that affect overtopping

2.2.1 Hydraulic parameters

In all wave run-up and overtopping formulas the used wave height is the estimated significant wave height, drawn from the wave spectrum at the toe of the structure, H_{m0}. The variance density spectrum expresses characteristics of the sea-state using spectral moments (see definition below and section 5.2 on spectral analysis). In deep water, H_{m0} equals the significant wave height H_s. In circumstances where long waves caused by wave breaking are formed, a short wave spectrum may completely transform to a long wave spectrum. In these (less well understood circumstances) the formulas presented here should not be trusted to be very accurate.

$$m_n = \int_0^\infty f^n E(f) df \ \ for \ n = \ ... , -2, -1, 0, 1, 2, ... \tag{5}$$

Where:

m_n	=	n^{th} order moment, where the variance of the surface elevation equals the zeroth-order moment	$[-]$
$E(f)$	=	the variance density spectrum, where f is frequency	$[m^2/Hz]$

For a given wave spectrum, various wave periods can be defined. For the determination of overtopping volumes, the mean wave period (T_m) and the spectral wave period ($T_{m-1.0} = m_{-1}/m_0$) are used. The spectral period gives more weight to longer periods in the spectrum and it is also used as it represents complex spectral shapes best (for single peak wave spectra, the peak wavelength T_p can also be used). For the wavelength often the spectral wave length in deep water is used ($L_{m-1.0} = g \cdot T_{m-1.0}^2 / 2 \cdot \pi$).

For the steepness of waves, a distinction can be made between swell and sea. For swell, the wave steepness $s_{m-1.0} = H_{m0}/L_{m-1.0}$ is around 0.01, indicating relatively long waves. For sea, an $s_{m-1,0}$ between 0.04 – 0.06 is usual. Swell waves can be difficult to predict as they are generated far away, hence they do not follow from local weather forecasts. Often the swell characteristics are used in the design calculations, also because the long waves tend to cause normative overtopping. Summarizing:

H_{m0}	=	estimate of the significant wave height, based on spectral analysis ($=4\sqrt{m_0}$)	$[m]$
H_s	=	significant wave height, representing the highest one-third of set of wave heights	$[m]$
T_m	=	average wave period from time domain analysis	$[s]$
$T_{m-1.0}$	=	average wave period from spectral analysis (one of various, this one defined by m_{-1}/m_0)	$[s]$
T_p	=	spectral peak period, period with the highest energy in the spectrum	$[s]$
$L_{m-1.0}$	=	spectral wave length in deep water, $L_{m-1.0} = g \cdot T_{m-1.0}^2 / 2 \cdot \pi$	$[m]$
$s_{m-1.0}$	=	wave steepness based on H_{m0} and $L_{m-1.0}$	$[-]$

In overtopping calculations, an important parameter is given by the Iribarren number (also known as the surf similarity parameter). The Iribarren number describes the type of wave breaking on a structure, which has an important influence on the run-up level of the waves. The Iribarren number relates the steepness of the structure's slope to the wave steepness:

$$\xi_{m-1,0} = \frac{tan\alpha}{\left(H_{m0}/L_{m-1,0}\right)^{0.5}}$$

Where:

$\xi_{m-1,0}$	=	Iribarren number based on $s_{m-1.0}$	$[-]$
α	=	slope of the front face of the structure	$[°]$

Note that this version of the Iribarren number does not use the wavelength at the toe of the breakwater but the spectral deep water wave length using the period at the toe of the structure. Then the calculated wave steepness is actually a 'notional' wave steepness. Based on the Iribarren number, a distinction is made between 4 types of wave breaking. These are given in Table 3 (description based on Bosboom and Stive, 2012). As mentioned, breakwaters have an angle between $4/3 < cot(\alpha) < 2$. So for swell waves, surging breakers can be expected. For sea, the waves can be plunging or collapsing for the more flat slopes.

Iribarren number (EurOtop, 2016):	Type of breaking:	Description:
$\xi_{m-1,0} < 0.2$	Spilling	Wave found at flat and long beaches, where all wave energy is dissipated through breaking which starts relatively far off-shore.

$0.2 < \xi_{m-1,0} < 2-3$	Plunging	Curling waves where the wave crest 'plunges' into the wave trough in front of the crest.
$\xi_{m-1,0} \approx 2-3$	Collapsing	Wave in between plunging and surging, so between breaking and non-breaking.
$\xi_{m-1,0} > 2-3$	Surging	Wave found along more steep slopes (and/or for long waves). The waves rarely break and a considerable part of the wave energy is reflected back into deeper water. It is possible to argue that surging waves are more like standing waves than like breaking waves.

Table 3: Typology of waves with various Iribarren numbers

2.2.2 Structural parameters

For the structure, the most important parameters are given by the slope of the front of the structure α, the freeboard and the width of the crest. For the freeboard the EurOtop manual defines the crest freeboard (R_c) as the point on the structure where overtopping water does not flow back to the seaside. For rubble mound breakwaters it is then often given by a crown wall. The armour freeboard (A_c) gives the distance of the horizontal part of the crest to the still water level. The EurOtop recommends using the maximum of either A_c or R_c, which could lead to a small under estimation of the wave overtopping, or proposes using the average of A_c and R_c. This latter method considers that permeable flow occurs through the armour layer on the crest. For the width of the crest two parameters are regularly found in literature, being B and G_c. The width is given by the horizontal part of the crest.

$$
\begin{array}{lll}
R_c & = & \text{crest freeboard} \hfill [m] \\
A_c & = & \text{armour crest freeboard} \hfill [m] \\
G_c, B & = & \text{width of the crest, either full width or width up to the crest wall} \hfill [m]
\end{array}
$$

2.2.3 EurOtop formulas

Currently four methods are used regularly to quantify overtopping:

1. Physical modelling is often used to verify designs that were made with the design formulas or to add to the knowledge on the various factors that are used in the empirical design formulas.
2. The ANN tool is a large database that uses machine learning to combine the results of many different measurements (both from full-scale measurements, as from model tests). Through this the tool is able to calculate overtopping for structures that are not specifically in the database.
3. Numerical models solve flow equations in a numerical domain. Validated models can give elaborate information on the overtopping phenomena, but the more complicated models are not often applied in engineering practice. This is because of the high computational effort that is required, as well as the need for skilled practitioners of the software. Numerical models are discussed in some more detail in chapter 3.
4. Empirical formulas are based on test data, which follows from extensive research on various structures both in real-life tests and scaled model tests in wave flumes and wave basins. The empirical formulas are often used in combination with physical model tests in the final design stages.

In this section the main empirical formulas for rubble mound breakwaters are summarised. The formulas given are following the mean value approach. For design approaches, factors are often conservatively altered (e.g. by adding a standard deviation to specific variables).

Wave run-up

Wave run-up is often expressed in the 2% wave run-up height ($R_{u2\%}$), being the height that is exceeded by 2% of the up-rushing waves. The 2% wave run-up is calculated with respect to the end of the seaward slope of the breakwater. Relevant input parameters are the influence factor for a berm (γ_b), the influence

14

factor for roughness and permeability (γ_f), the influence factor for oblique wave attack (γ_β) and the Iribarren number. Because rubble mound breakwaters have a considerable roughness and permeability, the run-up is significantly reduced compared to smooth, impermeable slopes. The roughness factor for rocks for example is 0.45 (1 layer, permeable core). The equation below describes the $R_{u2\%}$ on a breakwater.

$$\frac{R_{u2\%}}{H_{m0}} = 1.65 \cdot \gamma_b \cdot \gamma_f \cdot \gamma_\beta \cdot \xi_{m-1,0} \tag{6}$$

Where:

$R_{u2\%}$	=	Run-up level exceeded by 2% of the waves	$[m]$
γ_b	=	influence factor for a berm	$[-]$
γ_f	=	influence factor for permeability and roughness on a slope	$[-]$
γ_β	=	influence factor for oblique wave attack	$[-]$

With a maximum of $R_{u2\%} = 1.00 \cdot \gamma_{f\ surging} \cdot \gamma_\beta \cdot \left(4.0 - \frac{1.5}{\sqrt{\gamma_b \cdot \xi_{m-1,0}}}\right)$

$\gamma_{f\ surging}$ = influence factor for permeability and roughness on a slope under surging waves $\qquad [-]$

From $\xi_{m-1,0} = 1.8$ the roughness factor $\gamma_{f\ surging}$ increases linearly up to 1 for $\xi_{m-1,0} = 10$:

$$\gamma_{f\ surging} = \gamma_f + \left(\xi_{m-1,0} - 1.8\right) * (1 - \gamma_f)/8.2$$

With a maximum of $R_{u2\%}/H_{m0} = 2.0$ for structures with a permeable core.

It's clear that for steeper slopes the wave period and wave steepness have less and less influence on the wave run-up and so the maximum values are reached, where all waves follow a surging pattern. Roughness elements can be considered effective from $0.25 \cdot R_{u2\%,smooth}$ below the still water line up to $0.50 \cdot R_{u2\%,smooth}$ above the still water line. Hence, if the roughness is not homogeneous in this area, the roughness factor should be weighted for this effective area:

$$\gamma_f = \frac{\sum_{i=1}^{n} \gamma_{f,i} \cdot L_i}{\sum_{i=1}^{n} L_i} \tag{7}$$

Where:

$\gamma_{f,i}$	=	γ_f on section i of a slope	$[-]$
L_i	=	Length of section i of a slope	$[m]$

Mean overtopping discharge
The formula for the mean overtopping discharge q for steep slopes ($4/3 < \cot(\alpha) < 2$) is given by:

$$\frac{q}{\sqrt{g \cdot H_{m0}^3}} = 0.09 \cdot \exp\left[-\left(1.5\ \frac{R_c}{H_{m0} \cdot \gamma_f \cdot \gamma_\beta}\right)^{1.3}\right] \tag{8}$$

Where:

q	=	Mean overtopping discharge per meter width	$[m^3/s\ per\ m]$
g	=	Gravitational acceleration (9.81)	$[m/s^2]$

When the freeboard becomes negative, not only overtopping but also overflow can occur. The overflowing discharge can be calculated by the weir formula for a broad crested structure. This might however only be useful for breakwaters that experience tidal flow over the crest. Hughes and Nadal showed that for dikes wave overtopping becomes negligible once $R_c/H_{m0} < -0.3$ (Hughes and Nadal, 2009). This is a good indication for when overtopping starts to play a role for structures under

construction. When a negative freeboard is present, the wave overtopping can be calculated with the overtopping formula for a zero freeboard.

$$q_{overflow} = 0.54 \cdot \sqrt{g \cdot |-R_c^3|}$$ (9)

Where:

$q_{overflow}$ = Overtopping discharge when water level exceeds the crest freeboard, without wave overtopping $[m^3/s \, per \, m]$

Maximum overtopping volume

To calculate the maximum volume of overtopping waves, the percentage of overtopping waves is required. This is required as a probabilistic method determines the likely maximum wave volume. Assuming a Rayleigh distribution for the $R_{u2\%}$, the probability of overtopping can be determined:

$$P_{ow} = N_{ow}/N_w = \exp\left[-\left(\sqrt{-ln0.02}\frac{R_c}{R_{u,2\%}}\right)^2\right]$$ (10)

Where:

P_{ow}	=	probability of overtopping per wave	$[-]$
N_{ow}	=	number of overtopping waves	$[-]$
N_w	=	number of incident waves	$[-]$

Beware that the $R_{u2\%}$ is measured with respect to the end of the seaward slope, whereas overtopping is often measured further away from the seaward slope. So this method could give an overestimation of the number of overtopping waves. An additional method is given based on fitting a Weibull curve through test data for concrete armour units. This method requires the size of the armour unit (D_n) and the armour crest freeboard of the structure (A_c) compared to the significant wave height, instead of the wave runup. When the probability of overtopping waves is known the number of overtopping waves can be calculated using the storm duration and mean period.

$$P_{ow} = N_{ow}/N_w = \exp\left[-\left(\frac{A_c D_n}{0.19H_{m0}^2}\right)^{1.4}\right]$$ (11)

Where:

D_n = nominal diameter of a concrete armour unit $[m]$

When the overtopping discharge is known as well as the number of overtopping waves for a certain storm duration, a two parameter Weibull distribution can be used to give the probability of exceedance for a maximum wave volume:

$$P_{V\%} = N_{ow}/N_w = \exp\left[-\left(\frac{V}{a}\right)^b\right] \cdot (100\%)$$ (12)

$$a = \left(\frac{1}{\Gamma\left(1+\frac{1}{b}\right)}\right)\left(\frac{qT_m}{P_{ov}}\right)$$ (13)

$$b = 0.85 + 1500\left(\frac{q}{gH_{m0}T_{m-1,0}}\right)^{1.3}$$ (14)

Where:

$P_{V\%}$	=	$P_V \cdot (100\%)$	$[\%]$
P_V	=	probability of an overtopping volume V_i being larger or equal to a given volume V $(P(V_i \geq V))$	$[-]$
a	=	coefficient for the Weibull distribution, see equation (9)	$[-]$

| b | = | coefficient for the Weibull distribution, see equation (10) | $[-]$ |
| Γ | = | Gamma function | |

The maximum overtopping volume can then be calculated using:

$$V_{max} = a \cdot [\ln(N_{ow})]^{1/b} \tag{15}$$

Where:

| V_{max} | = | Maximum overtopping volume | $[m^3/m]$ |

In Figure 5 below, the distribution of overtopping volumes is given for a specific wave condition and for various overtopping discharges. It is clearly visible that only a few waves give large overtopping volumes, as indicated by the steepening graph.
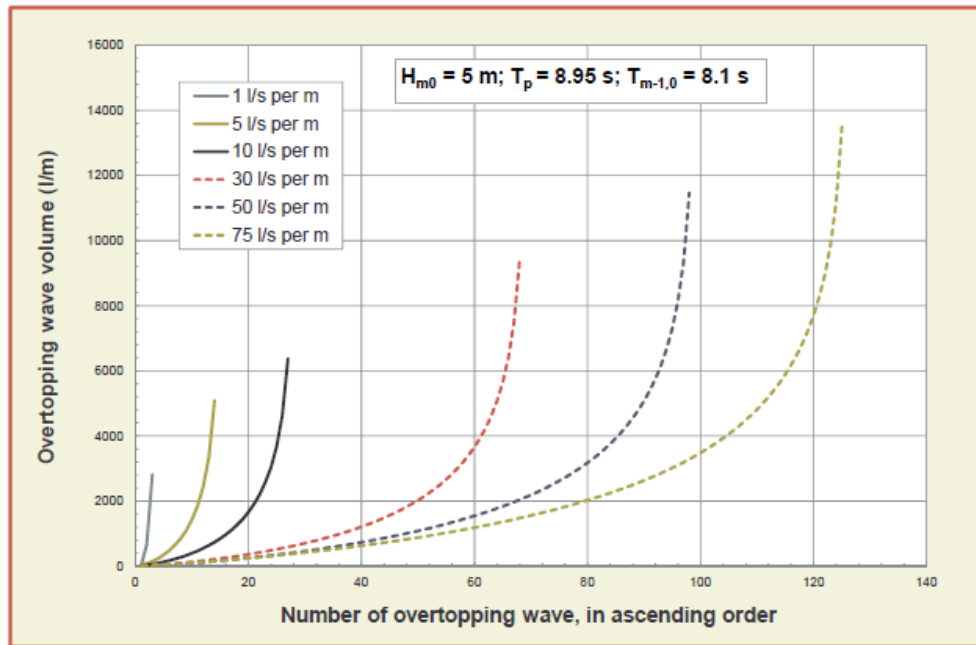
Figure 5: The graphs represent different discharges, resulting in volume distributions (Figure 3.5 in the EurOtop)

2.3 Overtopping flow: research on sea dikes

Most available research on overtopping flow characteristics has been done to study dike erosion. This research was motivated by the fact that sea dikes can be severely damaged by overtopping, which can lead to dike breaches. The theory discussed here has been developed for smooth, impermeable and mildly sloping embankments. The general findings discussed here might be applicable to breakwaters. The research on dikes indicates what parameters can influence the overtopping flow. A main assumption in this section is that overtopping occurs in the form of 'green water', and that spray can thus be neglected.

Schüttrumpf (Schüttrumpf, 2001) and van Gent (van Gent, 2002) simultaneously derived expressions for the flow velocity and flow depth at the seaward slope, crest and landward slope of a sea dike resulting from overtopping waves. Their joint paper (Schüttrumpf and van Gent, 2003) analyses the results of both researches. In (Schüttrumpf and Oumeraci, 2005) the theoretical background behind the applied formulas is given in more detail. In (Trung, 2014) a slightly altered method is given to relate the flow depth and velocity more directly to the overtopping volume. It should be noted that the formulas used for calculating the wave run-up differ per study. Figure 6 visualises the important parameters that are used in this section's formulas, and is adapted from (Schüttrumpf and van Gent, 2003). The parameter definitions are given below the figure.
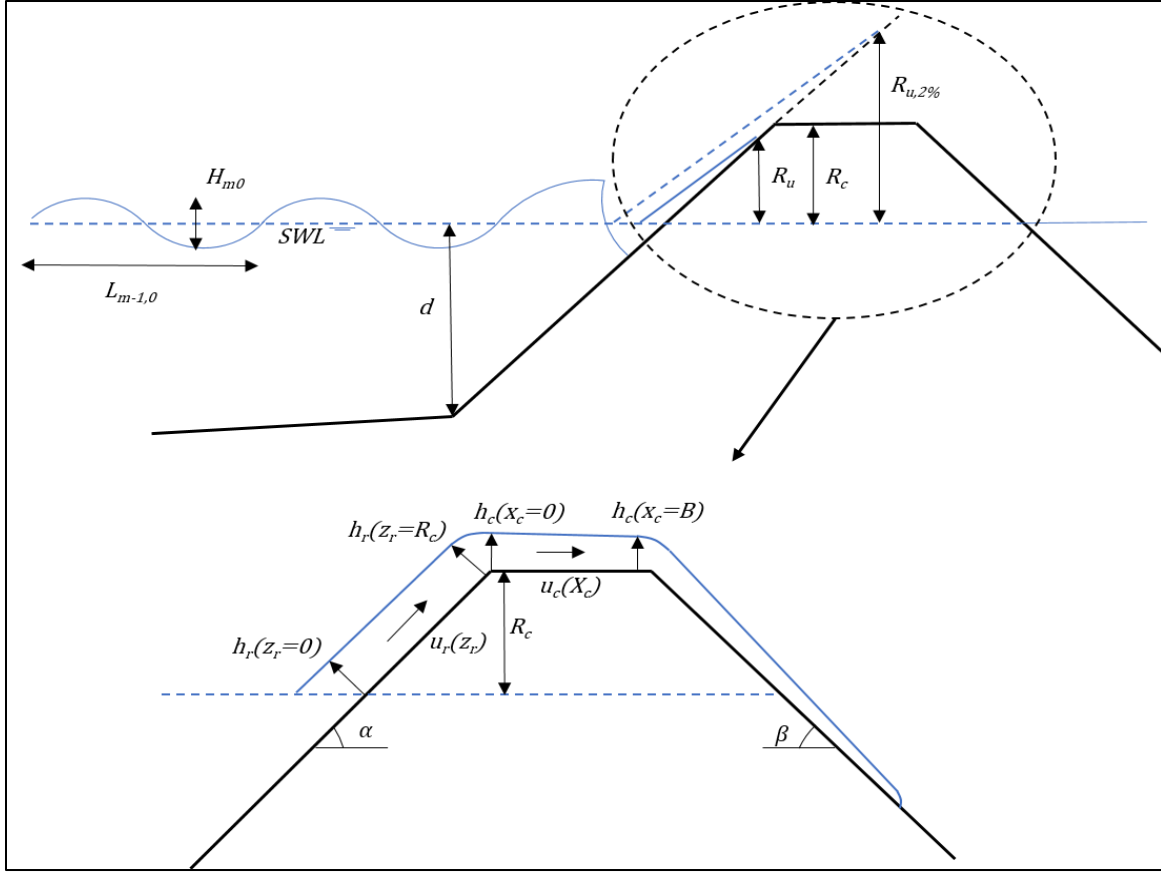
u_r	=	wave run-up velocity, subscript r denotes 'run-up'	$[m/s]$
h_r	=	water depth of wave during run-up	$[m]$
z_r	=	vertical coordinate, from the still water level (where it is 0) up to R_c	$[m]$
u_c	=	flow velocity over the crest, caused by a wave overtopping, subscript c denotes 'crest'	$[m/s]$
h_c	=	flow depth over the crest, caused by a wave overtopping	$[m]$
x_c	=	Horizontal coordinate, from the seaward crest edge (where it is 0) to B (crest width)	$[m]$

This section discusses literature on overtopping flow over the seaward slope and the crest of sea dikes. The overtopping on the crest is of main interest in this study, as the safety of personnel and equipment on the crest is investigated. To discuss flow velocities on the crest, the seaward slope is of relevance as the development of the wave tongue on this slope creates the boundary condition for flow over the crest. The landward slope is not discussed here as it is not relevant for the problem statement of this thesis.

2.3.1 Overtopping flow velocity and flow depth: Seaward Slope

The run-up velocity can be determined from a simple energy equation that neglects friction ($E_{kin} = E_{pot}$). Applying this equation for the run-down velocity (u_d), it is found that: $u_d = \left(2g(R_u - z_r)\right)^{0.5}$. Assuming that $u_{r,2\%} = c_{u2\%} * u_{d,2\%}$, where $c_{u2\%}$ is determined by model tests, the following equation is obtained:

$$u_{r2\%} = c_{u,r2\%}(g(R_{u,2\%} - z_r))^{0.5} \tag{16}$$

Where:

$c_{u,r2\%}$	=	empirical coefficient	$[-]$

18

If one assumes that the run-up velocity is equal to the run-down velocity, the value for $c_{u2\%}$ would be $2^{0.5} = 1.4$ (Van der Meer, 2011). The widely used 2% exceedance parameters are used to express the 'maximum' flow velocities and flow depths. In fact, the 2% denotes circumstances that are exceeded by 2% of the incoming waves. This approach is in line with the method widely used for the wave run-up ($R_{u2\%}$). Note that when the freeboard is larger than the $R_{u2\%}$, this method is not applicable, as the flow velocity and depth becomes zero for $R_{u2\%} = z_r$.

For the flow depth, no theoretical formula is derived. The flow depth is determined by assuming it decreases linearly from still water level up to $R_{u2\%}$. So for both the flow velocity as the flow depth the maximum is assumed to be found at the still water level.

$$h_{r2\%} = c_{h,r2\%}(R_{u,2\%} - z_r) \tag{17}$$

Where:

$c_{h,r2\%}$ =   empirical coefficient   [−]

In non-dimensional form, these formulas are often written as below (Schüttrumpf and van Gent, 2003). Note that the friction factors (γ_f) were not in the original formulas but have been added as suggested by (Bosman *et al.*, 2008). When $z_r = R_c$, the velocity and depth at the seaward crest edge can be determined.

$$\frac{u_{r,2\%}}{\sqrt{gH_s}} = c_{u,r2\%}\sqrt{\frac{R_{u,2\%} - z_r}{\gamma_f H_s}} \tag{18}$$

$$\frac{h_{r,2\%}}{H_s} = c_{h,r2\%}\left(\frac{R_{u,2\%} - z_r}{\gamma_f H_s}\right) \tag{19}$$

Where:

γ_f =   friction factor, as suggested by Bosman et al. (2008)   [−]

With the distribution of overtopping volumes known from equation (12), each overtopping volume with a specific discharge can be linked to a run-up level based on the assumption that the run-up level is Rayleigh distributed. This maximum run-up level for the given volume and discharge can then be used in the Schüttrumpf and van Gent formulas (Van der Meer, 2007).

$$R_{u,x} = \sqrt{\frac{\ln(Pov, x)}{\ln(0.02)}}\, R_{u,2\%} \tag{20}$$

Trung (Trung, 2014), using the dataset of van Gent (2002), also bases the relation for flow depth on the assumption that the depth decreases linearly upward the slope. The overtopping volume is then calculated as the triangle of 'fictive' runup above the crest (see Figure 7, left). This approach results in:

$$h_{r,2\%,(z_r=R_c)} = c_A^h \frac{V_{2\%} \sin\alpha}{R_{u,2\%} - R_c} \tag{21}$$

Where:

c_A^h =   empirical coefficient, valued 1.1 with 95% confidence bounds at 1.06 and 1.14   [−]
          The application range of this formula is within $0 < h_{r,2\%}/H_{m0} < 0.18$

Considering the fact that c_A^h is valued at 1.1, almost half of the theoretical value, the wave tongue must in reality be curved in order to give the same overtopping volume (see Figure 7, right). Trung made the assumption that the overtopping volume is equal to the water running up above the crest level if the slope was infinite. However, as overtopping starts when the flow reaches the crest, deformation of the triangular 'run-up wedge' could take place. From this it seems that the assumption that the flow depth reduces

linearly on the seaward slope is flawed. Hughes (Hughes, 2004) notes that in the case of surging breakers (which would occur for steeper slopes) the wave tongue has a more concave shape, adding to the uncertainty of the triangular shape assumption.
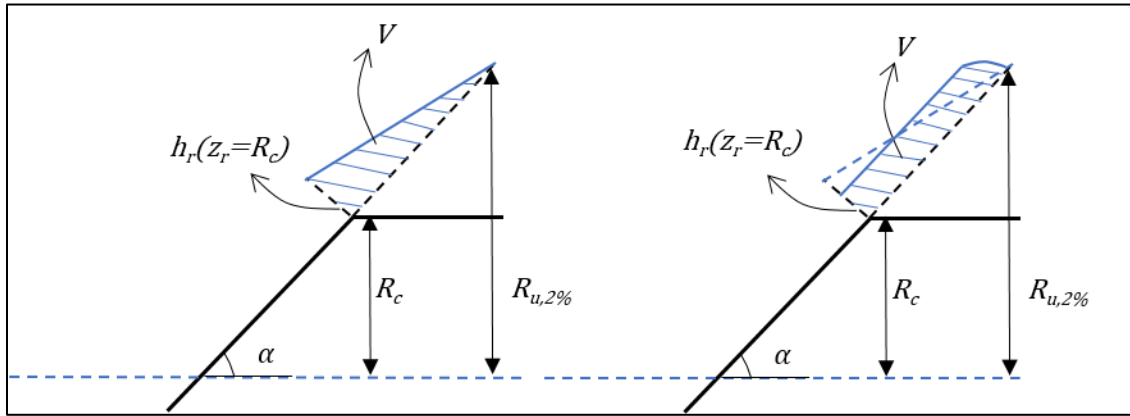
Figure 7: Wave-overtopping volume (based on Trung, 2014)

Considering the flow velocity, Trung (2014) analyses separately the velocity in vertical and horizontal direction. This results in a similar equation as was proposed by Schüttrumpf and van Gent, but decomposed in the horizontal direction which is deemed important for flow over the crest. Assuming that the flow over the dike crest is supercritical, the $u_{r,2\%}$ is related to $\sqrt{gh_{r,2\%}}$. Filling in the formula for $h_{r,2\%}$ and replacing c_A^h with an empirical coefficient for the flow velocity gives:

$$u_{r,2\%} = c_A^u \cos\alpha \sqrt{\frac{gV_{2\%}}{\sin\alpha H_{m0}}}$$
(22)

Where:

c_A^u = empirical coefficient, valued 0.88 with 95% confidence bounds at 0.85 and 0.90 $[-]$
The application range of this formula is within $0 < u_{A,2\%}/\sqrt{gh_{A,2\%}} < 1.49$

Above only the 2% values were evaluated. The maximum flow velocity and flow depth can be reasonably approximated by the Rayleigh distribution. Especially the upper 10% values (which are of interest for studying safety limits) are Rayleigh distributed (Hughes *et al.*, 2012). Different probabilities can then be calculated using (Van der Meer, 2011):

$$P_x = \exp\left(-\left((-ln(0.02))^{0.5}\frac{c_{x\%}}{c_{2\%}}\right)^2\right)$$
(23)

Where:

P_x = probability $[-]$
$c_{x\%}$ = coefficient for the flow depth or velocity for event with probability of exceedance x $[-]$

Van der Meer (2011) describes the results for the run-up velocities and flow depth on the seaward slope and compares the empirical coefficients from various researches, see Table 4. The theory applied in these studies is the same, and it's clear that the values of $c_{u,r2\%}$ and $c_{h,r2\%}$ are inconsistent. Van der Meer recommends the use of $c_{h,r2\%} = 0.2$ for slopes of $1:3$ and $1:4$ and $c_{h,r2\%} = 0.3$ for a slope of $1:6$, and $c_{u,r2\%} = 1.4 - 1.5$ for slopes between $1:3$ and $1:6$. It is mentioned that the large scatter in the results may come from the fact that measurement of this highly turbulent flow is difficult, or that the used assumptions may be incorrect. Bosman et al. (Bosman *et al.*, 2008) tried to find the difference in coefficients through the different slopes that were used in the researches of Schüttrumpf (2002) and van Gent (2002), but this method was not verified by the FlowDike tests.

Authors	Seaward slope, cotα	$C_{h2\%}$	$C_{u2\%}$
Van Gent (2002)	4	0.15	1.3
Van Gent H24 (2002)	4	0.21	1.7
Van Gent H1256 (2002)	3; 4; 4+berm	0.21	
Schüttrumpf (2001) small scale	4	0.22	
Schüttrumpf (2001) small scale	6	0.21	
Schüttrumpf (2001) large scale TMA	6	0.33	1.55
Schüttrumpf (2001) large scale	6	0.34	1.39
Schüttrumpf et al. (2002)	6	0.33	1.55
Schüttrumpf and Van Gent (2003)	4; 6	0.33/0.15	1.37/1.3
EurOtop (2007)	-	0.055cotα	1.55
Bosman (2008)	4; 6	0.10cot²α	0.30cotα
Flowdike 1 - Lorke et al. (2010)	3	0.20	0.35cotα
Flowdike 2 - Lorke et al. (2010)	6	0.29	

Table 4: Velocity and flow depth coefficients on the seaward slope for various researches (Van der Meer, 2011)

Van der Meer et al. (Van Der Meer, Provoost and Steendam, 2012) describe the analysis of run-up gauge records from model experiments and measurements at a sea dike. In contradiction to direct velocity measurements these show the progression of the front velocity of the wave tongue over the entire seaward slope. The extensive analysis shows that a velocity close to the maximum velocity is present between $15\% - 75\%$ of the maximum run-up level. This means that the description given by Schüttrumpf and van Gent largely underestimates the velocity on the seaward slope. This is visualized by Figure 8. Note also that the velocity increases over the first $\sim 40\%$ of the up rushing wave (so the maximum velocity doesn't take place around MWL). This might indicate that wave breaking can accelerate the wave tongue.
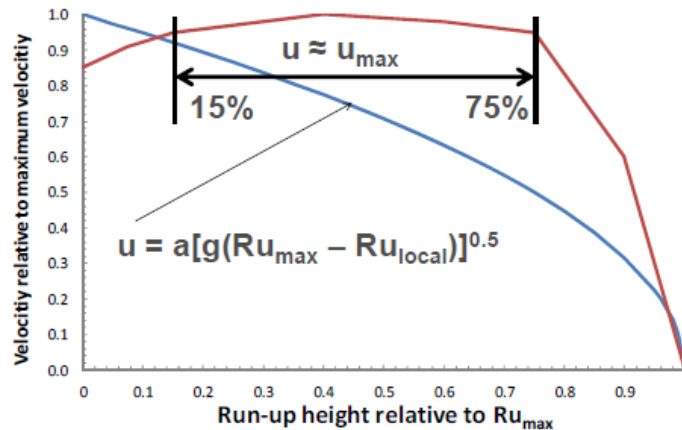
Figure 8: Red: 'average' measurement from wave run-up gauges,
Blue: Energy Balance method (Van Der Meer, Provoost and Steendam, 2012)

Van der Meer et al. (2012) also found a relation between the maximum velocity and the maximum run-up level of an individual up-rushing wave. A large scatter is however present, comparable to the distribution of wave heights and wave periods in a sea wave climate. It is concluded that this scatter might come from the fact that the maximum velocity is quite evenly distributed over the run-up length. This could cause the specific location of the maximum velocity to be defined 'by accident'. The (dimensionless) relation is given by a square root function:

$$\frac{u_{max}}{(gH_s)^{0.5}} = c_u \left(\frac{R_{umax}}{H_s} \right)^{0.5} \qquad (24)$$

Where:

u_{max}	=	The maximum run-up velocity	$[m/s]$
R_{umax}	=	The maximum run-up height	$[m]$
c_u	=	Stochastic variable, with $N(\mu = 1.0; V = 0.25)$	$[-]$

21

2.3.2 Overtopping flow velocity and flow depth: Crest

The flow velocity and flow depth at the seaward edge of the crest form the input parameters for the development of the wave tongue on the crest. The velocity on the crest can be calculated from a simplified momentum equation as given by (Schüttrumpf and Oumeraci, 2005):

$$\frac{u_{c,2\%}}{u_{r,2\%}(R_c)} = \exp\left(-c_{c,u}\left(\frac{x_c f}{h_{c,2\%}}\right)\right) \tag{25}$$

$$\frac{h_{c,2\%}}{h_{r,2\%}(R_c)} = \exp\left(-c_{c,h}\left(\frac{x_c}{B}\right)\right) \tag{26}$$

Where:

$c_{c,u}$	=	empirical coefficient for the flow velocity over the crest, equal to 0.5 (Schüttrumpf and van Gent, 2003)	$[-]$
$c_{c,h}$	=	empirical coefficient for the flow depth over the crest, equal to 0.89 (Schüttrumpf and Oumeraci, 2005) or 0.4 (van Gent, 2002)	$[-]$
f	=	Fanning friction factor	$[-]$

The bottom shear stress is incorporated in the momentum equation by replacing the viscous term in the momentum equation by the formula for bottom shear stress ($\tau = 0.5 \cdot \rho_w \cdot f \cdot u^2$; where f is the Fanning friction factor). For the flow depth on the crest an exponential decay is assumed. The decrease of both the flow depth and flow velocity does not contradict with the continuity equation, as it is not velocity and flow depth with respect to time that is considered ($q(t) = u(t) \cdot h(t)$). The flow velocity and depth become smaller over the crest due to bottom friction and dispersion respectively. Especially for small flow depths, the friction has a significant influence on the decrease of overtopping velocities (Schüttrumpf and Oumeraci, 2005). The flow depth also decreases because at the beginning of the dike crest a part of the water was found to flow back onto the seaward slope.

Bosman et al. (Bosman *et al.*, 2008) describe a relation for the flow depth that uses the deep water wavelength L_0 instead of crest width B to make the formula dimensionless. This makes sense as increasing the width of the crest shouldn't influence the flow depth or velocity on the beginning of the crest, because (usually) critical flow is present during overtopping. The equation by Bosman et al. can be used after the transition of the water from the seaside slope onto the crest (this transition causes significant turbulence and unpredictable flow). The $c_{trans,h}$ coefficient takes into account this transition over the seaward crest edge. The transition factor causes flow depths and velocities to decrease with approximately 20% over the seaward crest edge. Note also the friction factor for the crest (γ_c). The coefficients have been determined for regular waves by Bosman et al., who expects that the coefficients for irregular waves are almost the same ($\gamma_c = 1$, smooth slope).

$$\frac{h_{c,2\%}(x_c)}{h_{A,2\%}(x_c = 0)} = c_{trans,h}\exp\left(-c_{c,h2\%}\left(\frac{x_c}{\gamma_c L_0}\right)\right) \tag{27}$$

$$\frac{u_{c,2\%}(x_c)}{u_{A,2\%}(x_c = 0)} = \exp\left(-c_{c,u2\%}\left(\frac{x_c}{\gamma_c\, h_{c,2\%}(x_c)}\right)\right) \tag{28}$$

Where:

$c_{trans,h}$	=	empirical coefficient for the reduction of flow depth by the transition over the crest edge, equal to 0.81	$[-]$
$c_{c,h2\%}$	=	empirical coefficient, valued at 15	$[-]$
$c_{c,u2\%}$	=	empirical coefficient, valued 0.042	$[-]$

The EurOtop manual (2018) states that the flow depth on the crest decreases immediately after the crossing of the seaward slope, and remains relatively constant for a smooth crest. The flow depth is said to reduce to approximately $2/3$ of the flow depth at the seaward slope, so this is a bigger difference than

Bosman et al. (2008) propose. In the Overtopping Manual, use is also made of a velocity formula, specified for a $1:3$ slope and based on the Flow Dike experiments (van der Meer et al., 2011). This formula is very straightforward, it assumes an exponential reduction of the velocity and does not make use of a transition coefficient nor does it dependent on the flow depth.

Trung (2014), again based on data from van Gent (2002), also concludes that both flow velocity and flow depth decrease over the crest. The flow depth reduction over the crest is similar to the one proposed by Bosman et al., but Trung does not include a transition factor. Trung found that throughout most of the test data a decrease in velocity is visible after the crest is overtopped, but that occasionally an increase can be seen of the velocity. Trung notes that flow velocities are greater when the surface is more smooth and flow depths increase when the surface is more rough. As the effects are different, Trung introduces two friction coefficients.

It should be noted that it is assumed that the $u_{c,2\%}$ and the $h_{c,2\%}$ take place during the same overtopping wave (note for example that equation (25) uses equation (26) as input). To see if this correlation actually exists, Hughes et al. (Hughes *et al.*, 2012) examine how the maximum flow depths and velocities can be linked to the individual overtopping wave volume. This is done based on the dataset by Hughes and Nadal (Hughes and Nadal, 2009), which considers simultaneous overflow and overtopping. The flow depths and velocities were rank-ordered to find the 2% exceedance value for 9 runs. The corresponding maximum depth or velocity from the same wave was compared to this, as visualised by Figure 9.
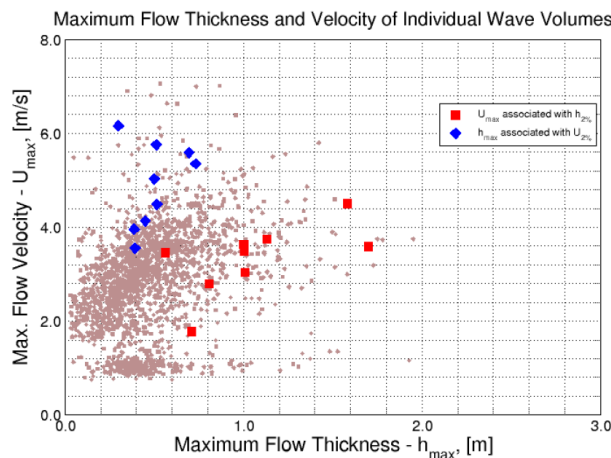
Figure 9: $u_{c,2\%}$ vs h_{max} for individual wave volume & $h_{c,2\%}$ vs u_{max} for individual wave volume (Hughes et al. 2012)

It can be seen that the u_{max} values associated with the $h_{2\%}$ values are well below typical values of the $u_{2\%}$ and vice versa. So, there is no proof that the 2% exceedance values of flow depth and velocity will occur in the same wave volume. Maximum velocities do thus not necessarily happen at the same moment that maximum flow depths take place. Different waves can give the same overtopping volume but different combinations of flow depth and velocity. Hughes et al. also plotted the $u_{2\%}$ and $h_{2\%}$ values of the same experiment (but from different wave volumes) against each other. Then a trend becomes visible that resembles a square root function. Trung (2014) also acknowledges a clear relation between the $h_{2\%}$ and $u_{2\%}$, but describes it as a linear dependency.

Van der Meer et al. (Van Der Meer *et al.*, 2011) suggest that more research could couple the wave period to the flow velocity and depth. Based on the assumption that the instantaneous loads are Rayleigh distributed, they argue that graphs linking flow velocity or depth to overtopping wave volumes give a discrepancy with the continuity equation. For the same overtopping volumes, lower flow velocities, flow depths and flow durations can be found for higher overtopping discharges. For flow durations the graph and results are however not given. The results are visualized by Figure 10 below, where it is visible that for the same volume, but for lower discharges, both lower velocities and flow depths are present.
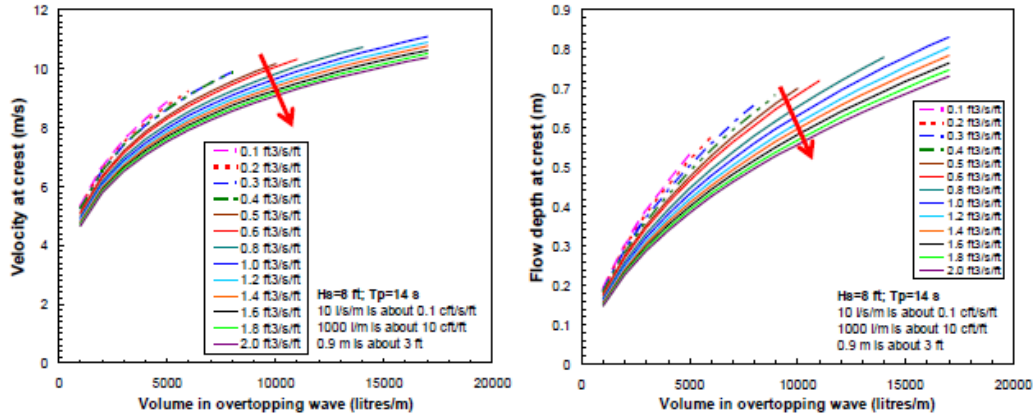
Figure 10: Flow velocity (left) and flow depth (right) at the seaward crest edge vs
the overtopping wave volume for various discharges (van der Meer et al., 2011)

2.3.3 Overtopping with respect to time

In the above two sections, the maximum overtopping flow velocity and flow depth over the seaward slope and crest have been discussed. In Appendix A, more insight is given into the time scale of overtopping flow. To characterise overtopping flow, the transformation of an overtopping flow with respect to time is briefly discussed here. Hughes (Hughes, 2011) describes the instantaneous flow velocity and depth following simple power functions:

$$h(t) = h_{max}\left[1 - \frac{t}{T_{ovt}}\right]^m \qquad \text{for } 0 \leq t \leq T_{ovt} \qquad (29)$$

$$u(t) = u_{max}\left[1 - \frac{t}{T_{ovt}}\right]^n \qquad \text{for } 0 \leq t \leq T_{ovt} \qquad (30)$$

Where:

T_{ovt} =   Overtopping time   [−]

Depending on the value of m and n (which are positive) the shape of $h(t)$ and $u(t)$ can be straight (linear), convex or concave. The general consensus is that the flow depth and velocity profiles are well represented by triangular shapes. These are given by a quick increase to a maximum and a more slow decrease back to zero (also described as 'saw-tooth' shaped). In this case, $m = n = 1$, and integration to get the overtopping volume gives:

$$V = \frac{u_{max}h_{max}T_{ovt}}{3} \qquad (31)$$

2.4 Overtopping flow: research on breakwaters

The literature treated in the previous section follows from research on smooth, gentle and impermeable slopes. Similar research on overtopping flow over breakwaters is less widely available. The research that is available on overtopping flow over breakwaters focusses mostly on the decrease of the mean overtopping discharge that occurs when overtopping water passes the crest. Overtopping discharges are often measured on the seaward crest edge. However this discharge isn't necessarily the same on the landward crest edge as losses can occur due to infiltration.

Various methods are available to determine the discharge for a certain distance away from the seaward crest edge. It is clear that often an exponential decrease is found when a overtopping wave flows over a crest or backfill. In the researches discussed here, the permeability was not specifically varied, and mostly the infiltration into the armour layer was studied. The used armour layers were chosen based on their stability for the chosen breakwater configuration under the used wave conditions. The research was performed for 'standard' breakwater designs, so no crest walls were part of the design.

24

Juhl and Sloth (1994)

Juhl and Sloth (Juhl and Sloth, 1994) measured the overtopping discharge at the inner crest edge of the breakwater and varied the width of the crest during experiments. The width of the crest (B) was incorporated in an overtopping formula (equation 32). It is clear from this formula that the freeboard has the largest influence on the overtopping discharge. The influence of the wave steepness and of obliquely incident waves was found to be significantly smaller than the reduction caused by the freeboard and the width of the crest.

$$\frac{q}{\sqrt{gH_s^3}} = \exp\left(-\frac{2R_c + 0.35B}{H_s}\right) \tag{32}$$

Besley (1999)

Besley (Besley, 1999) describes in a simple formula a reduction factor that can be used to express the losses in discharge over the crest. The reduction factor can be applied to the calculated overtopping discharge at the seaward crest edge. The formula is particularly made for simple, straight breakwaters with an armoured crest (see Figure 11, where $C_w = G_c$). The formula has a maximum of 1, no reduction, when the crest width equals $0.75 \cdot H_{m0}$. The obtained formula was derived for a rock slope with permeable under layer and core. This formula is also represented in the EurOtop manual (2018), where it is considered to be conservative.

$$C_r = 3.06 \exp\left(-1.5 \cdot \frac{G_c}{H_{m0}}\right) \tag{33}$$

Where:
  C_r = reduction factor for the mean overtopping discharge $[-]$
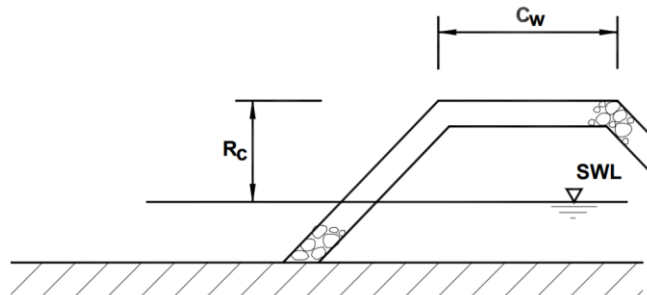
Figure 11: test set-up for Besley's reduction factor (Besley, 1999)

Other research

The reduction of discharge due to infiltration for breakwaters without a crest wall was also discussed in Jensen (Jensen, 1984), Steenaard (Steenaard, 2002), van Kester (van Kester, 2009) and Lioutas (Lioutas, 2010). These methods are discussed in some detail in Appendix B and are not used in further analysis in this thesis, as the methods are not considered to be suitable for a comparison with the study performed.

For Jensen (1984) the test set-up is not entirely clear, but appears to study overtopping over a backfill behind an armoured crest. Steenaard (2002) and van Kester (2009) study regular waves. Steenaard did find that as the overtopping discharge increases, the losses into the crest reach a constant value. This could indicate saturation of the armour layer. Van Kester adapted Besley and found an influence of the wave steepness on the reduction of the discharge over the crest. Lioutas (2010) is not studied further here as the used discharge formula is a fit for the specific test situation used. It uses a reduction factor (γ_c) similar to the reduction factor for e.g. roughness in the discharge calculation. This reduction factor incorporates the non-dimensional location on the crest x/B. As mentioned, this seems odd as making the crest width longer or shorter shouldn't influence the overtopping process before the end of the breakwater.

2.5 Conclusions on chapter 2

Considering the limits that are currently given in the EurOtop (Van der Meer *et al.*, 2018), it is clear that these are not based on instantaneous loads (the flow velocities and flow depths caused by overtopping waves). However, there is growing consensus that the overtopping limits should be based more on individual overtopping volumes instead of the mean overtopping discharge. Stability curves for people in fluvial flows can also be applied to people in overtopping flows (Sandoval, 2015). This gives more insight into the conditions that cause people to fall. The question is then what parameters influence the instantaneous loads over a breakwater caused by an overtopping wave.

From the EurOtop manual the most important overtopping formulas are given that are used in daily practice. It is clear that the parameters combined into the Iribarren number (α, $L_{m-1.0}$, H_{m0}) and structural parameters (R_c, γ_f) govern the run-up and overtopping formulas (both discharge and volume). Looking more in depth at the instantaneous loads, based on research on sea dikes, it is clear quite some debate still exists.

For the seaward slope of sea dikes, most theories use the $R_{u2\%}$, which includes the effect of friction and the Iribarren number, to define a 'maximum' run-up height (e.g. Schüttrumpf and van Gent, 2003; Bosman et al., 2008; Trung, 2014). Combining this with a simplified energy balance results in an equation for the velocity over the seaward slope. However, the empirical coefficients to fit these formulas are inconsistent. Van der Meer et al. (Van Der Meer, Provoost and Steendam, 2012) also note that the up rushing velocity based on the simplified energy balance does not accurately describe the actual flow velocity, as measurements showed that the maximum up-rushing velocity occurred over a significant part of the outer slope's length. For the flow depth on the seaward slope, the assumption that the depth decreases linearly from the mean water level seems flawed (Hughes, 2004; Van der Meer, 2011; Trung, 2014).

For flow over the crest of sea dikes, the velocity is often determined from a momentum equation or an assumed exponential decay, where results over the seaward crest edge form the boundary condition (Schüttrumpf and van Gent, 2003; Trung, 2014; Van der Meer *et al.*, 2018). The flow depth is approximated by an exponential decay, Bosman et al. introduce the $c_{trans,h}$ coefficient that takes into account the transition from the seaward slope to the flat crest (Bosman *et al.*, 2008). The flow depth forms an input variable in the momentum equation for the flow velocity. It is noted however that the $u_{c,2\%}$ and the $h_{c,2\%}$ do not take place during the same overtopping wave (Hughes *et al.*, 2012). Van der Meer et al. (Van Der Meer *et al.*, 2011) suggest that more research could couple the wave period to the flow velocity and flow depth. The general consensus is that the profiles of the flow velocity and flow depth versus time follow a triangular shape (Hughes, 2011).

From research performed on breakwaters, multiple overtopping formulas can be found that discuss the reduction of overtopping discharge over the width of the crest. Of these formulas, the one by Besley can be applied directly to the discharge formula from the EurOtop (Besley, 1999). Van Kester (van Kester, 2009) also describes the influence of the wave steepness on the overtopping discharge over the crest. Steenaard (Steenaard, 2002) describes saturation of the crest material. Besides the method of Besley, the method of Juhl and Sloth (Juhl and Sloth, 1994) can be used for comparison with this study.

Hypotheses
Concluding on the research described in this chapter, some hypotheses have been written down below. These hypothesize which parameters and processes described in this chapter are expected to influence the process of wave overtopping flows over a breakwater under construction.

   a) **The flow depth on the run-up crest edge** depends more explicitly on the characteristics of the up rushing wave ($\xi_{m-1,0}$) as the assumption that the flow depth decreases linearly over the

outer slope could be flawed. Also, the flow depth is influenced by the height of the 'cut-off' of the up rushing wave, the relative freeboard (R_c/H_{m0}). Depending on the shape of the wave at the cut-off point, the transition towards flow over the crest could differ. For the set-up in this thesis, which is likely to show mostly surging waves, it is hypothesised that the transition over the crest edge is relatively smooth;

b) **The flow velocity on the run-up crest-edge** depends more explicitly on the characteristics of the up rushing wave, where the velocity is influenced by the Iribarren number ($\xi_{m-1,0}$). This instead of using $R_{u,2\%}$ and $V_{2\%}$, formulas that incorporate similar parameters but have limitations of their own and which don't necessarily relate clearly to either u or h. The assumption of a very simple energy balance as in previous research seems too disputed, it is expected that the specific form of breaking of the wave could influence the run-up velocities;

c) **The mean overtopping discharge, flow depth and the flow velocity over the crest** follow an exponential decay over the length of the crest;

d) **A relation between the** $u_{c,2\%}$ **and** $h_{c,2\%}$ can be found, but the $u_{c,2\%}$ and $h_{c,2\%}$ do not occur within the same wave. This should be considered in defining a method that is used to define the safety of personnel in overtopping flows;

In the following chapters the approach to test the hypotheses and answer the research questions is given.

3 Numerical modelling

The empirical data for dikes that was presented in the previous chapter, mostly follows from wave-flume tests. For fitting the empirical formulas, various types of measurements are required. The flow depth and velocities of up-rushing and overtopping waves are measured by wave gauges and micro propellers respectively. The overtopping volumes are measured by overtopping tanks. On the seaward slope, the run-up velocity can also be determined by a capacitance wire stretched above the slope, the derivative of this data gives the up-rushing velocity. For a breakwater under construction, test data was not found for all parameters.

A large inconsistency can be found between the empirical constants from various physical model tests for overtopping flows over dikes. This could indicate that the process of wave overtopping is complex which makes measurement of flow velocity and flow depth difficult. It is expected that for breakwaters, with their rough and permeable characteristics and steep slopes, setting up an accurate measurement system could become expensive. That is why it is opted here to perform a numerical study.

It is important to understand what the overtopping actually looks like and what processes play a role. To give a total overview of the various processes that are going on, it is required to measure many different things simultaneously over a rather continuous area. Whereas the use of many wave gauges and velocity probes can become difficult and expensive in a physical model, their numerical counterparts are 'free' and can be installed at any point of interest. Numerical modelling then makes it easier to test various designs within a closely monitored environment.

Furthermore, the disadvantage of having a long computation time that can follow from extensive numerical simulations can be mitigated using a High Performance Computer (HPC). With the HPC, simulations can be performed simultaneously and sped up by running in parallel.

It is important to note however that numerical modelling always brings uncertainties with it. The choice for the specific numerical model, OpenFOAM, is elaborated below. A numerical model should always be validated with test data. So a specific experiment was chosen that concerns an unfinished rubble mound breakwater and where (some of the) relevant parameters were measured. This experiment is described in chapter 4. After validation of the numerical model (chapter 5), the model is used to study the overtopping process.

The numerical model can be set up using various Computational Fluid Dynamics (CFD) models. Care should be taken that the right model is chosen. Multiple branches of CFD models exist, which differ based on the assumptions that are employed when considering the equations of fluid motion. The choice for a model is based on what is required from the model. Using a discretized space (various methods of discretization exist) the equations are solved iteratively. Some examples of widely used CFD for overtopping applications are the nonlinear shallow water equation models (NLSW), Boussinesq type models and Navier-Stoke models (NS).

1. The NLSW models use the shallow water equations which can include hydrostatic or non-hydrostatic pressure terms. They are often used for 1D problems, where the velocity is depth averaged. SWASH is one of these models, which has also been applied to model overtopping discharges (Suzuki, Verwaest and Hassan, 2011). This study shows how the overtopping of an impermeable dike is calculated using $q(t) = u(t) \cdot h(t)$, where $u(t)$ and $h(t)$ are the overtopping flow velocity and flow depth over the dike respectively. It is important to note that the SWASH model incorporates a non-hydrostatic pressure term (as opposed to most NLSW models), which

showed to play an important role in the wave transformation. A disadvantage of the model is that it is not possible to combine the model with flow through a porous medium.

The XBeach-G model is similar to the SWASH model, but makes it possible to account for infiltration and erosion of gravel beaches. The results for the overtopping flows are promising as morpho dynamic updating is added to the model (McCall *et al.*, 2014). The model is also tested for composite beaches, but has not been validated against larger rock gradings like the ones used on breakwaters.

An advantage of SWASH and XBeach-G is that the models are computationally efficient and promising for applications on structures which are not too steep and don't possess sudden transitions.

2. Boussinesq type models can be employed for greater water depths than the depth of applicability for NLSW models. The Boussinesq equations (like the NLSW equations) also express the flow equations without dependence on the vertical coordinate. In contrast to NLSW models, Boussinesq models also model frequency dispersion besides non-linearity. Many variations on the Boussinesq models exist, all with varying capabilities like the inclusion of wave breaking, a good description of non-linear waves and models that consider changing bathymetries. Some Boussinesq type models have even been developed to represent the interaction of waves with steep walls (see e.g. (McCabe, Stansby and Apsley, 2013). Boussinesq type models and NLSW models can be very similar, depending on what the emphasis is on.

3. NS models solve the full Navier-Stokes equations. Often these models are Reynolds averaged, which means that the flow velocity is separated into a mean and a fluctuating component. The NS equations are then often called the Reynolds Averaged Navier Stokes (or RANS) equations. This operation creates a term in the Navier-Stokes equations that is known as the Reynolds stress, which is the component that allows for turbulence modelling. Turbulence models are used to close the Navier-Stokes equations. The advantage of RANS models is the level of detail that is obtained. It is possible to utilize advanced turbulence models. Relatively recently, models have been developed which can handle flow through porous media and these models have also been validated for breakwaters. The required computational effort is relatively high, but computational power is developing rapidly. Especially for 2D simulations, NS models are applied more and more.

4. A fourth method is given by smoothed particle hydrodynamic models (SPH models). Such models apply a Langrangian reference frame to study CFD. As these models however don't offer practical engineering applications yet, these are not discussed further here.

3.1 OpenFOAM and Waves2Foam

A Navier-Stokes model has been employed here: the open-source model OpenFOAM (see e.g.: Weller *et al.*, 1998). OpenFOAM is an open-source library which is used widely in the engineering community and is gaining traction in coastal engineering applications. It is basically an extensive structure of C++ libraries and codes that can solve CFD problems using finite volume discretisation. It also includes mesh generation and sampling tools, as well as an option to run simulations in parallel. Users with experience in C++ programming can relatively simply adapt applications and create new solvers.

OpenFOAM can solve two phase flows by linking the NS equations to a Volume Of Fluid (VOF) method to treat the free surface. OpenFOAM has been extended by a module called Waves2Foam, which allows for the generation and absorption of waves using 'wave relaxation zones'. A thorough description of the

model and the implementation into OpenFOAM is given in Jacobsen et al. (Jacobsen, Fuhrman and Fredsøe, 2012).

Waves2Foam has also been equipped with a module for flow through porous media, where the momentum equation is volume averaged. This averaging introduces terms that represent the frictional forces caused by the porous media. These terms are described by the (extended) Forchheimer equation. The method is described in detail in Jensen et al. (Jensen, Jacobsen and Christensen, 2014), but the basics are also discussed in section 3.3. Especially because the investigated structure is built up of (relatively fine) quarry run and underlayers, the structure is treated as a permeable continuum in 2D. A 2D set-up of the model is sufficient, as no interaction with obliquely incident waves is studied here nor is air entrapment a problem in the interaction of impacting waves with a porous structure (this is the case with crest walls, see e.g. (Jacobsen *et al.*, 2018)).

In this specific case, the waves that are created by the relaxation zone on the inlet have been generated with a potential flow solver called OceanWave3D (OCW3D, (Engsig-Karup, Bingham and Lindberg, 2009)). This is done because OCW3D can take the velocity of a wave-paddle as input and so can propagate the same waves as were used in the experiment. The link between these two models is described by Paulsen et al. (Paulsen, Bredmose and Bingham, 2014). This specific method was applied for investigations on rubble mound breakwaters before (see e.g. (Jacobsen *et al.*, 2018)).

3.1.1 Basic equations

In this thesis, the interFOAM solver is used in combination with the Waves2Foam extension. InterFoam is a solver for 2 incompressible fluids using a VOF interface capturing approach. In the following, some details of the VOF method and waves2Foam are elaborated, based on (Jacobsen, Fuhrman and Fredsøe, 2012).

The continuity and momentum equation that are solved within the computational domain are given by:

$$\frac{\partial \rho \mathbf{u}}{\delta t} + \nabla(\rho \boldsymbol{u} \boldsymbol{u}^T) = -\nabla p^* - \boldsymbol{g}\boldsymbol{x}\nabla\rho + \nabla(\mu\nabla\boldsymbol{u} + \rho\boldsymbol{\tau}) + \sigma_\tau \kappa_\gamma \nabla\gamma \tag{34}$$

$$\nabla \cdot \boldsymbol{u} = 0 \tag{35}$$

Where:

$\boldsymbol{u}$	=	(u, v, w); the velocity vector	$[m/s]$
p^*	=	pressure in excess of the hydrostatic	$[kg/ms^2]$
$\boldsymbol{g}$	=	Acceleration due to gravity	$[m/s^2]$
ρ	=	Density of the medium, depending on result of VOF method in each cell	$[kg/m^3]$
$\boldsymbol{x}$	=	(x, y, z); location vector (cartesian)	$[m/s]$
μ	=	$v \cdot \rho$; dynamic viscosity, depending on result of VOF method in each cell	$[kg/ms]$
v	=	kinematic viscosity	$[m^2/s]$
$\boldsymbol{\tau}$	=	$\frac{2}{\rho}\mu_t \boldsymbol{S} - \frac{2}{3}k\boldsymbol{I}$; specific Reynolds stress tensor	$[m^2/s^2]$
		μ_t = dynamic eddy viscosity	$[kg/ms]$
		$\boldsymbol{S} = 1/2(\nabla\mathbf{u} + (\nabla\mathbf{u})^T)$; Strain rate tensor	$[1/s]$
		$\boldsymbol{I}$ = Identity matrix;	$[-]$
		k = turbulent kinetic energy per unit mass	$[m^2/s^2]$
σ_τ	=	Surface tension coefficient	$[kg/s^2]$
κ_γ	=	Surface curvature	$[-]$
∇	=	$\left(\frac{\delta}{\delta x}, \frac{\delta}{\delta y}, \frac{\delta}{\delta z}\right)$; the Nabla operator	$[-]$

Note that the porosity as well as an additional term to account for the resistance of the porous medium is not represented in the continuity and momentum equations presented above. For a full description of the continuity and momentum equation, please refer to Jensen et al., where the full derivation is given

(Jensen, Jacobsen and Christensen, 2014). The additional resistance term is treated in more detail in section 3.3.

The Volume Of Fluid (VOF) method tracks the fluids (water and air) using a scaler field α. The distribution of the indicator function α is tracked by an advection equation given by:

$$\frac{\delta \alpha}{\delta t} + \nabla(\alpha \boldsymbol{u}) + \nabla\big(\boldsymbol{u}_r \alpha (1 - \alpha)\big) = 0 \tag{36}$$

Where:

α	=	Indicator function	$[-]$
$\boldsymbol{u}_r$	=	Relative velocity	$[m/s]$

The value of the indicator function is not rounded up or down when above or below (for example) 0.5 because then spurious oscillations occur. The convective term, including the relative velocity ($\boldsymbol{u}_r = \boldsymbol{u}_w - \boldsymbol{u}_a$), is a compression term which is used to keep the interface sharp (note that it only exists when the value of alpha is between 0 and 1). Still smearing can exist, so for visualisation one can choose what limit of alpha is considered air or water. With the indicator function, the spatial variation in a fluid property (here the local density ρ and dynamic viscosity μ), can be tracked by weighting:

$$\rho = \alpha \rho_w + (1 - \alpha)\rho_a \tag{37}$$
$$\mu = \alpha \mu_w + (1 - \alpha)\mu_a \tag{38}$$

Where the subscripts w and a denote water and air respectively.

3.1.2 Boundary conditions & Relaxation Zones

For the dry boundary faces, the boundary conditions have a pressure, velocity and indicator function value of zero. For the wet faces, the boundary condition is given analytically according to the chosen wave theory, which is evaluated at the face centres. For the boundary faces that are intersected by the free surface, the two intersections of the free surface with the face edges are computed and a local linear approximation to the real surface is defined (this is especially relevant for 3D applications). The indicator function equals the wet area divided by the area of the boundary face.

At the bottom of the domain, a slip condition is imposed, which means that viscous boundary layer effects are neglected. The front and back patches are empty (as we are dealing with a 2D case, so no solution is computed in the z direction). The upper boundary consists of an atmospheric boundary, which allows air to flow in and out of the domain whereas water can only flow out. In most coastal engineering applications the airflow is not of interest, so developments are directed towards excluding the air phase from the simulations to increase the computational efficiency.

For the indicator field, at the inlet, bottom and outlet the Neumann boundary condition is used (gradient equal to zero). At the atmosphere, the *inletOutlet* condition is used. This is normally the same as a Neumann boundary condition, but if the velocity vector of flow is away from the boundary (into the domain) the value is fixed to zero.

For the velocity field, the inlet is a Neumann condition. The bottom and outlet are given the slip condition. The slip condition erases the normal component of the velocity at that boundary, but keeps the tangential components untouched. So the flow doesn't feel the wall (no wall functions are implemented).

For the pressure field, the boundary conditions are the same as in the indicator field. The atmosphere has a *totalPressure* boundary condition, which makes the pressure uniform 0 at the boundary.

At both the inlet and outlet boundary, relaxation zones are used. Relaxation zones are implemented to avoid reflection of waves from the boundaries, and to avoid waves reflected internally (e.g. from the porous structure) to interfere with the wave maker boundaries (which would result in instabilities). Relaxation zones work by weighting the computed solution (of the velocity field and the indicator function) and the solution that has to be imposed (the target solution, based on the used wave theory). The velocity and indicator fields at every timestep follow:

$$\phi = \alpha_R \phi_{computed} + (1 - \alpha_R)\phi_{target} \tag{39}$$

$$\alpha_R(\chi_R) = 1 - \frac{\exp(\chi_R^{3.5}) - 1}{\exp(1) - 1} \qquad \text{for} \qquad \chi_R \in [0; 1] \tag{40}$$

Where:

ϕ	=	either **u** or α	$[-]$
α_R	=	relaxation function	$[-]$

Beware that α_R is the relaxation function, and so not the same as the α from the indicator function. χ_R is such that α_R is always 1 at the interface between the non-relaxed part of the computational domain and the relaxation zone. So when χ_R is equal to zero, only the computed value remains. When χ_R is equal to 1, only the target solution remains. From Jacobsen et al. (2012, their figure 3):
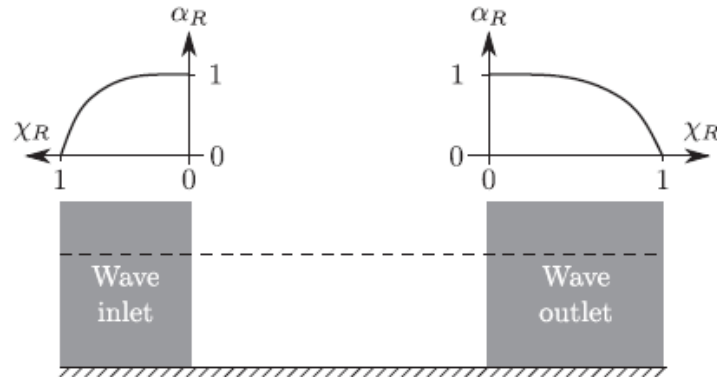
Figure 12: The relaxation function over the length of the inlet and outlet relaxation zones.

In this manner, relaxation zones also make sure the water level in the numerical flume stays fixed, which is relevant as the overtopping discharge can affect the water buffer in the wave flume in an experimental set-up. Also no accumulation of water in the domain due to Stokes drift is caused with this method.

3.1.3 Discretization

Considering the discretization of the domain, OpenFOAM uses a finite volume discretisation which makes use of conservation of mass and momentum between the control volumes. The numerical discretisation schemes that are used for the numerical approximation of the momentum, mass and advection equation for the indicator function are the same as for the settings of the case described in (Jacobsen, van Gent and Wolters, 2015). Also the solution algorithms for the pressure-velocity coupling (PISO, PIMPLE) are the same.

To reach numerical stability, the CFL (Courant-Friedrichs-Lewy, see section 5.1.1) condition has to be fulfilled, and a maximum Courant number of 0.35 is used. The timestep is set to be adaptive, so the CFL condition can be fulfilled by an automatically changing timestep. The mesh settings, as well as the utilisation of probes, wave gauges and overtopping faces, are discussed in chapter 5.

3.1.4 Coupling to OCW3D

As mentioned, OceanWave3D (OCW3D) is used to propagate the same wave signal as made by the wave paddle in the experiment. It is possible to simulate a part of the domain in OCW3D, reducing the relatively high costs of computations with OpenFOAM. Section 3.2 gives more details concerning OCW3D.

3.2 OceanWave3D

OceanWave3D (OCW3D) solves potential flow for propagating waves together with the fully nonlinear free surface boundary conditions (Engsig-Karup, Bingham and Lindberg, 2009). OCW3D uses high-order discretisation schemes on a vertically clustered grid (grid spacing more fine towards the free water surface) to transform waves over a long distance relatively accurately. This is possible for strongly non-linear waves up to their point of breaking.

Potential flow neglects viscous terms, which are mostly important close to boundaries or when waves break (especially turbulent viscosity then becomes important). The flow is assumed to be irrotational. Potential flow then describes the velocity field as the gradient of a scalar function which is the velocity potential. Combined with the continuity equation (for incompressible flow) the Laplace equation is obtained:

$$\nabla^2 \Phi = 0 \tag{41}$$

Where:

Φ =   The velocity potential for $\boldsymbol{u}$, where $\boldsymbol{u} = \nabla \Phi$ $[-]$

Using the Laplace equation, the number of unknowns can be reduced, as the velocity (a three dimensional vector) is then represented by a scalar (the flow potential). Besides the flow potential, the pressure is the other unknown. The solution to the Laplace equation completely depends on the chosen boundary conditions for the free surface, the bottom boundary and possibly structure boundaries (Engsig-Karup, Bingham and Lindberg, 2009).

3.3 Permeable flow

To model flow inside the breakwater, which comprises a porous medium, the RANS equations are volume averaged and the Volume Average Reynolds Averaged Navier-Stokes equations are obtained (VARANS, as documented in (Jensen, Jacobsen and Christensen, 2014)). The averaging is done over a volume that can be assumed larger than the length scale of the pores in the porous medium. In the volume averaging, a term is included that represents the frictional forces due to the presence of the porous medium (F_i). Also an added mass term is included, which considers that extra momentum is needed to accelerate a volume of water through a porous medium (Van Gent, 1995).

The Forchheimer equation forms the closure model for the VARANS equations. The Forchheimer equation represents the frictional forces from the porous medium and includes a linear and a non-linear resistance component. Here also the added mass term is included, giving the so-called extended Forchheimer equation:

$$F_i = a\rho[\overline{u_f}] + b\rho\sqrt{[\overline{u_f}][\overline{u_f}]}[\overline{u_f}] + (C_m)\frac{\delta}{\delta t}\frac{\rho[\overline{u_f}]}{n} \tag{42}$$

Where:

$[\overline{u_f}]$	=	the volume averaged ensemble averaged velocity over the total control volume including the solids of the porous media	$[m/s]$
a, b	=	resistance coefficients for which empirically derived equations exist	$[-]$
C_m	=	added mass coefficient	$[-]$
n	=	porosity	$[-]$

Depending on the flow regime, the linear and the non-linear resistance term influence the total resistance differently. These flow regimes can be distinguished using the Reynolds number:

$$Re_p = [\overline{u_f}]d_{n,50}/n\nu \tag{43}$$

Laminar (Darcy) flow is found for $Re_p < 1$, fully turbulent flow is present for $Re_p > 300$. For rougher gradings, the turbulent term (b) becomes dominant, for finer material the flow is laminar and the linear friction term (a) becomes dominant. To prevent scale effects of the model, it should be checked that the flow in the scaled core material is turbulent.

The relative importance of the turbulent resistance to the inertial resistance is also linear with the Keulegan-Carpenter number (($KC = u_m T/(nd_{n,50})$), where T is the wave or oscillation period and u_m is the maximum oscillation velocity; Van Gent, 1995). The KC number describes the importance of drag forces over inertia forces. It can be approximated by using the incident wave field and shallow water wave theory (Jacobsen, van Gent and Wolters, 2015):

$$KC = \frac{H_{m0}}{2} \sqrt{\frac{g}{h}} \frac{1.1T_{m-1.0}}{d_{n,50}} \tag{44}$$

For the formulation of the coefficients a, b and C_m, the van Gent equations are used:

$$a = \alpha \frac{(1-n)^2}{n^3} \frac{\mu}{\rho d_{n,50}^2} \tag{45}$$

$$b = \beta \left(1 + \frac{7.5}{KC}\right) \frac{(1-n)}{n^3} \frac{1}{d_{n,50}} \tag{46}$$

$$C_m = \gamma \frac{1-n}{n} \tag{47}$$

Where:
α	=	non-dimensional coefficient for laminar resistance	$[-]$
β	=	non-dimensional coefficient for turbulent resistance	$[-]$
γ	=	non-dimensional coefficient for inertial resistance (considers added mass)	$[-]$

Van Gent proposes to approximate α with 1000, β with 1.1 and γ with 0.34. Note that various values for these coefficients exist, and that this of course also depends on what equations are employed to determine a, b and C_m. Losada et al. (2008) note that one of the weaknesses of numerical modelling is the strong dependency of the model on the empirical constants α and β, which are still quite uncertain. Jensen et al. (2014) research the resistance coefficients for various flow regimes and multiple calibration cases. It is concluded from this parameter investigation that $a = 500$ and $\beta = 2.0$ should be used when no other values are available. These values make sense as turbulent flow is considered dominant in breakwater structures so relatively more weight should be given to the turbulent friction term.

In literature, like in (Jensen, Jacobsen and Christensen, 2014), the d_{50} is often used in the notation. It is considered that in fact the $d_{n,50}$ is meant here, as this is what van Gent uses in his 1995 publication.

It should be noted that the VARANS equations used in the porosity module do not take numerical turbulence modelling (eddy viscosity) into account. It is argued that the effect of turbulence in the porous structure is already included in the experimentally determined coefficients in the Forchheimer equation. Including a turbulence model would hence introduce an error into the porous medium.

3.4 Turbulence modelling

With the Navier-Stokes equations it is possible to solve fluid mechanics problems numerically, using initial conditions and boundary conditions. To this end the NS equations are discretised. If however we want to

solve turbulence down to the Kolmogorov length scales (the smallest scales in turbulent flows), the numerical grid needs to be scaled down to this scale. This would mean that the number of grid points goes into the millions for a barely turbulent flow in a simple geometry. The Courant criterion then also requires a very small timestep. So for engineering applications, such a Direct Numerical Solution (DNS) of the turbulent flow is not possible.

Turbulence however does play a role in fluid mechanical problems. For engineering applications, the Reynolds number (the ratio of inertia over viscosity, $Re = uL/\nu$) is often much larger than 100.000, indicating turbulent flow. When viscous forces are dominant, and the Reynolds number is low, the flow is laminar. To model turbulent flows in numerical models for engineering applications, 2 models are employed often: RANS models and Large Eddy Simulation (LES) models. LES resolves large eddies directly through a sufficiently refined mesh, whereas eddies smaller than the mesh are modelled. RANS models are used most often, due to their relative computational efficiency.

RANS models use the Reynolds Averaged Navier-Stokes equation. By ignoring the fluctuating part in the RANS equation, an error is introduced. This is solved by adding additional turbulence viscosity models, which model the transport and dissipation of the energy of the fluctuating part of the velocity. Especially when wave breaking is occurring, turbulence models are required. The turbulence model introduces a turbulent viscosity (or model viscosity) to the normal kinematic viscosity of the fluid. The turbulent viscosity is often a function of a turbulent kinetic energy and a dissipation rate.

Well known models are for instance the $k - \varepsilon$ model and the $k - \omega$ model, where k is the turbulent kinetic energy and ε and ω are turbulent dissipation rates. These models are also known as 2 equation models. For turbulent energy and dissipation, additional transport equations are required. The $k - \omega$ model, models the viscosity as such: $\nu_{turbulent} = k/\omega$. The total viscosity ($\nu_{tot} = \nu + \nu_{turbulent}$) of the fluid is thus increased when sufficient turbulent energy is present. Turbulent kinetic energy is generated in areas with fluid shear (steep velocity gradients, e.g. mixing layers) and zones with friction (e.g. close to walls). So the turbulent energy and dissipation often depend on characteristics of the flow. RANS models are often combined with wall functions, which model the flow near a wall boundary (following the Law of the Wall). This is done so it is not required to have a very fine mesh around the wall surfaces. Wall functions link the fully turbulent region to the inner viscous layer.

It should be noted that because the turbulent viscosity is a continuous field throughout the domain, it is not forced to zero at the free surface itself. The turbulence model causes the turbulent viscosity to be unphysically large near the air-water interface. In reality, at the interface of the lighter and heavier fluid, the turbulence is reduced to zero. These physics are however not incorporated in the turbulence models in OpenFOAM, where the turbulent parameters are continuous over the surface. For a thin layer of overtopping water, the turbulence at the air water interface could be much too high. If the air moves relatively slowly and the water rushes over, a shear stress is induced at the interface that in reality doesn't exist. This exacerbates the turbulent viscosity and dissipates even more energy.

This can cause diffusion of the boundary, which is counteracted by a term in the VOF method that sharpens the gradient. The effect of turbulence on the interface however is minor, but it is uncertain how it would affect the overtopping flow. Turbulence models that take into account the density variation between the two immiscible phases can avoid the diffusion of turbulent energy production around the free surface. This then more accurately describes breaking waves.

A problematic feature of the modelling of turbulence in OpenFOAM, is that it is currently not possible to model turbulence only outside the porous domain. The values for the porous characteristics of the breakwater were derived from experimental results and so already include all dissipative effects

(including turbulence). Introducing a turbulence model will then require modification of the resistance parameters of the porous structure, or double dissipation of the wave energy will occur. In the future, the system of equations could be different inside and outside of the structure. Multiple cases modelled in Waves2Foam, like Jacobsen, et al. (2015), therefore argue that for cases with limited wave breaking, it is possible to study the bulk hydrodynamics without the inclusion of a turbulence model.

This assumption is also used in (Jacobsen *et al.*, 2018), where the wave impact on a crest wall is modelled. Their results are very promising and it is reasoned that turbulence does not impact the dissipative and reflective properties of the structure significantly when wave breaking plays little or no role outside the permeable structure.

A check has been performed so no wave breaking occurs in the test set-up that is used in this research. In the wave field, turbulence is mostly induced by wave breaking. The runs to validate the wave field (chapter 5) are for this reason made without a turbulence model. The shear caused by the velocity difference between the flow in the porous medium and the overtopping flow is however expected to influence the velocity profile in the overtopping wave.

For this reason, a test run was performed with the $k - \varepsilon$ turbulence model, to study the effect on the velocity profile of some overtopping waves. It should be noted that near the wall, $k - \varepsilon$ makes a quite significant error so it is not to be used for modelling the viscous sublayer. Although for instance the $k - \omega$ model has improved near-wall treatment, $k - \varepsilon$ is used as the wall layer is not the area of interest. For this reason, no refinement around the bottom wall or any wall-functions are applied, but a slip boundary condition is applied. Note that on the structure itself it is not possible to impose a boundary layer, but this would also not be relevant considering the roughness of the porous medium.

To make use of the $k - \varepsilon$ turbulence model, initial values for k and ε have to be imposed. Two different runs were performed. One where the initial values at the inlet were based on very turbulent flow conditions, the other where the turbulent kinetic energy is set to zero. The latter is selected based on the facts that 1) no waves are expected to break before reaching the structure and 2) the wave forcing on the inlet is also based on this assumption (the theory of potential flow is imposed). The set-up and results of the two runs are described in detail in section 5.3.4.

4 Physical model

Where chapter 2 concluded with hypotheses to contribute to an answer to the main research question, chapter 3 has introduced the numerical method to study these hypotheses. This chapter will describe the experimental study that is reproduced in the numerical model and which is used for validation.

Considering intermediate phases during the construction process, 3 main situations occur during most projects where land-based construction is applied: 1) only the core material is placed, 2) the core material and the filter layer (also known as underlayer) are placed, and 3) the core material, underlayer and armour layer are placed. The three construction phases are schematically visualized in Figure 13. Data from a flume test was found for the second construction phase, which included measurements of the overtopping depth over the crest of the structure.

It is argued that this second stage is the most interesting to investigate here. If only core material is present, it is very likely that the structure will be unstable and will reshape under the influence of large overtopping waves. The third construction phase on the other hand is practically a finished breakwater and so large overtopping events are much less likely to happen. Of course there are also more intermediate stages to the ones visualised by Figure 13, but the second construction phase is likely to stay relatively stable under significant wave overtopping (see also section 5.4.2).
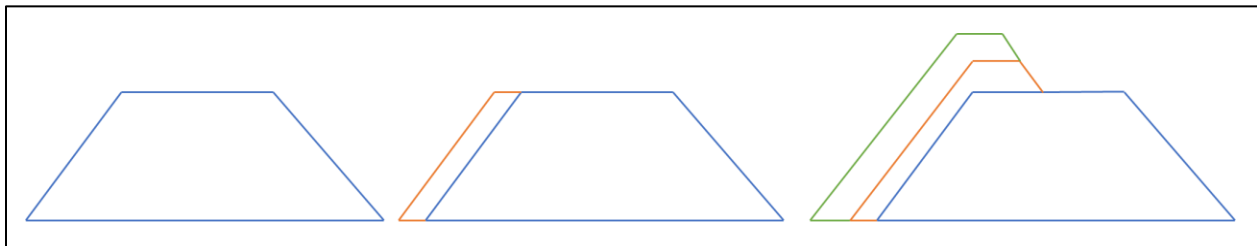

Figure 13: Construction stages

In 2012, 2D physical model tests were carried out as part of a final design optimization project of the Brass LNG breakwater. This breakwater was later realized near the town of Brass, Nigeria and shelters a LNG export facility. The tests aimed both at validating the stability of 3 partially constructed sections exposed to adverse weather conditions, as well as an assessment of a safe working level for the land-based equipment. For the assessment of the safe working level, a cross-section was studied that consisted of a core and underlayer (construction phase 2). Under these unfinished conditions the underlayer functions as a temporal armour layer. For the dimensions, see Figure 14 and Appendix Figure C.1.
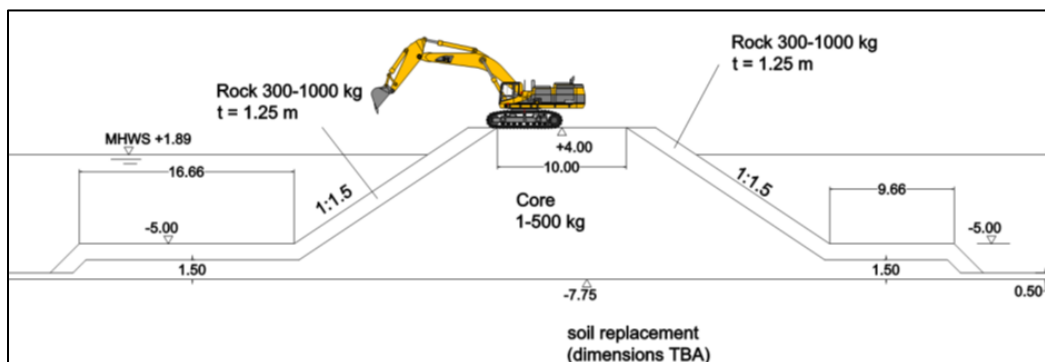

Figure 14: Cross section for the assessment of the safe working level (prototype scale, from model report)

The experimental set-up described in this chapter is used for the validation of the numerical model. Section 4.1 discusses the experimental set-up. Section 4.2 discusses the overtopping analysis that was performed with the results from the physical model tests. This indicates what parameters were deemed important for defining a safe working level. Section 4.3 shows some data from the wave gauges that measured the overtopping flow depth. Section 4.4 discusses scaling with the Weber number and the Reynolds number.

4.1 Test set-up

The tests were carried out by Delta Marine Consultants (DMC) in a flume with a length of 25 meters, a width of 0.6 meter and a height of the sidewalls of 1 meter. A model scale of $1:25$ was selected. The tests were performed with a water level at $+1.89\,[m]$ CD (so a water depth in front of the structure of $9.64\,[m]$). The waves were generated by a fully absorbing piston type spectral wave maker. This type of wave maker adjusts it's forcing based on the back pressure it experiences due to reflecting waves.

The water level was measured by resistance wave gauges which were recording at a frequency of $32\,[Hz]$. An additional set of wave gauges was installed on the crest of the breakwater, one at the transition from underlayer to core material on the seaward side, and one at the transition from core material to underlayer at the inner slope side. The spacing between the two gauges was $0.4\,[m]$. At the rear side of the structure, an overtopping tank was placed which was connected to an overtopping chute located near the side of the wave flume. This system measured the total volume of overtopped water during the test runs.

The seabed at the toe of the structure is situated at $-7.75\,[m]$ CD. The foreshore of the structure is very flat, and so is modelled as a horizontal bed. Because the water depth at the wave maker should be larger to generate the required wavefield at the breakwater, a step of $0.15\,[m]$ was built into the wave flume. This increases the water depth from $0.385\,[m]$ at the structure to $0.535\,[m]$ at the wave paddle (model scale). The step is located between 6.6 and 8.1 meters along the flumes' length (Figure 15).
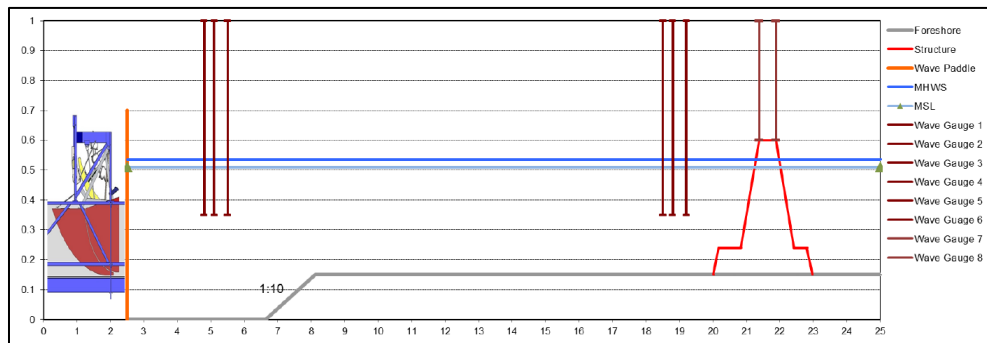

Figure 15: Schematized test set-up

During each run, 1000 waves were created, representing a storm with a duration of 3 to 4 hours, depending on the mean period for the different wave conditions simulated. The design wave conditions were translated to a JONSWAP spectrum with a peak enhancement factor of $\gamma = 6.0$ (swell). It was anticipated that the safe working level would be determined by the overtopping behaviour of swell waves.

The measured waves are given in Appendix C, test 3.04 is marked in red. This test was used for the validation of the numerical model as the structure stayed relatively stable under the incoming wave conditions (moderate progressive damage occurred, about 12 stones were displaced at the front under layer) whilst significant overtopping occurred.

The density of the used rock was $2.65\,t/m^3$ which is the same as in the prototype. Fresh water ($\rho = 1000\,kg/m^3$) was used in the physical model instead of seawater ($\rho = 1020 kg/m^3$), the scaling of the

rock grading was corrected for this. This resulted in a scaling factor λ_{rock} of 25.8 for the scaling of the armour stones.

$$\left(\frac{H_s}{\Delta D_n}\right)_{model} = \left(\frac{H_s}{\Delta D_n}\right)_{proto} \; ; \; \lambda_\Delta = \frac{\Delta_{model}}{\Delta_{proto}} = \frac{\lambda_{rock}}{\lambda_L} \tag{48}$$

Where:

Δ	=	$\frac{\rho_r}{\rho_w} - 1$; buoyant density, ρ_r = mass density of rock, ρ_w = mass density of water	$[-]$
λ_L	=	model length scale	$[-]$
λ_{rock}	=	scaling factor for rock	$[-]$
D_n	=	diameter of rock, where n is a percentage that states how much of the rocks in the grading are smaller than the diameter given.	$[m]$

A grading curve of the underlayer material is given by Figure 16. The graph gives a M_{50} of 700 $[kg]$, using $d_{n,50} = \sqrt[3]{M_{50}/\rho_s}$ and $\lambda_{rock} = 25.8$, it is found that the $d_{n,50} = 0.025\,[m]$. The core material was scaled according to Burcharth et al. (Burcharth, Zhou and Troch, 1999). Geometric scaling reduces the permeability of the core material too much, resulting in too high down rush pressures and hence a reduced stability of the rock layers. From Figure 17, it is visible that the d_{50} is given by 300 $[mm]$. The $d_{n,50}$ can then be given by approximately 0.0095 $[m]$.
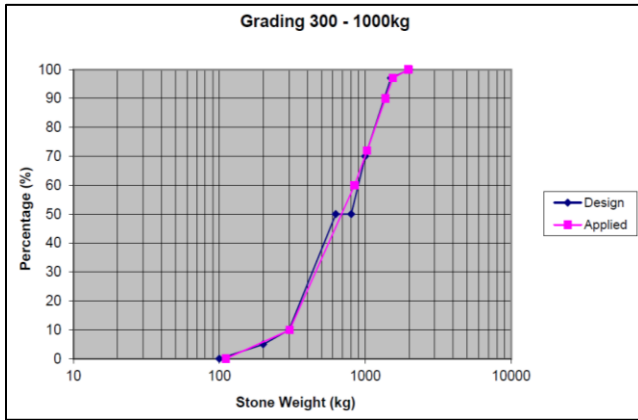

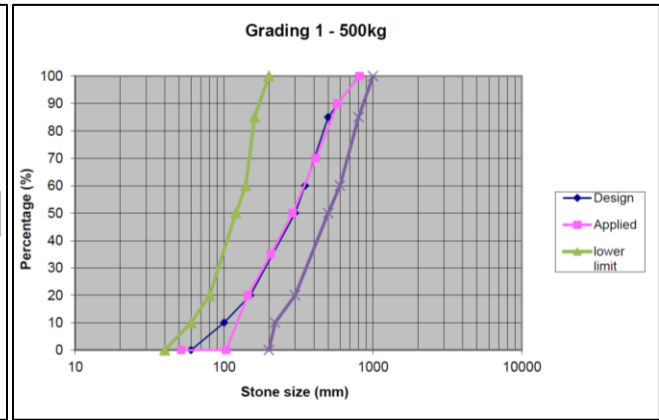Figure 16: Grading curve of underlayer (300 - 1000 kg)

Figure 17: Grading curve of core (1 - 500 kg)

It is possible to assume a porosity of 40% for the rock materials, like for example (Bruce *et al.*, 2009) suggest. A somewhat more intuitive method for the determination of the porosity of both the core material and the underlayer, is the method of Tsirel (Tsirel, 1997). Tsirel proposes to calculate the average porosity of bulk-placed materials using the steepness of the grading curves. The equation for the void ratio by Tsirel was derived from rock fragments packing experiments in many quarries. The manner of deposition, which for breakwaters is through an often dynamic water column, can alter the porosity. Also the length to thickness ratio of the material, the angularity and the d_{50} can influence the porosity. These observations are not included in the model of Tsirel, but should be kept in mind. The method of Tsirel is given by:

$$e = \frac{1}{90}(e_0)\arctan(0.645 n_{RRD}) \; ; \; n = \frac{e}{1+e} \tag{49}$$

Where:

e	=	void ratio (the volume of voids divided by the volume of solids)	$[-]$
e_0	=	void ratio associated with single-size particles of various shapes. Given in table 3.8 in the Rock Manual (CIRIA/CUR/CETMEF, 2007)	$[-]$

41

| n_{RRD} | = | Rosin-Rammler size uniformity, which is basically a measure for the steepness of the grading curve | $[-]$ |
| n | = | The porosity | $[-]$ |

The Rosin-Rammler size uniformity is given by:

$$n_{RRD} = 3 \log\left(\frac{ln(1 - y_{NUL})}{ln(1 - y_{NLL})}\right) / \log\left(\frac{NUL}{NLL}\right)$$ (50)

Where:

y	=	fraction passing value for both a nominal upper limit (NUL) and a nominal lower limit (NLL)	$[-]$
NUL	=	mass on the grading curve that is larger than 70% of the rest of the grading (M_{70})	$[kg]$
NLL	=	mass on the grading curve that is larger than 10% of the rest of the grading (M_{10})	$[kg]$

From table 3.8 in the Rock Manual (2007) it follows that for typical mechanically crushed rock the single-size void ratio e_0 ranges between $0.92 - 0.96$. For the underlayer material, the void ratio then ranges between $0.77 - 0.81$. Taking the average value, the porosity becomes 0.44. For the core material, the void ratio ranges between $0.41 - 0.43$. Taking the average value, the porosity becomes 0.296. The porosity for the core material is increased with 5%, which makes the porosity of the core 0.31. This is done because of the step that is seen in the applied grading curve in Figure 17. It is reasoned that this step slightly increases the permeability of the core material (less fines).

4.2 Assessment of safe working level

The assessment of the safe working level for the land-based equipment was performed by measuring the overtopping discharge (q), the percentage of overtopping waves (P_{ow}) and the overtopping flow depth ($h(x_c = 0)$) over the crest of the cross section. Results from the measurements, from 8 tests with different wave conditions, were used to calibrate equations for these parameters. The overtopping parameters were then calculated for various crest levels. The lowest working level that gives acceptable overtopping parameters then gives the safe working level. Using this method, the safe working level was $+4.25\,[m]$ CD.

The reasoning for analysing q, P_{ow}, $h(x_c = 0)$ was as follows. The percentage of overtopping waves was measured as it was considered to be a suitable measure for how safety is experienced by people working on the crest. The depth of the flow was seen as a 'direct measure for the safety level'. The parameter was analysed in its extreme ($h_{2\%}$) and for a significant level of overflow depth ($h_{10\%}$). The parameter q was analysed as it is studied extensively and used widely. In Appendix C the results for the overtopping parameters are given for various crest levels, based on the calibrated formula. The equations that were calibrated for the various parameters are:

- o q was calibrated using equations 5.9 & 5.10 from the 2007 edition of the EurOtop (Pullen *et al.*, 2007);
- o P_{ow} was calibrated according to equations 5.4 & 5.36 from the 2007 edition of the EurOtop;
- o $h(x_c = 0)$ was calibrated following equation 5.51 from the Rock Manual, which is the method of Van Gent (CIRIA/CUR/CETMEF, 2007).

4.3 Overtopping data

An example of the data produced by the gauges on the breakwater crest is given in Figure 18. This figure shows the overtopping depth for the gauge positioned on the seaward core crest edge. The fact that the flow depth doesn't return to the initial level seems to be caused by the fact that the wave gauge is positioned in a tube which retains some overtopped water. This also explains the small oscillations that

are visible after an overtopping wave, these could be free oscillations of the water surface in the tube. After some time has passed, this water infiltrates into the breakwater and the new tests start at the same level again.
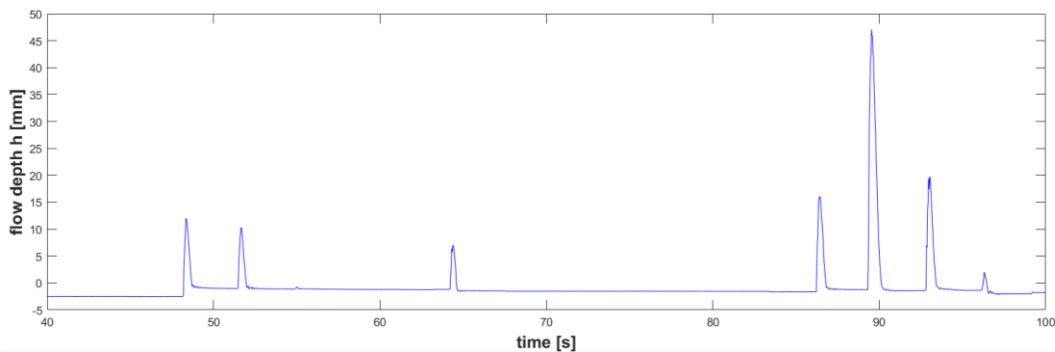

Figure 18: Overtopping depth for gauge on seaward core crest edge

It should be noted that the conductivity of the wave gauges is related to the temperature of the water. The results of the wave gauge are corrected for this by a sensor near the bottom of the gauge. So if the temperature of the water at the bottom is different than the overtopping water, the measurement will contain an error. However, it seems that the water is refreshed at every overtopping wave, so the temperature difference shouldn't have a significant influence.

Correlation analysis for overtopping patterns

It was found that during the physical experiment, the same wave signal was sent out multiple times. So, it is possible to see if different overtopping patterns occur for the same wave signals. The experiment lasted 3207 seconds. It is clear from correlation analysis, that the first 1159 seconds of the experiment were executed again after 2048 seconds. So whereas it seemed that a 1000 (different) waves were simulated, in fact the same shorter wave signal was used multiple times. Why this was done in the experiment is not clear.

Correlation analysis calculates the correlation sequence of two signals. By shifting signal A over signal B, the correlation is calculated at each timestep by taking the product of the two signals. This product is largest when the two signals are exactly equal and smallest when the signals are exactly out of phase. As the correlation is computed at each time lag (lag indicating that the signals are shifted with respect to each other over time) it is possible to see at what time-lag the maximum correlation occurs. A good way to visualize the largest correlation is by plotting the normalized correlation coefficient (the correlation coefficients are normalized to the maximum correlation coefficient in the data set). Here, the correlation between the calibration dataset and the experimental dataset is calculated.

Figure 19 shows what such an analysis results in. The y-axis shows the normalized correlation between the calibration dataset and the experimental dataset, and the x-axis shows time. The correlation analysis shifts the results from the calibration run over the experimental run, hence the time starts at minus the duration of the calibration run. As expected, the correlation when the time is zero is the largest. This shows that the experimental run starts with the calibration signal. At 2048 seconds, the correlation between the calibration and the experiment is very close to this maximum value again, and it can be concluded that the same signal is send out at that timestep.
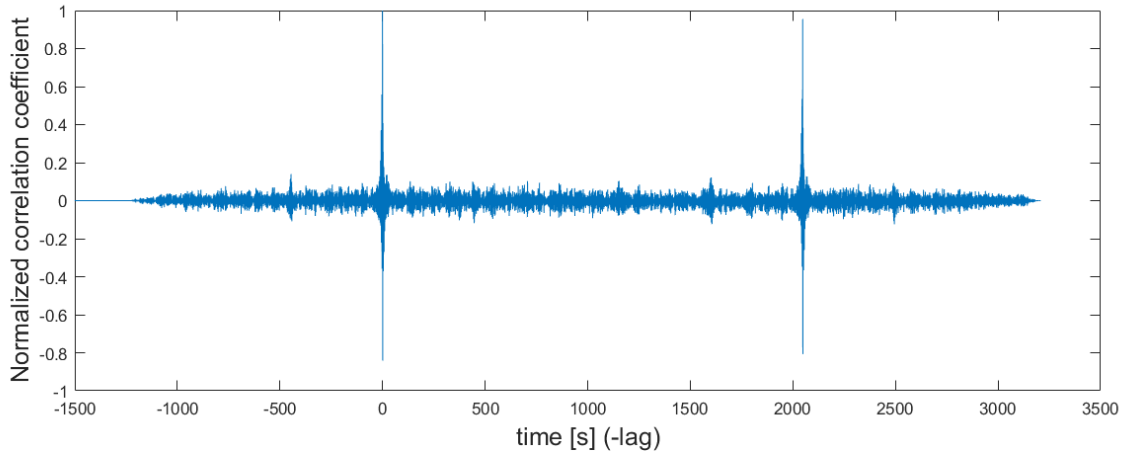
Figure 19: Cross-correlation between calibration dataset and experimental dataset

From taking the overtopping levels at the moments that the same waves were imposed, so at $t = 0 \ [s]$ and $t = 2048 \ [s]$, it is possible to see the correlation between the two overtopping signals (Figure 20).
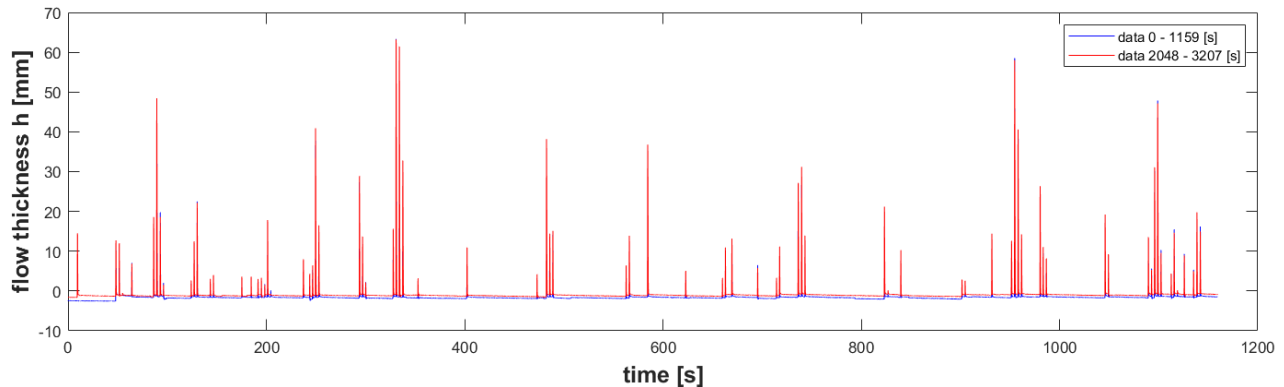

Figure 20: Flow thickness (depth) comparison at gauge 7 for two timeseries occurring during the same experiment

As is visually already quite clear, the results for the two timeseries are very similar. Also the PCC (0.9923) and the RMSE (0.6906) show that the mismatch is minimal (see section 5.2 for details on the PCC and RMSE). This indicates that the overtopping depth is not very stochastic in nature and does not vary significantly under the same wave forcing. This is relevant, as stochastic processes are impossible to reproduce with the deterministic numerical model employed here. It can also be concluded that reshaping of the structure is minimal, as well as the effect of water loss over the structure.

What should be noted about the results however is that the base level of the data visualised by the red line is somewhat higher than the baseline of the data visualised by the blue line. This is possibly explained by the slow saturation of the tube that the wave gauge is positioned in by water which might not be able to flow out as easily as in the beginning of the experiment.

4.4 Scaling with the Weber number and the Reynolds number

The experiment uses Froude similitude to scale from the prototype scale to the experimental scale. It should be noted that, although the experimental set-up investigates overtopping flow, the influence of the Weber number or the Reynolds number was not specifically checked.

The Weber number represents a ratio between a fluid's inertial forces and the forces related to surface tension. This number is especially investigated when for instance spray formation is studied, but also plays a role in the flow of thin layers of water. When the Weber number is larger than 120, the effect of

44

the surface tension is negligible (based on a study on fluvial flows, Peakall and Warburton, 1996). The Weber number is defined as:

$$We = \frac{\rho L v^2}{\sigma} \tag{51}$$

Where:

ρ	=	Density of the water	$[kg/m^3]$
L	=	Characteristic length-scale, e.g. flow depth or wavelength	$[m]$
v	=	Velocity	$[m/s]$
σ	=	Surface tension, usually equals $0.07\ N/m$	$[N/m]$

Although the surface tension will not have an effect on the waves in front of the structure, one can expect that the surface tension has in fact got an effect on the thin layers of water overtopping the structure. When the model would be scaled up to prototype scale, the results should take this into account. For the test program of simulations that will be performed in OpenFOAM it is chosen to set the surface tension to a small number, to make sure that the flows of interest are not affected by the surface tension. This is the only parameter that is adapted in this way, all other settings are made to represent as good as possible the model set-up from the experiment. This is done because the effect of the surface tension can have a significant influence on the stability curves if scaled up to prototype level.

To visualise the issue with the Weber number, some stability curves for humans are plotted combined with a combination of flow depth and flow velocity when the Weber number equals 120 (Figure 21). The flow depth and flow speed were calculated for the model scale and are scaled up in this picture to the prototype scale. The black line shows the critical line above which flows are unaffected by the Weber number. It is clear that a significant part of the flows that can destabilize people is influenced by the Weber number. When we reduce the surface tension to 0.001, we see that practically all flows that are of interest are now above the critical line. These flow combinations can now be analysed and scaled up without having to consider the changed effect of the surface tension.
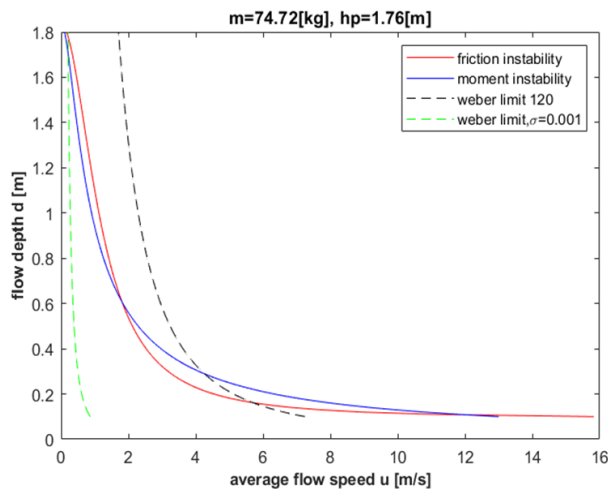
Figure 21: Stability curves and Weber limits

The Reynolds number was already mentioned in section 3.3. As during the experiment no measurements were made of the flow velocity within the core, it is not possible to say with certainty that the flow within the core was in fact turbulent. The numerical model showed however that at moments of maximum overtopping the flow velocity was sufficiently high to surpass the turbulence threshold set by the Reynolds criterion ($Re_p > 300$)

.

5 Numerical Model

This chapter discusses how the experimental set-up from chapter 4 is used in the numerical model that was introduced in chapter 3. The set-up is discussed, a validation procedure is followed and the runs are described that are used to test the hypotheses that followed from the literature research in chapter 2.

For the numerical set-up of this case, the approach described in Jacobsen et al. (2018) is followed. This is done because the case described there is similar to this case. The notional wave-steepness at the structure in the paper is $s_{op} = 0.015$ whereas here it is $s_{op} = 0.0038$. Considering CFD modelling can become time-consuming with very steep waves, this low steepness can be seen as beneficial. The main difference between the two cases is that in the case described in this thesis the water is shallow (following the criterion of linear wave theory: $h/L_{m-1.0} = 0.0241$) whereas the case in Jacobsen et al. is in intermediate waters: $h/L_{m-1.0} = 0.1122$ (this tends to the shallow water limit: $h/L_{(m-1.0)} < 0.05$).

5.1 Set-up of Numerical Model

The complete numerical set-up is visualised in Figure 22. It shows the experimental set-up, the OCW3D domain and the OpenFOAM domain. In Figure 22 the wave gauges are given ID-numbers (1-8), which are used to compare the data between the numerical and experimental gauges. The simulations are run in parallel on the HPC cluster that is available at Boskalis. Simulations are performed on 8 processors to increase the computation efficiency. To this end, the computational domain is split into 8 vertical sections.
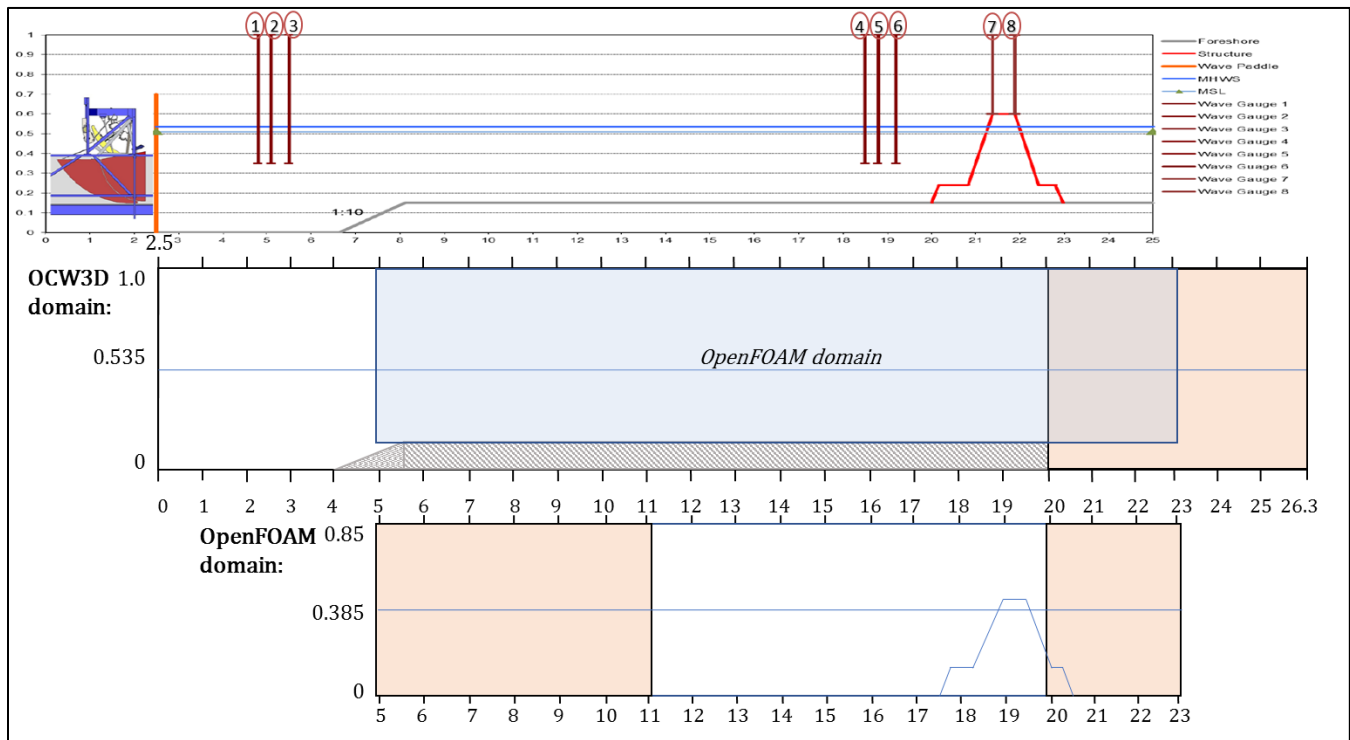

Figure 22: Set-up of numerical model

5.1.1 OCW3D Set-up

The OCW3D domain propagates the same waves as in the experiment by using the wave paddle velocity signal as a boundary condition. As only the incident waves should be imposed, a relaxation zone is added at the righthand side of the OCW3D domain. The relaxation zone has the length of the peak wavelength

of the wave spectrum in shallow water: $L_p = T_p \cdot \sqrt{gh} = 6.3\ m$. In the OCW3D domain the foreshore is implemented in the bathymetry.

The OCW3D simulation is computationally efficient, so as a start two runs were checked for accuracy that have a relatively fine grid spacing. Run 1 is based on recommendations by (Bingham and Zhang, 2007). Based on the wavelength that needs to be resolved a grid size in the x-direction is chosen following $\Delta x = L/20$. Because of the efficiency of the model, it is opted to resolve some of the smallest wavelengths of the experimental wave spectrum. The grid size in the y-direction is given by a stretched vertical grid of 15 points (stretched towards the free surface). The timestep is dimensioned using the Courant-Friedrichs-Lewy (CFL) criterion:

$$Co = \frac{|u|\Delta t}{\Delta x} \leq 1 \tag{52}$$

Where:
Co =   Courant Number $[-]$

The velocity used in the CFL criterion is the shallow water wave celerity. Note that the timestep of OCW3D adapts to the timestep in OpenFOAM, which in turn is adjusted following the set maximum allowable Courant number. Run 2 is used to check if a finer grid (both in x and y direction) gives significantly better results compared to Run 1 (see set-ups in Table 5). The numerical grid for Run 1 is given in Figure 23, where the stretching towards the free surface is clearly visible. Note that the y-axis shows '$z\ [m]$', this is because OCW3D uses the z coordinate in the vertical (unlike OpenFOAM, which uses y).

	RUN 1	RUN 2
Δx	0.05000	0.02500
Δy	0.03566	0.02430
Δt	0.02000	0.00326

Table 5: Set-up of OCW3D run 1 & 2.
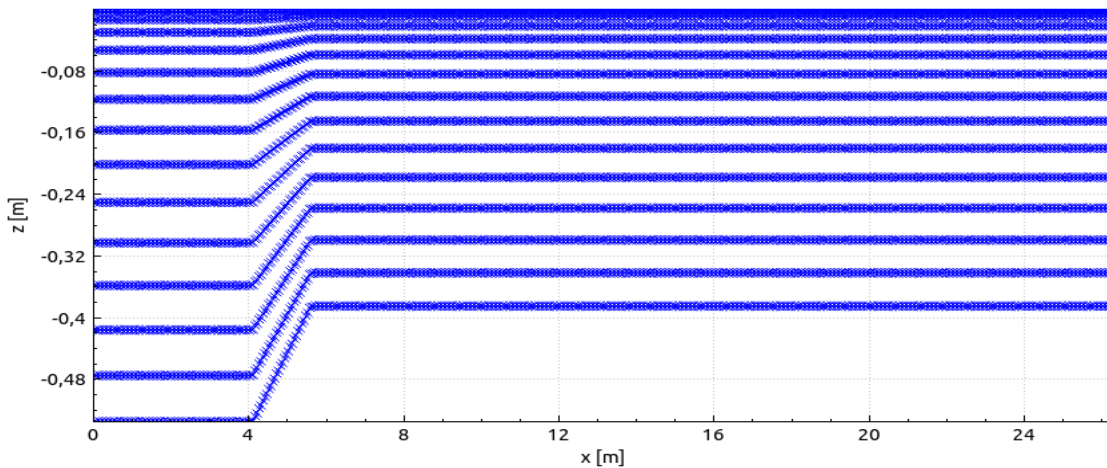
Figure 23: The numerical grid in OCW3D, Run 1.

5.1.2 OpenFOAM Set-up

For the validation of OpenFOAM, initially a relatively fine mesh is used ($\Delta x = \Delta y = 0.005\ [m]$). This is done to make sure that a difference between the OCW3D and the OpenFOAM results are not caused by a too coarse mesh in the OpenFOAM domain. The value of $0.005\ [m]$ is based on rules of thumb that suggests that the wave height of interest should be divided into 10-20 points. In this case the $H_{2\%}$ is chosen (estimated by $2 * H_s\ (= 0.12\ m)$) as this represents the larger waves well which are expected to cause overtopping. The fine mesh is used throughout the entire domain to ensure an aspect ratio (AR) of 1, which is mostly important around the free surface. The OpenFOAM domain has a relaxation zone

at the inlet (also referred to as the coupling zone) with length L_p. The relaxation zone at the outlet has a length of $1/2 * L_p$. Between the relaxation zone on the inlet and the toe of the structure, a distance L_p is imposed.

5.1.3 Measurement devices

This section describes the measurement devices that are supplied by waves2foam (Jacobsen, 2017). All measurements are performed at each timestep in the simulations, as it is near impossible to predict for an irregular wave field when exactly waves will be overtopping.

To measure the water elevation, numerical wave gauges are used. These integrate the indicator function over the vertical. This is an important consideration in the positioning of the gauges on the breakwater crest. The formation of air bubbles can cause the results from the wave gauges to underestimate the water level. The gauges should be positioned in a continuous sheet of water. With violently overtopping waves the transition over the crest edge should be checked for air pockets, this can be done using the velocity profiles from the probe output.

$$\zeta = \int_{y_0}^{y_1} \alpha dz - d \tag{53}$$

Where:

ζ	=	Free surface elevation	$[m]$
d	=	Reference level (here the still water level)	$[m]$

For velocity measurements, probes are used. These probes store a specified output data (u, α, p). By multiplication of the indicator function (α) with the velocity, the velocity field of a cell filled with only air is neglected. In this way the velocity profile of the water phase can be depicted. Probes are positioned in sets of vertical lines on multiple locations along the width of the crest.

Overtopping faces are used to determine the overtopping discharge (q) and the overtopping volumes (V). Overtopping faces are positioned over a group of cell faces, through which the discharge is calculated using a face flux across a face multiplied by the indicator function. The instantaneous directional overtopping discharge is then given by:

$$\boldsymbol{q} = \sum_{f \in F} \phi_{F,f} * \frac{\boldsymbol{S}_f}{\|\boldsymbol{S}_f\|_2} \tag{54}$$

Where:

q	=	Volume flux (vector in 3 directions)	$[m^3/s]$
$\phi_{F,f}$	=	The flux of fluid across a face f multiplied by the indicator function	$[m^3/s]$
S_f	=	Non-unit normal vector to the face, ϕ_F is positive in the direction of the normal vector	$[-]$

5.2 Validation procedure

A validation procedure is followed to ensure the numerical wave flume gives proper results. In this validation, the experimental run is recreated in OpenFOAM so the results from both the experimental and numerical wave gauges can be compared. To compare the data from the numerical simulations and the results from the experiment, the numerical output is rewritten to fixed time-steps. The numerical output is interpolated to have the same output frequency as the experimental output. The methods that are used for comparison are discussed below.

Pearson's Correlation Coefficient

For the comparison of two data sets (here: different gauge outputs), the Pearson correlation coefficient (PCC) can be used. A PCC of 1 shows that the two results are fully (linearly) correlated.

$$PCC(X,Y) = \frac{cov(X,Y)}{\sigma(X)\sigma(y)} \tag{55}$$

Where:

$cov(\dots,\dots)$	=	The covariance between two random variables, showing a tendency in the interaction between the variables	$[-]$
$\sigma(\dots)$	=	The standard deviation of a random variable	$[-]$

Root Mean Square Error (RMSE)

The RMSE is used as it is a measure for the magnitude of the error between datasets. This makes the measure complementary to the PCC, which shows the correlation of the signals, but not the magnitude of the error. A RMSE of 0 shows that the two results are identical.

$$RMSE = \sqrt{\frac{\sum_{n=1}^{N}(y_m - y_e)^2}{N}} \tag{56}$$

Where:

N	=	The total amount of data points	$[-]$
y_m	=	The model output at that data point	$[-]$
y_e	=	The experimental output at that data point	$[-]$

Spectral Analysis

Another measure of comparison is given by comparing the wave spectra of the numerical model and the experiment. Also subtracting the measured timeseries from each other to obtain the difference spectrum makes for a useful tool. A brief overview of spectral analysis is given here, based on (Holthuijsen, 2007).

With a wave spectrum, it is possible to describe in detail one observation of the sea surface as a stochastic process (that is to characterise all possible observations that could have been made under the conditions of the actual observation). An observation is then one realisation of the stochastic process. For ocean waves, we use the random-phase/amplitude model to obtain the energy-frequency spectrum, which is defined by:

$$E(f) = \lim_{\Delta f \to 0} \frac{1}{\Delta f} E\left\{\frac{1}{2}\underline{a}^2\right\} \tag{57}$$

Where:

$\underline{a}$	=	Amplitude of the harmonic component	$[m]$
Δf	=	Frequency band	$[Hz]$
$E\{\ \}$	=	The expected value of a certain measure	$[-]$

With Fourier analysis, a wave record can be reproduced as the sum of a large number of harmonic wave components with certain amplitudes and phases for each frequency $f_i = i/D$ (Where D is the duration of the measurement). The frequency interval is therefore $\Delta f = 1/D$ (which is the longest harmonic wave that can exist within the record). To determine the amplitude for each frequency, the surface elevation is written as a Fourier series with unknown amplitudes and phases. The Fourier analysis allows us to determine the values of the amplitude and phase for each frequency (giving us the amplitude-phase spectrum). This spectrum is applicable for independent wave components (the waves should not be too steep nor be in too shallow water) and stationary process (choice of the duration of the spectrum). The wave record should be long enough to obtain statistically reliable estimates.

From the amplitude-phase spectrum we can also perform the same action the other way around and create a surface elevation. For every wave frequency the expected value of the amplitude is known, and so the probability density function (pdf) for the amplitude can be drawn (the amplitude is Rayleigh distributed). From this pdf and from the pdf of the phases (uniformly distributed) a random value can be

chosen. Performing this exercise for every frequency, gives a list of frequencies linked to a specific amplitude and phase. Superposition of this results in a realisation of the wave record:

$$\eta(t) = \sum_{i=1}^{N} a_i \cos(2\pi f_i t + \alpha_i) \tag{58}$$

Where:

a_i	=	Amplitude for a certain frequency	$[m]$
f_i	=	Frequency, equal to $\frac{i}{D}$ so $\Delta f = \frac{1}{D}$, where D is the duration of the measurements. The latter formula is a requirement because the wave record is finite and is also called the frequency resolution	$[Hz]$
N	=	The total number of frequency components	$[-]$

Initially the variance density can be estimated from just one amplitude (no $E\{\ \}$), resulting in the raw estimate. By dividing the time record into multiple blocks, the expectation is given by averaging the values for the amplitude from the different blocks for each frequency separately. This is called the quasi-ensemble average. Because of the short duration of the simulations however, here the ('grassy') raw estimates are compared. To prevent aliasing, the spectrum is generated up to the Nyquist frequency which is determined by the measurement interval Δt through: $f_{Nyquist} = \frac{1}{2\Delta t}$.

Reflection Analysis
Using the method of Zelt and Skjelbreia (Zelt and Skjelbreia, 1993), reflection analysis can be performed for the simulated timeseries and the experimental timeseries. The result of this analysis is a timeseries of the incoming wave train and the reflected wave train, which can also be used to perform spectral analysis. The method of Zelt and Skjelbreia is based on linear wave theory. This assumption is required to express the surface elevations at multiple points (gauge locations) using Fourier analysis. An exact solution for the incoming and reflected wave can be given for 2 wave gauges, but the use of more gauges gives an increased accuracy. The method by Zelt and Skjelbreia is applicable for more than 2 gauges, which is achieved by estimating the incoming and reflected wave field through a weighted least squares approach. To quantify the reflection, the reflection coefficient can be determined using:

$$K_R = \frac{H_r}{H_i} = \frac{4 * \sqrt{m_{0,reflected}}}{4 * \sqrt{m_{0,incident}}} = \sqrt{\frac{m_{0,reflected}}{m_{0,incident}}} \tag{59}$$

5.3 Validation runs

The validation is subdivided into 4 parts: 1) validation of the wave generation signal in OCW3D, 2) validation of the link between OCW3D and OpenFOAM, 3) validation of the wave field in the complete test set-up, including the porous structure and 4) validation of the overtopping flow depth and velocity in the complete test set-up. In step 1 and 2 the results of the calibration of test 3.04 are used, in step 3 and 4 the experimental results with the porous structure in place are used (for experimental data, see Appendix C). This section ends with a subsection on increasing the efficiency of the numerical set-up.

5.3.1 Step 1: Validation of wave generation signal in OCW3D

The waves on the inlet boundary of the OpenFOAM domain are generated using OCW3D. This software allows the use of the wave paddle velocity signal to propagate waves through a domain for a specified bathymetry. The entire (empty) wave flume is modelled in OCW3D, the OpenFOAM domain is inserted into the domain afterwards. The OpenFOAM domain contains the breakwater model.

In the experiment, the wave signal was calibrated using an empty flume where the generated waves were absorbed by a mildly sloping beach of rough grading stones. This beach absorbs most of the waves, although some reflection still remains as is visualised by the reflection analysis in Figure 24. It is known

that during such calibration runs the reflection can be around 5%, but the impact can be more significant for longer waves. That this is true for this case is shown by determining the reflection coefficient for the calibration run, which equals $K_R = 0.18$.
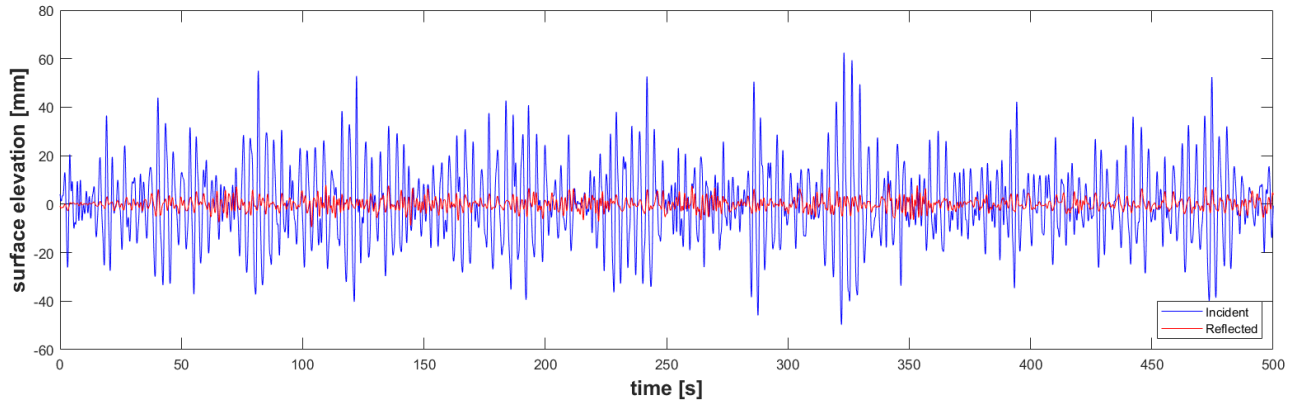

Figure 24: Reflection analysis at gauges 1-2-3 for the calibration run.

To validate that OCW3D is generating the same waves that were used in the experiment, the OCW3D results are compared to data from calibration tests from the experiment. Table 6 gives the time lag, the PCC and the RMSE for the 2 runs. It should be noted that the time-lag differed per wave gauge, where gauge 4 seems to be calibrated improperly. It's clear that Run 2 doesn't differ significantly from Run 1. The surface elevation output from gauge 6 (which is closest to the structure in the OpenFOAM domain) is given in Figure 25.

	RUN 1			RUN2		
	TIME-LAG [s]	PCC	RMSE	TIME-LAG [s]	PCC	RMSE
GAUGE 1	0.35	0.9425	7.7069	0.35	0.9416	7.7594
GAUGE 2	0.35	0.9390	8.6329	0.35	0.9383	8.6867
GAUGE 3	0.35	0.9395	8.6806	0.35	0.9376	8.7817
GAUGE 4	-6.20	0.7565	13.0856	-6.20	0.7584	12.9629
GAUGE 5	0.25	0.9319	6.1559	0.25	0.9278	6.3929
GAUGE 6	0.35	0.9227	6.1858	0.35	0.9238	6.1760

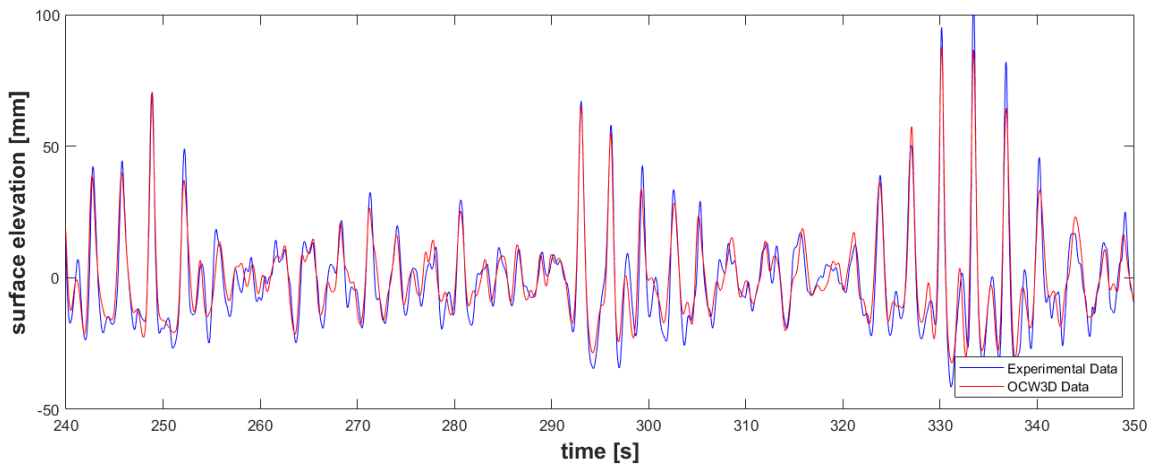Table 6: Time-lag and PCC values for OCW3D run 1 & 2

Figure 25: Run 2, gauge 6, 240-350 s.

52

It can be concluded from this analysis that the settings of Run 1 give sufficient accuracy when compared to Run 2. A mismatch is however present between the experimental gauge data and the OCW3D gauge data. Various reasons can explain this mismatch:

- The experimental gauge data is polluted by reflection from the beach. It is clear from the reflection analysis in Figure 24 that the experimental signal includes significant reflection from the beach. The OCW3D set-up has a fully absorbing zone at the end of the flume and this signal is then not polluted by reflection. It can be hypothesized that the result given by OCW3D is sufficiently close;
- The results differ because the imposed wave paddle velocity signal is not the steering velocity of the wave paddle, but the measured velocity. That this is true is shown in step 3 of the validation: a larger mismatch of the data occurs in the runs with the structure, because with the structure more waves are reflected and so the wave paddle has to adjust its steering velocity more;
- The difference can also follow from a slightly different positioning of the gauges (the exact locations of the gauges in the numerical set-up depends on the grid spacing). This effect should however be minimal.

In step 3, it is analysed how the results look when the calibration signal is imposed on the complete numerical set-up.

5.3.2 Step 2: validation of the link between OCW3D and OpenFOAM

To make sure the signal that OCW3D generates is properly coupled to the OpenFOAM domain, the OpenFOAM output and OCW3D output was compared at gauge 4, 5 and 6. The OpenFOAM run was performed with an empty flume, so without the structure in place. The results for the PCC are given in Figure 26. Figure 27 gives the surface elevation for gauge 6, both from the OCW3D run and the OpenFOAM run.

COMPARISON OCW3D & OPENFOAM		
	PCC	RMSE
GAUGE 4	0.9893	2.4582
GAUGE 5	0.9884	2.5211
GAUGE 6	0.9865	2.6652
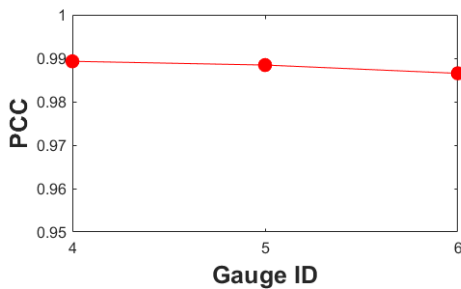
Figure 26: PCC between OCW3D run 1 and OpenFOAM run 1

Table 7: PCC and RMSE between OCW3D run 1 and OpenFOAM run 1
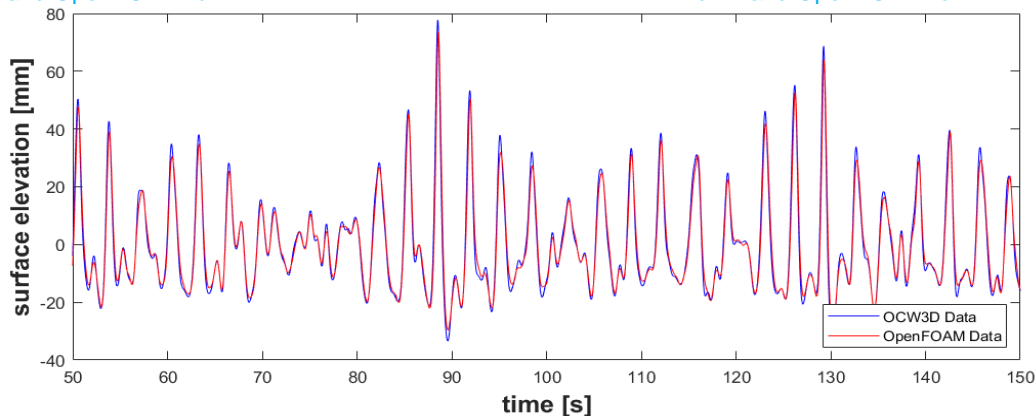
Figure 27: Run comparison OCW3D run 1 & OF run 1, gauge 6, 50-150 s.

From the PCC & RMSE values, which are also given in Table 7, it is clear that the wave paddle signal is propagating through the OpenFOAM domain quite well. It seems however that OpenFOAM slightly

underestimates most wave heights. This effect could be due to the different measurement methods of the numerical wave flumes. Another run was performed where the OpenFOAM domain was made slightly smaller, so the step in the bathymetry is entirely outside of the OpenFOAM domain. The relaxation zone is kept at the same length. See also Figure 28 for the configuration of the second test run, where the part that is cut-off is visualized by the red-striped box. The results of this second test run are given by Table 8. It is concluded that the results are good and in the rest of the simulations this slightly shorter OpenFOAM domain is used.

COMPARISON OCW3D & OPENFOAM

	PCC	RMSE
GAUGE 4	0.9890	2.4399
GAUGE 5	0.9881	2.4993
GAUGE 6	0.9862	2.6508

Table 8: PCC and RMSE values between OCW3D run 1 & OpenFOAM run 2.
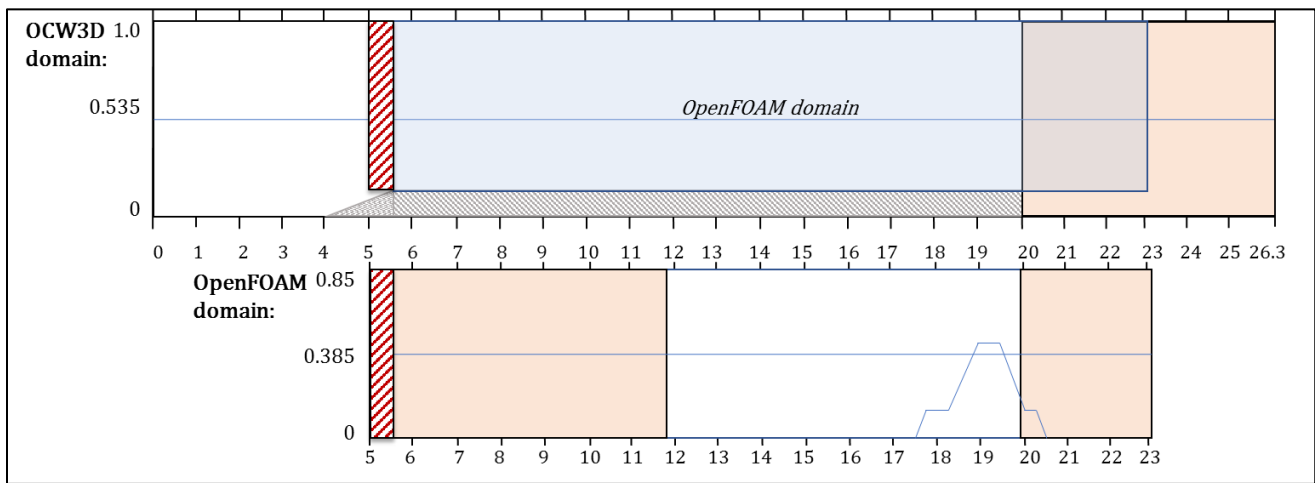
Figure 28: configuration of the second test run

5.3.3 Step 3: validation of wave field in the complete set-up

In this step of the validation, the total numerical set-up with the porous structure in place is assessed. As OCW3D seems to function correctly and the link between OpenFOAM and OCW3D is working properly, the third step of the validation looks at the entire numerical set-up. As mentioned, it should be checked if the velocity signal of the paddle in the experimental data is in fact the steering velocity or the measured velocity. From the first run with the porous structure in place it is clear that the errors with the experimental data increases, compared to the errors from the calibration run that was discussed in step 1. See Table 9 and Figure 29 below. Hence it is concluded that the paddle velocity signal is in fact the measured velocity signal, and not the imposed signal.

COMPARISON 3.04 & OPENFOAM

	PCC	RMSE
GAUGE 4	0.6677	16.9357
GAUGE 5	0.6484	15.8250
GAUGE 6	0.5613	14.2532

Table 9: PCC and RMSE values for comparison run of Experiment 3.04 and OpenFOAM.

Figure 29: Run comparison experiment 3.04 & OpenFOAM, gauge 6, 0-100 s.
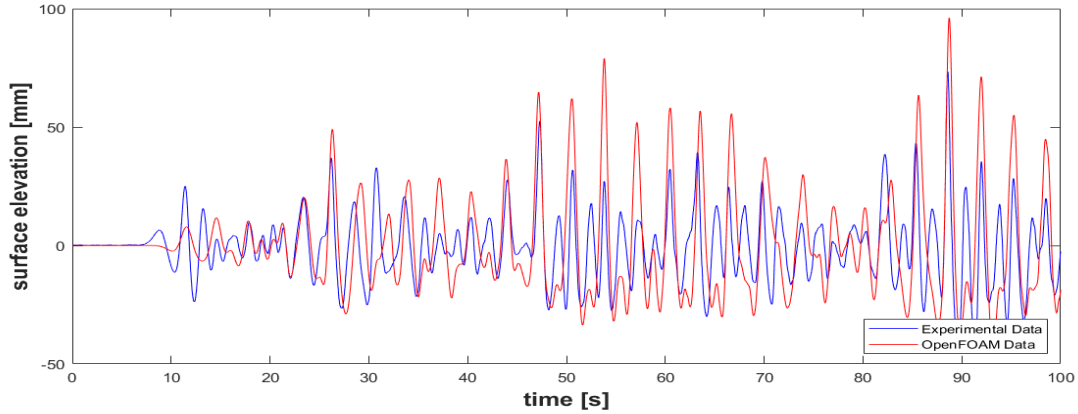
Subsequently it was tried to use the velocity signal from the calibration run in the experimental set-up. The steering file of the calibration has to compensate only for the 18% wave reflection coming from the 'absorbing' beach. First, to check if the same signal is imposed during the calibration run and the actual experiment, the results of a reflection analysis on the experimental data and the calibration data were compared. The reflection analysis was performed for gauge set 1-3. It is clear that the same signal is sent out as significant resemblance is visible (see Figure 30). Knowing that the paddle velocity signal is the measured velocity signal, this also explains why the data for the paddle velocity is different between the calibration run and the experimental run.
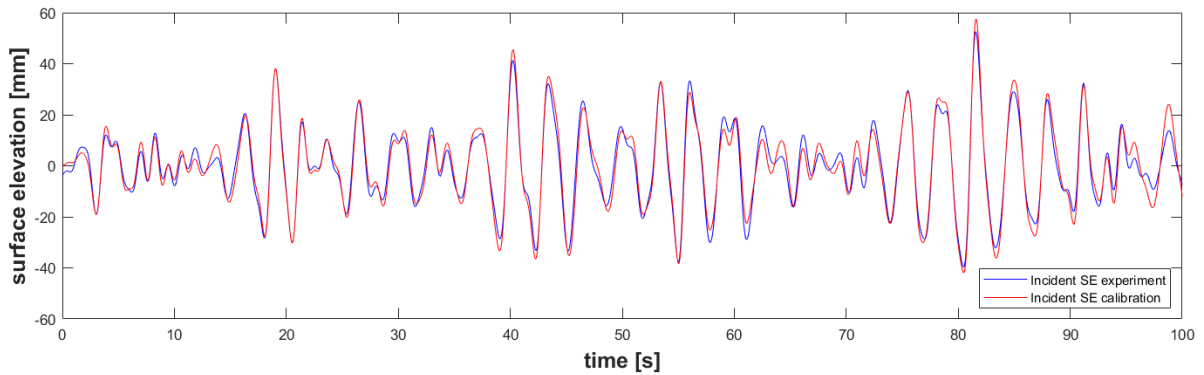
Figure 30: Comparison gauge 1-2-3 of incoming waves in calibration case and in experiment

Imposing the paddle signal from the calibration run should then give better results. In Table 10 the results are given, where OpenFOAM-CAL represents the OpenFOAM simulation where the wave signal from the calibration run is imposed. It is clear that the results are already significantly better (see also Figure 31).

COMPARISON 3.04 & OPENFOAM-CAL		
	PCC	RMSE
GAUGE 4	0.7785	13.4645
GAUGE 5	0.7481	13.0389
GAUGE 6	0.6437	12.4982

Table 10: PCC and RMSE values for comparison run of Experiment 3.04 and OpenFOAM-CAL
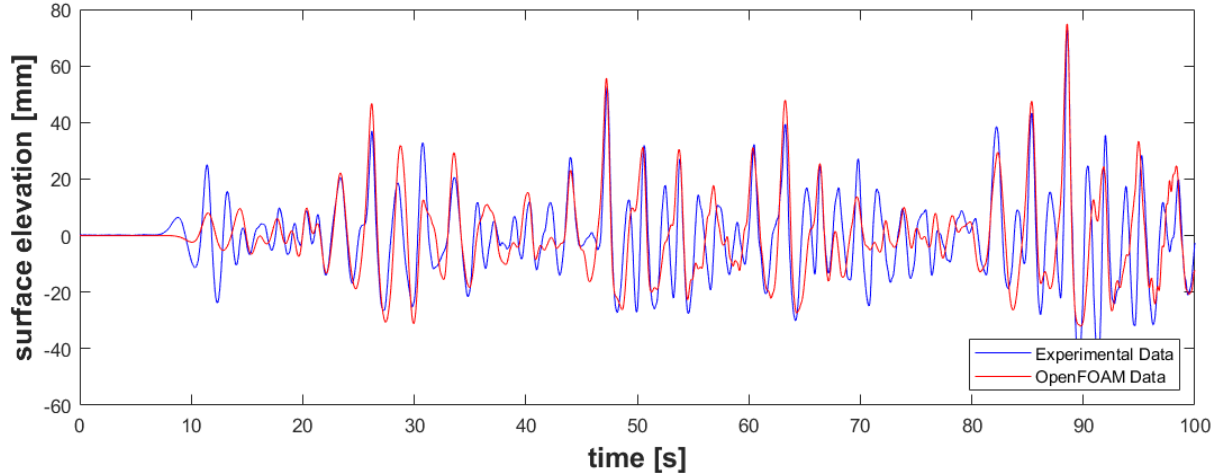
Figure 31: Run comparison experiment 3.04 & OpenFOAM-CAL, gauge 6, 0-100 s.

It is very plausible that a significant part of the mismatch that is visible in Figure 31 follows from the fact that the incident wavefield is generated by the measured wave paddle velocity, which is 'polluted' by the reflection in the calibration run. To study this effect, the incident wave fields during the experiment and simulation are compared. If a 'clean' paddle steering file would be used to generate the wave field in the simulation, the incident wave fields should all be practically equal.

To compare the incident wave fields, the reflection is studied at gauge set 4-6 (see Figure 32). A comparison of the H_{m0} of the two runs shows that the simulated $H_{m0}$ is about 9% smaller than the experimental wave height (for the calculation of these spectral quantities the first 15 seconds are left out). The PCC equals 0.9587 and the RMSE equals 4.7451. This means that because the incoming wave in the simulation is different compared to the wave that is actually imposed in the experiment, it can be expected that the reflected wave will also be somewhat different. The reflection coefficient for the experiment equals $K_{R,exp} = 0.6217$, for the run visualised in Figure 31 it equals 0.6734. It is expected that the porous characteristics of the structure also have an influence on the reflection.
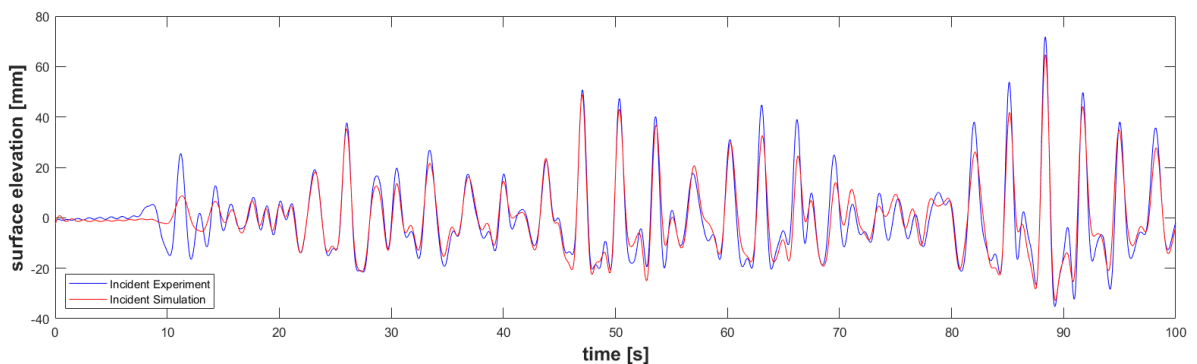
Figure 32: Comparison gauge 4-5-6 of incoming waves in experiment and in simulation

So, in the following, the effect of various settings on the wave signal and the reflection in particular are investigated by means of a sensitivity analysis. It is realised based on the analysis above however that a perfect match is not possible because the steering file for the wave paddle is not available. It is therefore also not aspired to find perfect settings (as this makes it unclear what error results from what adaptation) but the analysis functions as a way of understanding the influence of the various parameters.

Due to time limitations (the research already moved on with the validation presented in this thesis), it was not studied what the effects would be if not the velocity of the wave paddle but the surface level elevation of the incoming wave signal were implied on the OCW3D boundary condition. This is a recommendation

56

for further research on this case or other cases with similar information gaps, as this might significantly improve the reliability of the validation.

Sensitivity Analysis

To investigate the reflection, runs were performed were the porous parameters and the mesh refinement were altered. To get an idea of the impact of a certain variable using only a few runs, often some extreme values were chosen (in the style of a sensitivity analysis). Here the conclusions of this analysis are described. A more elaborate output for all the runs can be found in Appendix D. From the sensitivity analysis, the following becomes clear:

- The KC number: The KC number has a minor effect on the reflection coefficient. This is likely because the KC number has a relatively small influence in the used method (the van Gent equations). For a higher KC number, the reflection goes down very slightly. A higher KC number causes the turbulent friction term to become somewhat smaller and hence it is thinkable that more water is infiltrating into the structure instead of reflecting.

- The resistance coefficients (α and β): When the non-linear friction term (β) is increased and the linear friction term (α) is decreased, (following recommendations of (Jensen, Jacobsen and Christensen, 2014)) the reflection goes down. If the non-linear friction term would have a larger effect on the reflection, one would expect that these new settings would cause the reflection to go up. Apparently the linear friction term still has a significant effect on the reflection. It might be that the modelled waves are sufficiently long to experience a significant interaction with the core material of the breakwater. It is concluded that tuning the resistance coefficients of a coastal structure with multiple layers is challenging for numerical modelling, especially for new designs and with the lack of proper validation data (Jacobsen, van Gent and Wolters, 2015). The parameters from van Gent are thus used in the further analysis, as they are more widely used in other studies and so this choice makes this study more comparable to others.

- The porosity (n): The porosity very clearly influences the reflection. With a very open structure, the reflection drastically drops, whereas a very closed structure causes the reflection to increase. Using the method of Tsirel instead of a general porosity of 0.4, the decrease in porosity of the core material causes the reflection to go up. This could indicate that the long waves from the experiment are influenced by the porosity of the core material. This is complementary to the finding that the resistance coefficient of the core material had an effect on the reflection.

- Mesh refinement: An analysis using wave spectra showed that different mesh refinements did not particularly improve the representation of certain wave frequencies in the simulation. It is concluded that the mesh refinement used in the first stages of the validation does not cause a larger mismatch in the reflection coefficients.

5.3.4 Step 4: Validation of overtopping flow depth and velocity

Validation of the flow depth

To validate the overtopping flow depth, the output from gauges 7 and 8 are compared. Due to a wrong placement of the wave gauges on the crest in a large part of the numerical simulations, only the results from test 15131 and 15132 are useful for the analysis of the overtopping depth over the crest. The wrong placement was caused by positioning the wave gauges through the porous material, where air between the still water level and the overtopping flow caused a significant mismatch between the measurements and the simulations. The differences between the two runs are the area and level of refinement and the fact that the porosity of the filter material in run 15132 was decreased from $n = 0.4413$ to $n = 0.40$. This was done as it was tested how the overtopping flow depth would change for less permeable material. The results are visualised in the plots below, for runs 15131 & 15132 combined (Figure 33). Note that run 15132 ended prematurely.
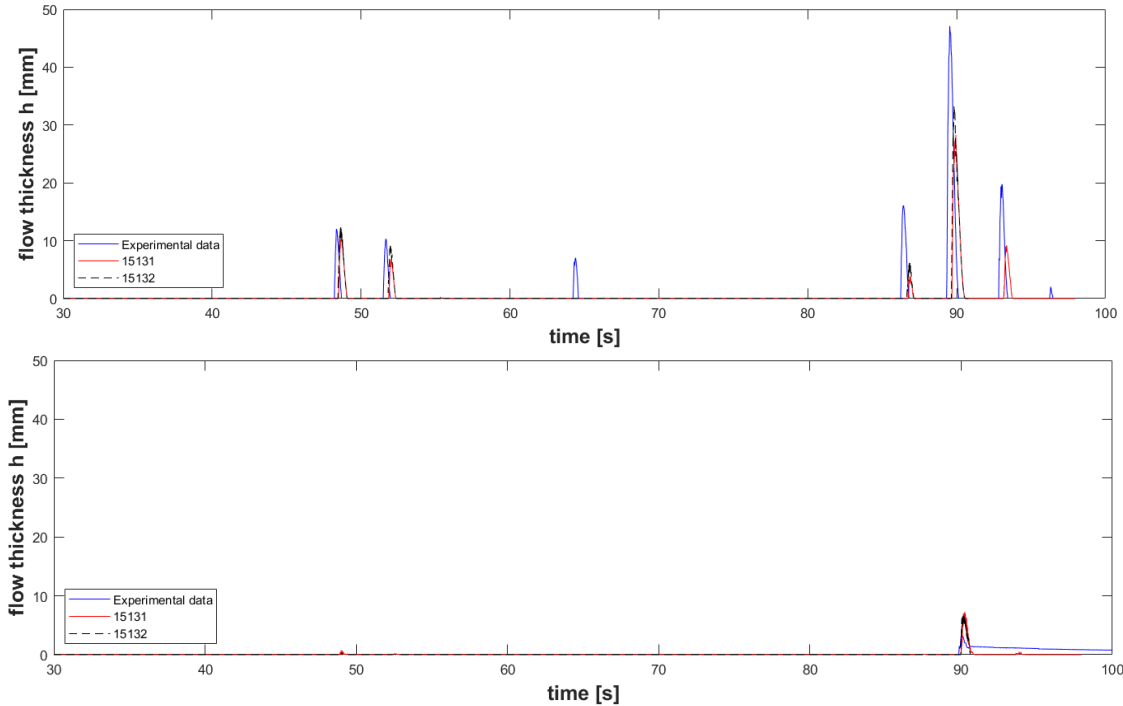
Figure 33: run 15131 & 15132, Top) flow thickness (depth) measured at gauge 7; Bottom) flow thickness measured at gauge 8

In the simulations, 5 out of 7 of the overtopping waves are identified. It is clear that run 15132 comes closer to the correct overtopping depth, however the third wave is not recognized in either simulation and most flow depths are underestimated. The overtopping wave flowing over the entire structure reduces less significant in the simulation as opposed to the experiment. It is reasoned that as the accuracy of the wave field is not improving due to the problem with the wave signal, these results are not likely to improve significantly either. It is chosen to continue with the porosity that was found with the method from Tsirel, to avoid 'fudge factoring' to obtain better results. The results in Figure 33 show clearly that decreasing the porosity also increases the flow depth. Note that the time lag is caused by the inherent time lag from the experiment (about $0.3 [s]$) as was described in section 5.3.1. As turbulence could also influence the results, its effects are investigated below.

Effect of Turbulence on flow depth

As mentioned in section 3.4, two runs are performed with the $k - \epsilon$ turbulence model. For these runs, the same 3 waves are simulated that were described in the section above. The differences between the run without turbulence model and the turbulent run can then be studied, to evaluate which results more closely represent the experimental data. Two runs were performed, where 1) the turbulent parameters ($k \& \epsilon$) on the inlet are based on rules of thumb for very turbulent flows and 2) the turbulent kinetic energy is made very small on the inlet. It is expected that the latter case gives the most realistic result, as no waves are expected to be breaking before reaching the structure.

The analysis of the first turbulent run showed that the dissipation of wave energy was so severe that no waves were overtopping at all. From comparing the data from wave gauges in the water in front of the structure, it is clear that the wave height is quite significantly reduced when using the turbulence model (see Appendix F). It can be concluded that these settings indeed are too dissipative and do not represent the experimental set-up well.

In the second turbulent run, the initial turbulent kinetic energy (k) is set to equal 0.0001. It is not set to zero, as in the transport equation of the turbulent dissipation rate a division by k is incorporated in the production terms. The initial value for the turbulent dissipation rate is set at 0.3 (close to the calculated

58

value), to make sure that the turbulent viscosity is significantly lowered in this simulation (as $\nu_t = C_\nu k^2/\epsilon$). The results for the surface level elevation are given by Figure 34 and Figure 35. The turbulent results are more smooth, which was expected due to the added viscosity in the turbulent runs.
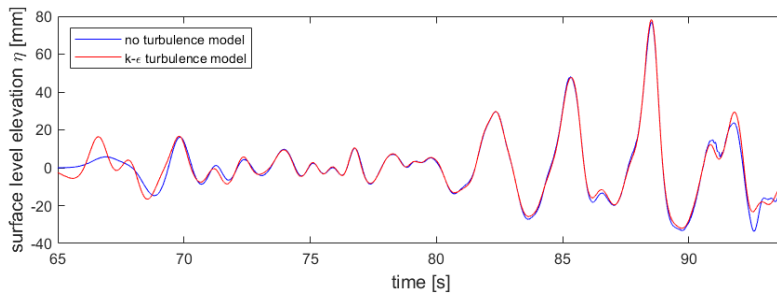

Figure 34: Comparison of surface level at gauge 6 (Turbulence run 2)
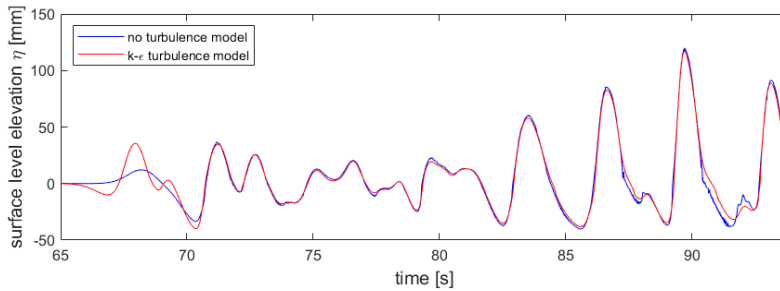
Figure 35: Comparison of surface level at intersection of SWL and front slope (Turbulence run 2)

Comparing the output for gauges on the crest, a comparison is made on the outer crest edge (the edge of the filter layer), the outer core crest edge (gauge 7) and in the middle of the filter layer (Figure 36). Two processes are visible: 1) the smaller waves reduce very quickly over the filter material and 2) the largest wave reduces in height less quickly for the turbulent run than for the laminar run.
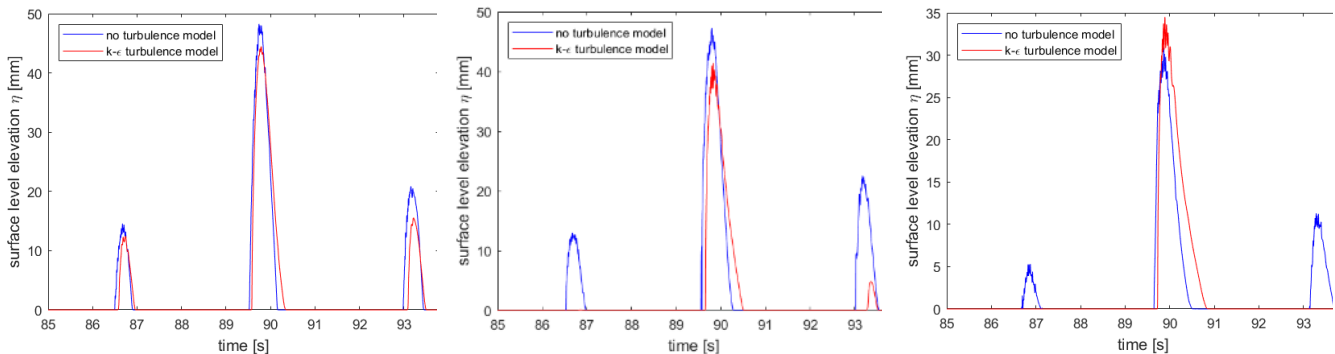
Figure 36: Comparisons of overtopping flow depth with and without turbulence model, near the seaward crest edge

The first process can be explained by the fact that the turbulence model causes the shear that is created by the velocity gradient to be represented by an increased production of turbulent viscosity (in the x-direction: $\tau = \rho\nu\,(\delta u/\delta y)$). This significantly slows down the flow, which allows more water to infiltrate into the structure. This slowing down of the flow is also clear from the graphs, where the run with a turbulence model lags behind the run without a turbulence model. The second process can be explained by the fact that as the turbulence slows down the flow, this allows for more water to infiltrate but only up to the point that the crest material is saturated. After that, the slowing down of the flow is likely to cause the water to pile up. This can be compared to flow over an impermeable dike with a rough surface. It is concluded that as for the simulation without turbulence the water surface elevation is approximated better. In the following the flow velocity is analysed and also the effect of the turbulence on the flow velocity profiles is analysed.

Validation of the flow velocity

In the experiment, no direct velocity measurements were performed. In the first 100 seconds, only one large overtopping wave reached both wave gauges on the crest. The velocity from this wave was taken based on the moment that the flow reached the gauges on the crest. The experimental velocity is compared to its simulated counterpart to check the order of magnitude of the flow velocity. The experimental velocity equals $u_{exp} = 1.275 \ m/s$ and for run 15131 it equals $u_{sim} = 0.8 \ m/s$. So it is found that the velocity for the experiment is higher. This could be explained by the fact that the initial flow depth is larger in the experiment, so it is very possible that the larger overtopping event also had a larger velocity both because flow velocity and flow depth are related and because the flow is less influenced by friction from the crest material.

It is concluded that the order of magnitude comparison is sufficient based on the available data. This section continues to study the velocity profiles of the overtopping waves. With the probes on top of the breakwater, the velocity in the x-direction (U_x) is measured over the depth of the overtopping flow. The wave gauges integrate the α-field continuously over their height, the probes need to be positioned in such a way that they measure the velocity profile with sufficient accuracy. This implies that the probes should be spaced sufficiently close together over the depth of the overtopping wave. Smaller overtopping depths require more closely spaced probes to give an accurate velocity profile than larger waves.

To see how the scale of the overtopping wave affects the velocity profile, 3 overtopping waves are simulated in detail for various levels of refinement. The analysis was performed with waves from the validation case that were of different magnitudes. The waves overtop at around $t = 85, 90$ and 93 seconds, with heights of approximately $4.0 \ [mm]$, $28.1 \ [mm]$ and $9.1 \ [mm]$ respectively (Figure 33, top). Following recommendations by Jensen et al. (Jensen, Christensen and Jacobsen, 2015) to reproduce a specific event from an irregular wave field, the wave generation is started using a phase offset equal to:

$$\varphi = cx + NT_p \tag{60}$$

Where:

φ	=	phase offset	$[s]$
c	=	shallow water wave celerity ($c = \sqrt{gh} = 1.95 \ [m/s]$)	$[m/s]$
x	=	the distance from the inlet boundary (the relaxation zone) to the point of reproduction (the breakwater crest edge)	$[m]$
N	=	the number of peak periods to apply as warm-up	$[-]$

Jensen et al. found that specific events were reproduced correctly for $N = 4$. The total simulation time then becomes $37.6 \ [s]$ (including the time that needs to be simulated, which is set to $15 \ [s]$). Refinement is performed around the breakwater crest for 3 levels. The finest mesh size is $1.25 * 1.25 \ [mm]$. The results are compared at the core crest edge, which is the same location as in the experiment.

Overtopping flows with a depth lower than $0.1 \ [m]$ ($0.04 \ [m]$ on model scale) rarely cause instability on the stability curves. So the velocity profile for waves larger than $0.04 \ [m]$ should be modelled accurately. Therefore the finest mesh size of $1.25 \ x \ 1.25 \ [mm]$ is suggested, which makes sure that at least 3 velocity probes are located over the depth of this smallest wave. Of course a finer mesh is possible, but this increases the computational cost too much. The used refinement zone is the same as in Appendix Figure D.8. Figure 37 shows the velocity profiles during the maximum flow depth for the 3 studied overtopping events. This velocity profile, as well as the velocity profile that was obtained during the maximum flow velocity, is obtained using a threshold-crossing analysis (see Appendix I).

Note that the crest level for these runs is positioned at $0.085 \ [m]$ above the free water surface, which is why the y-axis starts at 0.085. The probe spacing is the same for the 3 runs, note that for refinement levels 1 and 2 multiple probes get the velocity output from the same cell centre. For the flow depth, measured by the gauges, the difference is quite small between the various refinement levels. In the titles

of the graphs, the flow depths are given as calculated by the wave gauges. Note that the probes may suggest a larger flow depth than the gauges, which can be explained by diffusion around the free water surface. This causes cells filled with α-values between 0 and 1 to be represented in the probe velocity profiles while the gauges 'compress' these cells' output.

No.	Level 3: 0.00125*0.00125	Level 2: 0.0025*0.0025	Level 1: 0.005*0.005
1	$h_{max} = 5.3\,[mm];\, u_{hmax} = 0.60\,[m/s]$	$h_{max} = 7.2\,[mm];\, u_{hmax} = 0.70\,[m/s]$	$h_{max} = 8.7\,[mm];\, u_{hmax} = 0.45\,[m/s]$
2	$h_{max} = 30.9\,[mm];\, u_{hmax} = 0.90\,[m/s]$	$h_{max} = 33.8\,[mm];\, u_{hmax} = 0.88\,[m/s]$	$h_{max} = 37.2\,[mm];\, u_{hmax} = 0.96\,[m/s]$
3	$h_{max} = 11.3\,[mm];\, u_{hmax} = 0.76\,[m/s]$	$h_{max} = 12.2\,[mm];\, u_{hmax} = 0.72\,[m/s]$	$h_{max} = 14.4\,[mm];\, u_{hmax} = 0.73\,[m/s]$
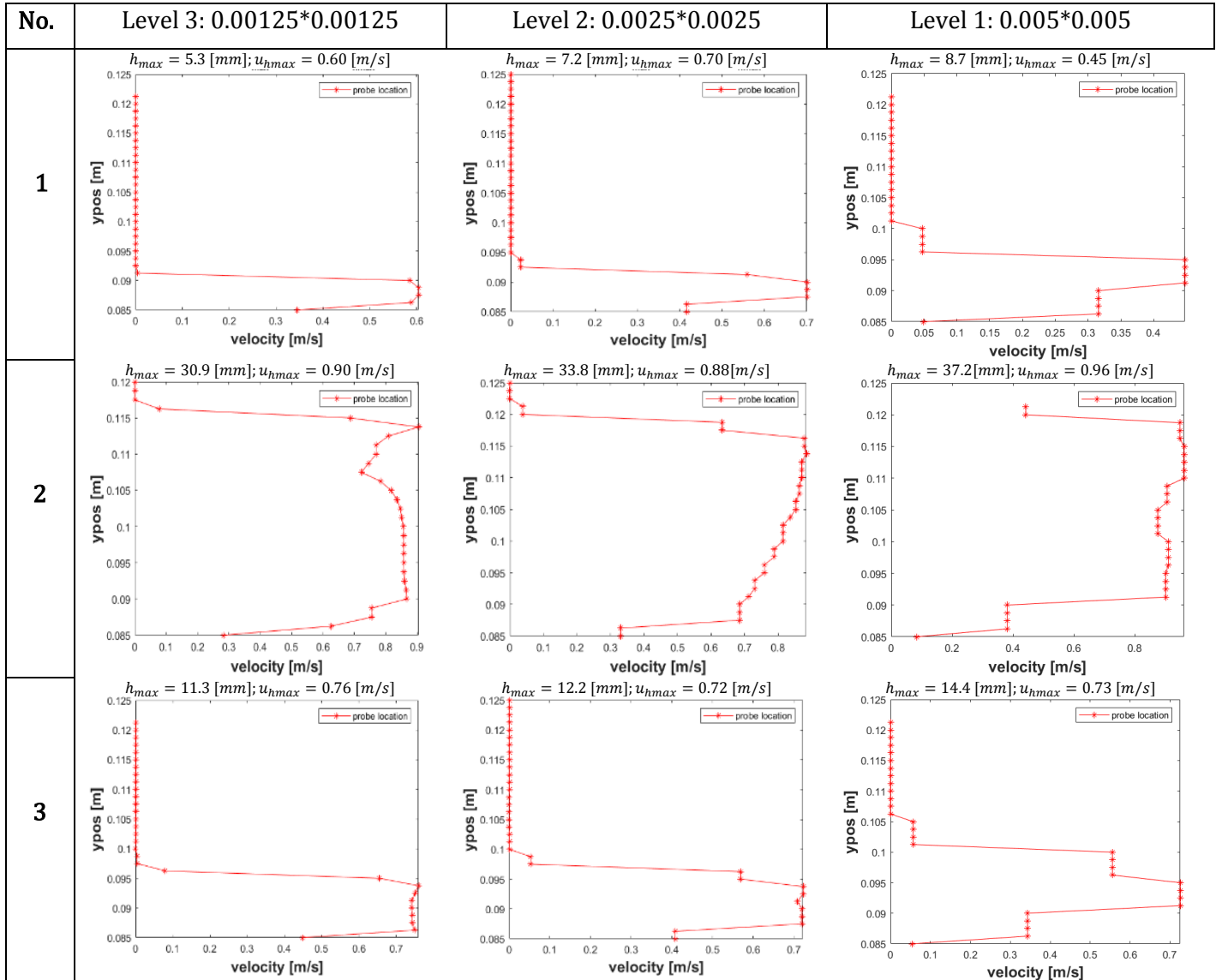
Figure 37: Flow profiles at the moment of maximum overtopping depth for various refinement levels

The flow velocity changes quite significantly between the refinement levels for the smallest wave (No. 1). Where refinement level 3 shows a clear velocity profile, levels 2 and 1 are much more coarse. It can be seen that the flow velocity is quite uniformly distributed over the depth. In Appendix E also the velocity profiles are given for the moments of maximum flow velocity and the simultaneously occurring flow depth. The conclusions are the same as the conclusions drawn here.

Effect of Turbulence on flow velocity
When looking at the velocity of the large overtopping wave, comparing again at the transition between the filter and the core material (gauge 7), the effect of turbulence can be clearly observed (Figure 38). The turbulence generated by the shear causes the formation of a so called momentum boundary layer, where the mixing of momentum smooths the transition from the velocity in the porous medium to the free

overtopping flow. It is clear that the maximum velocity is reduced significantly in the case with turbulence. This is explained by the fact that the boundary layer is not fully developed and so there is no free flow on top of the boundary layer (the boundary layer is present throughout the entire flow depth).
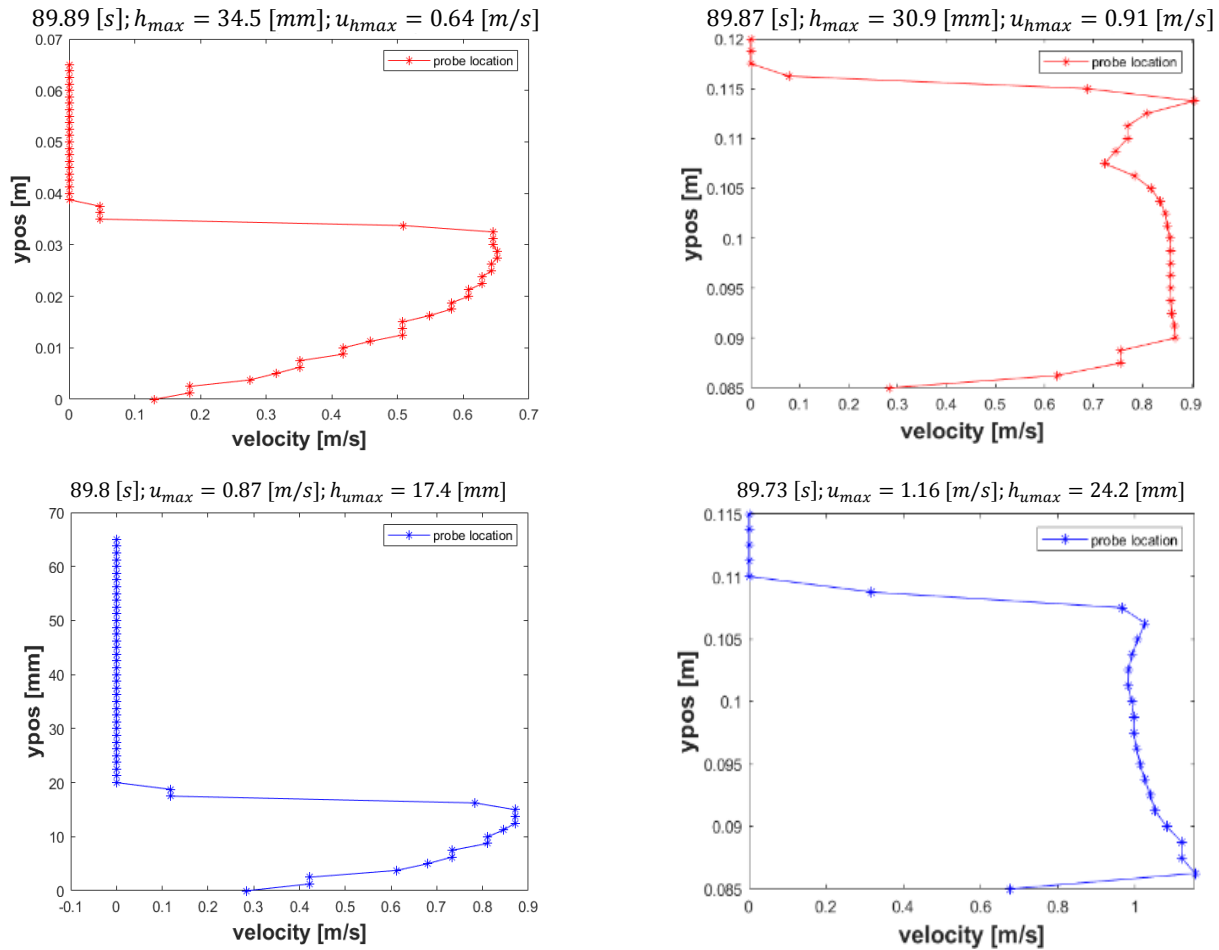

Figure 38: Row 1: velocity profiles at maximum flow depth; Row 2: velocity profiles at moment of maximum velocity; Column 1: with turbulence model, Column 2 without turbulence model.

It can be concluded from this analysis, that the approach with a simulation without turbulence likely overestimates the maximum velocity, which makes the approach conservative. Of course, the turbulence results are far from perfect, as for the simulation without turbulence the water surface elevation is approximated much better. Using a turbulence model for this type of analysis then requires a much more in depth analysis, possibly a different turbulence model and a proper analysis of the effect of the turbulence model on the flow inside the porous medium. It is concluded that the simulations will be performed without a turbulence model.

5.3.5 Efficiency

The final step of the validation looks at increasing the efficiency of the numerical model. This is done by creating different meshes, based on refinement around the free water surface and the zone of interest, the breakwater crest. It was concluded in the validation steps that for the following domain size suitable results are obtained: $RLZ_{inlet} \approx L_p$, the distance between RLZ_{inlet} and the structure should be about L_p, $RLZ_{outlet} \approx 1/2\,L_p$. After some runs, it was found that a domain with a discretisation as in Figure 39 gave good results. Halving the length of the distance between the RLZ_{inlet} and the structure made the mismatch slightly larger. It could be that the simulation in OpenFOAM is impacted more by the bottom in comparison to OCW3D.

For the refinement of the mesh, quite some efficiency can be gained by refining only the areas of interest. Especially the refinement zone around the breakwater crest should be compact. Here the most refinement is required and so this zone is computationally expensive and dominates the Courant criterion. It was observed that different levels of refinement didn't alter the result significantly, but did speed up the computational time. It was also found that the overtopping height went up slightly with the finer mesh. This could be due to the fact that the finer mesh estimates the area around the free water surface better. Especially in overtopping waves, this could influence the results more.
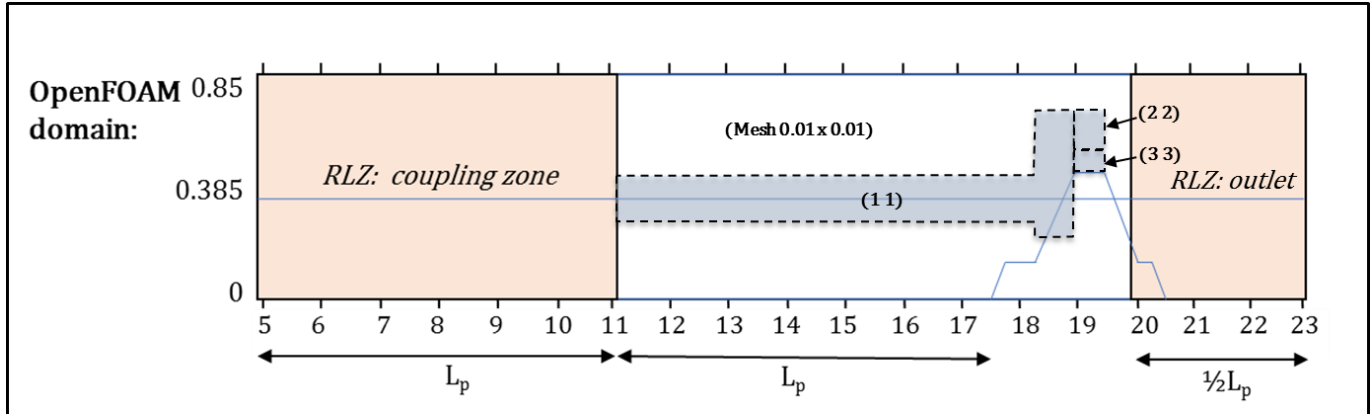

Figure 39: Efficient domain

Throughout this domain, the aspect ratio equals 1. The background mesh is set to equal $10 * 10 \, [mm]$, which is twice more coarse than in the previous validation runs. The refinement around the free water level is of level 1 ($5 * 5 \, [mm]$), and again based on the significant wave height. Around the structure, the free water surface rushes up and down the breakwater slope, and so the height of the run-down zone should also be incorporated in the refinement around the water surface. The run-down level can be estimated by the method proposed by (Van Der Meer, 1988), given by:

$$\frac{R_{d2\%}}{H_s} = 2.1 * \sqrt{tan\alpha} - 1.2P^{0.15} + 1.5 \exp(-60s_{om}) \tag{61}$$

Where:

$R_{d2\%}$	=	Run-down level exceeded by 2% of the incoming waves	$[m]$
P	=	Notional permeability, indicating how much wave energy is dissipated by the structure's armour layers and core	$[-]$

To be conservative this is taken for a value of $P = 0.1$, which results in $R_{d2\%}/H_s \approx 2$. The next part of the refined zone is refined to $2.5 * 2.5 \, [mm]$, and is incorporated because using a refinement of $1.25 * 1.25 \, [mm]$ over the entire zone of the crest is computationally very expensive. The $1.25 * 1.25 \, [mm]$ refinement is only required near the crest to properly study the velocity profiles of overtopping flows in more detail there.

5.3.6 Conclusions on the validation

In section 5.3 the validation procedure was discussed. Although the used experiment made a proper validation tricky (the clean steering file was not available and only the flow depth was measured on 2 parts of the crest) it is concluded that the experiment and the numerical set-up are in sufficient agreement. See also the discussion and the recommendations on this topic (section 7.1 and 9.1). This section also described a sensitivity analysis for the wave field, the effects of turbulence on the overtopping process and the efficiency of the model-set-up.

5.4 Test program

Now the validation of the OpenFOAM set-up has been completed, this set-up can be used to run the tests required to answer the main research question. It is aimed to use combinational numbers (like the Iribarren number) in the simplest way possible. It is argued that such an analysis is more valuable then deriving over-simplified analytical solutions. This thesis will therefore study the influence of the main hydraulic parameters (H_{m0} and $L_{m-1.0}$) and the freeboard (R_c) on the critical overtopping parameters ($u_{2\%}, h_{2\%}$). The front slope of the structure (α), the nominal rock diameters ($d_{n,50}$), the porosities (n) and the water depth in front of the structure (h) are not varied.

This study differs from the studies of flow over dikes because the breakwater structure has a different slope and porous flow characteristics. It is argued that altering these parameters however should be done carefully as quite some debate exists on differing from the 'standard' values of the Forchheimer equation. It is therefore chosen to keep the research here limited to the aforementioned parameters and the porous characteristics of the validated test case. The testcase is considered representative for a 'standard' situation, with regularly used gradings for both the core material and the filter layers.

Simulations with irregular waves are used, for which the Joint North Sea Wave Project (JONSWAP) spectrum is used. The JONSWAP spectrum is a fetch-limited sea state based on experiments in the North Sea (Hasselmann et al., 1973).

5.4.1 JONSWAP: Background & Discretization

The JONSWAP spectrum is a widely used spectrum in engineering practice. It has been shown that the JONSWAP spectrum is not only present for idealised fetch-limited conditions, but also for other arbitrary wind conditions in deep water (like storms). The JONSWAP spectrum does not apply to swell, the steepness of swell waves is low and so the quadruplet wave-wave interactions which normally tend to stabilize the shape of a spectrum into a JONSWAP shape are not present. Due to the absence of a standardized swell spectrum, the JONSWAP spectrum is also often used by engineers to model waves with a low steepness (Holthuijsen, 2007). Also in this research this approach will be adopted.

It should be mentioned that the random phase-amplitude spectrum of course has its limitations. It is mostly suitable for waves in deep water where the linear wave theory is applicable and the wave components are harmonic and independent. Again, as there is no easy alternative, the wave spectrum is often also used to study nearshore coastal processes.

Waves2Foam makes it possible to impose a JONSWAP spectrum, giving as an input the H_s, T_p and the peak enhancement factor γ. To keep the set-up similar to the validated test case, OCW3D is used in this thesis to generate the JONSWAP. The peak enhancement factor is often used to model swell waves, as it can be opted that for varying the wave steepness, also the γ-factor in the JONSWAP should be adapted. The γ-factor can be for example 2.0 for sea and 6.0 for swell. This is often done to give the peak of the spectrum a certain steepness around the peak frequency (see Figure 40), making it resemble either a sea or a swell spectrum. The peak enhancement factor is however not adapted in this thesis and the standard value of 3.3 is used. This is done to keep the total number of variables low.

As OCW3D takes the peak period T_p as an input and the test program varies the mean spectral period $T_{m-1.0}$, the relation between the two is of importance. The peak enhancement factor influences the relation between the peak period and the mean spectral period, and so some calculations were made for JONSWAP spectra with a peak enhancement factor between 1 and 6. The relation is only required for $\gamma = 3.3$, but for future reference more results are listed (see Table 11). Besides this, OCW3D takes as input the maximum $k * h$, where k is the wavenumber and h is the water depth. This controls the smallest wave length that will be resolved in the generation of the JONSWAP.
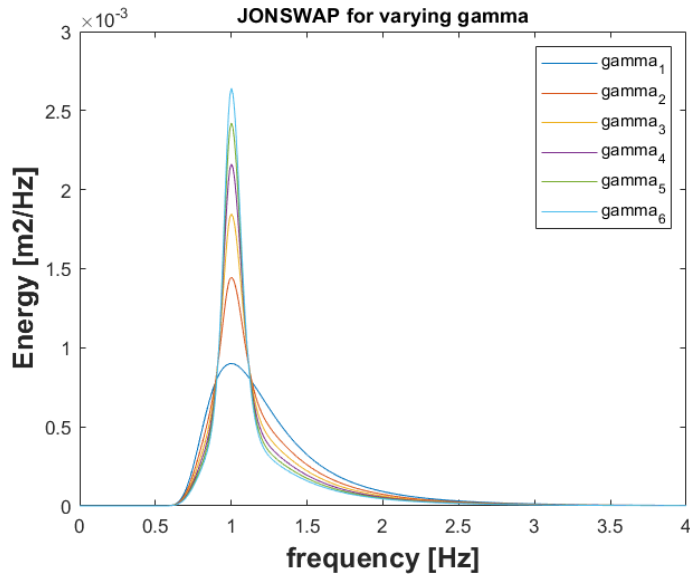
Figure 40: the JONSWAP spectrum for various values of the peak enhancement factor.

γ	$T_p = x \cdot T_{m-1.0}$, x:
1	1.166
2	1.132
3.3	1.107
4	1.098
5	1.088
6	1.088

Table 11: the relation between T_p and $T_{m-1.0}$ for various values of γ

As mentioned, the JONSWAP is generated using OCW3D, which is computationally efficient. Waves2Foam however also has possibilities to discretise the JONSWAP using enhanced methods, this is discussed in some more detail in Appendix G.

5.4.2 Runs

The test program is discussed in this section. As mentioned, H_{m0}, $L_{m-1.0}$ and R_c are altered in these runs. To vary these parameters, combinational (non-dimensional) numbers are used. Non-dimensional numbers are a way to characterize complex systems with multiple interacting physical parameters. Often it is aimed to use established non-dimensional numbers which are used more widely in hydraulic engineering. Non-dimensional numbers make it possible to compare results from different test configurations and scales.

The non-dimensional numbers that are employed here are the relative freeboard R_c/H_{m0} and the wave steepness $s_{m-1.0}$. The front slope of the structure is not adapted, hence the Iribarren number $\xi_{m-1,0}$ is only affected by the changing wave steepness. Two different levels of steepness in the waves are used, $s_{m-1.0} = 0.01 \, \& \, 0.05$, creating waves with a steepness comparable to a swell state and a sea state respectively. With the fixed angle of the front slope ($\tan(\alpha) = 2/3$) this means the Iribarren number varies between 6.67 (surging) and 2.72 (collapsing-surging).

For the relative freeboard, three values are adopted: $R_c/H_{m0} = 0.5, 1.0 \, \& \, 1.5$. With these values, various levels of overtopping rates are expected (see for example (Van der Meer *et al.*, 2018; their figure 6.7). Also it incorporates a rule of thumb that is used in the field more often, being $WorkingLevel = MHW + H_{m0}$ (when $R_c/H_{m0} = 1$).

The runs are set-up by selecting wave heights to serve as input for the model. The wave periods and freeboard are calculated using this and the non-dimensional numbers. Some considerations for selecting wave heights are important, being wave breaking and the stability of the structure:

Depth induced wave breaking should not be present in the model runs. As it was chosen not to model turbulence with a turbulence closure model (see Section 5.3.4) it is best to keep wave breaking outside this analysis to prevent additional uncertainty in the results. To check when wave breaking occurs, the method of (Battjes and Stive, 1985) is used. The maximum wave height is expressed as a fraction of the

water depth by: $H_{max} = \gamma(d + \bar{\eta})$, where γ is the breaker index, d is the local water depth and $\bar{\eta}$ is the wind-induced set-up.

The value of γ is not universal, to be conservative a value of 0.6 is chosen. Taking into account the toe of the structure and how it reduces the water depth, this gives $H_{max} = 0.6 \cdot 0.275 = 0.165\ m$ (on model scale). It is clear from this notion that a maximum wave height exceeding this limit could result in wave breaking. Considering $H_{max} \approx 2H_{m0}$, H_{max} should not exceed $0.08\ m$ in the simulations.

This is also in agreement with observations from the experiment, where some wave breaking was spotted on the foreshore for a H_{m0} of $0.08\ [m]$ in height and a period of $3.2\ [s]$. It seems that besides a H_{max} of $0.08\ [m]$, also the wave period should not be too long. This was also observed by Battjes and Stive, who observed that for low incident wave steepness, the breaker index decreases and so the H_{max} decreases. Hence the runs should include wave fields with $H_{m0} < 0.08\ m$ and $T_p < 3.2\ s$.

The stability of the structure should be guaranteed up to a certain level, as the overtopping process will be different when the structure is reshaping. Based on the experiment report, it is clear that similar wave conditions that cause wave breaking, also cause significant instability of the outer filter layer. For $H_{m0} = 0.08\ m$ and $T_p = 2.4\ s$ the structure is relatively stable although movement is present (7.5% of under layer stones displaced). For $H_{m0} = 0.08\ m$ and $T_p = 3.2\ s$, the test was stopped and the under layer was found instable. For both tests, core material was displaced to the rear side of the crest.

As this thesis looks at extreme overtopping events, it is chosen to assume that the structure stays stable enough up until $H_{m0} = 0.08\ m$ and $T_p = 2.4\ s$. It is argued that for studying overtopping limits, the reshaping up until this level is acceptable.

For the wave heights, it is then chosen to use $1, 1.5$ and $2\ [m]$ (on prototype scale). The total test set-up is visualized by Figure 41.
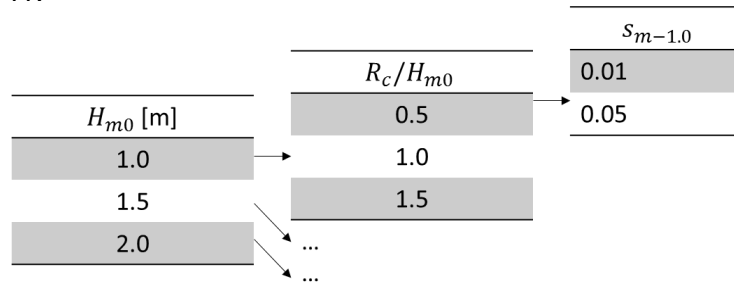
Figure 41: Test set-up for 18 runs

In this study the 2% exceedance values of the overtopping velocities and flow depths are analysed. This means that for every 50 incoming waves, the largest overtopping event will give this 2% exceedance value. Considering the reliability of the result it is insufficient to do only 1 test with this, so it is chosen to use at least 5 times 50 waves. Of course it is best to simulate the full length of a storm, but this is computationally very expensive. Hence, 250 waves are simulated. Table 12 and Table 13 below show the test input for the wave field, both on prototype scale and model scale.

Prototype scale ($s_{m-1.0} = 0.01$)					Model scale					
H_{m0}	$L_{m-1.0}$	L_p	$T_{m-1.0}$	T_p	H_{m0}	$L_{m-1.0}$	L_p	$T_{m-1.0}$	T_p	$250\ waves\ [s]$
1.0	100	122.54	8.01	8.86	0.04	4	4.90	1.60	1.77	400
1.5	150	183.82	9.81	10.86	0.06	6	7.35	1.96	2.17	490
2.0	200	245.09	11.32	12.53	0.08	8	9.80	2.26	2.51	565

Table 12: Test input for waves with $s_{m-1.0} = 0.01$

Prototype scale ($s_{m-1.0} = 0.05$)					Model scale					
H_{m0}	$L_{m-1.0}$	L_p	$T_{m-1.0}$	T_p	H_{m0}	$L_{m-1.0}$	L_p	$T_{m-1.0}$	T_p	$250\ waves\ [s]$
1.0	20	24.51	3.58	3.96	0.04	0.8	0.98	0.72	0.79	180
1.5	30	36.76	4.38	4.85	0.06	1.2	1.47	0.88	0.97	220
2.0	40	49.02	5.06	5.61	0.08	1.6	1.96	1.01	1.12	252

Table 13: Test input for waves with $s_{m-1.0} = 0.05$

With the runs described by Figure 41 it is possible to make 18 combinations. However, it is chosen to use 1 base-case and to vary this through changing one parameter at a time. In this way, in total 6 combinations can be made. It is chosen to add 2 extra runs to this, so more sea-state runs can be studied. The 8 studied runs are summarized in Table 14.

Run-ID	$H_{m0}[m]$	$T_p[s]$	max (kh)	$f_{max}[Hz]$	R_c/H_{m0}	R_c
1_H06-S1-R10	**0.06**	**2.17**	**4.0**	**1.6**	**1.0**	**0.06**
2_H04-S1-R10	0.04	1.77	4.0	1.6	1.0	0.04
3_H08-S1-R10	0.08	2.51	4.0	1.6	1.0	0.08
4_H06-S1-R15	0.06	2.17	4.0	1.6	1.5	0.09
5_H06-S1-R05	0.06	2.17	4.0	1.6	0.5	0.03
6_H06-S5-R10	0.06	0.97	10.0	2.5	1.0	0.06
7_H04-S5-R10	0.04	0.79	10.0	2.5	1.0	0.04
8_H08-S5-R10	0.08	1.12	10.0	2.5	1.0	0.08

Table 14: Main settings of the 8 runs, and accompanying run ID's

For the swell runs the maximum kh is set to 4.0, meaning that the smallest wave length that will be imposed is about $0.6\ [m]$. For the sea runs, the maximum kh is set to 10.0, the smallest wave length will then be $0.24\ [m]$ For runs 1, 2, 3, 6, 7 and 8 also the wave spectrum is visualised, which are cut-off at $1.6\ [Hz]$ for the swell runs and $2.5\ [Hz]$ for the sea runs (these are the cut-off frequencies corresponding to the cut-off wavelengths).
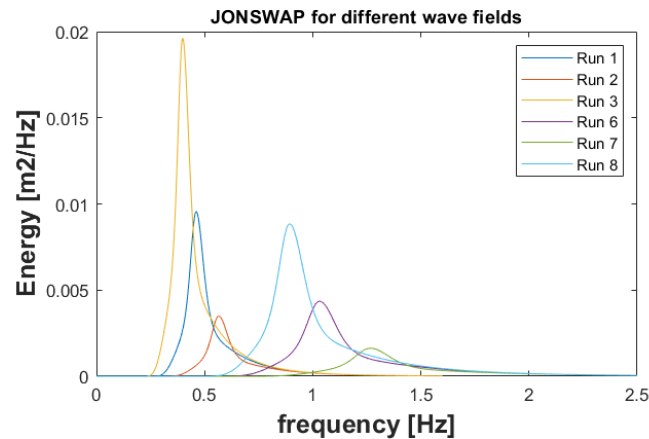
Figure 42: JONSWAP for 6 runs

The OpenFOAM domain can be adjusted following the indications that were described in the validation. For the sea runs, the domain is made larger (relatively) as no specific validation tests were done for sea states. Also, for the OCW3D domain a wave generation zone needs to be added. An additional peak wave length is added in front of the simulated area where the JONSWAP is imposed. This means that the OCW3D domain becomes $1.56 * 2.5^2 \approx 10\ [m]$ longer, based on the longest peak period in the test program (assuming deep water conditions). A total overview of the set-up is given in Appendix H.

6 Results

Chapter 6 discusses the results from the test program that is described in section 5.4.2. First, an introduction is given to recap briefly the previous chapters and to give an overview of the contents of chapter 6. All postprocessing discussed in this chapter is performed using either MATLAB or ParaView.

6.1 Introduction

Based on the considerations in chapters 2 (Quantifying Overtopping) and 3 (Numerical Modelling) it was chosen to use a numerical model to give answers to the research questions that were described in chapter 1. With the validated numerical model (chapters 4 and 5) a test program was made that consists of 8 runs.

The parameters that are varied in the test program are considered to have an effect on the overtopping flow velocity (u) and the overtopping flow depth (h). These characteristics of overtopping flow were linked to the safety of personnel and hydraulic excavators on the partially built breakwater through limit functions. The limit function for personnel describes what combinations of flow velocity and flow depth cause a person to fall. The limit function for the hydraulic excavator describes that the flow depth cannot exceed a certain limit. The freeboard is expected to influence the flow characteristics and can thus be adapted (lowered or raised) to create a situation that is economically efficient and safe.

This chapter aims to describe what the empirical relations could look like to describe the relations between the variables in the test program and the overtopping flow characteristics. To this end, section 6.4 describes the flow characteristics on the core crest edge, whereas section 6.5 describes the development of the flow characteristics over the width of the crest. Besides this indicative analysis, this chapter attempts to answer how and what we should measure when using OpenFOAM for overtopping flow as well as showing where the biggest uncertainties are in the results. Section 6.6 combines this knowledge to show how the results can be used in engineering practice.

Before diving into this analysis however, the next section will first discuss the 'transition zone'. Based on the analysis that was done in the validation it was assumed that all overtopping flow was flowing directly over the breakwater. In other words, it was assumed that the overtopping water was in direct contact with the crest of the breakwater (and so, no overtopping through the air, at a distance away from the breakwater crest). From a first analysis of the results however, it turned out that in fact 2 'flow-regimes' can be distinguished for various overtopping waves. For 1 of these flow regimes, the limit functions that were set up are not useful. The next section will thus go into some more detail on this.

6.2 The transition zone

Analysis of the overtopping flow depth and overtopping flow velocity is performed over the core material. This is done because overtopping is often measured on the core crest edge, as people and equipment don't traverse the filter and armour layers. Besides this, it was found from the flow profiles studied in section 5.3.4 that the flow appeared to be attached to the breakwater crest for the moment of maximum flow depth and the moment of maximum flow velocity at the core crest edge. From this it was assumed that the wave tongue was flowing directly over the breakwater crest.

It appeared that the transition of the wave tongue over the breakwater crest edge did not cause the flow to be detached from the breakwater at the point of interest. This was also the rationale for the waves created by the test program. In section 2.5 it was also hypothesized that for the set-up in this thesis with mostly surging waves the transition over the crest edge would be relatively smooth. However, looking at the results, it was found that the flow was in fact detached for quite some waves in the test program. This

influences the intended analysis. Before specifying in more detail what exactly is going on with the generated data, here it is visualised what is meant by 'flow detachment' and the concepts of 'transition zone' and 'flow zone' are introduced.

6.2.1 Flow detachment, transition zone and flow zone

Figure 43 and Figure 44 show the same overtopping wave during two different time steps. The figures show α-contour plots, which means that the air-water interface is represented by a line showing when the indicator function equals 0.5. Note that this output was not generated by runs from the test program. These plots follow from an additional run that was made with (relatively large) regular waves, to gather more in depth information on the overturning of a wave onto the breakwater.
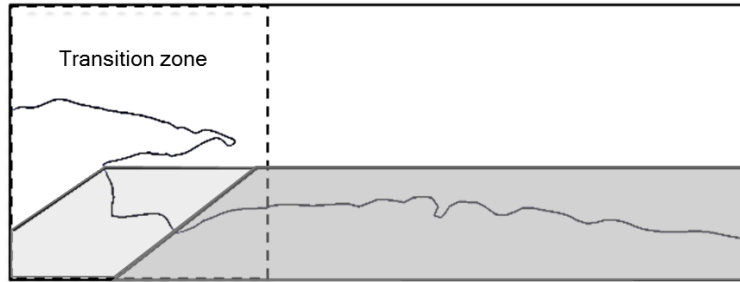

Figure 43: An overtopping swell wave, the 'transition zone' is indicated by the dashed line

Figure 43 shows that, as the wave has rushed up the seaward slope, it detaches from the breakwater at the crest edge. At the crest edge, the flow is directed parallel to the breakwater slope. After passing the breakwater crest edge, the flow is directed towards the breakwater crest under the influence of gravity. This causes the flow to 'reattach' after some time to the breakwater. The length along the breakwater crest up until this reattachment point is called the 'transition zone'. Because the water is not attached to the crest of the breakwater, the limit functions that were set up are not applicable for such waves.
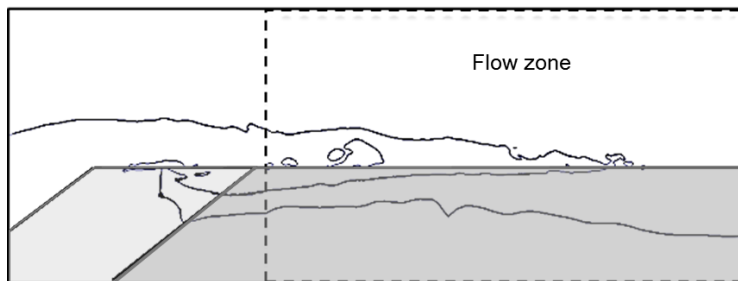
Figure 44: An overtopping swell wave, the 'flow zone' is indicated by the dashed line

Figure 44 shows what the wave looks like when it is (for the largest part) attached to the breakwater. After the reattachment point, the wave is directed to flow parallel to the breakwater crest. This area is called the 'flow zone', here the limit functions are applicable that were discussed in section 2.1.4.

Because the transition zone was found to be much more significant than was considered beforehand, the analysis using the limit functions does not always make sense. Therefore it should be studied what the length of the transition zone is and what kind of limit functions are applicable there. This is not a straightforward assignment with the data-set that was generated for this study.

In Appendix I, the output from OpenFOAM is discussed. It goes into measurement errors and describes how the velocity is measured. The next section describes how the transition zone affects the data that was generated and in what way this is used in the analysis throughout this chapter.

6.2.2 OpenFOAM output and the transition zone

Because the wave gauges measure through an integration over the vertical, the overtopping water can in fact reach higher than what is measured by the wave gauge. The numerical wave gauge functions similarly to an experimental wave gauge. The gauge output shows all measured water flows as if these occur directly over the crest, while in fact the water could be shooting over the breakwater at some distance upward from the crest. This can happen through the previously described phenomenon of the detached overtopping flow.

To visualise this, the velocity profile of an overtopping event can be used. Figure 45 shows this for a wave overtopping during Run 8, at around $36.4\,[s]$. This measurement is performed on the core crest edge (see also Figure 48).The maximum overtopping depth, as measured by the wave gauge, is about $9\,[mm]$. It is clear that for this wave the timing of the maximum velocity (as indicated by the black dot), almost coincides with the maximum measured flow depth (as indicated by the red dot). Looking at the probe output at the moment of maximum velocity on the right, it appears that in fact not a continuous sheet of water is overtopping from the crest upward. The overtopping wave consists of a part that flows directly over the crest, accompanied by some water overtopping at around $15\,[mm]$ and $40\,[mm]$ above the crest. Note that the main overtopping flow is centred around $15\,[mm]$ height. Such detachment from the crest is also seen for some of the larger waves.
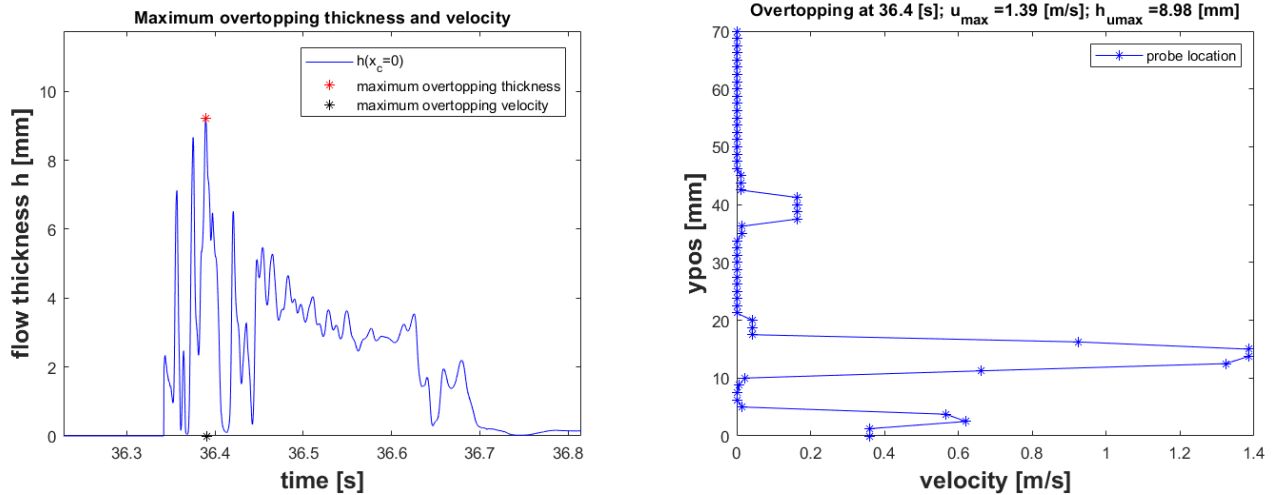

Figure 45: Overtopping event at 36.4 [s]

This sort of problem is mostly an issue near the seaward edge of the breakwater. It is difficult to deal with this. Measurement of the surface elevation with the probes alone would require thought on what is defined as water (what α value defines the air-water interface). Also the measured velocity from flows detached from the breakwater crest are less well represented by the more coarse grid higher away from the breakwater. Besides this it should be studied how unsafe some of the overtopping is (e.g. one could argue that the overtopping centred around $40\,[mm]$ in Figure 45 should not be considered). These considerations would require the definition of a new safety criterium in the transition zone.

It can also be chosen to only study the flow over the breakwater after the transition point. It is important then to define where the transition over the breakwater is complete. So, we need to quantify the length of this transition zone. To this end, in this example some more results along the crest of Run 8 should be studied.

Looking at the velocity profiles of the waves, it becomes clear that the transition over the crest edge is not complete after the wave has passed the filter layer. Especially when plotting the velocity profiles at the moment the maximum velocity occurs, it is clear to see that a part of the flow is detached from the crest material. This is the case for 12 of the 25 overtopping events studied in Run 8. Ignoring these waves

in the analysis is then not a serious option as it would overlook an important aspect of the overtopping flow. Three examples of such detached flow profiles are given here:
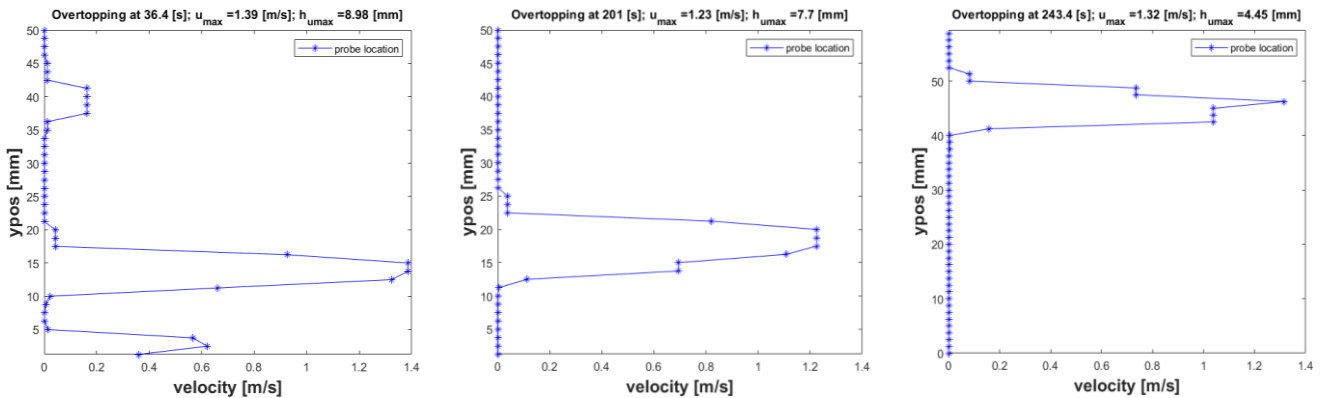

Figure 46: Overtopping flow at the moment of maximum flow velocity

Plotting the velocity profiles at the moment that the maximum flow depth is occurring, it is clear that for 8 of the 25 overtopping waves the flow is detached from the crest. These waves were also found in the analysis based on the maximum flow velocity. Again some examples are given (Figure 47).
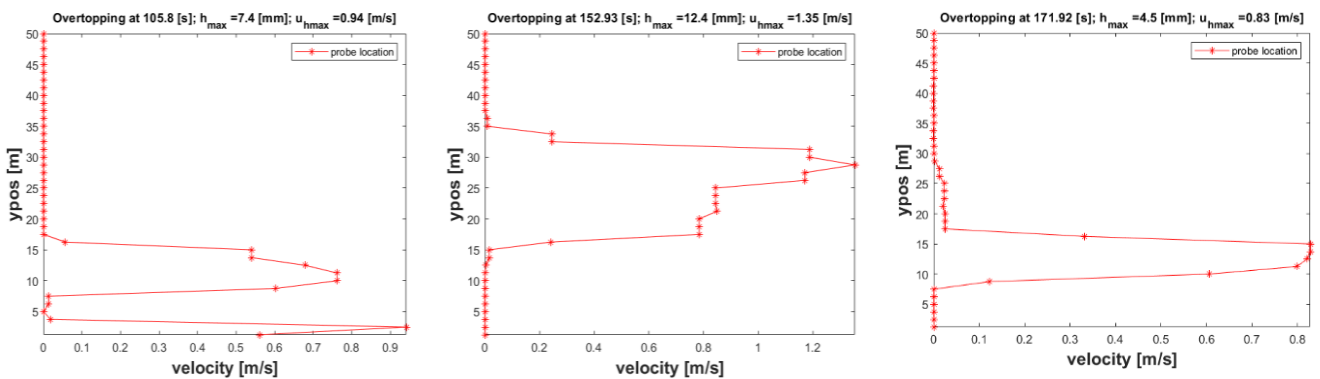

Figure 47: Overtopping flow at the moment of maximum flow depth

It should be noted that the three largest waves in this particular run are attached to the breakwater crest. These are waves that are of interest, but the velocity profiles for the maximum velocities of these waves are detached from the breakwater crest. There is quite a significant transition for the waves from run 8, with high velocities in flows detached from the breakwater.

Here only the velocity profiles for the maximum flow velocity and the maximum flow depth are checked. These are assumed to be the critical flow situations, it should however be realised that many other stages of the overtopping wave tongue are not checked in this analysis.

Looking further down the breakwater crest, it is possible that some waves are still detached from the breakwater. Defining the end of the transition zone when al waves are attached again then causes many waves to be left out of the analysis as these are already infiltrated to a great extent into the breakwater. Defining the exact location where the transition is complete is also difficult because the gauge and probe spacing was not set-up to measure this phenomenon.

It is therefore checked when all the velocity profiles for the maximum flow depth are attached to the crest. This criterion is chosen as it was observed that the velocity profiles for the maximum flow velocity were detached more often. With this criterion, Table 15 was set-up, where the transition length (starting at the core crest edge) is given relative to the spectral wave height. We can see that the largest swell run experiences detachment, as well as all sea waves. For the sea waves, the detachment seems to get

72

more significant when the wave is larger. Run 7 doesn't seem to follow this pattern, however for run 7 so few waves overtop that only measurements are available at the first two wave gauges and not in between. So the value presented here is likely an overestimation.

Run	$L_{transition}/H_{m0}$
3	0.77
6	1.58
7	1.67
8	1.95

Table 15: Transition length

As discussed, it is difficult currently to define the length of the transition zone properly. Hence in the further analysis, the data is processed quantitatively ignoring the effect of the transition zone but keeping it in mind in a qualitative analysis of the results.

6.3 The 2% exceedance value

This section describes the method that is used to generate the 2% exceedance values for the waves. In this analysis we take all overtopping waves into account, also the waves that are detached from the crest. To clarify, the 2% value is used to make it easy to compare to literature. Because the Rayleigh distribution is employed, it is easy to calculate a different exceedance probability based on the 2% exceedance value.

To get the 2% exceedance value, a statistical distribution is fitted. In this case, a Weibull distribution was fitted to the data. This was done based on the method described in (Van den Bos and Verhagen, 2018). In short, this method works as follows for each run:

1. The studied parameter (h or u) is ranked smallest to largest;
2. For each parameter value i the non-exceedance probabilities and the exceedance probabilities are calculated, following:

$$P_i = \frac{i}{N+1}; \; Q_i = 1 - P_i \tag{62}$$

Where:

P_i =   the non-exceedance probability for measurement i $[-]$
Q_i =   the exceedance probability for measurement i $[-]$
N =   the total number of incident waves $[-]$

3. The Weibull distribution will be fitted, given by:

$$Q = \exp\left(\left(-\frac{X - \hat{\gamma}}{\hat{\beta}}\right)^{\hat{\alpha}}\right) \tag{63}$$

Where:

X =   the studied parameter $[-]$
$\hat{\gamma},\hat{\beta},\hat{\alpha}$ =   distribution parameters, these need to be fitted $[-]$

To fit the $\hat{\gamma}$ and $\hat{\beta}$ parameters of this equation, linear regression is used and so the studied parameter is plotted against the x-axis where the Weibull distribution is given by:

$$X_{W,i} = \left[\ln\left(\frac{1}{Q_i}\right)\right]^{1/\hat{\alpha}} \tag{64}$$

Where:

$X_{W,i}$ =   The linearized Weibull distribution $[-]$

Then $\hat{\gamma}$ and $\hat{\beta}$ can now be fitted following:

$$X = \hat{\gamma} + \hat{\beta} X_{W,i} \tag{65}$$

4. By varying $\hat{\alpha}$, the RMSE between X and the linearized Weibull distribution can be minimised. In this way all three distribution parameters can be fitted for all runs.

It was found from this analysis that the 2% exceedance values don't necessarily follow a Rayleigh distribution. In the case of a Rayleigh distribution, the $\hat{\alpha}$ with the lowest RMSE would be $\hat{\alpha} = 2$. There was no clear indication of what value fitted the data best. There was a large variety, both for the flow depth and the flow velocity.

It was however found that the error between the perfect fit and the Rayleigh distribution was relatively small (in the worst case the difference for the $h_{2\%}$ was 7.7% and for the $u_{2\%}$ 1.8%). It was therefore concluded to use the Rayleigh distribution for the calculation of all 2% exceedance values, in order to have one and the same method for all calculated data points. An example of an output table of the 2% exceedance values is given in Appendix J.

6.4 $h_{2\%}$ and $u_{2\%}$ on the core crest edge

With the method to find the 2% exceedance flow depth and flow velocity as described in section 6.3, it is now possible to characterize the $h_{2\%}$ and the $u_{2\%}$ on various positions on the breakwater crest. First, these are characterised on the seaward core crest edge of the breakwater. This location is indicated by the red line in Figure 48.
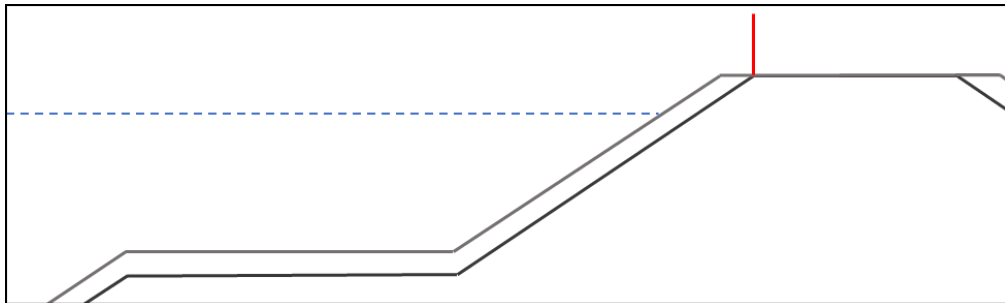

Figure 48: location of the core crest edge in the runs

6.4.1 Overtopping flow depth $h_{2\%}$

In section 2.5 it is hypothesised that: *The flow depth on the run-up crest edge depends more explicitly on the characteristics of the up rushing wave $(\xi_{m-1,0})$ as the assumption that the flow depth decreases linearly over the outer slope could be flawed. Also, the flow depth is influenced by the height of the 'cut-off' of the up rushing wave, the relative freeboard $(R_c \, / \, H_{m0})$.*

As a starting point, a comparison is made between the generated data and literature on dikes. Figure 49 shows the non-dimensional $h_{2\%}$ plotted with the method as proposed by (Schüttrumpf and van Gent, 2003). The value for the $c_{h2\%}$ equals 0.328. To find this value, a least squares fitting method is adopted, where the coefficient is calculated for the smallest RMSE and highest R-squared value. The R-squared gives the squared value of the correlation coefficient for the equation and the data ($R^2 = 0.718$ for this curve). It is clear from the plot that quite a large scatter is present. As expected, a lower relative freeboard and a lower wave steepness (and so higher $R_{u,2\%}$) appear to increase the $h_{2\%}$. This is as hypothesised, but it is also clear that these two parameters can't fully explain the spread that is visible.
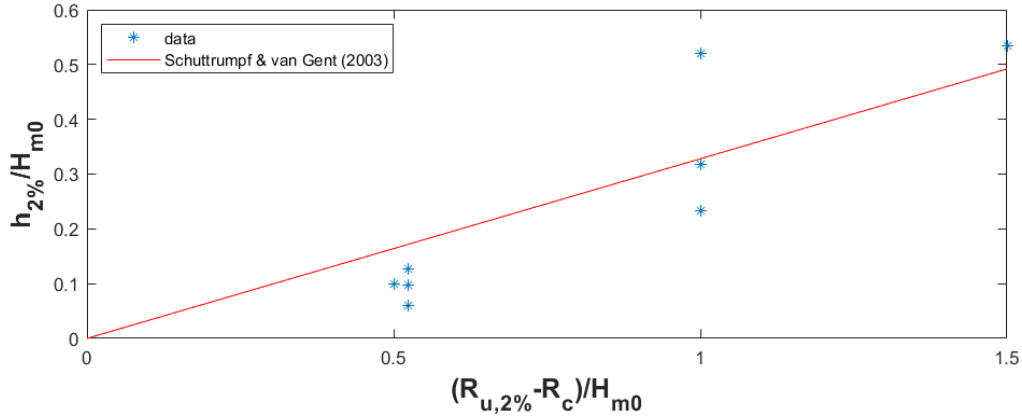
Figure 49: the non-dimensional $h_{2\%}$ plotted against Schüttrumpf & van Gent (2003)

It appears that an additional parameter is required to describe the variations in the flow depth on the core crest edge for various wave heights. It appears that the sea waves have a less large spread as compared to the swell waves. This could indicate that the way the waves break (collapsing or surging) influences the flow depth on the crest. As it is seems that the length of the transition zone increases for larger wave heights and sea waves, it could be that larger quantities of water more easily saturate the outer slope of the porous structure, diverting more water up against and over the structure. Besides this, also the longer swell waves have more time to infiltrate into the structure, as opposed to the collapsing shorter sea waves. This causes a more instantaneously forced infiltration of the filter layer of the breakwater, diverting the water coming in later. This effect of the porosity can be included through introducing the relative filter layer thickness. Through incorporating the layer thickness of the filter layer, a significantly better fit can be made ($R^2 = 0.875$; $RMSE = 0.067$; the linear coefficient now equals 0.495). Figure 50 can now be plotted.

$$H_{m0}/t_f \tag{66}$$

Where:

t_f =   Filter layer thickness in the horizontal direction $[-]$

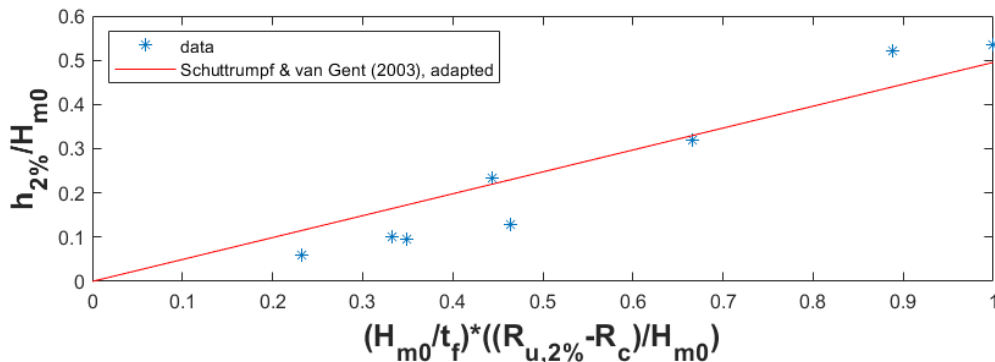Figure 50: the non-dimensional $h_{2\%}$ plotted against the adapted Schüttrumpf & van Gent

Assuming a power relation between the non-dimensional parameters results in an even better fit, see Figure 51 ($R^2 = 0.959$; $RMSE = 0.042$). The found formula is given by:

$$\frac{h_{2\%}}{H_{m0}} = 0.57 * \left(\left(\frac{H_{m0}}{t_f} \right) * \left(\frac{R_{u2\%} - R_c}{H_{m0}} \right) \right)^{1.50} \tag{67}$$

75
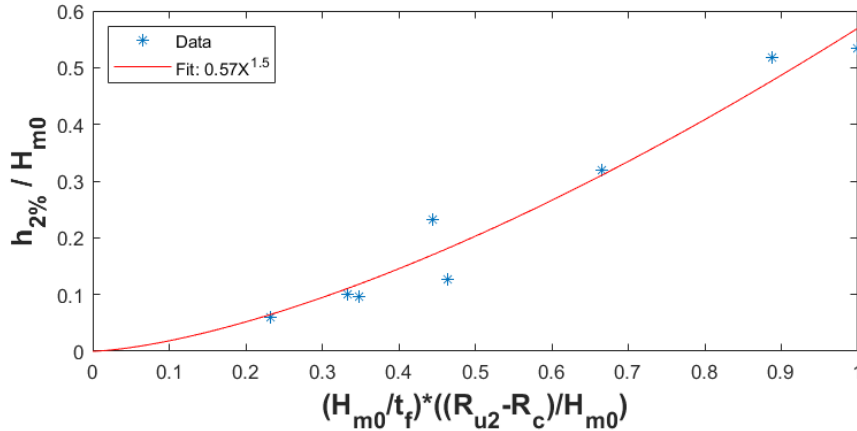
Figure 51: the non-dimensional $h_{2\%}$ plotted against the adapted power function Schüttrumpf & van Gent

It appears that the $R_{u2\%}$, when corrected for the relative filter layer thickness, can quite well predict the findings from this research. It appears that a power function describes the relation best.

6.4.2 Overtopping flow velocity $u_{2\%}$

With a similar approach as for the $h_{2\%}$, the $u_{2\%}$ on the core crest edge was studied. In section 2.5 it was hypothesised that: *the flow velocity on the run-up crest-edge depends more explicitly on the characteristics of the up rushing wave, where the velocity is influenced by the Iribarren number ($\xi_{m-1,0}$).*

Various relations between the non-dimensional parameters and the non-dimensional flow velocity were analysed. It was found that the flow velocity did not clearly depend on the varied parameters. The R-squared for a similar power function was only 0.370. This likely has to do with the stochastic nature of the up rushing waves. Based on findings in other research however, it was checked if a relation could be found between the non-dimensional overtopping flow depth and overtopping flow velocity.

It was indeed found that a stronger relation ($R^2 = 0.70$) could be found between these variables. The result is plotted in Figure 52. The formula describing it is given by:

$$\frac{u_{2\%}}{\sqrt{g * H_{m0}}} = 1.83 * \left(\frac{h_{2\%}}{H_{m0}}\right)^{0.14} \tag{68}$$
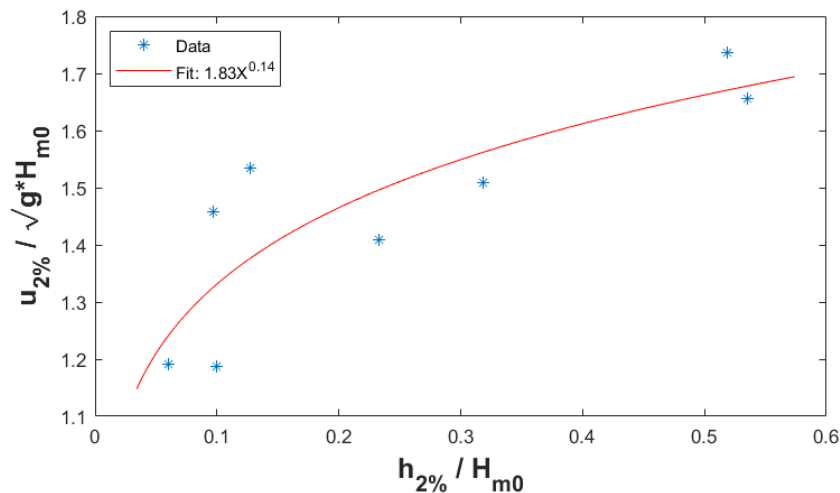
Figure 52: the non-dimensional flow velocity plotted against the non-dimensional flow depth

When comparing this relation to a relation for the data of van Gent and Schüttrumpf as analysed in (Bosman *et al.*, 2008), it is clear that the found formula flattens out quicker (the exponent is smaller than the 0.5 suggested by Bosman). This could follow from the influence of runs 3 & 5, see the upper right side of Figure 52. For these runs, the most overtopping occurred, also accompanied by the highest overtopping flow depths. It could be that for such limit-states the overtopping velocity tends to a maximum.

To study where the large spread in the velocity comes from, the flow over the run-up side should be studied in some more detail. This quite complex flow pattern is difficult to study based on the results generated with the test program, so 2 additional runs were performed with regular waves (1 sea, 1 swell) to visualise the overtopping flow process. For these regular runs, run 3 and run 8 were used as base-case. The simulated wave height was equal to $1.5 * H_{m0} = 0.012\,[m]$ in order to simulate some of the larger overtopping waves that can be found in the irregular wave train.

Figure 53 shows an overview of the flow in the run-up zone, with stills from the regular swell run. The dashed red line represents the mean water level. It can be seen from this that the flow accelerates on the run-up slope above the mean water level. The maximum velocity thus occurs above the mean water line, underpinning the observations of (Van Der Meer, Provoost and Steendam, 2012).

Figure 53: Stills of large swell wave overtopping, vectors indicate the velocity magnitude

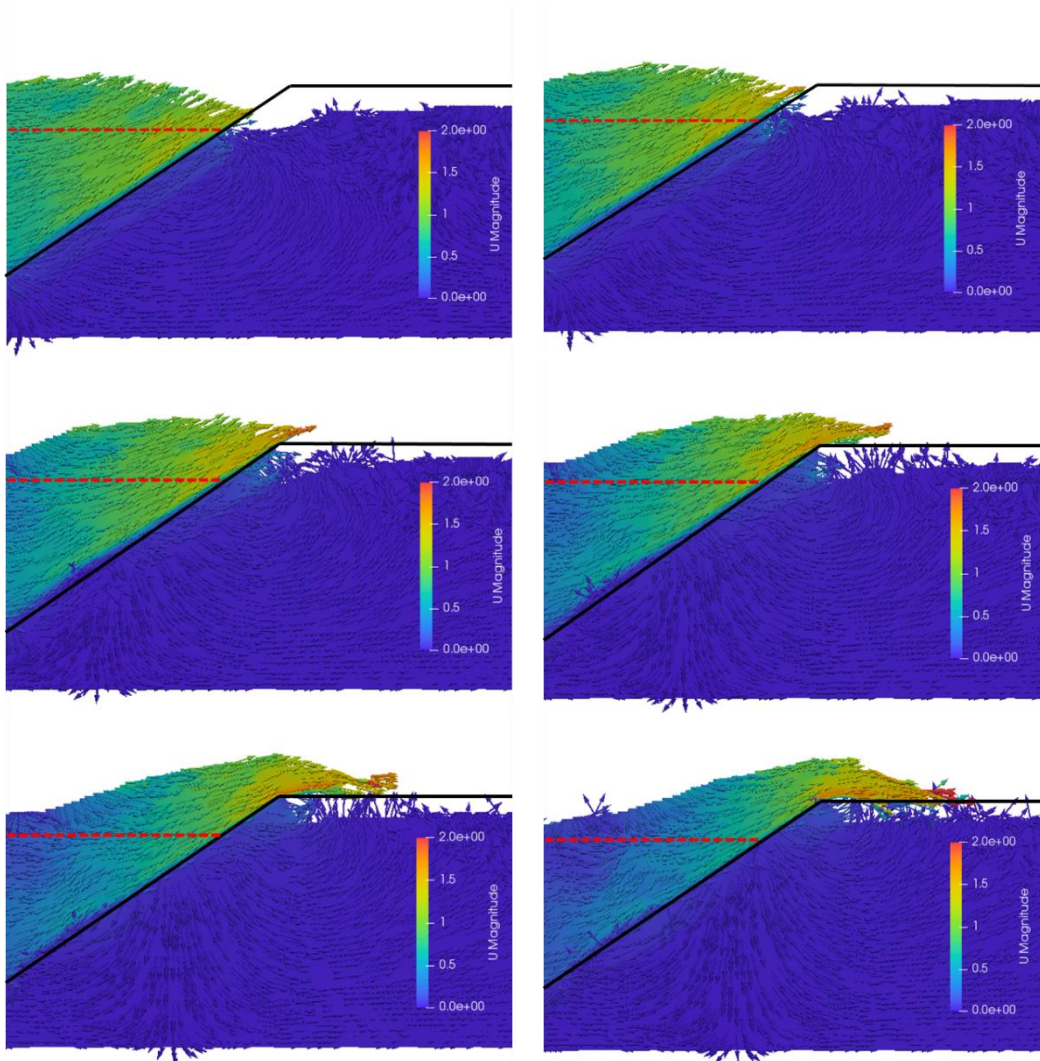To analyse the run-up velocity for an irregular wave field, probes were used as 'run-up gauges'. Probes can be used in this way when spaced along a line over the outer slope. When the indicator function is larger than 0.5, it is considered that water is located at the probe and the y-position of that probe is stored. In this way the run-up level can be tracked. Taking the derivative from this data also gives the run-up velocity. Plotted together, it can be seen what velocities occur for which run-up levels. Figure 54 shows this for a part of Run 4. For this analysis run 4 was used, as only few waves were overtopping and so the process of run-up could be studied without the effect of an overtopping wave.
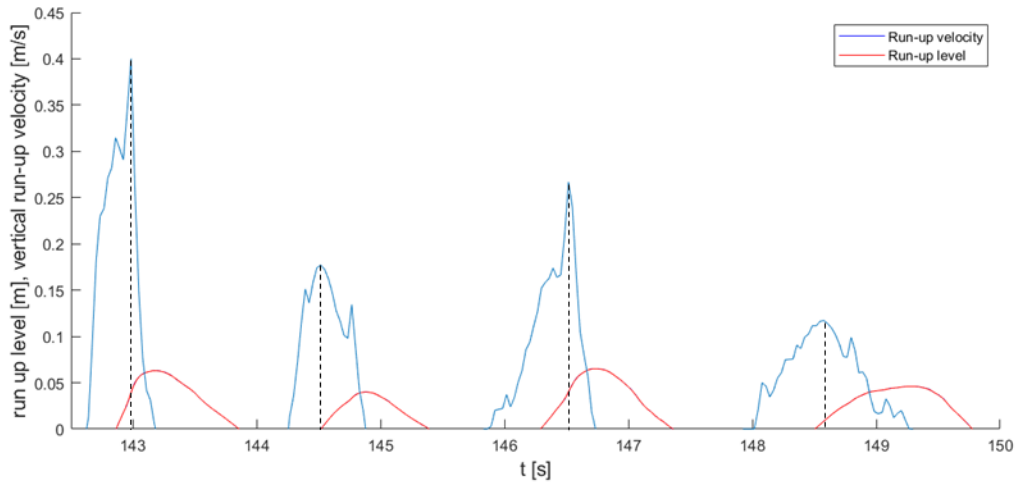
Figure 54: Run-up velocity based on the derivative of the position of the water level for Run 4

The result shows for 4 randomly selected waves that the maximum flow velocity doesn't necessarily occur at the free water surface (see also the intersection between the black dotted lines and the run-up level). The velocity also often has a high value over a larger part of the run-up height. Sometimes even multiple accelerations are visible. It is clear that the velocity over the run-up side appears to be very variable, which likely explains the large spread measured in the results for the velocity on the core crest edge.

6.5 Development of q, $h_{2\%}$ and $u_{2\%}$ over crest

In this section, the $2\%-$exceedance values for h and u over the crest are analysed (the area treated in this section is indicated by Figure 55). Based on the literature study it is hypothesised that the mean overtopping discharge, flow depth and the flow velocity over the crest follow an exponential decay over the length of the crest. As the only reference from literature of flow over breakwaters were studies on the overtopping discharge q, the distribution of q over the breakwater crest is studied as a starting point for this section.
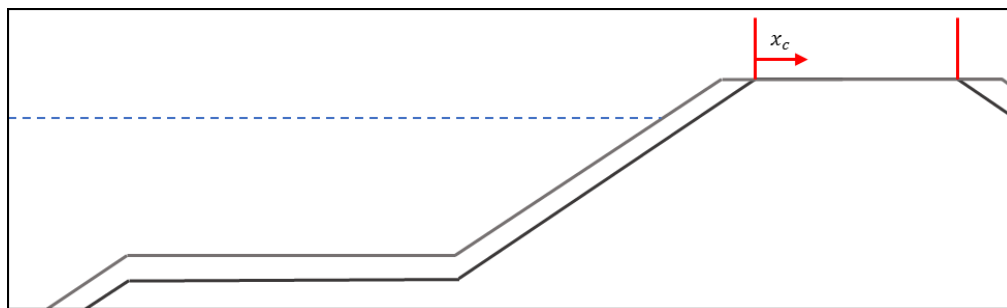
Figure 55: area studied in this section and definition of x_c

6.5.1 Overtopping discharge q

This section studies the development of mean overtopping discharge q over the crest. Figure 56 shows the results of the normalised discharge (normalised to the maximum overtopping as measured at the seaward core crest edge) against the non-dimensional distance away from the core crest edge (x_c/H_{m0}). As discussed in section 2.4, these results can be compared to the methods of (Juhl and Sloth, 1994) and (Besley, 1999). Their methods are plotted here for the settings of run 1.
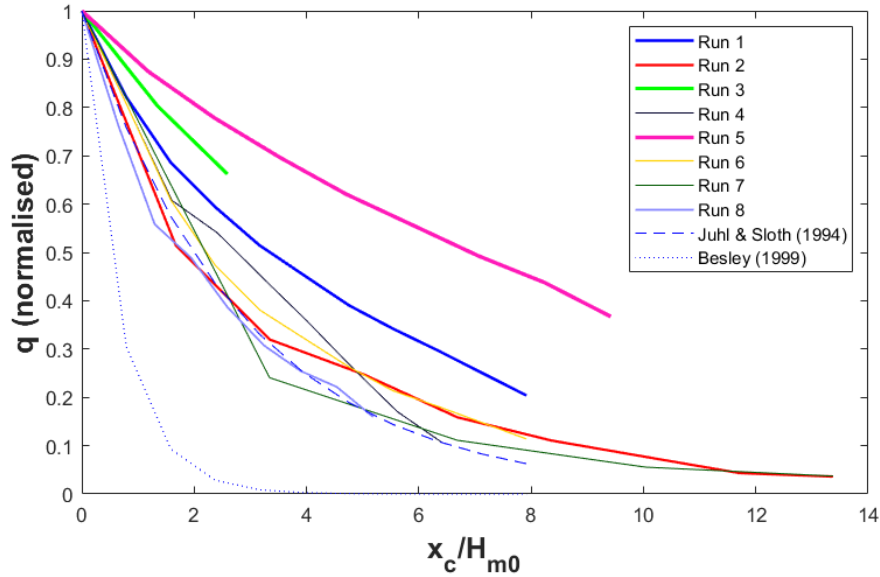
Figure 56: Discharge q for run 1-8, Juhl & Sloth and Besley for $H_{m0} = 0.06; R_c = 0.06$

First, it should be noted that the overtopping faces for run 3 where not completely functional, hence run 3 shows only few results. Looking at the results, it seems that the decrease of the normalised q is similar for runs 2, 4, 6, 7 and 8. For these runs, an exponential decay is visible. It appears that for runs 1, 3 and 5 (but especially for run 3 and 5) the decrease in discharge tends towards a more linear function. These runs are also the runs that have the highest discharge. In the figure, the thickness of the plotted line is related to the discharge on the core crest edge, where the largest discharge is related to the thickest line.

Table 16 shows the measured overtopping discharge, overtopping volume and the number of overtopping waves. Also the values calculated by the EurOtop are given. Note that the number of overtopping waves as calculated by the EurOtop is often the same for different cases. This is because the maximum run-up in these cases is limited by the same maximum ($2 * H_{m0}$) and the ratio $R_{u2\%}/R_c$ is the same for these runs. The comparison shows the same order of magnitude for modelled and calculated overtopping.

	Measured			EurOtop		
Run-ID	$q\ [l/s/m]$	$V_{max}\ [l/m]$	N_{ow}	$q\ [l/s/m]$	$V_{max}\ [l/m]$	N_{ow}
1_H06-S1-R10	0.1433	8.1213	45	0.1542	4.3056	94.0151
2_H04-S1-R10	0.0416	3.0757	24	0.0839	1.9136	94.0151
3_H08-S1-R10	0.6146	23.7331	77	0.2374	7.6545	94.0151
4_H06-S1-R15	0.0203	3.3649	10	0.0157	1.0488	27.6866
5_H06-S1-R05	0.8394	14.0447	165	1.0886	13.9548	195.7737
6_H06-S5-R10	0.0281	1.7707	26	0.0157	0.3316	46.3092
7_H04-S5-R10	0.0054	0.1548	10	0.0086	0.1474	46.3092
8_H08-S5-R10	0.0722	2.9806	25	0.0242	0.5896	46.3092

Table 16: Overtopping, measured & calculated by the EurOtop

The facts that 1) a more linear approximation seems suitable for the runs with the highest discharge, and 2) both Juhl & Sloth and Besley overestimate the decrease in overtopping discharge (their tests use armoured crests), it stands to reason that the relatively decreased porosity of the breakwater under construction causes a less rapid infiltration. It can be argued that the waves with relatively large overtopping discharges saturate the porous medium and cause more waves to flow over the breakwater instead of following the same infiltration pace as the runs with smaller overtopping discharges. Especially in run 5 the crest was inundated for a significant amount of time (165 out of 250 waves were overtopping), and this line clearly tends towards a more linear infiltration pattern. It should be added to this that also Steenaard found that as the overtopping discharge increases, the losses into the crest reach a constant value (Steenaard, 2002). Also this indicates saturation of the armour layer.

The method of Besley is adapted for these findings, to suit a breakwater under construction. For clarity, the formula proposed by Besley is repeated here:

$$C_r = 3.06 \exp\left(-1.5 \cdot \frac{G_c}{H_{m0}}\right) \tag{69}$$

Where:

C_r	=	reduction factor for the mean overtopping discharge, maximum $C_r = 0$	$[-]$
G_c	=	crest width	$[m]$

This method results in no reduction for a crest width smaller than $0.75 * H_{m0}$. The formula can be rewritten to a more general form, where 3.06 is left out of the formulation because the decrease in discharge starts for all runs right at the seaward core crest edge. In the following notation, the reduction factor is also replaced with q_{x_c}/q_0. Note that the discharges are given in $[l/s/m]$.

$$\frac{q_{x_c}}{q_0} = \exp\left(-B \cdot \frac{x_c}{H_{m0}}\right) \tag{70}$$

Where:

x_c	=	distance over the breakwater, starting at the core crest edge	$[m]$
B	=	Fitting parameter	$[-]$
q_0	=	Mean overtopping discharge at $x_c = 0$	$[l/s/m]$
q_{x_c}	=	Mean overtopping discharge at x_c	$[l/s/m]$

It is chosen to adapt the method of Besley, as the method of Juhl & Sloth includes a freeboard. The freeboard is however already integrated in the (widely used) EurOtop method to calculate the discharge. The method of Besley can be directly applied to a calculated discharge. To find for which settings of B the curves from Figure 56 are best approximated, a least squares fitting method is adopted, where B is adapted for the smallest RMSE and highest R-squared value. The results are presented in Table 17.

	B	Lower bound	Upper bound	R^2	$RMSE$
$Run\ 1$	0.2046	0.1927	0.2164	0.9955	0.01880
$Run\ 2$	0.3145	0.2627	0.3662	0.9803	0.04550
$Run\ 3$	0.1601	0.1551	0.1651	0.9998	0.00235
$Run\ 4$	0.2797	0.2549	0.3044	0.9861	0.03476
$Run\ 5$	0.1022	0.0998	0.1046	0.9983	0.00852
$Run\ 6$	0.2965	0.2799	0.3132	0.9962	0.99620
$Run\ 7$	0.3901	0.3006	0.4796	0.9930	0.03397
$Run\ 8$	0.3689	0.3430	0.3947	0.9903	0.02731
$Average$	0.2646				
Min	0.1022				
Max	0.3901				

Table 17: B-value, 95% confidence bounds, R^2 and RMSE for the discharge reduction over the crest

It is found that the best fitting value for B approximates the discharge reduction for the various runs in the range $0.1 - 0.4$. The minimum and maximum bounds are given by run 5 (which has the most overtopping waves and the highest overtopping discharge) and run 7 (which has the least overtopping waves and the lowest overtopping discharge) respectively. Especially run 5 can be seen as a sort of limit state due to the very high overtopping.

In this approach it is argued that the porosity (or, more precisely, the infiltration rate) is the limiting factor for the reduction of the flow depth over the crest. We then need a criterion for when it is best to use $B = 0.3$ (which represents runs 2, 4, 6, 7, 8) or $B = 0.1$ (which represents runs 1, 3, 5). The value 0.3 is a conservatively rounded average of runs 2, 4, 6, 7 and 8. The value 0.1 is based on the B for run 5, as this run is considered to be a limit state. Both values were selected based on conservative considerations, for most runs the B-value was actually higher. It is hypothesized that large overtopping discharges and volumes cause saturation of the core material. To underpin this theory, for each run the results for B are sorted smallest to largest, as well as the measured q, V_{max}, and N_{ow}.

Rank nr.	1	2	3	4	5	6	7	8
B	7	8	2	6	4	1	3	5
q	7	4	6	8	2	1	3	5
V_{max}	7	6	8	2	4	1	5	3
N_{ow}	7	4	2	8	6	1	3	5

Table 18: Runs sorted based on fitted B and measured q, V_{max}, and Now

From Table 18 it appears that indeed a relation between the fitted B and the measured overtopping characteristics is visible. It is clear from Figure 56 that the graphs of runs with the same order of magnitude of q cross each other quite often (runs 2, 4, 6, 7, 8). Because for these runs relatively few waves have overtopped, these lines are not very smooth. It is hypothesized that more data and more measurement points along the crest will give a more smooth result and also an increased similarity between the ranked B and q. Based on this analysis, it is proposed to introduce the non-dimensional discharge:

$$q_0 / \sqrt{g * d_{n,50}^3} \tag{71}$$

This parameter uses the $d_{n,50}$ to make the discharge dimensionless. This is done as the porosity of the material can be related to the $d_{n,50}$. The $d_{n,50}$ of the core material is used here, as the flow over the core material is studied. Giving this non-dimensional discharge for the various runs, it can be seen that for the runs with the highest discharge (Run 3 and Run 5) this number is an order of magnitude larger compared to the other runs (Table 19). Runs 2, 4, 6, 7 and 8 have comparable numbers, run 1 is somewhat larger.

It is argued to be conservative and to use $q_0 / \sqrt{g * d_{n,50}^3} = 25$ (the value for run 8) as the threshold between B values of 0.1 or 0.3.

	Run 1	Run 2	Run 3	Run 4	Run 5	Run 6	Run 7	Run 8
$\dfrac{q_0}{\sqrt{g * d_{n,50}^3}}$	49	14	212	7	289	10	2	25

Table 19: non-dimensional discharge for simulated runs

Summarizing, the method of Besley has been adapted to suit the observations in this research in the following form. It is argued that this adaptation suits the determination of the reduction of the mean discharge better for unfinished structures, where the core material lays bare and so limits quick infiltration when significant overtopping is occurring. This rule gives a general and conservative description for this process.

$$\frac{q_{x_c}}{q_0} = \exp\left(-0.3 * \frac{x_c}{H_{m0}}\right); \text{ when } \frac{q_0}{\sqrt{g*d_{n,50}^3}} \leq 25$$

$$\frac{q_{x_c}}{q_0} = \exp\left(-0.1 * \frac{x_c}{H_{m0}}\right); \text{ when } \frac{q_0}{\sqrt{g*d_{n,50}^3}} \geq 25$$

(72)
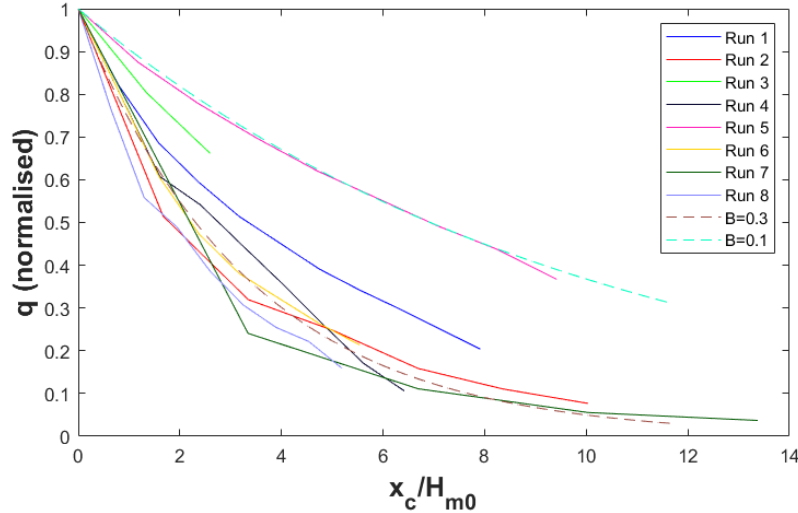
Figure 57: The adapted Besley formulas

6.5.2 Overtopping flow depth $h_{2\%}$

Figure 58 shows the normalised $h_{2\%}$ over the crest of the breakwater against the same non-dimensional x_c that was introduced for the discharge. It should be noted that for a proper exceedance analysis, sufficient overtopping waves are required. This is why runs 4 and 7 are relatively short in this figure as their results further along the crest are not reliable.

As expected from the literature study, an exponential decrease is visible. Similar to the comparison performed for the mean overtopping discharge, it is possible to see that the larger overtopping discharges cause a less rapid decrease of the $h_{2\%}$, although the effect is less emphasized as in the results for the discharge. This could indicate that the flow is accelerating over the crest of the breakwater (to fulfil continuity). However this is not directly comparable, due to the different nature of the parameters, where q is averaged over the entire simulation length, and the $h_{2\%}$ is based on an exceedance analysis of single events. The flow velocity is discussed in detail in the next section.

Figure 58: overtopping flow depth $h_{2\%}$ vs. x_c/H_{m0} for run 1-8

Using the same approach as for the mean overtopping discharge, the following table is constructed:

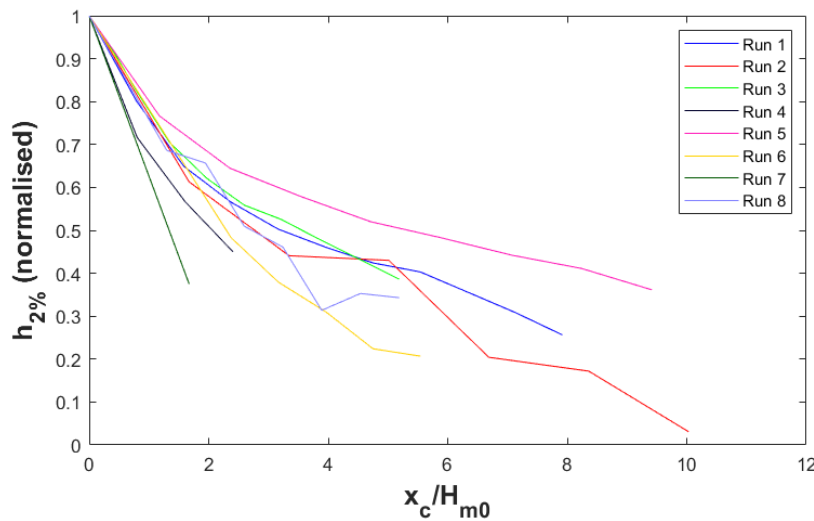|	B	Lower bound	Upper bound	R^2	$RMSE$
$Run\ 1$	0.1883	0.1658	0.2107	0.9412	0.05397
$Run\ 2$	0.2284	0.1819	0.2749	0.9626	0.06285
$Run\ 3$	0.2040	0.1861	0.2220	0.9741	0.03373
$Run\ 4$	0.3529	0.3002	0.4057	0.9890	0.02489
$Run\ 5$	0.1272	0.1065	0.1478	0.9040	0.06232
$Run\ 6$	0.2973	0.2824	0.3123	0.9963	0.01714
$Run\ 7$	0.5864	0.5864	0.5864	1.0000	$2.17e-08$
$Run\ 8$	0.2443	0.2159	0.2726	0.9654	0.04327
$Average$	0.2346				
Min	0.1272				
Max	0.3529				

Table 20: B-value, 95% confidence bounds, R^2 and RMSE for the flow depth reduction over the crest

It should be noted that the result for Run 7 is unreliable, as it only links 2 data points (hence the fit produces a correlation of 1 and an RMSE of practically 0). For the calculation of the average, Run 7 is therefore left out of the analysis. It is in line with the expectations however that the reduction over the crest is significant for this run. Also the B-value for run 4 could for this reason be somewhat overestimated, as the lower tail of the exponential curve is not very well represented by the data.

From Table 21 it is clear to see that B reduces in correlation with an increasing q. Only run 1 and 3 are mixed up in this analysis, also their B-values show a more close resemblance than for the study of the development of q over the crest.

Rank nr.	1	2	3	4	5	6	7	8
B	7	4	6	8	2	3	1	5
q	7	4	6	8	2	1	3	5
V_{max}	7	6	8	2	4	1	5	3
N_{ow}	7	4	2	8	6	1	3	5

Table 21: Runs sorted based on fitted B and measured q, V_{max}, and Now

It should be noted that the fit for run 5 is relatively poor ($R^2 = 0.9$). It also appears from a visual representation of this fit (Figure 59) that this 1 equation exponential approximation overestimates the flow depth over the beginning of the crest, and underestimates it at the rear part of the crest. This could be caused by the fact that at the beginning of the crest a more wide distribution of overtopping depths is present, whereas the end of the crest is only reached by the higher waves. It can be imagined that the smaller waves feel the influence of the porous medium and slow down quicker (relatively to the larger waves) while travelling over the crest as a consequence. This could cause the tail of the $h_{2\%}$ distribution, further away from the core crest edge, to be somewhat higher. This is not further analysed in this research, as the fit to the data is deemed good enough for an indicative description of the reduction of the flow depth. For the B-value of run 5, this fit could be used as only after $x_c/H_{m0} \approx 6$ the mismatch is no longer a conservative estimate.
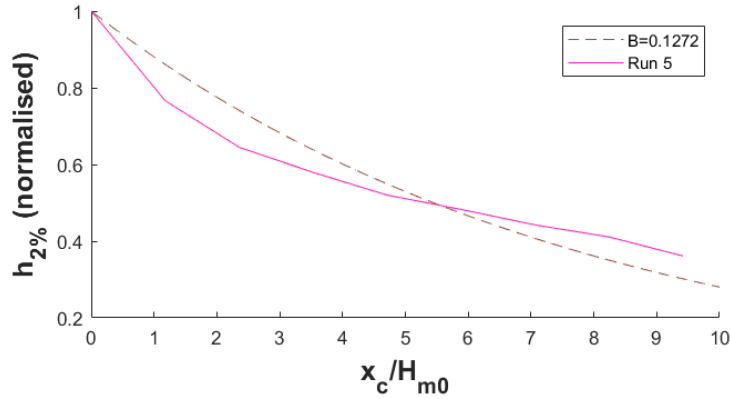
Figure 59: Run 5 and best fit for exponential function

It is concluded here that the reduction of the $h_{2\%}$ over the breakwater crest can be approximated by B-values between 0.1 and 0.2, resulting in a very similar equation as for the reduction of q over the breakwater crest. The value 0.1 is based on rounding down (conservatively) the B-value for run 5. The value 0.2 is chosen by rounding down the average of runs 2, 6 and 8. It is concluded that the discharge and flow depth over the crest are closely coupled and both significantly influenced by the relative porosity of the core material.

$$\frac{h_{2\%,x_c}}{h_{2\%,0}} = \exp\left(-0.2 * \frac{x_c}{H_{m0}}\right); \text{ when } \frac{q_0}{\sqrt{g*d_{n,50}^3}} \leq 25$$

$$\frac{h_{2\%,x_c}}{h_{2\%,0}} = \exp\left(-0.1 * \frac{x_c}{H_{m0}}\right); \text{ when } \frac{q_0}{\sqrt{g*d_{n,50}^3}} \geq 25$$

(73)

Where:

$h_{2\%,0}$ = $h_{2\%}$ at $x_c = 0$ $[m]$

$h_{2\%,x_c}$ = $h_{2\%}$ at x_c $[m]$

Figure 60: The adapted Besley formulas

Finalizing this section, the normalised $h_{2\%}$ is also compared to a different non-dimensional x_c, which was introduced by Bosman et al.: $(x_c/L_{m-1.0})$. The result is given in Figure 61. It follows that with this non-dimensional parameter, the quite significant difference in the wave lengths between the sea and the swell runs appear to make it more difficult to 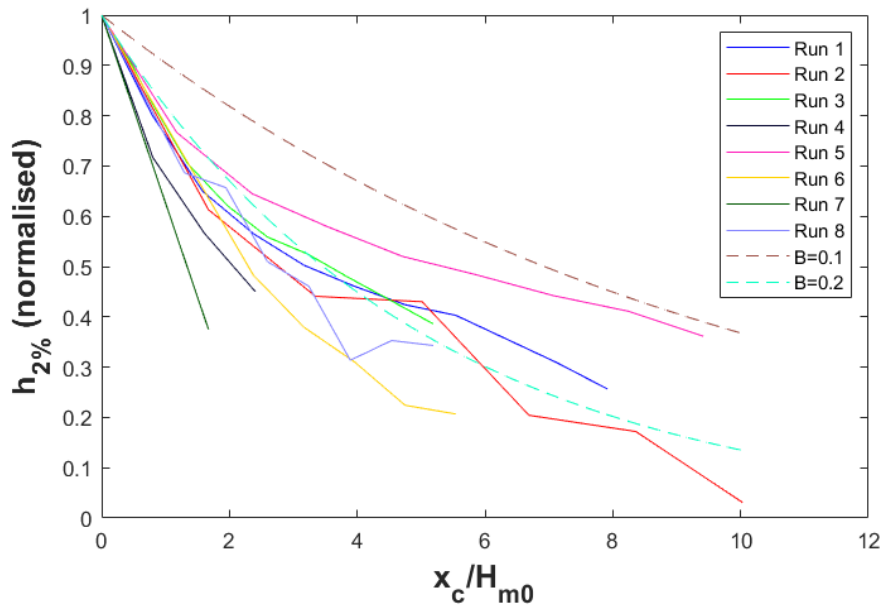compare the two using the criterium set up with the previously described method. It appears that relative to the wave length, the flow depth reduces less significant for the sea waves. Between the swell runs and the sea runs separate, the pattern is visible where the runs with the largest overtopping have the least reduction in the flow depth. For taking the correct value for B, an additional requirement would be needed that considers the steepness of the waves.

Bosman uses two datasets where the wave steepness is varied between $0.02 - 0.03$ and $0.01 - 0.06$. It is proposed to use a value of 15 for the B-value $(c_{c,h2\%})$. In the tests performed here, the average value for B is found to be 16.58. This indicates that the reduction in flow depth would be somewhat larger to what Bosman proposes. As Bosman uses an impermeable dike structure, it is understandable that the reduction for the permeable medium used here is larger.

	B	Lower bound	Upper bound	R^2	$RMSE$
$Run\ 1$	18.83	16.58	21.07	0.9412	0.05397
$Run\ 2$	22.84	18.19	27.49	0.9626	0.06285
$Run\ 3$	20.4	18.61	22.20	0.9741	0.03373
$Run\ 4$	35.3	30.02	40.57	0.9890	0.02489
$Run\ 5$	12.72	10.65	14.78	0.9040	0.06232
$Run\ 6$	5.947	5.647	6.247	0.9963	0.01714
$Run\ 7$	11.73	11.73	11.73	1.0000	$1.542e-07$
$Run\ 8$	4.885	4.319	5.452	0.9654	0.04327
$Average$	16.5815				
Min	4.885				
Max	35.3				

Table 22: B-value, 95% confidence bounds, R^2and RMSE for the flow depth reduction over the crest

It is concluded from this analysis that for the current dataset the adapted Besley formula is well applicable to the flow depth and more easy to use for the varying wave steepness in the test program (as opposed to the method of Bosman).
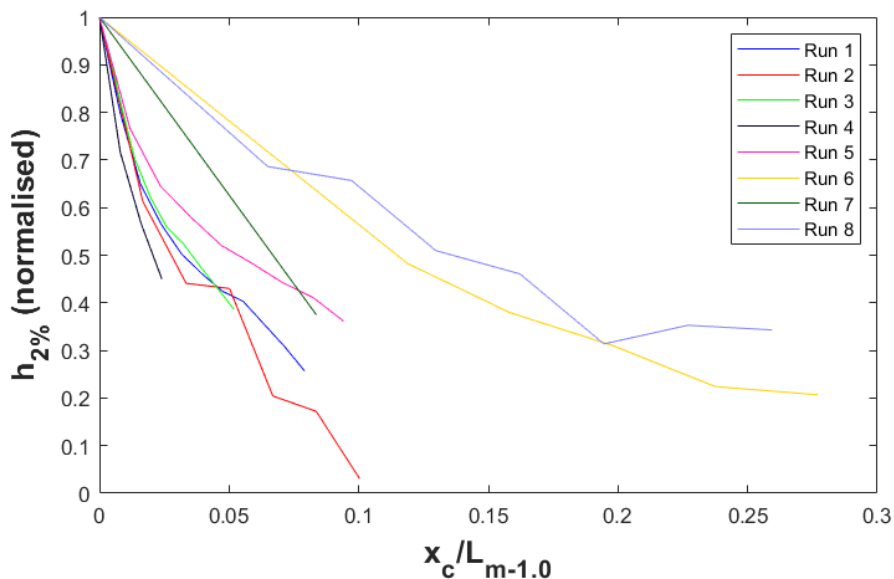

Figure 61: overtopping flow depth $h_{2\%}$ vs. $x_c/L_{m-1.0}$ for run 1-8

6.5.3 Overtopping flow velocity $u_{2\%}$

In this section, the development of the $u_{2\%}$ over the crest is analysed. It was found that both the discharge and the flow depth can be approximated by an exponential decay. The studies discussed in chapter 2 conclude that also for the overtopping velocity an exponential decay is found over the crest (Schüttrumpf and van Gent, 2003; Bosman *et al.*, 2008; van Bergeijk *et al.*, 2019). From the $u_{2\%}$ values generated in this research however it appears that the $u_{2\%}$ does not always seem to be reducing over the crest of the breakwater. On the contrary, often an acceleration is even observed.

From Figure 62 it can be seen that the overtopping velocity is not necessarily reduced over the crest. The maximum velocity is even increased with about 40% for run 5. It is hypothesized that with wave overtopping the inertia of the flow (and not the friction) dominates the velocity development over the crest. It seems that the difference in the flow depth during overtopping forces an acceleration mostly on the beginning of the crest. The larger the initial flow depth the larger this acceleration appears to be. For smaller flow depths, also friction (through the porosity) could play a role, as can for instance be seen by the reducing flow velocities from runs 4 and 7.

This is contrary to what was found in the literature on dikes, and difficult to quantify as it seems the effects are slightly different for each run. Also another aspect of the overtopping flow seems to have an effect here, being the transition over the crest edge. For the three runs (3, 6 and 8) where detachment is visible and it is possible to study the process over the crest (contrary to run 7 where the process over the crest is very limited) it seems that the wave accelerates in the transition zone. For the runs without detachment, a more smooth progression of $u_{2\%}$ over the crest is visible. The length of the transition zone is indicated in Figure 62 by the red circles. Around this point where the maximum flow depths are attached to the breakwater, the initial strong acceleration for these waves seems to be ending. This acceleration could be caused by the deflection of the wave tongue on the crest from a sort of falling jet to a more horizontal direction.
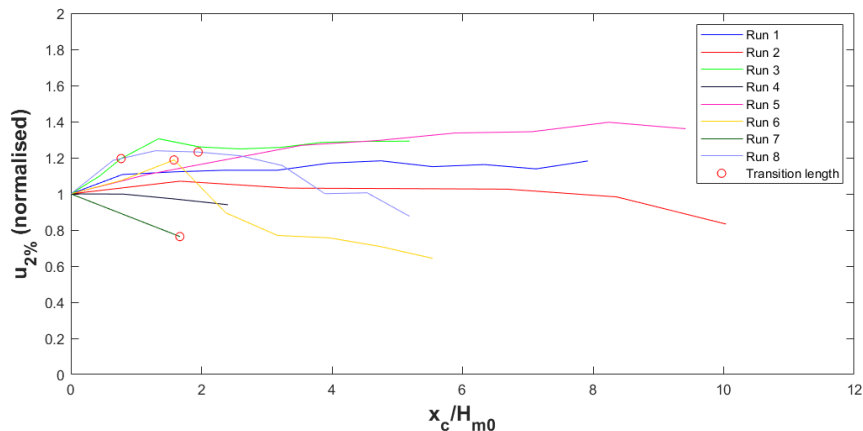
Figure 62: overtopping flow velocity $u_{2\%}$ vs. x_c/H_{m0} for run 1-8

Note for example the results for Run 5. For this run, the flow is not detached and for this run the highest flow depths can be found. A quite clear and gradual increase of the velocity is found for this run. Compare this to run 3, which has also significant overtopping but where the flow is strongly influenced by the transition zone. For this run the acceleration continues up to the defined end of the transition zone, after which the velocity is more or less constant.

It is expected that for the smaller waves the boundary layer starts to play a role (especially when turbulence is accounted for). A more detailed analysis could show that all runs in Figure 62 actually show the same velocity pattern, where the velocity is initially increased due to flow that is unaffected by the boundary layer and due to the transition over the crest edge, after which a reduction of the velocity occurs when the boundary layer develops.

Qualitative analysis

The goal of this subsection is then to explain what processes play a role in the accelerating velocity over the crest, by means of a qualitative analysis. The stills in Figure 63 show the flow over the crest for a regular swell wave. It is clear from this that the maximum velocities occur on the crest after the flow is deflected through impact on the crest. This could thus indeed partly explain the increase of the velocity that was also observed in Figure 62. The velocity vector plot for the sea run gave very similar results.

Figure 63: Velocity vectors for overtopping swell wave
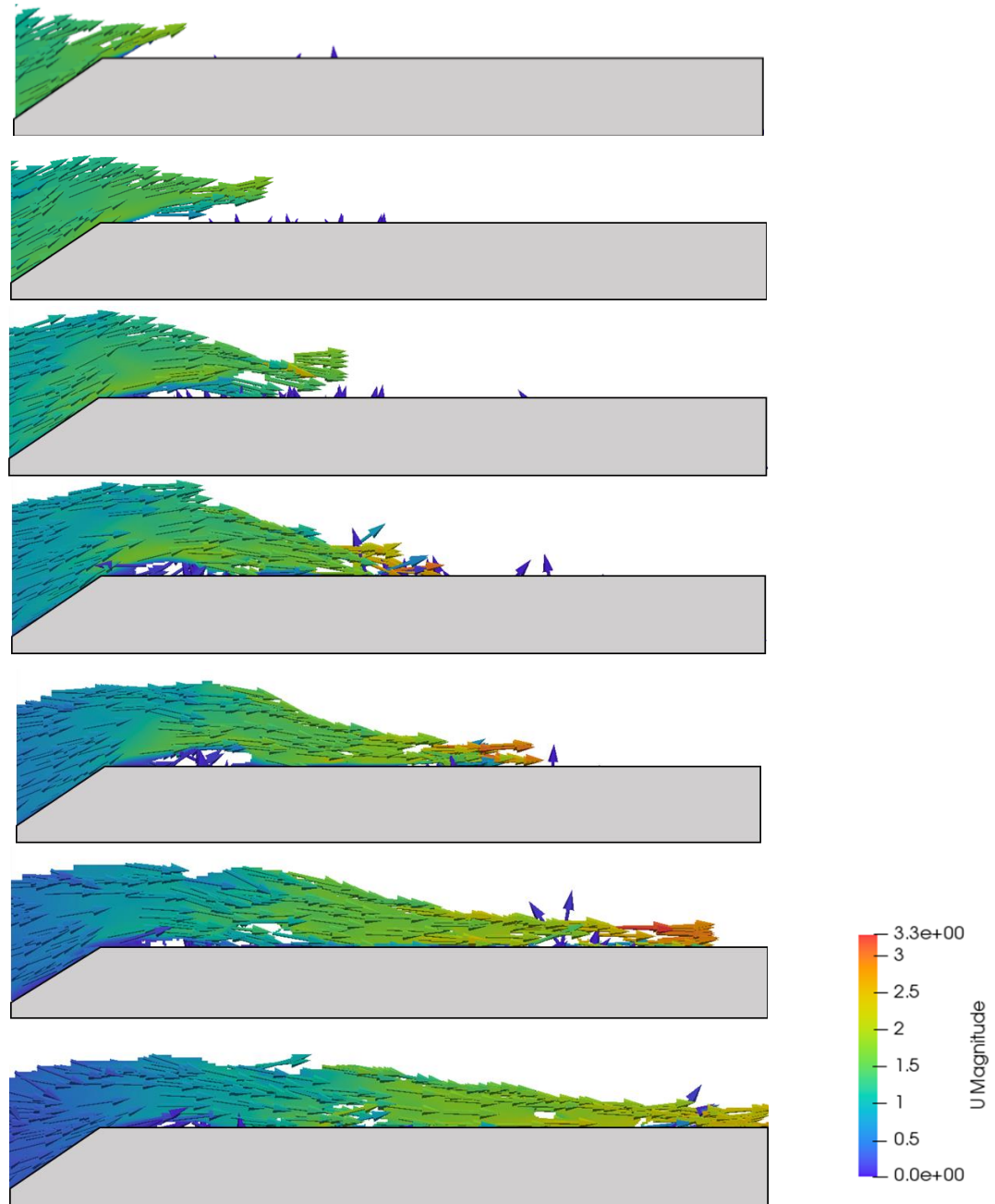
To understand better the process of deflection of the flow and infiltration into the porous medium, Figure 64 was created. These show contour plots where the indicator function equals 0.5 for 3 stages of the

overtopping swell wave. With these plots, the process of deflection can be studied in more detail (stills of the entire overtopping process can be found in Appendix K, both for sea and swell waves).
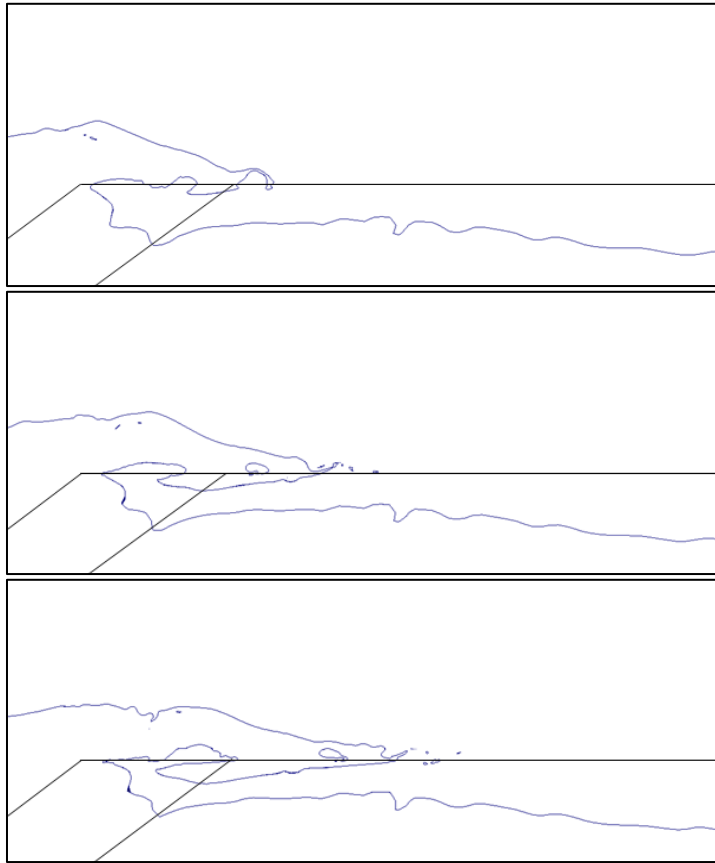

Figure 64: α contour 0.5, swell run, 3 stages of the overtopping process

Figure 64 shows that the overturning wave causes rapid (forced) infiltration into the crest material. After this initial infiltration, it can be seen that this patch of water doesn't increase in size rapidly (the time stepping between each plot is the same). Further along the crest the infiltration is also less quick. This shows that the redirection of the flow causes the infiltration to be high initially, but to become lower further down the crest. This supports the findings in sections 6.5.1 and 6.5.2, where the reduction of the mean overtopping discharge q and the $h_{2\%}$ is large initially but becomes less further down the crest.

The main difference between the sea and swell plots show that for the sea run the detachment is not necessarily more emphasized. It can however be argued that for sea runs the detachment occurs also for smaller overtopping waves, based on the fact that also run 6 ($H_{m0} = 0.06$) and run 7 ($H_{m0} = 0.04$) displayed detachment of the overtopping wave.

It was found that the moment of maximum velocity relative to the moment of maximum flow depth is more trivial for an overtopping sea wave, whereas in an overtopping swell wave the maximum flow depth almost always follows the maximum flow velocity. This likely has to do with the steepness of sea waves. The sea waves are shorter and so have a more collapsing way of breaking onto the breakwater structure.

Comparison to literature

As the process is better understood now, the question rises why the findings for the velocity are so different compared to the literature that is available for the research on dikes. It is expected that the following reasons could explain some of the differences found:

88

1. Bosman et al. (2008) note that the highly turbulent, non-stationary, air containing flow was difficult to measure. Also in this research this is clear. Especially when the flow detaches from the crest edge, the velocity can vary significantly over the wave tongue. Depending on where in the flow the velocity is measured, it is possible to measure different velocities;
2. Van Gent (2002) measured the velocity only on the front slope edge and the rear slope edge of the crest and so it is possible that the friction plays a bigger role in this situation, as its path of influence is larger. However, the used set-up had a smooth surface, so the effects of the porous medium from this research likely cause more friction (Trung makes use of the same dataset);
3. All tests on dikes are for more gentle slopes and so more gentle transitions over the crest edge. This could mean that the acceleration caused by the redirection of the flow velocity is less emphasized in these set-ups;
4. Schüttrumpf (2001) found that the overtopping velocity reduced over the crest with 1% to 8%, and so stayed practically constant. Considering the variable velocity also found in this study, it should be considered what the significance of this difference is;
5. Bergeijk et al. (2019) also used the assumption that the flow decelerates due to friction. For this however the same tests as for van Gent (2002) were used as well as tests created with the wave overtopping simulator. The wave overtopping simulator is placed on top of the dike, near the seaward crest edge and is calibrated using the Schüttrumpf and van Gent formulations. Here also the effect of the transition over the crest is not incorporated, as the flow is directed to flow parallel over the crest.

6.6 Results with respect to safety and workability

Concluding this chapter, the results are discussed in light of the main research question. The knowledge gathered on overtopping over breakwaters as described in the previous sections should be linked to the determination of a safe working crest level of a breakwater under construction.

This chapter started out with discussing the transition zone. In section 6.6.1, the consequences of this transition zone for the applicability of the found knowledge is discussed. Section 6.6.2 discusses how the found empirical relations can be used. Section 6.6.3 describes how the results contribute to a pragmatic method to define the safe working level.

6.6.1 Safety within the transition zone

First of all, it should be made clear that the limit functions as described in section 2.1.4 are not applicable in the transition zone of an overtopping wave. This transition zone often plays a role for sea waves and large swell waves. Although the phenomenon has been described in some more detail now, the current dataset does not yet allow for a detailed study of the length of the transition zone for various wave conditions.

It may be possible to describe the length of the transition zone using the initial flow velocity at the beginning of the crest edge. Knowing that the flow is directed parallel to the slope, for various waves the maximum front velocity of the up rushing wave can be taken to study the projectile track of this wave. The knowledge gap for performing such an analysis is currently mostly given by a lack of understanding of the velocities in the up rushing waves. It was shown (also in this study) that an acceleration occurs above the mean water level, but this has not been quantitatively analysed for various types of waves. The up rushing velocity resulting from an irregular wave field also appears to be very stochastic in nature.

In the quantitative analysis shown in this research, the effect of the transition zone is not explicitly represented. For calculations of the safety of the hydraulic excavator, this is not necessarily a problem. The safety of the hydraulic excavator is often based on storm conditions (in normal conditions, the safety of the staff is normative). The main question then is not if the hydraulic excavator should be moved away from the core crest edge (as this will always be done when a storm is approaching) but if it should be

taken of the breakwater. So knowing what the $h_{2\%}$ is after the transition zone could be sufficient to make this decision. But for people on the breakwater, a different limit function should be found for safety in the transition zone.

6.6.2 Use of found relations and stability limits

Section 6.4 describes how the $h_{2\%}$ and $u_{2\%}$ can be derived at the core crest edge and related to the varied parameters. Section 6.5 subsequently showed the progress of these parameters over the crest. These sections were written to give a first indication of what a completely empirical method could look like and to show the influence of the varied parameters on these flow characteristics.

Because only very little research on overtopping flows over breakwaters has been performed, the presented results rely only on the data produced in this thesis. The found empirical relations should thus only be consulted in a preliminary design stage, when a breakwater is being designed with a very similar lay-out and incident wave field. For this reason a case was analysed with a relatively standard design. This section shows how the found empirical relations could be applied for design purposes. Section 6.6.3 describes in more detail how the developed knowledge can be used for different designs and how numerical modelling can be used to identify the transition zone.

To define the safety of the hydraulic excavators and the staff, first an exceedance probability should be selected. The 2%-exceedance probability is not suitable for this as this will definitely occur for a storm of 1000 waves. When for each wave the probability of exceedance is 2%, 20 out of 1000 waves are expected to overtop dangerously. The probability that at least one of these waves will occur in the 1000 wave storm equals 100%. This can be determined using the Poisson distribution:

$$P_f = 1 - e^{-T_L/R} \tag{74}$$

Where:

P_f	=	the probability of failure	$[-]$
T_L	=	the lifetime, here: the number of waves in a storm (in this analysis: 1000)	$[-]$
R	=	the return period, here: the number of waves exceeding the safety level divided by the total number of waves in a storm	$[-]$

Using the Poisson distribution, a tolerable probability of failure can be selected and the accompanying $h_{...\%}$ and $u_{...\%}$ can be calculated (using the assumption that these are Rayleigh distributed). For the hydraulic excavator and the safety of personnel, a probability of failure of 10% is selected. The return period then becomes $R \approx 9500$. This means that the tolerable exceedance probability per wave is 1 in 9500, or (approximately) $1 * 10^{-4} \approx 0.01\%$.

Required freeboard for Hydraulic Excavator

In this section an example exercise is given with the newly developed formulas to determine the safe working level for the hydraulic excavator. Before describing this situation, it is important to note that when water hits the hydraulic excavator, it can rush up the excavator and reach the control cabin. Therefore some safety should be included in the limit. For instance, in this example the cabin of the excavator is positioned at $1.5 \, [m]$ height, so for safety the limit for the $h_{0.01\%}$ is set at $0.5 * h_{limit} = 0.75 \, [m]$. The other parameters are:

$$H_{m0} = 1.5 \, [m]; \; s_{m-1.0} = 0.01; \; t_f = 2.25 \, [m]$$

Next, the formula for the $h_{2\%}$ on the core crest edge should be adapted for the defined tolerable exceedance probability: $h_{0.01\%}$. The formula for the $h_{2\%}$ is repeated here:

$$\frac{h_{2\%}}{H_{m0}} = 0.57 * \left(\left(\frac{H_{m0}}{t_f} \right) * \left(\frac{R_{u2\%} - R_c}{H_{m0}} \right) \right)^{1.50}$$

This is then adapted for the new exceedance probability following (see also section 2.3.1):

$$P_x = \exp\left(-\left((-\ln(0.02))^{0.5}\frac{c_{0.01\%}}{c_{2\%}}\right)^2\right)$$

$$c_{0.01\%} = c_{2\%}\frac{\sqrt{-\ln(0.0001)}}{\sqrt{-\ln(0.02)}} = 0.88$$

$$\frac{h_{0.01\%}}{H_{m0}} = 0.88 * \left(\left(\frac{H_{m0}}{t_f}\right)*\left(\frac{R_{u2\%}-R_c}{H_{m0}}\right)\right)^{1.50}$$

The freeboard can now be computed using (where the $R_{u2\%}$ equals $3\,[m]$ as is computed following the EurOtop manual, section 6.2, mean value approach):

$$R_c = R_{u2\%} - t_f * \left(\frac{h_{0.01\%}}{H_{m0}*0.88}\right)^{\frac{1}{1.50}} = 1.46\,[m]$$

So, for a freeboard of $1.46\,[m]$ there is a 10% probability that the hydraulic excavator is damaged during a 1000 wave storm. This exercise can of course also be done the other way around, to check if a certain given freeboard is safe or gives an $h_{0.01\%}$ that exceeds the h_{limit}.

The failure cases described above is for failures on the seaward core crest edge. If a storm is approaching, the first measure taken is removing the excavator from the crest edge and moving it towards the lee side of the breakwater. The effect of this can be studied using the formula that studies the decay of the $h_{2\%}$ over the breakwater.

This is analysed using the example from above, where the required freeboard was $1.46\,[m]$. If this breakwater is attacked by waves with $H_{m0} = 1.80\,[m]$ (all other parameters stay the same), the occurring $h_{0.01\%}$ becomes $0.90\,[m]$. Considering that the safety limit is at $h_{0.01\%} = 0.75\,[m]$, the limit is exceeded. To determine at what position away from the crest the excavator is safe, the reduction function is applied to the $h_{0.01\%}$:

$$\frac{h_{0.01\%,\,x_c}}{h_{0.01\%,0}} = \exp\left(-0.2*\frac{x_c}{H_{m0}}\right); \text{ when } \frac{q_0}{\sqrt{g*d_{n,50}^3}} \leq 25$$

$$\frac{h_{0.01\%,\,x_c}}{h_{0.01\%,0}} = \exp\left(-0.1*\frac{x_c}{H_{m0}}\right); \text{ when } \frac{q_0}{\sqrt{g*d_{n,50}^3}} \geq 25$$

As is clear first the q_0 should be determined to select the right formula. Following the 2018 overtopping manual (2018, section 6.3.4, design and assessment approach) this discharge equals $88\,[l/m/s]$, the $d_{n,50}$ equals $0.01*25 = 0.25\,[m]$ (prototype scale), giving:

$$\frac{q_0}{\sqrt{g*d_{n,50}^3}} = 56$$

And so the following calculation can be made:

$$0.75 = 0.90 * \exp\left(-0.1*\frac{x_c}{1.8}\right)$$

$$x_c = 3.3\,[m]$$

This could help to make the decision if wide safety zones are cost-effective in the design of the breakwater, if these high waves are not expected often and removing the excavator is cumbersome.

Required freeboard for Personnel

In this section an example exercise is given to determine the safe working level for the staff working on the breakwater. For the safety of the staff, it should be checked if the found combinations of the overtopping flow depth and velocity exceed the safety limits as described by Sandoval's stability curves. One could simply fill in the formula for the $h_{0.01\%}$ and find the accompanying $u_{0.01\%}$. Then, similar to the exercise with the hydraulic excavator, this can be compared to the failure limit. In this case this can be done by plotting onto the failure curves of Sandoval. Figure 65 shows this for settings following an example by Sandoval (m=72.54 [kg] and $h_p = 1.76$ [m]), on prototype scale. Below the formula for the $u_{2\%}$ is repeated, as well as another version to determine the $u_{0.01\%}$:

$$\frac{u_{2\%}}{\sqrt{g * H_{m0}}} = 1.83 * \left(\frac{h_{2\%}}{H_{m0}}\right)^{0.14}$$

$$\frac{u_{0.01\%}}{\sqrt{g * H_{m0}}} = 2.81 * \left(\frac{h_{0.01\%}}{H_{m0}}\right)^{0.14}$$
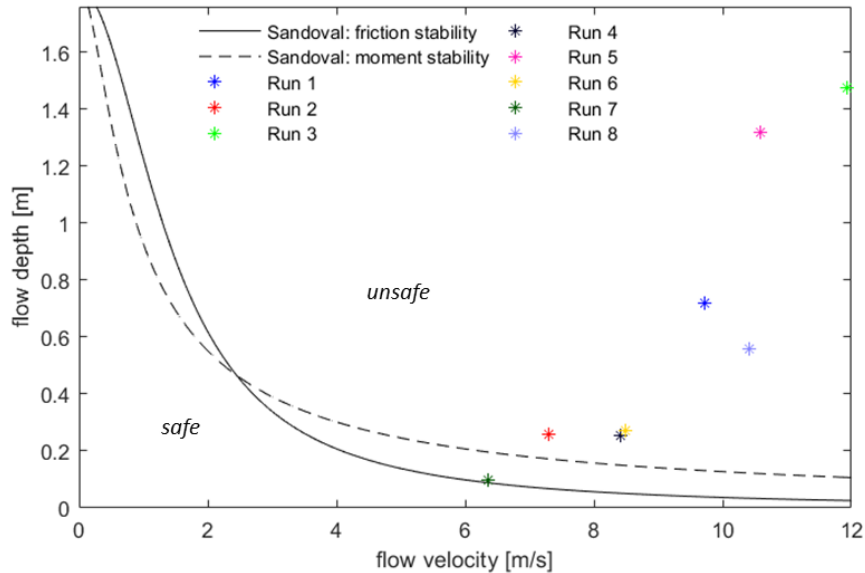

Figure 65: Sandoval for m=72.54 [kg] and $h_p = 1.76$ [m], with the $u_{0.01\%}$ and $h_{0.01\%}$ plotted for each run set-up

Figure 65 shows that with this approach, all 8 runs are deemed unsafe. Similar to what was done in the previous example, the safety can be checked on a distance further away from the core crest edge. It is then however important to make an assumption about the development of the $u_{0.01\%}$ over the crest, as no clear trend was visible based on the available test data. It can for instance be assumed that the $u_{0.01\%}$ doesn't decrease over the crest. The rest of the exercise is then quite similar to the example for the hydraulic excavator.

However, it is known that the $h_{2\%}$ and the $u_{2\%}$ (and the $h_{0.01\%}$ and $u_{0.01\%}$) don't necessarily occur during the same wave and almost certainly not at the same moment. So it should be studied in some more detail what combinations of h and u are occurring within the overtopping waves. If a combinational number can be made of these h and u, for instance the 2%-exceedance value of this number can be determined. It is clear from Figure 65 that the friction stability is limiting in the area where the overtopping flows can be found. This is the same for the findings of Sandoval, who described that for overtopping flows often thin layers of fast flowing water caused instability. The formula for the friction stability is however implicit, so extracting a combinational number out of this equation is not directly possible. However, a curve can be

fitted that approximates the friction stability line and the found relation can give a stability number that can be studied in more detail. This approximation is given by Figure 66.
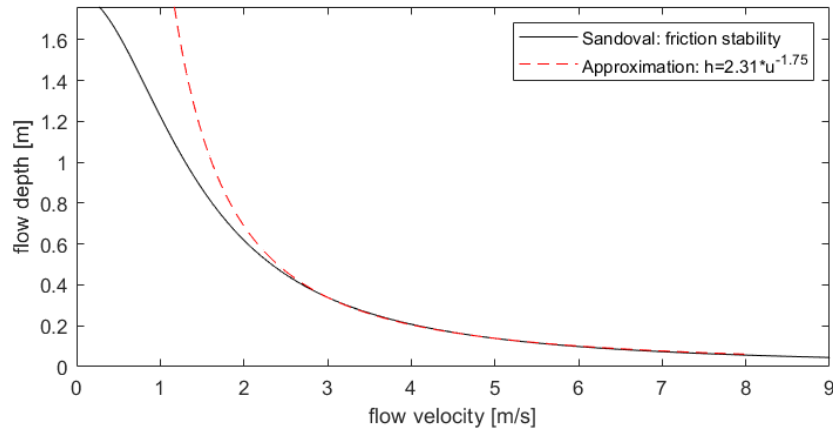
This approximation was made for the stretch of the stability curve that runs between a flow depth of $0.4 - 0.01$. With this approximation, we can define a new limit:

$$\text{When } 0.43 * h * u^{1.75} > 1 \text{ an unsafe situation occurs} \qquad (75)$$

Note that this approximation is specifically fitted for this version of the stability curve, for different personal characteristics (subject weight and length) the approximation should be fitted again. With this new stability number it is possible to look into different flow situations that occurred during the simulations and to derive the 2% value for the stability number (note that for 1000 waves the 2% should not actually be used, as explained before). In this study, we look into the stability when the maximum velocity occurs and the flow depth at that moment (u_{max} & h_{umax}), as well as the combination of maximum flow depth and the velocity at that moment (h_{max} & u_{hmax}). If we perform this exercise for the data found on the core crest edge, we can plot Figure 67.
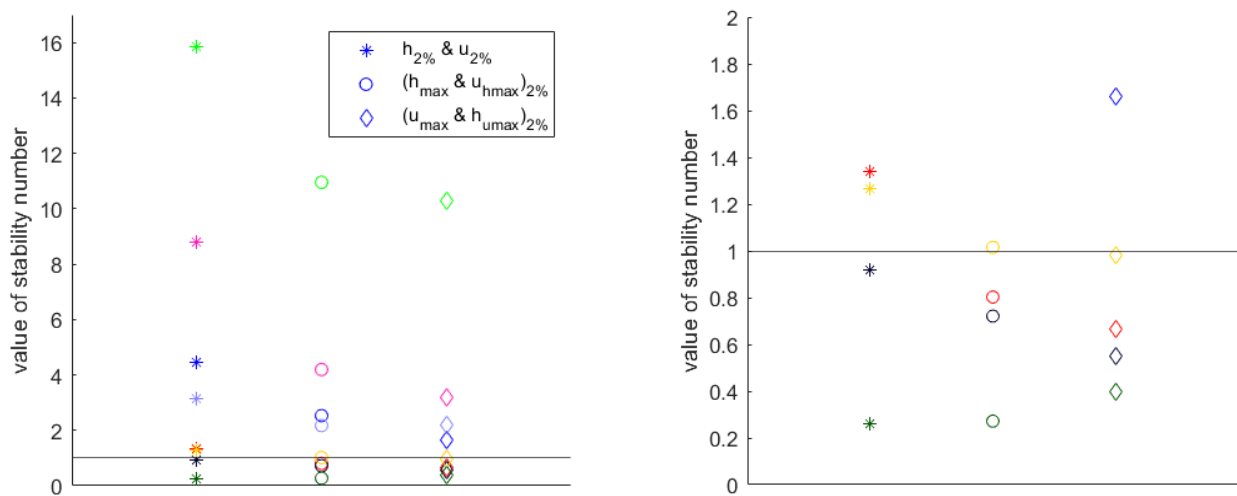
Figure 67: The stability for various combinations of u and h, see Figure 65 for colour definition

Figure 67 shows the new stability limit, represented by the horizontal line. The left part of the figure shows for all runs the stability number for three situations: 1) for the combination of $u_{2\%}$ and $h_{2\%}$, like in Figure 65; 2) for the 2%-exceedance value of the combination of h_{max} & u_{hmax} and 3) for the 2%-exceedance value of the combination of u_{max} & h_{umax}. The right part of the figure shows a close-up around the failure

line. Here it is clear to see that with the first combination, 2 runs were considered acceptable. From the 2 other combinations it appears that the combination h_{max} & u_{hmax} is normative (in 6 out of 8 runs). In this situation, 3 runs are considered acceptable (for each incoming wave there is a 2% risk that it overtops and destabilizes a person). On average, the combination $(h_{max}u_{hmax})_{2\%}$ is 70% of the combination $h_{2\%}u_{2\%}$. A large spread is however visible, ranging from $48 - 105\%$ (for 1 run the $(h_{max}u_{hmax})_{2\%}$ is 5% larger than the $h_{2\%}u_{2\%}$).

It can thus be argued that what we need as input for the stability relations are not the $h_{...\%}$ and $u_{...\%}$ combined but the exceedance value of the combinational number at critical moments in the flow. Empirical relations could then best be found that relate this combinational number to the varied test parameters. However, due to the stochastic nature of the flow velocity (which is almost squared in the stability number), such an exercise currently results in a formula with a very poor fit. This is why the stability number is not given as a function of the varied parameters.

For a practical application of the empirical formulas presented here, it is then recommended to use the conservative combination of the $u_{0.01\%}$ and $h_{0.01\%}$ (if a failure probability of 10% is accepted). When however no use is made of the developed empirical relations, the stability number suggested here can be drawn from measurements in OpenFOAM using the methods described in this research.

Under the conservative assumption that the combination $h_{0.01\%}u_{0.01\%}$ can be used, the freeboard can be determined. For this, the same example is used as for the hydraulic excavator:

$$H_{m0} = 1.5\ [m];\ s_{m-1.0} = 0.01;\ t_f = 2.25\ [m]$$

$$\frac{h_{0.01\%}}{H_{m0}} = 0.88 * \left(\left(\frac{H_{m0}}{t_f}\right) * \left(\frac{R_{u2\%} - R_c}{H_{m0}}\right)\right)^{1.50}$$

$$\frac{u_{0.01\%}}{\sqrt{g * H_{m0}}} = 2.81 * \left(\frac{h_{0.01\%}}{H_{m0}}\right)^{0.14}$$

The freeboard that gives the acceptable failure level can be solved by filling in various values for R_c and seeing which value gives an acceptable combination of the $u_{0.01\%}$ and the $h_{0.01\%}$. This is done by calculating the $h_{0.01\%}$ for various freeboards, and calculating the $u_{0.01\%}$ for the found $h_{0.01\%}$ values. These results can be plotted onto the Sandoval failure curve. This is done in Figure 68, where the red line gives the $h_{0.01\%}$ and $u_{0.01\%}$ values for various freeboards. The intersection of this line with the failure probability line is the critical point between safe and unsafe situations. With the solution of the $h_{0.01\%}$ at this point ($\approx 0.07\ [m]$) the minimum required freeboard can be found.
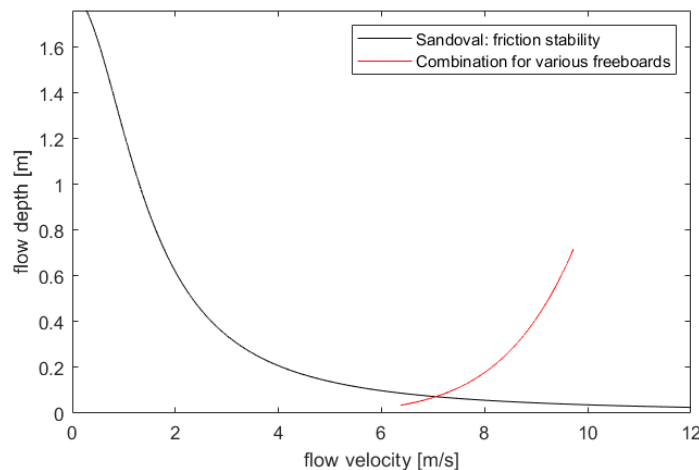

Figure 68: The combinations for the $u_{2\%}$ and $h_{2\%}$ for various values of R_c

In this case, it is found that the formulas yield a required freeboard of $2.67\ [m]$. To check how the found freeboard relates to the use of mean overtopping discharge, the design and assessment approach of the EurOtop is checked. For an acceptable q of $1\ l/m/s$, the recommended freeboard equals $2.78\ [m]$. This is in the same order of magnitude, and so the found result is considered to be realistic.

To study the safety further down the crest, the same example is used but the freeboard is set to $2.50\ [m]$. The $h_{0.01\%}$ now becomes $0.14\ [m]$ and the accompanying $u_{0.01\%}$ becomes $7.7\ [m/s]$. This combination is above the failure line and so unsafe. It is examined at which point away from the core crest edge a safe situation is reached again, under the assumption that the $u_{0.01\%}$ stays constant. Again following the design and assessment approach, the q_0 becomes $2.3\ [l/s/m]$, and using the formula for $h_{0.01\%,\,x_c}/h_{0.01\%,0}$, it is found that when $x_c = 5.20\ [m]$ the combination of $h_{0.01\%}$ and $u_{0.01\%}$ is stable. The reliability of this result largely depends on the assumption of a constant flow velocity. The result can be compared to the adapted Besley formula, for the reduction of the discharge:

$$\frac{q_{x_c}}{q_0} = \exp\left(-0.3 * \frac{x_c}{H_{m0}}\right);\ \text{when}\ \frac{q_0}{\sqrt{g * d_{n,50}^3}} \leq 25$$

q_{x_c} equals $1\ l/m/s$ when x_c equals $4.16\ [m/s]$. It appears that for this situation, the method for the mean overtopping discharge combined with the adapted Besley formula is less conservative.

Comparison of limits runs to EurOtop guidelines

The following presents a comparison of the found safety limits and the guidelines given by the EurOtop. Table 23 shows for each of the test runs if it is judged as safe by the EurOtop limits and by the $u_{0.01\%}h_{0.01\%}$ limit discussed in this section. Note that the calculations were performed on the prototype scale, for 1000 incoming waves. For $H_{m0} = 1.5$ it is assumed that q can maximally equal $1\ l/s/m$. When $H_{m0} = 1\ [m]$, the tolerable discharge equals $20\ [l/m/s]$.

Safety criterion→ Run↓	Sandoval $u_{0.01\%}h_{0.01\%}$	EurOtop ($q\ [l/m/s]$)	EurOtop ($V\ [l/m]$)
1_H06-S1-R10	Unsafe	34.0	6262
2_H04-S1-R10	Unsafe	18.0	2784
3_H08-S1-R10	Unsafe	52.0	11133
4_H06-S1-R15	Unsafe	5.00	2314
5_H06-S1-R05	Unsafe	186	13309
6_H06-S5-R10	Unsafe	5.00	695
7_H04-S5-R10	Unsafe	3.00	309
8_H08-S5-R10	Unsafe	7.00	1235

Table 23: The safety of the various runs based on presented limit for Sandoval and the EurOtop (prototype scale)

This comparison shows that the presented limit of Sandoval (10% exceedance during a storm of 1000 waves) is more conservative for case 2 and 7 when compared to the discharge method. However, run 7 is also very nearly safe using the method of Sandoval (see Figure 65).

As was shown in this section, the assumption of a coinciding $h_{0.01\%}$ and $u_{0.01\%}$ is often quite conservative. So, if numerical modelling is available, this is recommended over the use of the empirical relations. With the method presented in this thesis, it is possible to find exceedance values of unsafe situations. Using numerical modelling is then beneficial to design cost-effective. The method presented creates more intuitive limits than the mean overtopping discharge and gives realistic results.

6.6.3 Workability

Sections 6.6.1 and 6.6.2 discuss the applicability of the quantitative analysis that was performed in this thesis. The introduced empirical relations are shown and it is studied how these can be applied, yet it is emphasized that more research is required to make these equations reliable. Considering the fact that the effects of the transition zone are not incorporated in the empirical relations, it is strongly advised to study the found empirical relations more thoroughly to improve them. The qualitative analysis of the transition zone as presented in this thesis is expected to assist in this pursuit.

Using the methods described in this thesis, numerical modelling of overtopping flows can already be studied in detail for engineering purposes. By performing test runs like the ones presented in this thesis for different breakwater designs and measuring the same parameters, the safety in terms of exceedance values can be assessed for both the staff and hydraulic excavators on the breakwater. This research shows some important parameters that should be varied in OpenFOAM that influence the overtopping flows, besides indicating what should be measured and how it could be measured.

Considering the transition zone, more closely spaced probes can show where the transition is complete. This can be used for instance to indicate where uncertainty lies in the results and so where it is better to rely on the limits set by EurOtop manual for the staff on the breakwater. As mentioned, for the hydraulic excavator the transition zone is not necessarily a problem, as during a storm the excavator will always be moved away from the crest edge and therefore possibly positioned in the flow zone of the overtopping wave.

7 Discussion

7.1 Experiment

The experiment discussed in chapter 4 was used for the validation of the numerical model. However, the measurements performed in the experiment made that an accurate validation of the numerical model was difficult. This adds uncertainty to the outcomes of the numerical model.

The principal uncertainty following from the used experiment is the used incoming wave field. For the incoming wave field in the numerical model, the wave paddle velocity was used. After analysis however, it turned out that the wave paddle velocity in the experimental dataset was not in fact the steering file, but the velocity of the paddle actually measured during the experiment. In the calibration run of the experiment, an absorbing beach was used to calibrate the wave gauges. However, this absorbing beach still allowed for 18% reflection back into the wave tank. This means that the measured paddle velocity from the calibration run included the effect of reflection. As no clean steering file was available the paddle velocity of the calibration run was used as an input for the numerical model. This made the validation of the overtopping flows difficult, as the different wave field was likely the main cause for different overtopping patterns. Due to time limits (the research already moved on with the validation presented in this thesis), the validation was continued with this wave input. However, it is probable that a better validation is possible when the incoming wave field is filtered out and the water level elevation is directly used as an input in the OCW3D domain.

Despite the goal to measure the overtopping depth, no specific check was done in the set-up of the experiment to verify if the surface tension had any effect on the chosen model scale. Based on a criterium for fluvial flows, it was found that the Weber number could have some effect. Although this effect is likely only of influence on slow flowing overtopping, it should be considered in an experimental set-up when looking at the stability of people in overtopping flows.

A validation of the velocity was barely performed, as no direct measurements of the velocity were available. Video-recordings or more gauges along the crest of the breakwater could significantly enhance this part of the validation. This would also allow for a better validation of the flow pattern along the crest.

Based on pictures of the wave tank taken at different times during the experiment, it was found that the water level varied slightly between measurements. It is possible that during tests with significant overtopping, water from the wave tank was lost to the rear of the breakwater. This could result in waves arriving at a later point in the test run to overtop less. It is unclear if the used test started with a too low water level.

7.2 Numerical set-up

As the wave transition over the crest edge had a more significant effect than was considered beforehand, it was found that quite some smearing around the free water surface existed. Especially for thin layers of water reaching the more coarse mesh that was positioned higher up from the breakwater, this resulted in measurement discontinuities and numerical wiggles in the result of the numerical wave gauges.

The numerical set-up did not make use of a turbulence model. One can reason that due to the friction of the crest material turbulence is created, reducing the flow velocity and allowing the permeability of the crest to reduce the flow depth. As friction has more effect in shallow water, these two effects could strengthen each other. It was found that a run with a turbulence model indeed caused a significant reduction in the flow velocity and a strong reduction in the flow depth of the smaller overtopping flows. It was concluded that the measurements better fitted with the runs without a turbulence model. It can be

argued that the flow pattern can be estimated better with a better calibrated turbulence model. The effects of the turbulence model on the porous medium should then however also be studied.

The numerical set-up was not specifically validated for sea waves. As these are steeper and can break on the structure in a more violent manner, the accuracy of the runs with sea waves could be less than for the swell waves.

7.3 Scale effects

Like most wave flume models, the breakwater model used in the simulations was scaled following Froude scaling. Through this scaling some of the effects that occur on the large prototype scale are not well represented by the model. These scale effects should be kept in mind when studying the effects discussed in this thesis.

The effects of Reynolds and Weber scaling and how these were dealt with is detailed in section 4.4. When it comes to Reynolds scaling, the prototype scale will have more turbulence. Besides a possibly different velocity distribution in the overtopping wave tongue, also the flow regime in the structure may be different. The resistance coefficients may vary between these various flow regimes. Especially for the armour (or filter layers) the Reynolds numbers may be significantly higher than for the model described here. This could result in a higher dissipation of wave energy on the prototype scale. The sensitivity analysis performed in this study showed that the wave reflection was sensitive for variations in the resistance coefficients. It is difficult however to calibrate these in a multi-layered structure without any actual measurements performed on the used materials. The same goes for the determination of the porosity of the used material.

Another part of the study where scale effects could play a role is given by what would happen if the overtopping flow actually impacts on a hydraulic excavator. When the unsteady, turbulent, air-entrained flow impacts, this may cause a different uprush pattern for both model scales or prototype scales. This effect was not studied in this study, but could have an effect on the failure modes.

Lastly, it should be noted that the overtopping flow depths that were measured are small compared to the rock gradings in the structure. In the model the breakwater is represented by a porous continuum with sharp edges, whereas in a real-life situation the border between the structure and its surroundings is certainly not so clear-cut. This also affects the flow characteristics, especially concerning the creation of turbulence caused by the roughness of the structure.

7.4 Safety limits and found relations

The results given in this thesis are first steps towards describing the flow patterns of overtopping waves over an unfinished breakwater. The results are currently only applicable for breakwaters with similar designs (chapter 4), for the parameter ranges given in this report (section 5.4.2).

Results for the flow depth and flow velocity where found to depend on the transition zone. This notion is ignored in the quantitative analysis but it is important for the safety limits. It is therefore very important to keep in mind that these limits (especially for the staff) are not directly workable for overtopping in the transition zone. In the recommendations, some more steps are set out through which the acquired knowledge from this thesis in that respect can be used for further research and engineering practice.

8 Conclusions

This thesis discusses tolerable wave overtopping during the construction of a breakwater. It focusses on the safety of personnel and hydraulic excavators on the crest of a breakwater under construction. The results describe the main characteristics of overtopping flow over the structure, as well as a preliminary empirical method to determine the safe working level of a breakwater. This chapter sums up the main conclusions that follow from the thesis on the basis of the research questions that were discussed in chapter 1. The main research question is repeated here:

Can a calculation methodology be developed to determine the safe working crest level of a breakwater under construction?

An answer to this question is formulated through conclusions formed for each research sub question.

What knowledge is available on quantifying overtopping-phenomena?

Based on a literature study, it was found that for the determination of unsafe situations often the mean overtopping discharge q is addressed. A review of the available literature on overtopping shows how widely used empirical methods allow for a calculation of q and the overtopping volume V for various coastal structures. For the progression of the overtopping parameters over the width of the breakwater crest, only methods were available that describe the progression of q over a finished breakwater.

What are the limits for safe operation and which parameters are expected to influence these limits?

In this study, the limits for safe operations are based on the safety limits for the staff and the hydraulic excavators, as these are assumed to be the most critical for the construction process. The literature study yielded a limit function that can be used for the stability of people in overtopping flows (Sandoval, 2015). This requires as input the flow depth and the flow velocity caused by an overtopping wave and gives more insight in what causes an unsafe situation as opposed to the use of limits set based on q or V. Unstructured interviews with experienced project-engineers based the safety of the hydraulic excavators is mainly on the overtopping flow depth, e.g. the flow depth should not exceed the cabin-level.

To study what parameters could influence these limits, literature on the instantaneous loads (i.e. the flow depth and flow velocity) over dikes was studied. Also this literature was checked for its applicability on breakwaters and its validity in general. It was concluded that the existing theory is as of yet not able to adequately describe instantaneous loads on dikes, let alone on breakwaters. Hypotheses were set up based on the literature analysis to assist in answering the fourth research sub question.

How can the parameters be tested that are expected to influence the limits for safe operations?

In this study, the CFD model OpenFOAM in combination with the waves2foam toolbox (Jacobsen et al., 2012) is used to model wave overtopping over a breakwater under construction to characterize the flow depth and velocity caused by overtopping waves. The software was chosen based on the literature study that showed that detailed measurements like the ones used in this thesis can be expensive to perform in wave flume experiments. 2D physical model test results on a partially constructed breakwater were processed in order to obtain benchmark data to validate the numerical model.

A sensitivity analysis showed the relevance of validation of the porous medium parameters. It was found that a run without a turbulence model currently fitted the data best. A grid was selected that improved the efficiency of the model. It was concluded that the validation could be improved for tests with more specific

measurements and varying wave conditions. The tested parameters that were deemed most relevant (H_{m0}, R_c/H_{m0} and $s_{m-1.0}$) were varied in a test program.

What hydraulic and structural parameters have an influence on the limits for safe operations?

It was found that the transition over the crest edge differed significantly between wave conditions. Two distinct areas on the breakwater crest can be identified: a "transition zone" where the flow is detached from the breakwater crest and a "flow zone" with attached flow where the limit functions are applicable. The effects of the transition zone were noticeable over the seaward part of the breakwater crest for sea waves and large swell waves. The dataset did not allow for an in depth analysis, and the quantitative effects on the developed formulas are ignored. The transition zone was however described in some more detail based on additional runs with regular waves.

The flow depth ($h_{2\%}$) on the core crest edge was found to be clearly influenced by the Iribarren number and the relative freeboard. However it was also found that for varying H_{m0} an additional parameter was required to describe the flow depth on the core crest edge. Based on the observations related to the transition zone (the length of the transition zone became more significant for larger waves) it was considered that the infiltration limits of the structure influenced the flow depth on the core crest edge. Incorporating the relative filter layer thickness (H_{m0}/t_f), the formula of (Schüttrumpf and van Gent, 2003) was adapted for these findings, giving ($R^2 = 0.96$):

$$\frac{h_{2\%}}{H_{m0}} = 0.57 * \left(\left(\frac{H_{m0}}{t_f} \right) * \left(\frac{R_{u2\%} - R_c}{H_{m0}} \right) \right)^{1.50}$$

It was found to be difficult to develop an empirical relation based on the varied parameters for the flow velocity on the run-up crest edge. It was found that the 2% exceedance value of this velocity could be related to the 2% exceedance value of the flow depth on the core crest edge, following ($R^2 = 0.70$):

$$\frac{u_{2\%}}{\sqrt{g * H_{m0}}} = 1.83 * \left(\frac{h_{2\%}}{H_{m0}} \right)^{0.14}$$

This formula has a much more flattened maximum compared to the ones found in previous literature (Bosman *et al.*, 2008). This possibly shows that for large overtopping depths the flow velocity tends to a maximum. It is found that considerable scatter exists in the velocity on the core crest edge. A qualitative analysis showed that the run-up velocity pattern varied significantly between waves. It was found that the up rushing waves often accelerate above the mean water level on the run-up slope of the breakwater.

Considering the development of the overtopping flow over the crest, the q, $h_{2\%}$ and the $u_{2\%}$ were studied. The mean overtopping discharge was found to decrease over the crest following an exponential function, however for higher discharges saturation of the crest material became apparent. This made that the methods of Besley (Besley, 1999) and Juhl and Sloth (Juhl and Sloth, 1994) were not applicable. With this knowledge, the method of Besley was adapted using the introduced non-dimensional discharge:

$$\frac{q_{x_c}}{q_0} = \exp\left(-0.3 * \frac{x_c}{H_{m0}} \right); \text{ when } \frac{q_0}{\sqrt{g*d_{n,50}^3}} \leq 25$$

$$\frac{q_{x_c}}{q_0} = \exp\left(-0.1 * \frac{x_c}{H_{m0}} \right); \text{ when } \frac{q_0}{\sqrt{g*d_{n,50}^3}} \geq 25$$

Similar observations for the flow depth resulted in a similar reduction factor. It was concluded that like q, the $h_{2\%}$ was influenced by saturation of the core material. The formula developed here is given by:

$$\frac{h_{2\%,x_c}}{h_{2\%,0}} = \exp\left(-0.2 * \frac{x_c}{H_{m0}}\right); \text{ when } \frac{q_0}{\sqrt{g*d_{n,50}^3}} \leq 25$$

$$\frac{h_{2\%,x_c}}{h_{2\%,0}} = \exp\left(-0.1 * \frac{x_c}{H_{m0}}\right); \text{ when } \frac{q_0}{\sqrt{g*d_{n,50}^3}} \geq 25$$

The flow velocity did not necessarily show a decrease over the crest. In multiple occasions an acceleration over the crest was observed. A qualitative analysis was performed that showed that the wave accelerates both when it crosses the seaward crest edge and when it impacts on the crest. The latter acceleration seems to follow from a quick saturation of the crest material and a followed deflection of the wave directed parallel to the breakwater crest. For the waves that did not detach from the breakwater crest, the acceleration appeared to be larger for larger flow depths. A review of literature on dikes showed where the difference in conclusions on the flow velocity likely follows from.

The found results are applicable for a breakwater with a similar design as the one presented in this study, for the studied ranges: $H_{m0} = 1.0, 1.5, 2.0 \, [m]$; $R_c/H_{m0} = 0.5, 1.0, 1.5$; $s_{m-1.0} = 0.01, 0.05$ (prototype scale).

Main Research Question

Can a calculation methodology be developed to determine the safe working crest level of a breakwater under construction?

This research is one of the first to specifically study the development of the flow depth and flow velocity over a rubble mound breakwater caused by overtopping, in the context of workability. The results described in this thesis are in that sense important to qualitatively understand the process. Besides this, an initial quantitative analysis has been performed on a test case. These first steps could help to develop a fully empirical method to define a safe working level. The study also shows the main uncertainties in the definition of a safe working level following the methods described here. Especially the velocity of the up rushing waves and the effects of the transition zone are important (and related) fields of research for developing this empirical method further.

A relation between the $u_{2\%}$ and the $h_{2\%}$ was found on the core crest edge. However, to find if a situation is safe based on the stability curves of Sandoval, the notion that the $u_{2\%}$ and $h_{2\%}$ do not occur within the same wave is important. To define a safety level based on this, it is better to describe the overtopping flow using a combinational number of the flow velocity and flow depth occurring for each wave. To this end, Sandoval's stability curve can be approximated by a power function and the resulting stability number can be used to check the safety of various combinations of $h \& u$. By simulating new designs in OpenFOAM for normative wave conditions, the safety for the staff can then be assessed based on these combinations of $h \& u$. Using the empirical formulas found in combination with the Poisson distribution and the assumption that u and h are Rayleigh distributed, the safety of the staff and hydraulic excavators can also be defined in terms of exceedance values.

To answer the main research question: in this thesis, a preliminary empirical methodology is proposed to determine the safe working crest level of a breakwater under construction. This method can be used for similar designs and outside the transition zone. Using numerical modelling the stability limits can also be used for different designs and hydraulic conditions. The measurements that should be performed have been described in this thesis.

9 Recommendations

9.1 Validation

An improved validation of the model in OpenFOAM is possible if a physical experiment is available where more specific measurements have been performed. Especially more focus on the measurement of the overtopping velocity is interesting considering the outcomes of this research. A model set-up where Weber scaling is considered could remove the scale effect of surface tension from the results. Also simulations on prototype scale can be used to study scale effects in more detail.

It would be good practice to validate the model specifically for sea waves. Especially when also the transition zone needs to be studied in more detail (section 9.3). Also a sensitivity analysis of the reflection of different wave types for various porous parameters would be interesting in this validation.

As it was found that quite some diffusion occurs at the free water surface for the overtopping waves, research that goes into capturing the sharp interface better could in the near future help more accurate modelling. The effects of such an improved method (namely: isoAdvection) have recently been integrated into the new waveFlow solver which can be used with waves2foam. This new method and its effect on wave overtopping is described in (Patil, 2019).

An analysis that was not performed in this research considers an analysis of the numerical schemes and solvers that should be employed in OpenFOAM for the most efficient solution for the applications described in this thesis. This is interesting to further reduce computational cost.

9.2 Enhance found formulas

It is argued that to enhance the found formulas for the flow depth and flow velocity, more different designs and hydraulic conditions should be tested. It could be that also an air-pocket forms in the 2D model which inhabits some of the infiltration into the porous medium, whereas in a 3D situation sideways escape of the air is possible. This effect can for example be studied using 3D simulation.

Another interesting field of development lies in making the method more probabilistic. For instance, this research did not go into the probability that a storm with certain hydraulic conditions actually occurs.

9.3 Study on the transition zone

One thing that clearly came forward from the results is that for many overtopping waves, a considerable transition zone is present. In this zone, the wave is detached from the crest and is airborne over some distance. As the limit functions set up for this research are then not applicable, more research should go into the study of this transition zone. In general, it would be interesting to use the capacities of numerical modelling to look in detail at what exactly happens when a wave runs up and overtops a breakwater structure.

In the run-up zone, it was found that the wave often accelerates above the free water level. The process appears to be quite stochastic. Numerical studies with waves running up 'infinite' slopes could help understand how various wave types run-up the outer slope of a structure. Cutting of this infinite slope allows for an analysis of the transition zone.

The length of the transition zone and the height the water reaches can be used to formulate new safety limits within the transition zone. It is reasoned that studying swell waves could be a good starting point, as most waves are expected to be surging for such a wave climate. For a sea state, there could be much more variation between the waves that can be found in the wave spectrum (and so different breakers).

Knowing that the up rushing flow is directed parallel to the slope, for various waves the maximum front velocity of the up rushing wave can be taken to study the projectile track of a wave detaching from the breakwater crest edge. The knowledge gap for performing such an analysis is currently mostly given by a lack of understanding of the velocities in the up rushing waves. It is however likely that the length of the transition zone is related to the up-rushing velocity at the crest edge.

9.4 Use of OpenFOAM for limit functions

As long as it is difficult to express the effects of the transition zone into empirical formulas, OpenFOAM can also be used to recreate specific extreme events and to study these in detail. This is based on the method also discussed in section 5.3.4 for the validation of the flow velocity, following recommendations by (Jensen, Christensen and Jacobsen, 2015).

Without using too much computation power, a wave climate can be simulated on a coarse mesh (and in combination with the computationally efficient OCW3D). The wave climate can be selected based on an analysis of the prevailing wave conditions and water levels in a certain construction area (probabilistic analysis). Using measurement tools like the ones used in this thesis, the largest overtopping events can be filtered out. The method by Jensen et al. can then be used to reproduce these extreme events for more detailed meshes, even making it possible to adapt the structural configuration to study how violently this wave overtops for varying configurations. This can also be done as a check for various uncertain parameters, like the effects of various values of the filter layer porosity (if this is an uncertain parameter in the design). The critical overtopping waves can then be studied in the flow zone using the limits described in this thesis. For the transition zone, the detailed study can shed some light on the acceptable risk or the transition zone can be avoided altogether.

As the computation times for OpenFOAM modelling are reducing, it is interesting to model new designs completely with numerical test runs. This way it is possible to take away the implicit information that is present in empirical relations, following from the used test set-up.

It is also interesting to study if combinations of h and u exist that are possibly more destabilizing than the combinations that were studied in this research. For instance a large flow velocity could occur combined with a large flow depth, however both are not the maximum value occurring in that wave. These flows could in fact be destabilizing. A method to analyse these waves could be to measure e.g. 10 different combinations of h and u at fixed time intervals during an overtopping wave, and to select the most destabilizing combination. After this an exceedance value of this parameter can be computed.

9.5 Gather field data

It is recommended to start gathering downtime reports during the construction of breakwaters. This can be combined with measurements of the wave climate at the same time, to form a database on wave conditions combined with building stages that result in downtime. This generates knowledge on when the staff constructing a breakwater decides to abandon the site. This can help understand what situations cause the staff to feel unsafe.

Bibliography

Battjes, J. A. and Stive, M. J. F. (1985) 'Calibration and verification of a dissipation model for random breaking waves', *Journal of Geophysical Research*, (90.C5), pp. 9159–9167. doi: 10.1029/jc090ic05p09159.

van Bergeijk, V. M. *et al.* (2019) 'An analytical model of wave overtopping flow velocities on dike crests and landward slopes', *Coastal Engineering*. Elsevier B.V., 149, pp. 28–38. doi: 10.1016/j.coastaleng.2019.03.001.

Besley, P. (1999) *Wave overtopping of seawalls, design and assessment manual*, *R&D technical report W178*. Available at: https://repository.tudelft.nl/islandora/object/uuid:0cd1c50d-0957-4599-aa37-e6328da73988?collection=research.

Bingham, H. B. and Zhang, H. (2007) 'On the accuracy of finite-difference solutions for nonlinear water waves', *Journal of Engineering Mathematics*, 58(1–4), pp. 211–228. doi: 10.1007/s10665-006-9108-4.

Van den Bos, J. P. and Verhagen, H. J. (2018) *Breakwater Design*. Edition 20. Delft, The Netherlands.

Bosboom, J. and Stive, M. J. (2012) *Coastal Dynamics I: Lectures Notes CIE4305.* VSSD.

Bosman, G. *et al.* (2008) 'Individual overtopping events at dikes', *Coastal Engineering*, pp. 2944–2956.

Bruce, T. *et al.* (2009) 'Overtopping performance of different armour units for rubble mound breakwaters', *Coastal Engineering*. Elsevier B.V., 56(2), pp. 166–179. doi: 10.1016/j.coastaleng.2008.03.015.

Burcharth, H. F., Zhou, L. and Troch, P. (1999) 'Scaling of core material in rubble mound breakwater model tests', in *The International Conference on Coastal and Port Engineering in Developing Countries*.

CFD-Wiki (2014) *Turbulence free-stream boundary conditions*, *15 January*. Available at: https://www.cfd-online.com/Wiki/Turbulence_free-stream_boundary_conditions (Accessed: 11 February 2019).

CIRIA/CUR/CETMEF (2007) *The Rock Manual. The use of rock in hydraulic engineering (2nd edition)*, *C683, CIRIA,London*. doi: 10.1002/esp.1950.

Endoh, K. and Takahashi, S. (1995) 'NUMERICALLY MODELING PERSONNEL DANGER ON A PROMENADE BREAKWATER DUE TO OVERTOPPING WAVES', *Coastal Engineering*, pp. 1016–1029.

Engsig-Karup, A. P., Bingham, H. B. and Lindberg, O. (2009) 'An efficient flexible-order model for 3D nonlinear water waves', *Journal of Computational Physics*, 228(6), pp. 2100–2118. doi: 10.1016/j.jcp.2008.11.028.

Franco, L., de Gerloni, M. and van der Meer, J. W. (1994) 'Wave Overtopping on Vertical and Composite Breakwaters', *Coastal Engineering Proceedings*, pp. 1030–1045. doi: 10.9753/icce.v24.

Geeraerts, J. *et al.* (2004) 'Hazards from wave overtopping : Full scale measurements', *Coastal Structures*, pp. 481–493.

Van Gent, M. R. A. (1995) 'Wave interaction with permeable coastal structures', *Ph.D.-thesis, Delft University of Technology, ISBN 90-407-1182-8, Delft University Press, Delft.*, 6(33), p. 277A.

van Gent, M. R. (2002) 'Wave overtopping events at dikes.', in *Proceedings of the 28th International*

Conference on Coastal Engineering, pp. 2203-2215. doi: 10.1142/9789812791306.

Hasselmann, Klaus, et al. (1973) *Measurements of wind-wave growth and swell decay during the Joint North Sea Wave Project (JONSWAP), Ergänzungsheft.* Available at: https://repository.tudelft.nl/.

Holthuijsen, L. H. (2007) *Waves in oceanic and coastal waters*, *Waves in Oceanic and Coastal Waters.* Delft, The Netherlands. doi: 10.1017/CBO9780511618536.

Hughes, S. A. (2004) 'Estimation of wave run-up on smooth, impermeable slopes using the wave momentum flux parameter', *Coastal Engineering*, 51(11–12), pp. 1085–1104. doi: 10.1016/j.coastaleng.2004.07.026.

Hughes, S. A. (2011) 'Adaptation of the levee erosional equivalence method for the hurricane storm damage risk reduction system (HSDRRS)', *U.S. Army Corps of Engineers - ERDC\CHL TR-11-3*, (May), pp. 1–142.

Hughes, S. A. *et al.* (2012) 'Improvements in Describing Wave Overtopping Processes', *Coastal Engineering Proceedings*, 1(33), p. 35. doi: 10.9753/icce.v33.waves.35.

Hughes, S. A. and Nadal, N. C. (2009) 'Laboratory study of combined wave overtopping and storm surge overflow of a levee', *Coastal Engineering.* Elsevier B.V., 56(3), pp. 244–259. doi: 10.1016/j.coastaleng.2008.09.005.

Jacobsen, N. G. (2017) 'waves2Foam Manual', (August), pp. 1–3. Available at: https://www.researchgate.net/profile/Niels_Jacobsen3/publication/319160515_waves2Foam_Manual/links/5995c1e7aca27283b11b21a2/waves2Foam-Manual.pdf.

Jacobsen, N. G. *et al.* (2018) 'Numerical prediction of integrated wave loads on crest walls on top of rubble mound structures', *Coastal Engineering.* Elsevier, 142(April 2017), pp. 110–124. doi: 10.1016/j.coastaleng.2018.10.004.

Jacobsen, N. G., Fuhrman, D. R. and Fredsøe, J. (2012) 'A wave generation toolbox for the open-source CFD library: OpenFoam®', *International Journal for Numerical Methods in Fluids*, 70(9), pp. 1073–1088. doi: 10.1002/fld.2726.

Jacobsen, N. G., van Gent, M. R. A. and Fredsøe, J. (2017) 'Numerical modelling of the erosion and deposition of sand inside a filter layer', *Coastal Engineering.* doi: 10.1016/j.coastaleng.2016.09.003.

Jacobsen, N. G., van Gent, M. R. A. and Wolters, G. (2015) 'Numerical analysis of the interaction of irregular waves with two dimensional permeable coastal structures', *Coastal Engineering.* Elsevier B.V., 102, pp. 13–29. doi: 10.1016/j.coastaleng.2015.05.004.

Jensen, B., Christensen, E. D. and Jacobsen, N. G. (2015) 'SIMULATION OF EXTREME EVENTS OF OBLIQUE WAVE INTERACTION WITH POROUS BREAKWATER STRUCTURES', *Coastal Engineering Proceedings.* doi: 10.9753/icce.v34.structures.1.

Jensen, B., Jacobsen, N. G. and Christensen, E. D. (2014) 'Investigations on the porous media equations and resistance coefficients for coastal structures', *Coastal Engineering.* Elsevier B.V., 84, pp. 56–72. doi: 10.1016/j.coastaleng.2013.11.004.

Jensen, J. (1984) *A monograph on rubble mound breakwaters*, *Danish Hydraulic Institute (DHI).* Available at: http://resolver.tudelft.nl/uuid:133be463-5f43-45cd-9115-3ef9ebe245b3.

Juhl, J. and Sloth, P. (1994) 'Wave overtopping of breakwaters under oblique waves', *Coastal Engineering Proceedings*, 1(24), pp. 1182–1196.

van Kester, D. (2009) *SPATIAL DISTRIBUTION OF WAVE OVERTOPPING.* TU Delft. Available at:

https://doi.org/10.4233/uuid:5e91b150-3d62-462e-83f0-0efe570df822.

Lioutas, A. (2010) *Experimental research on spatial distribution of overtopping*. TU Delft. Available at: http://resolver.tudelft.nl/uuid:0122fe2e-0260-489f-b258-6e167fa9a621.

Losada, I. J. *et al.* (2008) 'Numerical analysis of wave overtopping of rubble mound breakwaters', *Coastal Engineering*, 55(1), pp. 47–62. doi: 10.1016/j.coastaleng.2007.06.003.

McCabe, M. V., Stansby, P. K. and Apsley, D. D. (2013) 'Random wave runup and overtopping a steep sea wall: Shallow-water and Boussinesq modelling with generalised breaking and wall impact algorithms validated against laboratory and field measurements', *Coastal Engineering*. Elsevier B.V., 74, pp. 33–49. doi: 10.1016/j.coastaleng.2012.11.010.

McCall, R. T. *et al.* (2014) 'Modelling storm hydrodynamics on gravel beaches with XBeach-G', *Coastal Engineering*. Elsevier B.V., 91, pp. 231–250. doi: 10.1016/j.coastaleng.2014.06.007.

Van der Meer, J. M. (2007) *Design, construction, calibration and use of the wave overtopping simulator*. Available at: http://resolver.tudelft.nl/uuid:5656bf8b-e799-4c7f-87d4-82d4f8a26fef.

Van Der Meer, J., Provoost, Y. and Steendam, G. J. (2012) 'THE WAVE RUN-UP SIMULATOR, THEORY AND FIRST PILOT TEST', *Coastal Engineering Proceedings*.

Van der Meer, J. W. (2011) *The Wave Run-up Simulator Idea, necessity, theoretical background and design*. Available at: Van der Meer Consulting Report vdm11355, www.vdm-c.nl.

Van der Meer, J. W. *et al.* (2018) *EurOtop*.

Van Der Meer, J. W. (1988) *Rock Slopes and Gravel Beaches under Wave Attack*, *PhD Thesis*. TU Delft.

Van Der Meer, J. W. *et al.* (2011) 'FLOW DEPTHS AND VELOCITIES AT CREST AND INNER SLOPE OF A DIKE, IN THEORY AND WITH THE WAVE OVERTOPPING SIMULATOR', *Coastal Engineering Proceedings*, 1.32.

Patil, A. (2019) *Numerical investigation of nearshore wave transformation and surf zone hydrodynamics*. TU Delft. Available at: http://resolver.tudelft.nl/uuid:1b6037cf-6cb9-4ebf-b9c2-25e7fa6cf575.

Paulsen, B. T., Bredmose, H. and Bingham, H. B. (2014) 'An efficient domain decomposition strategy for wave loads on surface piercing circular cylinders', *Coastal Engineering*. Elsevier B.V., 86, pp. 57–76. doi: 10.1016/j.coastaleng.2014.01.006.

Peakall, J. and Warburton, J. (1996) 'Surface tension in small hydraulic river models - The significance of the Weber number', *Journal of Hydrology New Zealand*.

Pullen, T. *et al.* (2007) 'EurOtop - Wave Overtopping of Sea Defences and Related Structures: Assessment Manual (Die Kuste version)', (August).

Sandoval, C. (2015) *Direct personnel hazard in wave overtopping flows at seadikes*. THE UNIVERSITY OF EDINBURGH. doi: 10.1002/j.1556-6978.1968.tb02068.x.

Schüttrumpf, H. F. R. (2001) *Wellenüberlaufströmung bei Seedeichen-Experimentelle und theoretische Untersuchungen*. Braunschweig University. Available at: http://www.tu-bs.de.

Schüttrumpf, H. and van Gent, M. R. A. (2003) 'Wave Overtopping at Seadikes', in *Coastal Structures 2003*. doi: 10.1061/40733(147)36.

Schüttrumpf, H. and Oumeraci, H. (2005) 'Layer thicknesses and velocities of wave overtopping flow at seadikes', *Coastal Engineering*, 52(6), pp. 473–495. doi: 10.1016/j.coastaleng.2005.02.002.

Steenaard, J. (2002) *Verdeling van overslaand water over een golfbreker*. Available at: http://resolver.tudelft.nl/uuid:5f6f0f6f-9001-40a6-9724-b61b0696e7a4.

Suzuki, T., Verwaest, T. and Hassan, W. (2011) 'The applicability of SWASH model for wave transformation and wave overtopping: A case study for the Flemish coast', *Fifth International Conference on Advanced COmputational Methods in ENgineering*, 2011(November), pp. 14–17. doi: 10.1016/j.jcps.2010.06.014.

Trung, L. H. (2014) *Overtopping on grass covered dikes*. TU Delft. Available at: https://doi.org/10.4233/uuid:8b33536e-fd2b-4d65-b493-410694b46131.

Tsirel, S. V. (1997) 'Methods of granular and fragmented material packing density calculation', *International journal of rock mechanics and mining sciences & geomechanics abstracts*. doi: 10.1016/S0148-9062(96)00029-0.

Weller, H. G. *et al.* (1998) 'A tensorial approach to computational continuum mechanics using object-oriented techniques', *Computers in Physics*. doi: 10.1063/1.168744.

Zelt, J. A. and Skjelbreia, J. E. (1993) 'Estimating Incident and Reflected Wave Fields Using an Arbitrary Number of Wave Gauges', *Coastal Engineering 1992*, pp. 777–789. doi: 10.1061/9780872629332.058.

Appendices

Appendix A. Overtopping over time

A formula for overtopping time T_{ovt} can be given by the equations of motion for velocity and distance, which assume a constant acceleration and motion occurring in a straight line (along the seaward slope). The latter assumption makes it possible to simplify the problem to 1 dimension. Bosman et al. (Bosman *et al.*, 2008) give the overtopping time as the time that wave run-up would occur if the slope would not end at the freeboard. These formulas are given by:

$$t = \sqrt{\frac{R_{u,2\%} - R_c}{2g}} \tag{76}$$

$$\frac{T_{ovt,2\%}(x_c = 0)}{T_{m-1,0}} = c'_{Tovt,2\%} \sqrt{\frac{R_{u,2\%} - R_c}{\gamma_f H_s}} \tag{77}$$

Where:

t	=	time for water to flow to from the R_c to the $R_{u,2\%}$ if the seaward slope was infinite	$[s]$
$T_{ovt,2\%}$	=	overtopping time that is exceeded by two percent of the overtopping waves	$[s]$
$c'_{Tovt,2\%}$	=	empirical coefficient, valued at 1.15	$[-]$

Bosman et al. also give a relation for the overtopping time on different positions on the crest. As the formulas for flow velocity and depth show a decrease over the crest, the overtopping time must increase (continuity):

$$\frac{T_{ovt,2\%}(x_c)}{T_{ovt,2\%}(x_c = 0)} = \left(1 + c''_{Tovt,2\%}\left(\frac{x_c}{L_0}\right)\right) \tag{78}$$

Where:

|			
$c''_{Tovt,2\%}$	=	empirical coefficient, valued at 2.8	$[s]$

Appendix B. Discharge over breakwaters

Jensen (1984)

In a breakwater design guide composed by Jensen (1984), the overtopping from various tests is measured at some distance from the still water level. This distance is given by B^*, which is the representative dimension of the breakwater, being the horizontal distance from the intersection of the SWL to the armour layer and the limit of the reclamation or the rear side of the crown wall. See also Appendix Figure B.1. As all overtopping is measured at B^*, it is not clear what discharge reduction has already occured due to infiltration in the crest. The use of B^* makes sense however, as the overtopping often causes damage to property or people behind the crest, not on it.
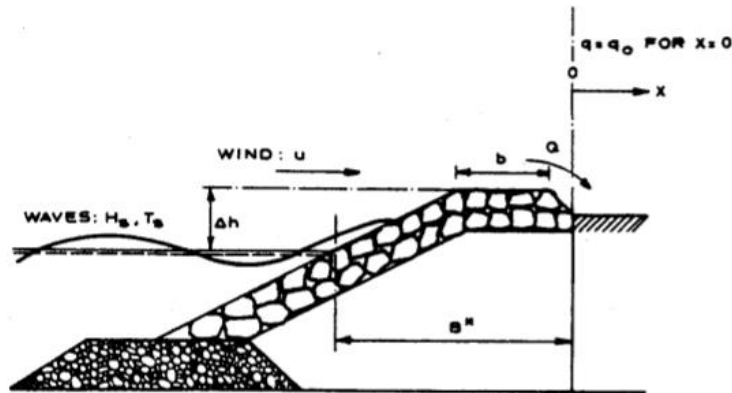
Appendix Figure B.1: Definition of representative dimension B^* and distance from crest x (Jensen, 1984)

Jensen also describes a formula which gives the overtopping intensity at a distance x from the crest. It is not entirely clear what the test set-up is, and if a backfill is implemented. It seems that overtopping trays are just spaced at different distances from $x = 0$. It is therefore likely that this method underestimates the actual discharge at some distance away from the crest. From the tests an equation for the overtopping intensity was fitted, the total mean overtopping discharge is given by integration. If the total is known, the discharge at some distance from the crest can be determined.

$$q(x) = q_o 10^{-\left(\frac{x}{\beta}\right)} \tag{79}$$

$$Q = \frac{q_o \beta}{\ln(10)} \tag{80}$$

Where:

$q(x)$	=	intensity of overtopping (the mean overtopping discharge per meter length away from the crest edge) at a distance x away from the crest	$\left[\frac{m^2}{s}/m\right]$
q_o	=	overtopping intensity at $x = 0$	$\left[\frac{m^2}{s}/m\right]$
β	=	distance for which the overtopping intensity decreases by a factor 10, between $0.4 - 0.55$ for a rubble mound breakwater without a crest wall	$[m]$
Q	=	total overtopping discharge	$\left[\frac{m^3}{s}/m\right]$

Steenaard (2002)

Steenaard (2002) performed tests on overtopping reduction on an armoured crest, under the influence of regular waves. Under the assumption that the overtopping layer thickness was significantly smaller

than the thickness of the armour layer, the tests were performed without a filter layer. Secondly it was assumed that the water of an overtopping wave is gone when the next overtopping event occurs. In this way saturation of the armour layer does not influence the test results. Steenaard assumed that the infiltration losses on the crest of the breakwater are dependent on the incoming discharge, the width of the crest and gravity.

$$\frac{q_3}{q_{tot}} = \frac{Q_{tot}^* - Q_d^*}{Q_{tot}^* + 7.0 \cdot 10^{-2}} \qquad \text{for} \qquad Q_{tot}^* > Q_d^* \qquad (81)$$

$$\frac{q_3}{q_{tot}} = 0 \qquad \text{for} \qquad Q_{tot}^* < Q_d^* \qquad (82)$$

Where:

q_{tot} = overtopping at the front side of the crest $\left[\frac{m^2}{s} per\ m\right]$

q_3 = overtopping at the rear side of the crest $\left[\frac{m^2}{s} per\ m\right]$

Q_{tot}^* = $q_{tot}/\sqrt{gB^3}$, the dimensionless crest width $[-]$

Q_d^* = the threshold value for Q_{tot}^*, $Q_d^* = 8.1 * 10^{-3}$ for this test set-up $[-]$

Steenaard stressed that the formulas should not be used where the non-dimensional total overtopping discharge is close to the threshold value. It is noted that when the overtopping discharge increases, and the construction configuration stays the same, the losses into the crest reach a constant value. This can indicate that the system gets saturated.

Van Kester (2009)

Van Kester (2009) noted that for the formulas used by Steenaard a significant spread was found compared to newly generated test results (also for regular waves). Van Kester uses a new dimensionless factor that also takes into account the wave steepness and crest freeboard. Van Kester uses the ratio between the dimensionless overtopping discharges Q_{tot}^* and Q_{over}^* to express the change of discharge over the crest.

$$\frac{Q_{over}^*}{Q_{tot}^*} = \left(\frac{H^* - H_d^*}{H^* - 15}\right)^2 \qquad \text{for} \qquad H^* \geq H_d^* \qquad (83)$$

$$\frac{Q_{over}^*}{Q_{tot}^*} = 0 \qquad \text{for} \qquad H^* \leq H_d^* \qquad (84)$$

Where:

Q_{over}^* = $Q_{over}/\sqrt{g \cdot H_s^3}$, dimensionless overtopping discharge directly behind the crest $[-]$

Q_{tot}^* = $Q_{tot}/\sqrt{g \cdot H_s^3}$, the dimensionless total wave overtopping $[-]$

H^* = $\frac{H \cdot L}{B \cdot R_c}$, dimensionless factor for overtopping discharge directly behind the crest $[-]$

H_d^* = 26, threshold value for H^* $[-]$

Van Kester also adapted the formula of Besley to calculate the reduction factor for both an impermeable and a permeable backfill. A relation was found that incorporates the wave-height and wave steepness into the reduction factor, through introducing the wave energy-flux. The formula for the permeable backfill, is presented here (for the mean fit). In the tests the backfill is made up of armour rock.

$$\frac{Q_{over,x}^*}{Q_{over,0}^*} = \exp\left(-1.64 \cdot 10^5 \left(\frac{x}{H_s} \cdot \frac{1}{(H^* T^*)^3}\right)\right) \qquad (85)$$

Where:

$H^* T^*$ = $\frac{H_s}{R_c} \cdot T_s \cdot \sqrt{\frac{g}{R_c}}$, dimensionless presentation of wave energy flux $[-]$

Lioutas (2010)

Lioutas (2010) presents a follow-up research on van Kester (2009), to validate the findings for irregular waves. It was concluded that the findings of van Kester did not apply to this specific research. This could also have to do with the fact that the backfill was made up of core material in this research, as opposed to an armour layer in the research by van Kester. An overtopping formula from the EurOtop (Pullen *et al.*, 2007) was adapted to fit the data correctly and adds a reduction factor γ_c that considers the reduction of overtopping discharge over the crest (which had a fixed width of $3.4\ m$). The reduction factor is used in the overtopping formula in the same way as the other reduction factors.

$$\gamma_c = -0.164 \cdot \frac{x}{B} + 0.677 \tag{86}$$

Where:

γ_c	=	reduction factor for overtopping discharge over the crest. The minimum ($\gamma_c = 0.677$) is applicable for the width of the crest only, so without a backfill made of core material	$[-]$
B	=	width of the crest	$[m]$

Appendix C.   Data from physical model
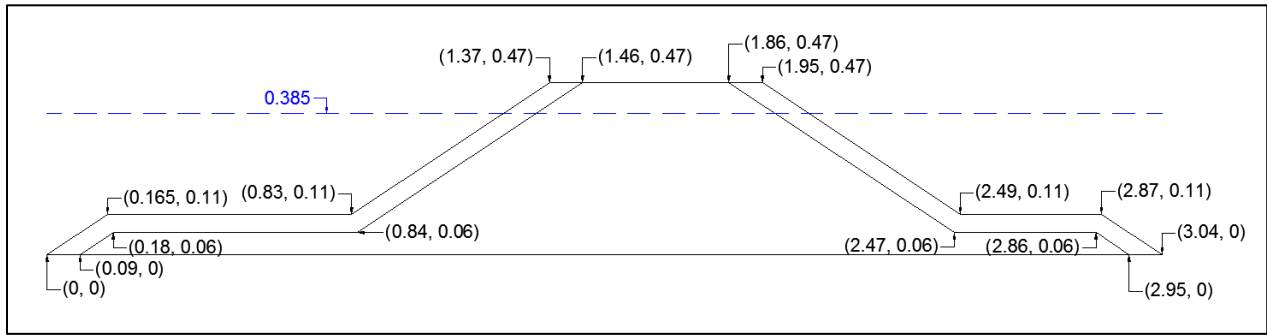
Appendix Figure C.1: Cross section for the assessment of the safe working level (model scale)

Test Data — Model scale 25

	General test parameters		Input parameters Prototype			Incident waves at paddle							Incident waves at structure					
		Percentage %	Hs [m]		SWL	No waves	Hm0	Hs	Hmax	Tp	Tm-1,0	Tm	RC	Hm0	Hs	Hmax	Tp	Tm-1,0	Tm	RC
Test	Date	Design wave height	Design	Tp [s]	[mCD]	[-]	[m]	[m]	[m]	[s]	[s]	[s]	[-]	[m]	[m]	[m]	[s]	[s]	[s]	[-]
1.01	19-03-12	Normal	2.00	14.0	1.19	1293	2.06	2.1	4.23	13.91	12.77	11.31	0.13	1.97	1.9	3.36	13.91	11.83	10.63	0.13
1.02	20-03-12	1/1 yr	2.80	15.9	1.19	1228	3.13	3.2	5.82	16.00	14.33	12.82	0.16	2.50	2.4	3.91	8.31	11.16	9.40	0.24
1.03	20-03-12	1/10 yr	3.10	16.8	1.19	1223	3.92	4.0	6.39	17.30	15.11	13.67	0.15	2.88	2.7	4.25	8.31	11.13	9.17	0.26
1.04	20-03-12	1/1 yr	2.80	15.9	0.34	592	3.16	3.3	5.61	16.00	14.34	12.83	0.14	2.42	2.3	3.61	8.21	10.54	8.83	0.22
1.05	20-03-12	short waves	1.30	6	0.34	677	1.52	1.5	2.71	6.40	5.74	5.28	0.11	1.34	1.4	2.81	6.04	5.86	5.40	0.40
2.01	22-03-12	Normal	2.00	14.0	1.19	1251	2.05	2.1	4.14	13.91	12.76	11.32	0.15	2.05	2.1	3.98	13.91	11.80	10.85	0.08
2.02	22-03-12	1/1 yr	2.80	15.9	1.19	447	3.12	3.3	5.63	16.00	14.38	12.86	0.16	2.61	2.4	3.91	16.00	11.26	9.59	0.13
2.04	22-03-12	Normal	2.00	14.0	1.19	1237	2.09	2.1	4.24	13.91	12.75	11.34	0.12	1.83	1.8	3.35	13.91	11.32	10.11	0.28
2.05	22-03-12	1/1 yr	2.80	15.9	1.19	1241	3.16	3.2	5.75	16.00	14.35	12.84	0.13	2.50	2.4	4.02	8.31	10.94	9.26	0.24
3.01	27-03-12		1.00	12.0	1.89	1232	1.05	1.0	1.92	12.31	11.05	9.86	0.52	1.02	1.0	1.87	12.31	11.30	10.23	0.61
3.02	27-03-12		1.00	16.0	1.89	1211	1.00	1.0	1.83	16.00	14.81	13.20	0.56	0.98	1.0	1.93	16.00	13.81	12.93	0.66
3.03	27-03-12		1.50	12.0	1.89	1240	1.59	1.6	2.98	12.31	10.97	9.75	0.51	1.56	1.5	2.85	12.31	11.24	10.00	0.60
3.04	27-03-12		1.50	16.0	1.89	1215	1.52	1.5	2.85	16.00	14.75	13.16	0.53	1.47	1.5	2.85	16.00	13.06	12.39	0.64
3.05	28-03-12		2.00	12.0	1.89	1244	2.10	2.1	4.00	12.31	10.86	9.71	0.48	2.07	2.0	3.84	12.31	11.24	9.97	0.57
3.06	28-03-12		2.00	16.0	1.89	735	1.91	1.9	3.70	16.00	14.64	13.05	0.49	1.88	1.9	3.58	16.00	12.68	11.77	0.60
3.07	28-03-12		1.50	12.0	1.19	1224	1.62	1.6	3.00	12.31	10.95	9.86	0.50	1.53	1.5	2.85	12.31	11.23	10.01	0.59
3.08	28-03-12		1.50	16.0	1.19	1231	1.55	1.6	3.02	16.00	14.73	12.98	0.51	1.46	1.5	2.76	16.00	12.79	11.91	0.62
3.09	28-03-12		1.00	12.0	1.89	643	1.05	1.0	1.87	11.85	11.06	9.80	0.48	1.02	1.0	1.87	11.85	11.22	10.21	0.57
3.10	28-03-12		1.00	16.0	1.89	571	1.02	1.0	1.84	16.00	14.88	13.12	0.52	1.00	1.0	1.91	16.00	13.98	13.11	0.64
3.11	28-03-12		1.50	12.0	1.89	792	1.57	1.5	2.91	11.85	10.94	9.84	0.45	1.54	1.5	2.83	12.31	11.23	10.00	0.51

Appendix Figure C.2: Wave measurements from physical tests

Test	Hs	Tp	Water level	Overtopping model scale		Test duration	Overtopping rate model scale	Overtopping rate prototype	Overtopping rate prototype
	[m]	[s]	[m CD]	[gr]	[m³]	[s]	[m3/s/m]	[m3/s/m]	[l/s/m]
3.01	1.0	12	1.89	4.4	4.40E-06	2437	1.20E-08	1.50E-06	0.002
3.02	1.0	16	1.89	1961.2	1.96E-03	3213	4.07E-06	5.09E-04	0.51
3.03	1.5	12	1.89	11305.7	1.13E-02	2422	3.11E-05	3.89E-03	3.89
3.04	1.5	16	1.89	46011.9	4.60E-02	3107	9.87E-05	1.23E-02	12.3
3.05	2.0	12	1.89	86311.4	8.63E-02	2420	2.38E-04	2.97E-02	29.7
3.06	2.0	16	1.89	111354.0	1.11E-01	1925	3.86E-04	4.82E-02	48.2
3.07	1.5	12	1.19	1010.0	1.01E-03	2217	3.04E-06	3.80E-04	0.38
3.08	1.5	16	1.19	11506.9	1.15E-02	3213	2.39E-05	2.98E-03	2.98

Appendix Figure C.3: Overtopping discharge measurements

Crest	H_{m0}	T_p	cot α	WL	R_c	Q	P_{ov}	$h_{10\%}$	$h_{2\%}$
m CD	m	s	-	m CD	m	l/m/s	-	m	M
3.50	1.30	16.0	1.5	1.89	1.61	18.0	0.18	0.79	1.15
3.75	1.30	16.0	1.5	1.89	1.86	9.7	0.12	0.59	0.96
4.00	1.30	16.0	1.5	1.89	2.11	5.2	0.07	0.40	0.76
4.25	1.30	16.0	1.5	1.89	2.36	2.8	0.04	0.20	0.57
4.50	1.30	16.0	1.5	1.89	2.61	1.5	0.02	0.00	0.37

Appendix Figure C.4: Working levels and accompanying wave conditions and overtopping parameters

sieve curve	1-500kg	(model scale)		needed volume		stone gradings to be used		
cumulative		percentage of total		350 litres				
0 %		0 %					2	
0 %		0 %		0.0 litres		2	4 mm	
20 %		20 %		70.0 litres		4	5.6 mm	
35 %		15 %		52.5 litres		5.6	8 mm	
50 %		15 %		52.5 litres		8	11.2 mm	
70 %		20 %		70.0 litres		11.2	16 mm	
90 %		20 %		70.0 litres		16	22.4 mm	
100 %		10 %		35.0 litres		22.4	31.5 mm	
				0.0 litres		31.5 >	mm	

Appendix Figure C.5: overview of data from sieve curve of core material. The d_{50} is then given by 11.2 mm

Appendix D.   Sensitivity analysis

Appendix Table D.1 shows the 9 runs that were performed, and the parameters that were altered. Run 14899 is the base-run in this case, this is also the run that was described in the main text (Table 10 and Figure 31).

RunID	α	β	γ	KC (filter, core)	n (filter, core)	Refinement
14899	1000	1.1	0.34	$(19.9, 51.8)$	$(0.4, 0.4)$	-
14900	500	2	0.34	$(10000, 10000)$	$(0.4, 0.4)$	-
14901	1000	1.1	0.34	$(10000, 10000)$	$(0.4, 0.4)$	-
14958	1000	1.1	0.34	$(19.9, 51.8)$	$(0.4, 0.1)$	-
14959	1000	1.1	0.34	$(19.9, 51.8)$	$(0.4, 0.99)$	-
14959 (b)	1000	1.1	0.34	$(19.9, 51.8)$	$(0.99, 0.99)$	-
15127	1000	1.1	0.34	$(19.9, 51.8)$	$(0.4413, 0.2960)$	-
15131	1000	1.1	0.34	$(19.9, 51.8)$	$(0.4413, 0.2960)$	SWL & Struct (1, 1)
15132	1000	1.1	0.34	$(19.9, 51.8)$	$(0.40, 0.2960)$	Struct (2, 2)

Appendix Table D.1: Runs for sensitivity analysis

D.1 Varying α, β, KC (14899, 14900, 14901)

The first run (14899) is largely based on Jacobsen et al. (Jacobsen *et al.*, 2018) and uses the standard van Gent parameters and a porosity of 0.4 for both the filter layer and the core. The results for this run are given in Table 10 and Figure 31 in the main text.

In run 14900 it is assessed what the effects are of changing the resistance coefficients α and β, according to Jensen et al. (Jensen, Jacobsen and Christensen, 2014). The values presented by Jensen also makes sense for a breakwater, as for turbulent flow (which especially occurs in the filter layers) the non-linear friction coefficient is expected to influence the flow process more significantly than the linear friction coefficient. Run 14901 was performed with the van Gent parameters, but with a KC of 10000 to take away the effect of the KC-number in resistance coefficient β. Appendix Table D.2 shows the RMSE and PCC for these runs, compared with the experiment at gauge 6. Also the reflection coefficient is given.
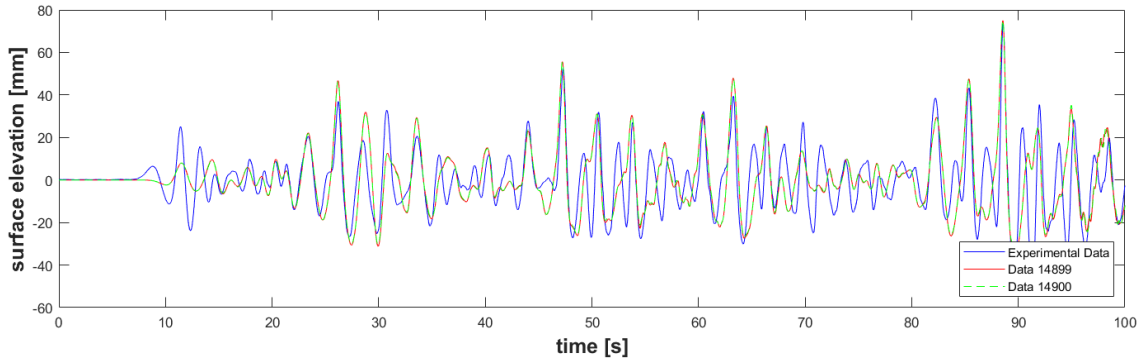
COMPARISON 3.04 & 14899, 14900, 14901			
	14899	**14900**	**14901**
PCC	0.644	0.654	0.640
RMSE	12.498	12.451	12.313
K_R	0.673	0.656	0.667

Appendix Table D.2: Comparisons for runs 14899, 14900, 14901 at gauge 6

It is clear that both the KC number and the resistance coefficients following Jensen have an effect on the reflection coefficient. For the higher KC number, the effect is minimal. This is likely because the KC number has a relatively small influence as is clear from the van Gent equations. A higher KC number causes the turbulent friction term to become somewhat smaller and hence it is thinkable that more water infiltrates into the structure instead of reflects back.

For the Jensen parameters, it is found that the reflection goes down. It can thus be expected that the laminar friction term does play a role also in the reflection back from the structure, as a reduction of this term could be allowing more water to infiltrate into the structure. Tuning the resistance coefficients of a coastal structure with multiple layers is challenging for numerical modelling, especially for new designs and with the lack of proper validation data (Jacobsen, van Gent and Wolters, 2015). The parameters from van Gent are thus used in the further analysis, as they are more widely used in other studies and this
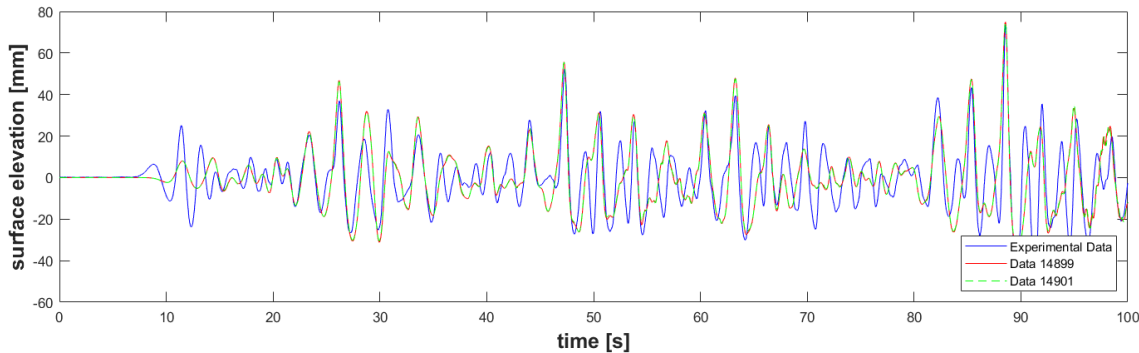
makes this study more comparable to others. Below figures and tables show the surface elevation, PCC and RMSE for runs 14900 and 14901.

Appendix Figure D.1: 14900, comparison of data at gauge 6

COMPARISON 3.04 & 14900

	PCC	RMSE
GAUGE 4	0.7545	14.6992
GAUGE 5	0.7441	13.6191
GAUGE 6	0.6541	12.4505

Appendix Table D.3: PCC and RMSE values from comparison experiment 3.04 and run 14900

Appendix Figure D.2: 14901, comparison of data at gauge 6

COMPARISON 3.04 & 14901

	PCC	RMSE
GAUGE 4	0.7704	13.5092
GAUGE 5	0.7431	12.9863
GAUGE 6	0.6397	12.3125

Appendix Table D.4: PCC and RMSE values from comparison experiment 3.04 and run 14901

D.2 Varying porosity (14958, 14959, 14959b,15127)

To investigate the extent of the influence of the porosity, extreme values were chosen. For run 14958, the porosity of the core was reduced to 10%, the porosity of the filter was kept at 40%. For run 14959, the porosity of the core was increased to 99%, the porosity of the filter again kept at 40%. For run 14959b the porosity of both the core and the filter were set to 99%. In run 15127 it was assesed what the effects would be if the porosity of the core and filter layer would be determined using the method by Tsirel, as described in Chapter 4. These altered porosities are kept in future runs as it is argued that these are likely to be more represarive than the uniform porosity of 40% over the entire structure.

It is clear from the results that the PCC and the RMSE are not significantly influenced by varying the porosities to its extremes. The reflection however, is significantly affected by the variations in porosity.

With run 14958, where the core is much more impermeable, the reflection goes up. This was expected, a lower porosity allows for a lower infiltration and so a quicker saturation of the core material, causing more of the wave energy to be reflected back.

In the opposite scenario, when the structure is made very open, the reflection goes down significantly. Also the PCC and the RMSE are somewhat enhanced by this. Apparently the incoming signal resembles the total experimental signal better than the signal with reflection. For run 15127, where the porosity follows the method of Tsirel, the reflection is higher. Although the porosity of the filter layer is thus increased, the decrease in porosity of the core material causes the reflection to go up. This shows that the long waves from the experiment are influenced by the porosity of the core material.

COMPARISON 3.04 & 14958, 14959, 14959B,15127				
	14958	**14959**	**14959b**	**15127**
PCC	0.6155	0.6731	0.6857	0.6201
RMSE	13.6857	11.1695	11.4061	13.0376
K_R	0.7969	0.2475	0.1072	0.7338

Appendix Table D.5: Comparisons of runs 14958, 14959, 14959B, 15127 at gauge 6

Below figures and tables show the surface elevation, PCC and RMSE for runs 14958, 14959, 14959B and 15127.

COMPARISON 3.04 & 14958		
	PCC	RMSE
GAUGE 4	0.7419	15.9873
GAUGE 5	0.7409	14.8221
GAUGE 6	0.6155	13.6857

Appendix Table D.6: PCC and RMSE values from comparison Experiment 3.04 and run 14958
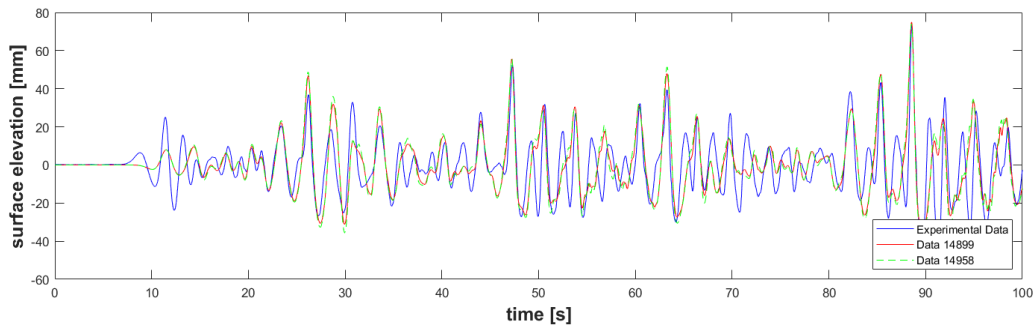
Appendix Figure D.3: 14958, comparison of data at gauge 6.

COMPARISON 3.04 & 14959		
	PCC	RMSE
GAUGE 4	0.7686	12.0239
GAUGE 5	0.7067	11.6309
GAUGE 6	0.6731	11.1695

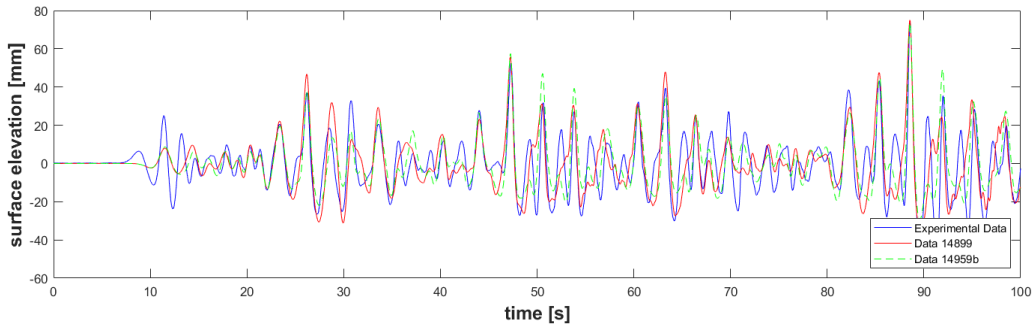Appendix Table D.7: PCC and RMSE values from comparison Experiment 3.04 and run 14959
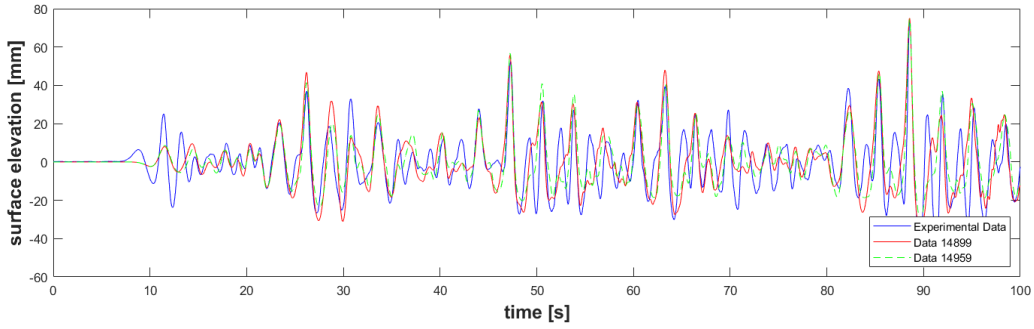
Appendix Figure D.4: 14959, comparison of data at gauge 6.

COMPARISON 3.04 & 14959B		
	PCC	RMSE
GAUGE 4	0.7613	12.7243
GAUGE 5	0.6845	12.0996
GAUGE 6	0.6857	11.4061

Appendix Table D.8: PCC and RMSE values from comparison Experiment 3.04 and run 14959b
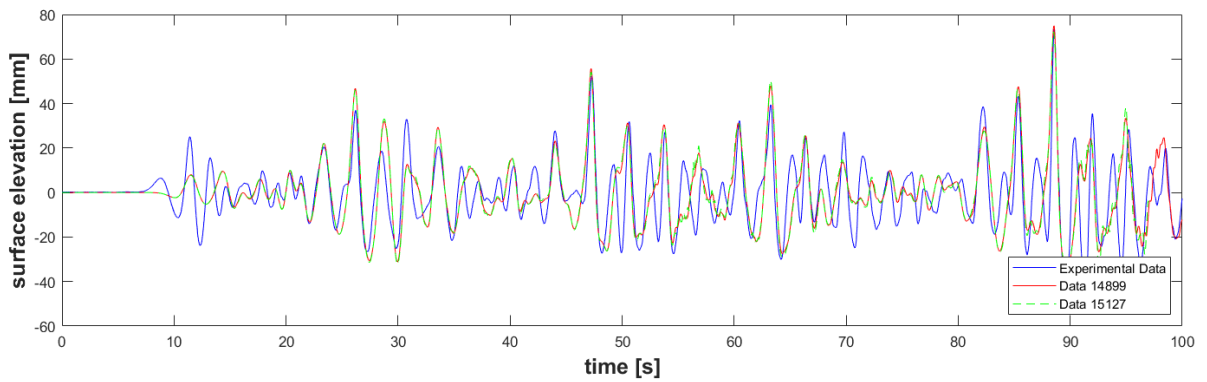

Appendix Figure D.5: 14959b, comparison of data at gauge 6.

COMPARISON 3.04 & 15127		
	PCC	RMSE
GAUGE 4	0.7661	13.8896
GAUGE 5	0.7353	13.4947
GAUGE 6	0.6201	13.0376

Appendix Table D.9: PCC and RMSE values from comparison Experiment 3.04 and run 15127

Appendix Figure D.6: 15127, comparison of data at gauge 6.

D.3 Refinement Zones (15131, 15132)

Although the mesh that is used in the previous runs should be fine enough to represent well most of the waves in the experiment, it is assessed here what the influence is of using refinement around the free water surface and the structure. Appendix Figure D.7 shows the set-up of run 15131, with refinement around the free surface and the porous structure. The area of refinement is chosen by adding and subtracting one significant wave height relative to the water level, and by adding $10\ [cm]$ to the crest level (enough for the highest overtopping). The refined zone is made with the grid generator *snappyHexMesh*. The refinement is of level 1, which indicates that the $0.005 * 0.005$ mesh becomes a $0.0025 * 0.0025$ mesh.
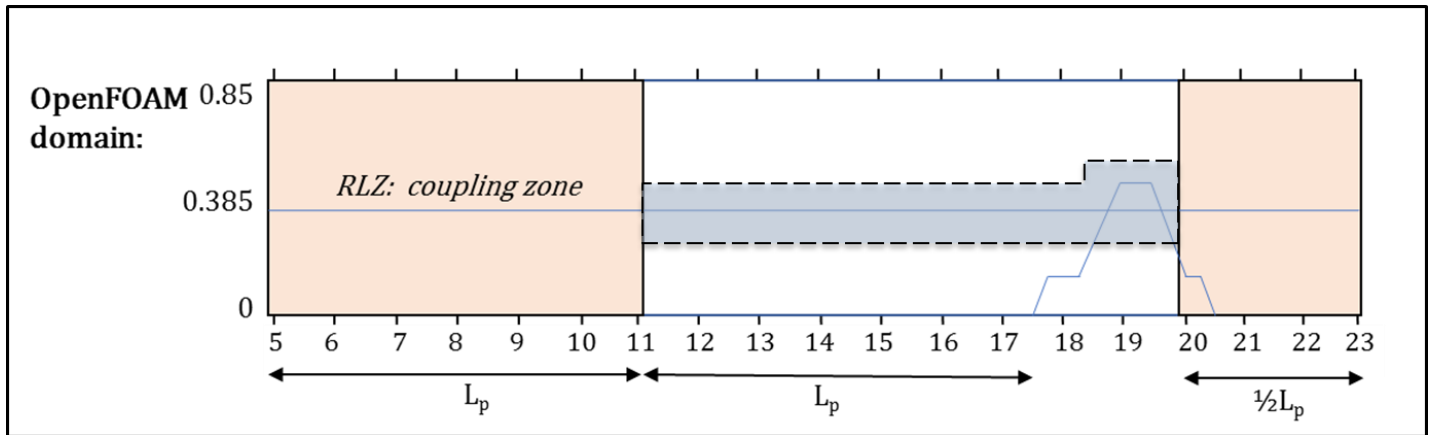
Appendix Figure D.7: set-up of run 15131, showing the refinement zone in light blue

The second refinement run (run 15132) has a refinement only around the porous structure. Appendix Figure D.8 shows the set-up. The refinement is of level 2, which indicates that the $0.005 * 0.005$ mesh becomes a $0.00125 * 0.00125$ mesh. This refinement is used to get a high resolution around the zone of interest (the breakwater crest) and to see the influence of this on the overtopping flow.
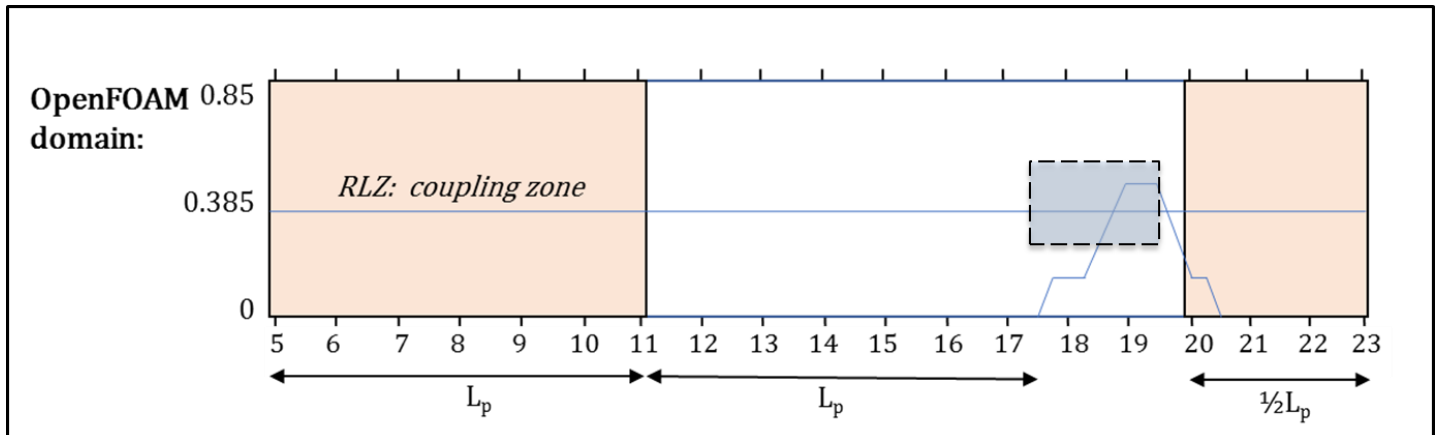
Appendix Figure D.8: set-up of run 15132, showing the refinement zone in light blue
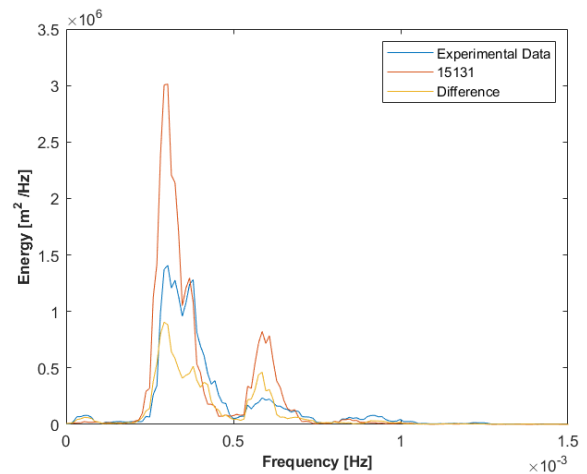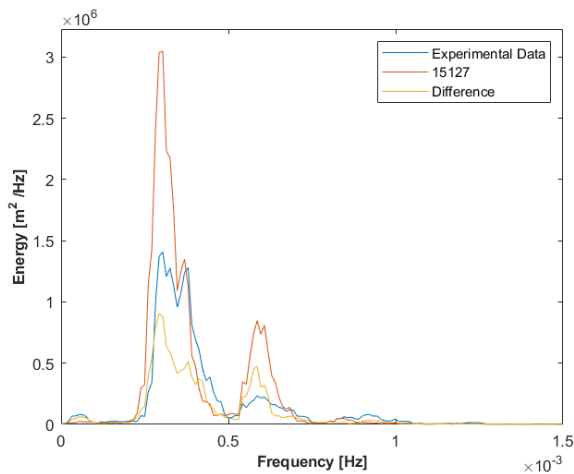
COMPARISON 3.04 & 15131, 15132

	15131	15132
PCC	0.6141	~
RMSE	13.0511	~
K_R	0.7250	~

Appendix Table D.10: Comparisons of runs 15131, 15132 at gauge 6

The reflection coefficient, PCC and RMSE from run 15132 are not reliable because the simulation was ended prematurely. Comparing the reflection for the first 90 seconds however shows that the reflection coefficient is very similar, slightly higher reflection occurs for the run with the finer mesh (0.6744 compared to 0.6821). However, in this run also the filter layer was made more impermeable for the flow depth analysis, which is likely to explain this difference in reflection. The RMSE and PCC were again found to be in the same order of magnitude. The reflection coefficient of run 15131 as compared to run 15127 is however slightly lower. This difference might be caused by some more waves being resolved by the finer mesh, causing the incoming wave field to be slightly different.

Wave spectra are used to see if specific parts of the spectrum are represented better for the changed mesh. Below the spectra for run 15127 (without refinement) and run 15131 are given, both for the 1 block ('grassy') spectrum. For visual representation, a moving average of 5 points is used. The spectrum of the difference looks very similar. It appears that most frequencies are represented by the two simulations and the mismatch mostly results from the different energy in the frequencies. The results are given at gauge 5.


Appendix Figure D.9: Spectrum experiment and Run 15127

Appendix Figure D.10: Spectrum experiment and Run 15131

Below figures and tables show the surface elevation, PCC and RMSE for runs 15131 and 15132.

	COMPARISON 3.04 & 15131	
	PCC	RMSE
GAUGE 4	0.7653	13.8231
GAUGE 5	0.7334	13.3922
GAUGE 6	0.6141	13.0511

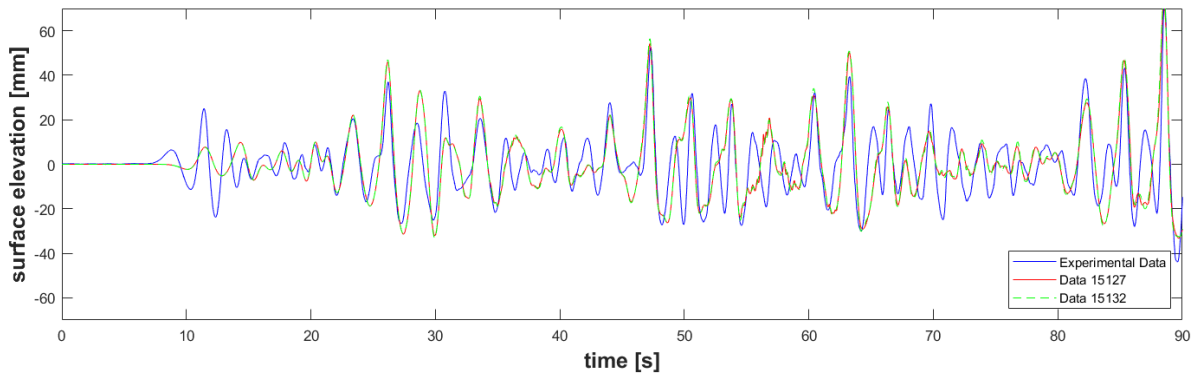Appendix Table D.11: PCC and RMSE values from comparison Experiment 3.04 and run 15131
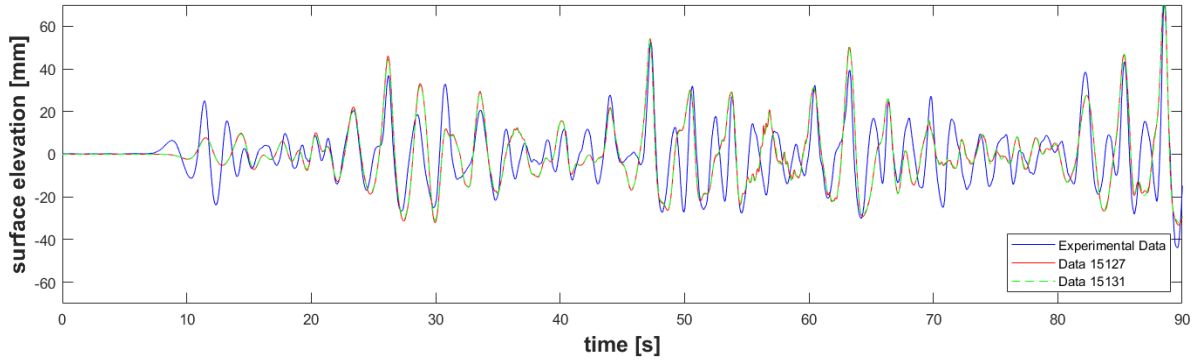
Appendix Figure D.11: 15131, comparison of data at gauge 6.
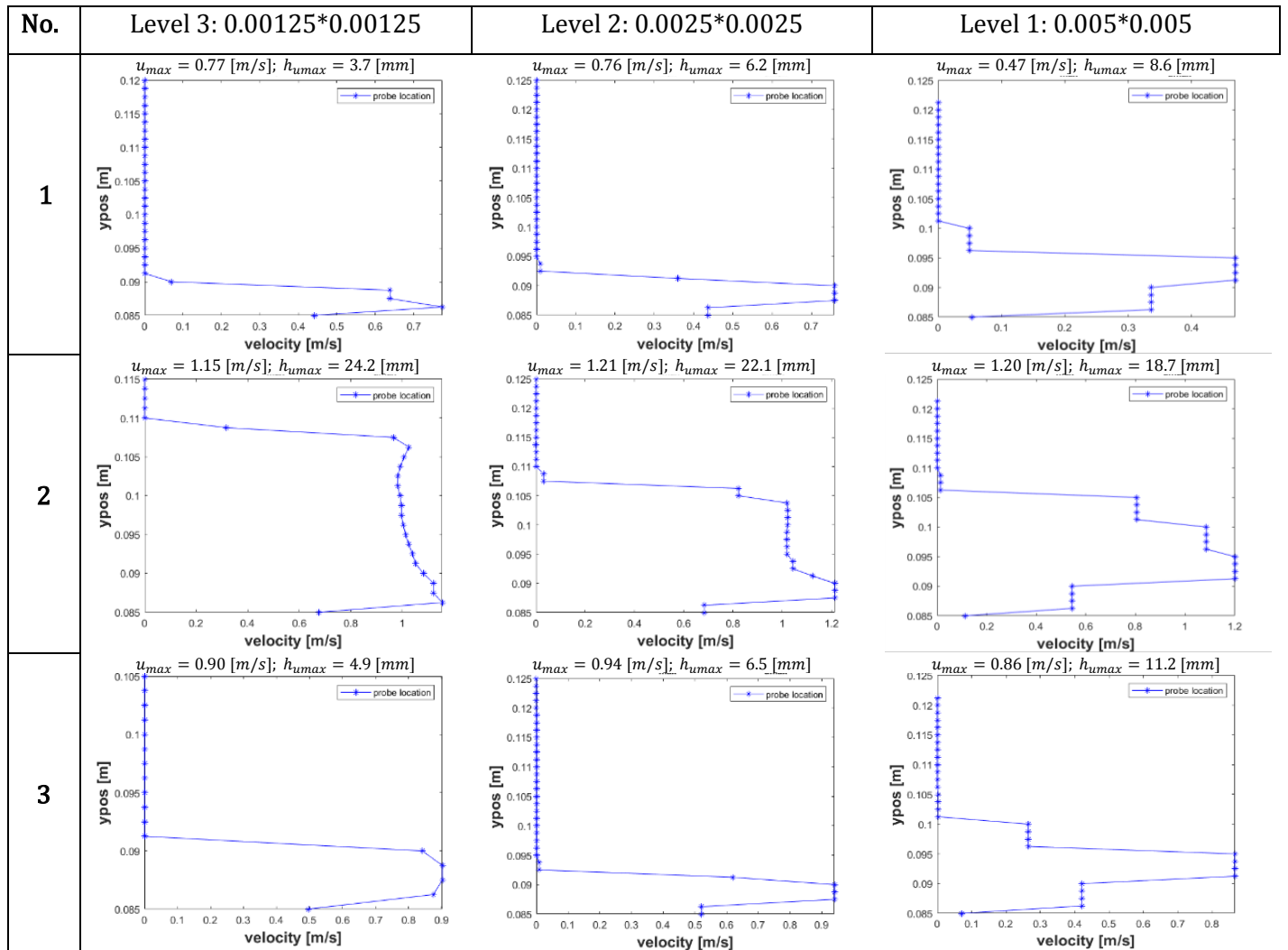
COMPARISON 3.04 & 15132

	PCC	RMSE
GAUGE 4	0.7712	13.2229
GAUGE 5	0.7542	12.7160
GAUGE 6	0.6763	11.8614

Appendix Table D.12: PCC and RMSE values from comparison Experiment 3.04 and run 15132

Appendix Figure D.12: 15132, comparison of data at gauge 6.

Appendix E.   Velocity Profiles

No.	Level 3: 0.00125*0.00125	Level 2: 0.0025*0.0025	Level 1: 0.005*0.005
1	$u_{max} = 0.77\ [m/s];\ h_{umax} = 3.7\ [mm]$	$u_{max} = 0.76\ [m/s];\ h_{umax} = 6.2\ [mm]$	$u_{max} = 0.47\ [m/s];\ h_{umax} = 8.6\ [mm]$
2	$u_{max} = 1.15\ [m/s];\ h_{umax} = 24.2\ [mm]$	$u_{max} = 1.21\ [m/s];\ h_{umax} = 22.1\ [mm]$	$u_{max} = 1.20\ [m/s];\ h_{umax} = 18.7\ [mm]$
3	$u_{max} = 0.90\ [m/s];\ h_{umax} = 4.9\ [mm]$	$u_{max} = 0.94\ [m/s];\ h_{umax} = 6.5\ [mm]$	$u_{max} = 0.86\ [m/s];\ h_{umax} = 11.2\ [mm]$

Appendix F. Very Turbulent Run

For the first simulation, rules of thumb are used for the calculation of the values on the inlet (see e.g. CFD-Wiki, 2014). For the turbulent dissipation rate we use:

$$\varepsilon = \frac{0.09^{\frac{3}{4}} k^{\frac{3}{2}}}{l} \tag{87}$$

Where:

ε	=	The turbulent dissipation rate	$[m^2/s^3]$
k	=	The turbulent kinetic energy	$[m^2/s^2]$
l	=	The turbulent length scale, which equals $0.7 * L$ where L is the characteristic length scale, here equal to the depth	$[m]$

$$k = \frac{3}{2}(UI)^2 \tag{88}$$

Where:

U	=	The mean flow velocity, here equal to the wave celerity $\sqrt{gh}$	$[m/s]$
I	=	The turbulence intensity, for highly turbulent cases in between 5% and 20%, here set to 18%	$[-]$

For the first turbulent simulation, rules of thumb are used for the calculation of the values on the inlet. The analysis of the first turbulent run showed that the dissipation of wave energy was so severe that no waves were overtopping at all. The following 2 figures show the wave field just in front of the breakwater toe (Appendix Figure F.1) and at the point where the mean water level intersects with the front slope (Appendix Figure F.2). It is clear that the water depth is significantly reduced by the settings of the turbulence model, with as result that no waves overtop the structure.
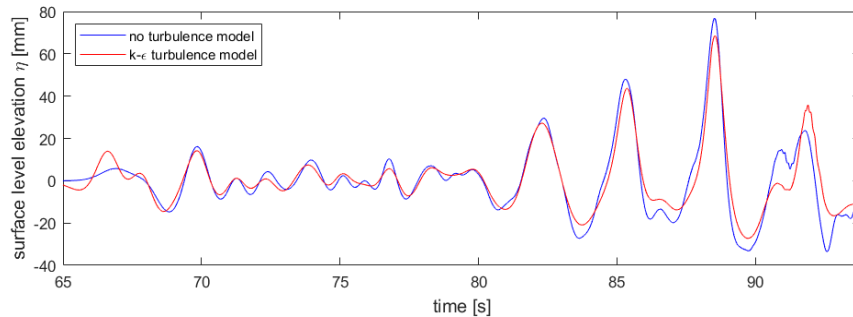
Appendix Figure F.1: Comparison of surface level at gauge 6 (Turbulence run 1)
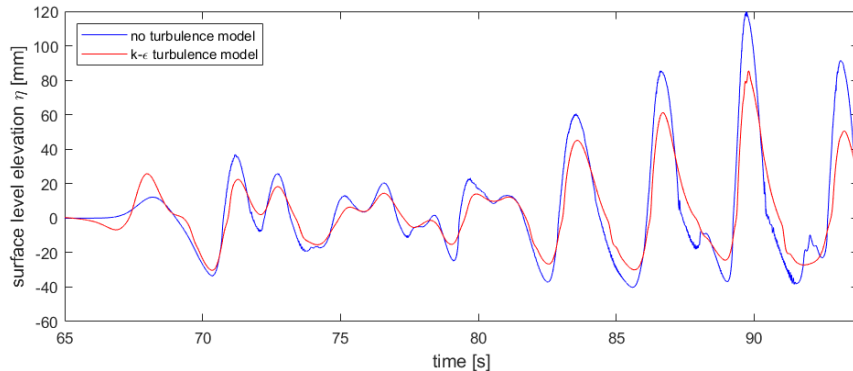
Appendix Figure F.2: Comparison of surface level at intersection of SWL and front slope (Turbulence run 1)

Appendix G.   JONSWAP in W2F

This entire section is adapted from (Jacobsen, 2017). Waves2Foam uses a simple linear superposition of the various wave components. As input it requires a phasing method, besides the spectral shape (JONSWAP) and the spectral discretisation method. By giving a fixed value for the generation of random numbers of the random phasing method, the results can be reproduced.

For the discretisation of the JONSWAP, 2 methods are available. The first method uses an equidistant discretisation of the frequency spectrum, where $\Delta f = 1/D$. With this discretisation, the frequency resolution is equal over all parts of the spectrum. Where in physical experiments often around 1000 discrete wave components are imposed, this becomes computationally expensive for numerical models (especially combined with the use of relaxation zones). It is hence much more practical to use a smaller number of wave components. The second method of discretisation of the spectrum therefore gives an option to use a different type of discretisation, which needs less wave components to represent the characteristics of the spectrum.

The return period and the wave height distribution are affected by the discretisation and the total amount of wave components. If the period of repetition of the wave signal is small compared to the mean wave period, a limited number of wave heights can be given by the wave signal. This will cause the wave height distribution to deviate considerably from a Rayleigh distribution, especially so for small values of the exceedance probability. So the period of repetition should be as large as possible. For an equidistant discretisation the period of repetition is equal to $T_r = N/f_N$, where N is the number of wave components and f_N is the upper cut-off frequency. So the more wave components are used, the longer the period of repetition becomes.

A non-equidistant discretisation method called cosine stretching is supplied by Waves2Foam. This discretisation is finer around the peak of the spectrum. With the cosine stretched discretization, an increase in the repetition time by a factor of 30 was obtained compared to the equidistant discretisation (for $N = 20$, JONSWAP with $\gamma = 3.3$). It can be shown that spectral wave properties (like H_{m0} and $T_{m-1.0}$) are relatively insensitive for the method of discretisation (for $N > 30$). However, the exceedance probabilities of wave heights and wave periods are significantly affected by the discretisation method that is applied.

It can be shown that the spectral wave properties for the non-equidistant discretisation are much less sensitive to variations in N. Even for $N = 100$ it is clear that the non-equidistant discretisation of the spectral wave height closely represents a Rayleigh distribution for an exceedance probability of 0.1%. This while the equidistant discretisation does not even represent well the 1.0% exceedance probability for 100 wave components. For further details, see the exceedance curves in (Jacobsen, 2017; their Figure B.5).

Concluding, when it is chosen to use waves2foam to generate the JONSWAP, the non-equidistant (cosine stretching) discretisation method should be considered. With this method it is possible to use 100 wave components and to get the correct Rayleigh distribution in the wave heights produced by the spectrum (so the correct exceedance statistics). This method has for instance also been applied in (Jacobsen, van Gent and Fredsøe, 2017).

Appendix H. Domain runs

For runs 1 – 5 the swell domain is used, for runs 6-8 the sea domain is used. The OCW3D grid is kept the same as in the validation runs, as all waves in the test runs have a smaller wave length than the waves in the validation case. The OpenFOAM mesh is adapted following the recommendations from the validation.
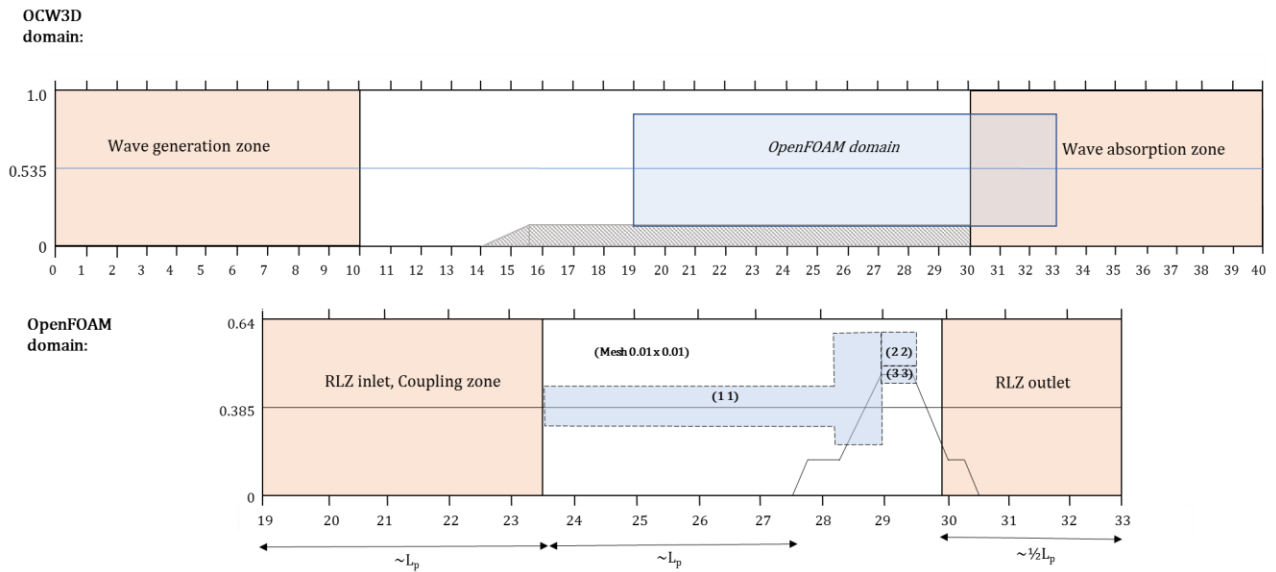
Appendix Figure H.1: Domain for the swell runs (run 1-5)
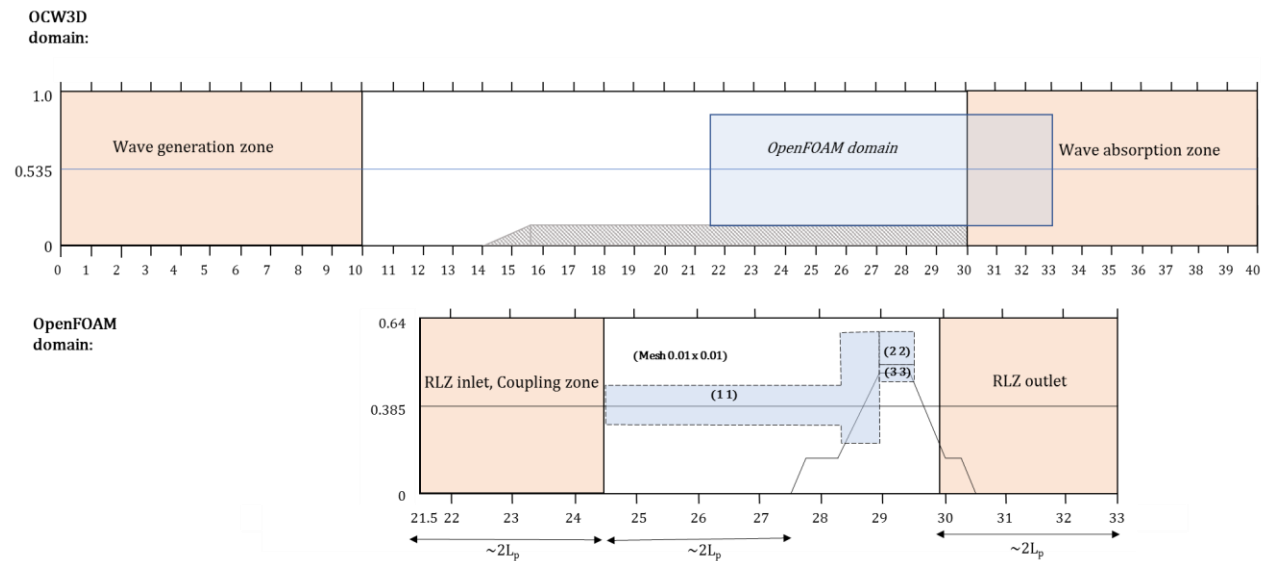
Appendix Figure H.2: Domain for the sea runs (run 6-8)

126

Appendix I. OpenFOAM data

In the validation case the analysis was introduced where from each wave the maximum flow depth and the maximum velocity are obtained. This analysis takes the maximum flow depth from an analysis of the gauge data. The maximum flow velocity is measured by taking the maximum measured velocity in one of the probes positioned in the overtopping flow. For this purpose, a 'threshold-crossing analysis' was used. This means that the surface elevation from the gauge output is plotted against time, where individual overtopping waves are distinguished by a combination of a zero-upward crossing and a consecutive zero-downward crossing of the elevation signal through a certain threshold level. This threshold level is set at a very small number above the crest level, so practically all overtopping waves are included.

With this analysis it is possible to study the maximum flow depth and maximum flow velocity on various positions on the crest. To illustrate how the output data is processed, some results from run 8 are discussed here. Appendix Figure I.1 shows from top to bottom the simulated result of: 1) the wave field close to the breakwater; 2) the overtopping flow depth measured at the transition from filter to core material; 3) the instantaneous discharge measured at the transition from filter to core material. What should be noted about the results is that the instantaneous discharge plot doesn't recognize the smallest overtopping waves that are measured by the wave gauges. See for instance the overtopping events occurring around $30\ [s]$.
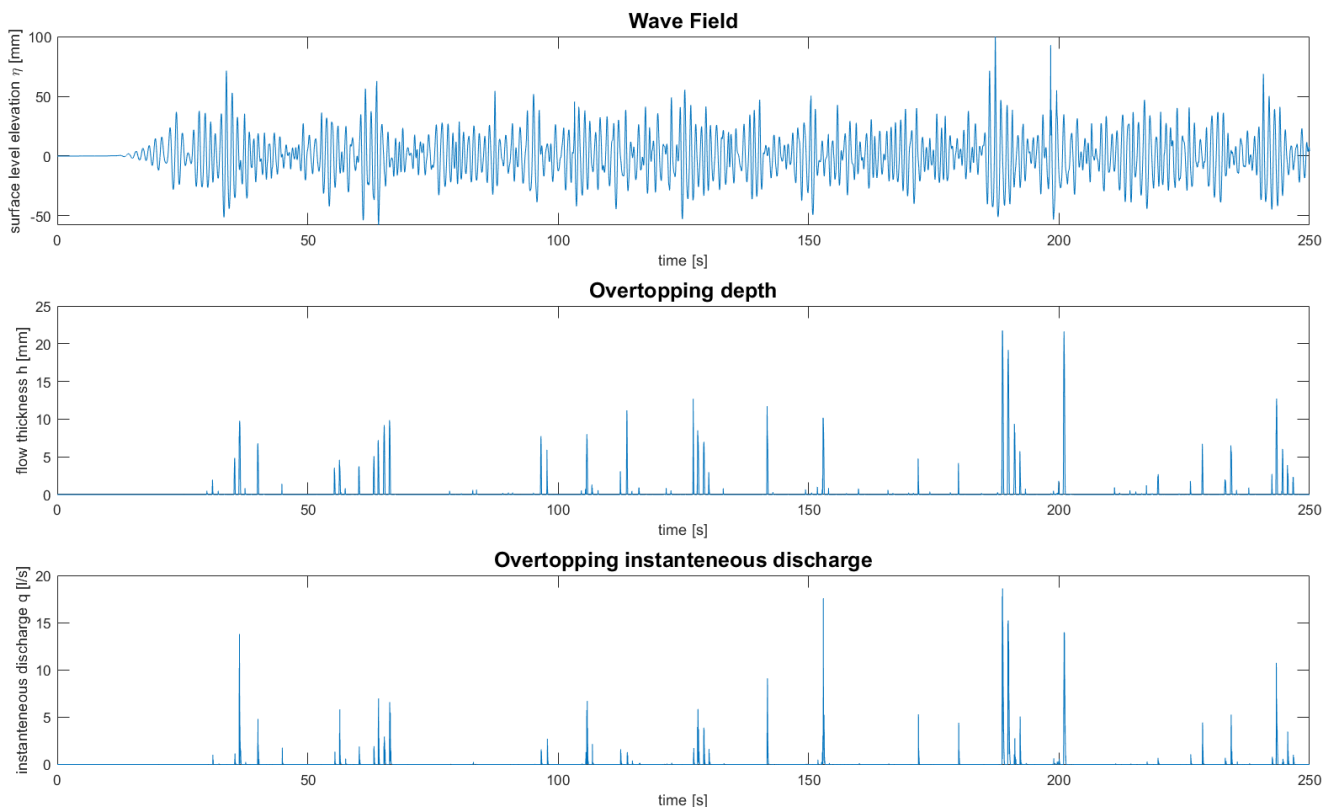
Appendix Figure I.1: Overview of output from run 8: Wave field; Overtopping depth; Overtopping instantaneous discharge

As the overtopping face uses a flux through a face and the wave gauge uses the cell value of the indicator function, it is possible that the overtopping face measures a flow when the wave gauge does not measure a flow or vice versa because of the slightly different positioning of the measurement devices. Also due to the refinement, it was found that the crest level was sometimes positioned 1 cell level higher than the

original input value for the crest level. Because of this, for run 2, 3, 7 and 8 the wave gauges protrude slightly into the breakwater, causing an error of maximally one cell height ($1.25\,[mm]$).

## I.1   Smallest waves neglected

In the analysis it is chosen to neglect waves that are smaller than 1 cell height. Reasons for this are: 1) these very small waves are sometimes just drops of water ('splash') flowing over, which we want to keep out of the analysis; 2) waves smaller than 1.25 mm would probably not have been measured in the model experiment and are not interesting for stability issues; 3) the mesh is relatively coarse for these waves, and so the resulting flow depth and velocity measurements are less reliable.

The analysis ignores waves that are smaller than one cell height on top of the crest. In the case of run 8, where the gauge is protruding with one cell height into the crest, this means that the gauge output smaller than twice the cell height is ignored. The result can be seen in Appendix Figure I.2, where all waves smaller than $2*0.00125 = 0.0025\,[mm]$ are ignored. It is clear from this figure, which employs the peak-over-threshold analysis, that quite some waves have multiple maximum flow depths.
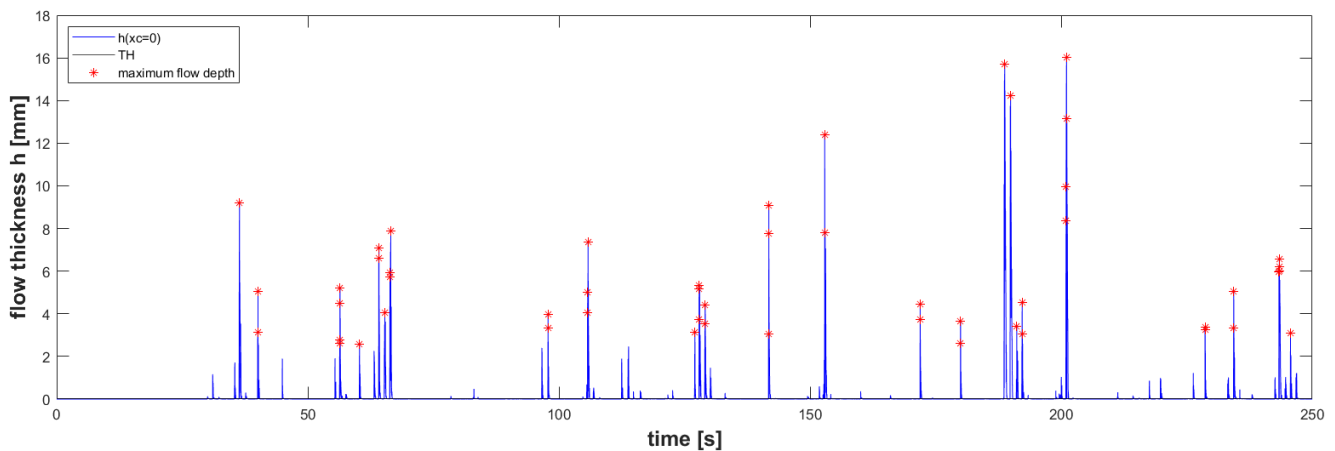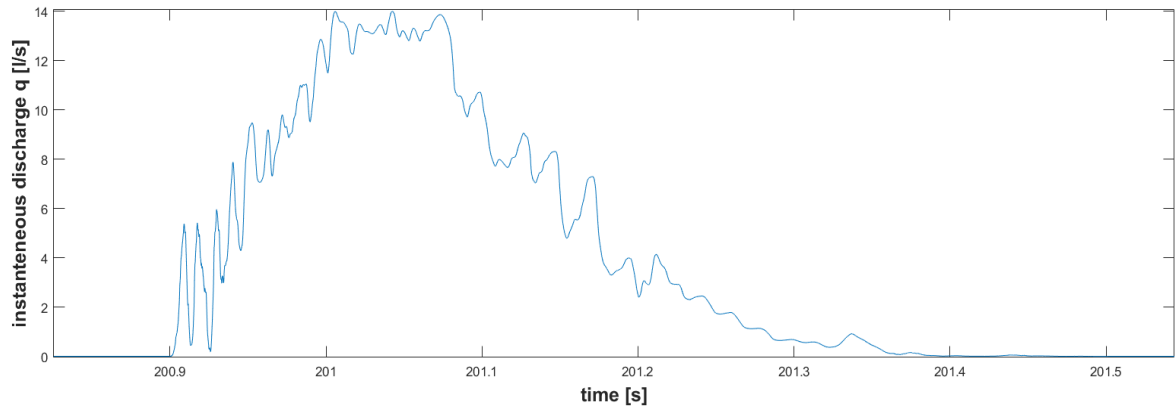

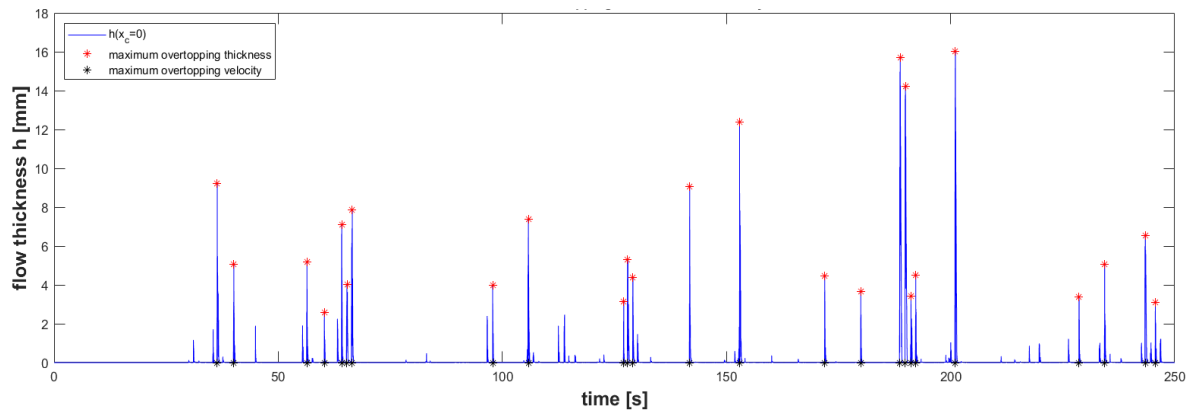Appendix Figure I.2: Overtopping flow depth at the transition from filter to core material

Upon closer inspection, it is clear that most of these waves have measurement discontinuities. One of these waves, overtopping around $t = 201\,s$, is shown in Appendix Figure I.3. Obviously, these are not physical effects and they seem to be caused by the incomplete integration of the overtopping flow. We can verify that this is in fact one wave overtopping by looking at the overtopping instantaneous discharge results for the same wave (Appendix Figure I.4). To avoid that individual waves are represented by multiple maximum velocities and flow depths, the script is adapted to keep only the largest of the multiple maxima. The result is given in Appendix Figure I.5.
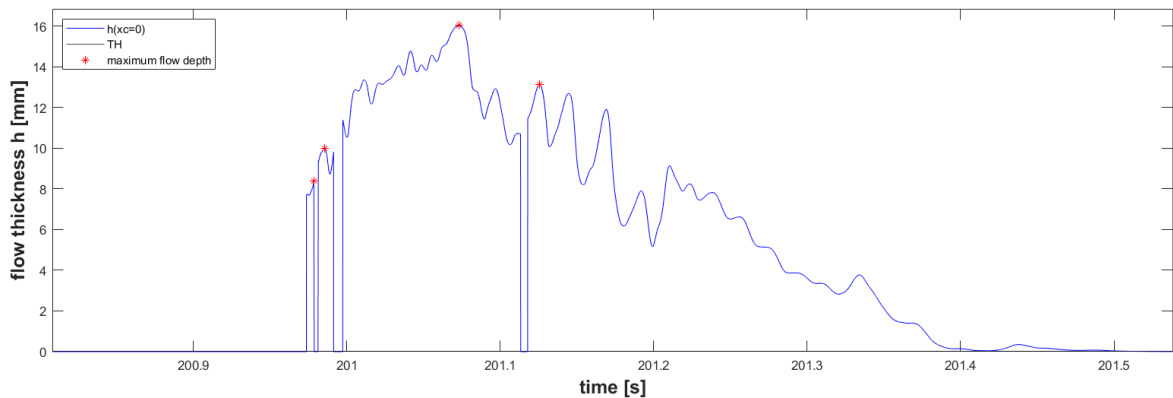
Appendix Figure I.3: Overtopping flow depth, around 201 [s]

Appendix Figure I.4: Overtopping instantaneous discharge, around 201 [s]

Appendix Figure I.5: Overtopping flow depth, with adapted method for determination of the maximum

I.2 Determination of the overtopping velocity

To understand the implications of the measurement methods it is important to characterise the overtopping characteristics in time. Here a description is given of the options to measure the velocity and the chosen method.

From the analysis in the validation, it is clear that the velocity is distributed quite evenly over the depth of the wave tongue. Sandoval (Sandoval, 2015) uses this fact and the assumption that the front of the wave tongue travels with the maximum velocity to take the front velocity of the wave as the destabilizing velocity. In this research, this information could be used to use wave gauges on the crest to measure the velocity of an overtopping wave, by taking the derivative of the location of the front of the wave over time. It is then however difficult to study for what flow depth the maximum velocity occurs.

Also, the combinations of maximum flow velocity and flow depth and maximum flow depth and flow velocity are uncertain. This research opts to take this effect into account, and so proposes not to look at the velocity of the front of the wave tongue, but at the maximum velocity that is occurring in each wave as well as the velocity that is occurring during the maximum flow depth of that wave.

A different method to calculate the flow velocity, is by using the overtopping faces and $q = u * h$. The problem with this method however is that due to the numerical oscillations in the results for both the overtopping depth and the overtopping instantaneous discharge, the maximum found velocity is often the result of this numerical error. This is visualised by Appendix Figure I.6, where the red dot indicates the points in the graphs that give the largest overtopping velocity for the wave overtopping at $191.1\ [s]$. The resulting velocity is almost $7\ [m/s]$, which is definitely too high. It was tried to use a moving average to overcome this error, however this reduced the maximum (credible) flow depth very significantly. In the worst cases, this caused a reduction of 40%.

129

Looking at the shape of the velocity shown in Appendix Figure I.6, the saw-tooth shape can easily be recognized that is expected for velocity in an overtopping flow (see e.g. Hughes, 2011). Looking at the wave where the largest velocity is measured in this run, the wave around $191.1\ [s]$, it is found that after the peak the maximum stabilizes to a maximum of around $1.15\ [m/s]$. The measurement method used in this thesis (where the maximum velocity is measured by probes positioned in the overtopping flow) predicts a maximum of $1.19\ [m/s]$, which is in this case quite representative.
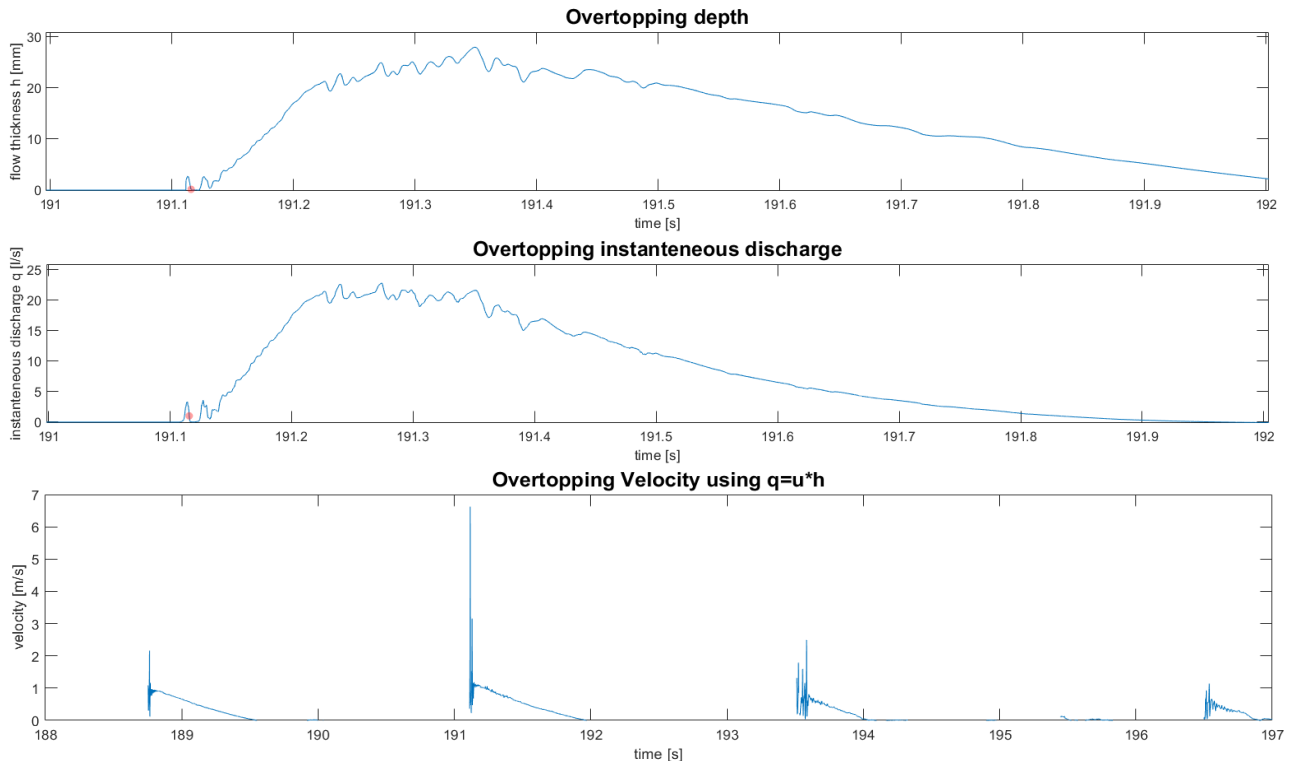
Appendix Figure I.6: Overtopping depth, Overtopping discharge, resulting Overtopping velocity

Appendix Figure I.7 shows the output of some of the probes that are located in the overtopping wave. All these 3 probes are located on the same x-coordinate, but on varying vertical positions. The measurement projected here is shown at the moment of maximum overtopping flow depth. The first picture shows a probe just above the crest level. The middle picture shows the measured velocity closer to the centre of the overtopping wave tongue. Note that the saw-tooth shape is again clearly visible. The last picture shows the measured velocity around the interface of the overtopping wave and the air, and so has quite a low overtopping velocity. Also the characteristic saw-tooth shape cannot be recognized. This last plot clearly shows why averaging the result using the data of multiple probes is not directly an option, as it will seriously underestimate the maximum flow depth. It is concluded that the measurement technique of taking the maximum velocity from the probe output is the best alternative with this dataset.
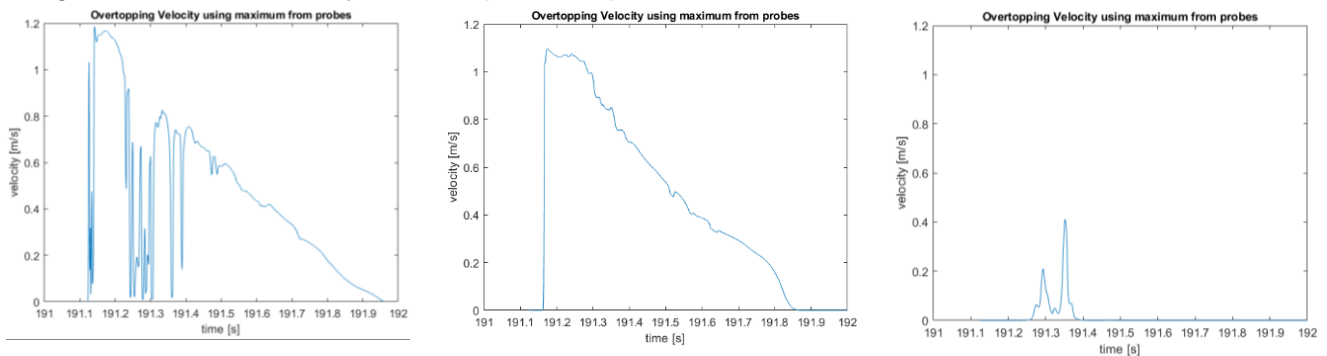
Appendix Figure I.7: Overtopping velocity for various probes in the wave overtopping at 191.1 [s]

130

Appendix J. 2% exceedance values

The table below shows the 2% exceedance values for the results calculated at the seaward core crest edge. As discussed in the main text, the output results for the Rayleigh distribution is used in the analysis of the results. A table like this was made for every measurement point along the breakwater crest.

Run-ID	Best alpha	h RMSE	$h_{2\%}$	Best alpha	u RMSE	$u_{2\%}$	No. analysed	Difference
1_H06-S1-R10	1.2	6.2940e-04	0.0190	∞	0.0446	1.1529	45	h: ~0.5%
RAYLEIGH		7.6391e-04	0.0191		0.0597	1.1580		u: ~0.4%
2_H04-S1-R10	1.2	3.7300e-04	0.0091	∞	0.0253	0.8848	24	h: ~2.2%
RAYLEIGH		4.0559e-04	0.0093		0.0288	0.8819		u: ~0.3%
3_H08-S1-R10	2	0.0014	0.0415	∞	0.0509	1.5111	77	h: ~0.0%
RAYLEIGH		0.0014	0.0415		0.0600	1.5387		u: ~1.8%
4_H06-S1-R15	1	9.1410e-04	0.0058	∞	0.0890	0.9217	10	h: ~3.3%
RAYLEIGH		9.3552e-04	0.0060		0.0965	0.9111		u: ~1.1%
5_H06-S1-R05	1.3	2.9844e-04	0.0338	∞	0.0303	1.2022	165	h: ~5.4%
RAYLEIGH		6.1732e-04	0.0321		0.0476	1.2708		u: ~1.8%
6_H06-S5-R10	0.6	3.4202e-04	0.0055	∞	0.0565	1.1250	26	h: ~5.1%
RAYLEIGH		4.7688e-04	0.0058		0.0689	1.1183		u: ~0.6%
7_H04-S5-R10	1.4	3.5748e-04	0.0024	∞	0.0480	0.7391	10	h: ~0.0%
RAYLEIGH		3.5861e-04	0.0024		0.0486	0.7457		u: ~0.9%
8_H08-S5-R10	1	7.1666e-04	0.0100	∞	0.0435	1.3627	25	h: ~2.0%
RAYLEIGH		7.7005e-04	0.0102		0.0479	1.3585		u: ~0.3%

Appendix Table J.1: 2% exceedance values for all runs, values at gauges on seaward core crest edge.
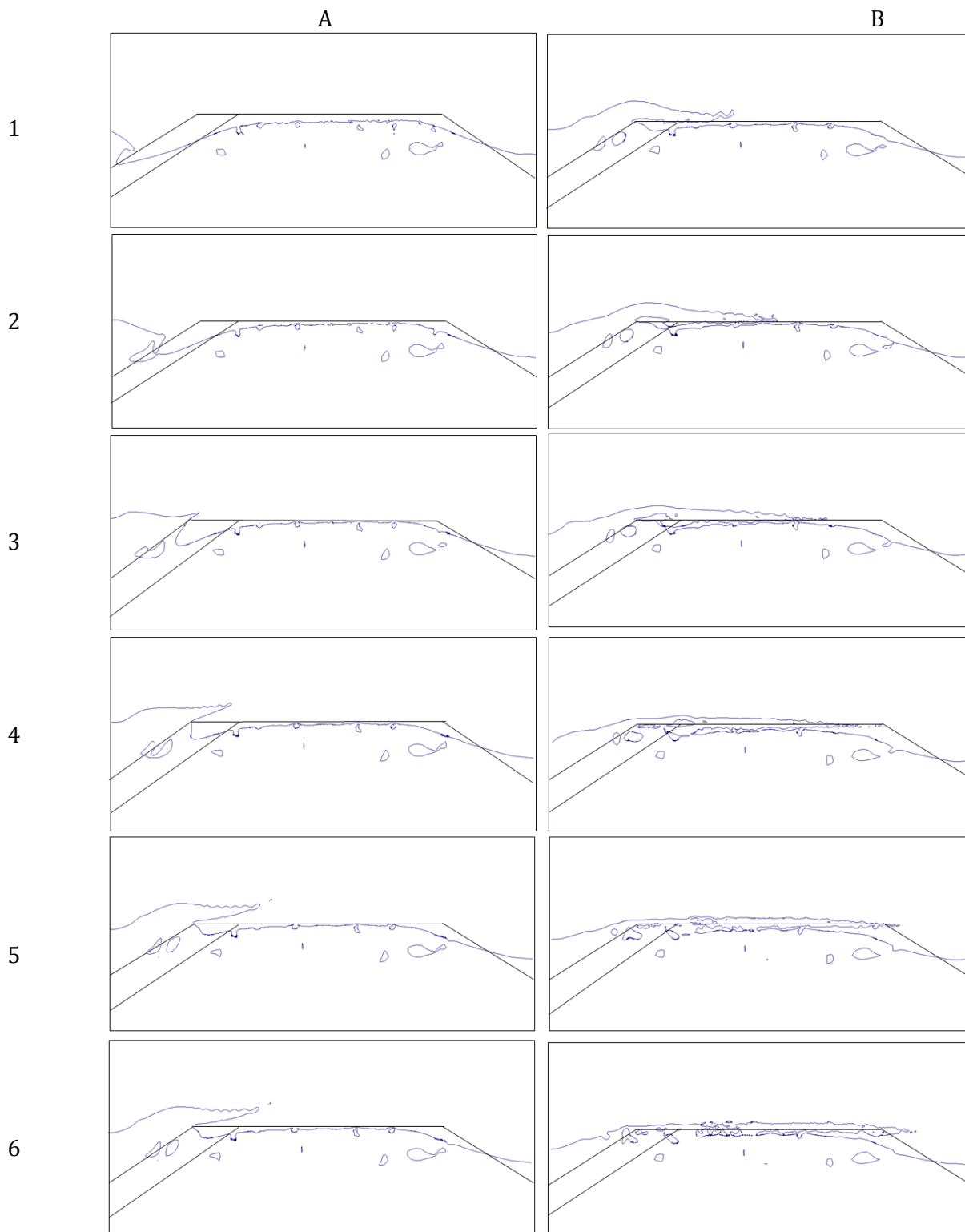
Appendix K. Contour plots

Appendix Figure K.1 shows contour plots of an overtopping swell wave. The time order of occurrence of these images is: A1, A2, A3, A4, A5, A6, B1, B2, B3, B4, B5, B6. The seaward filter layer is indicated.
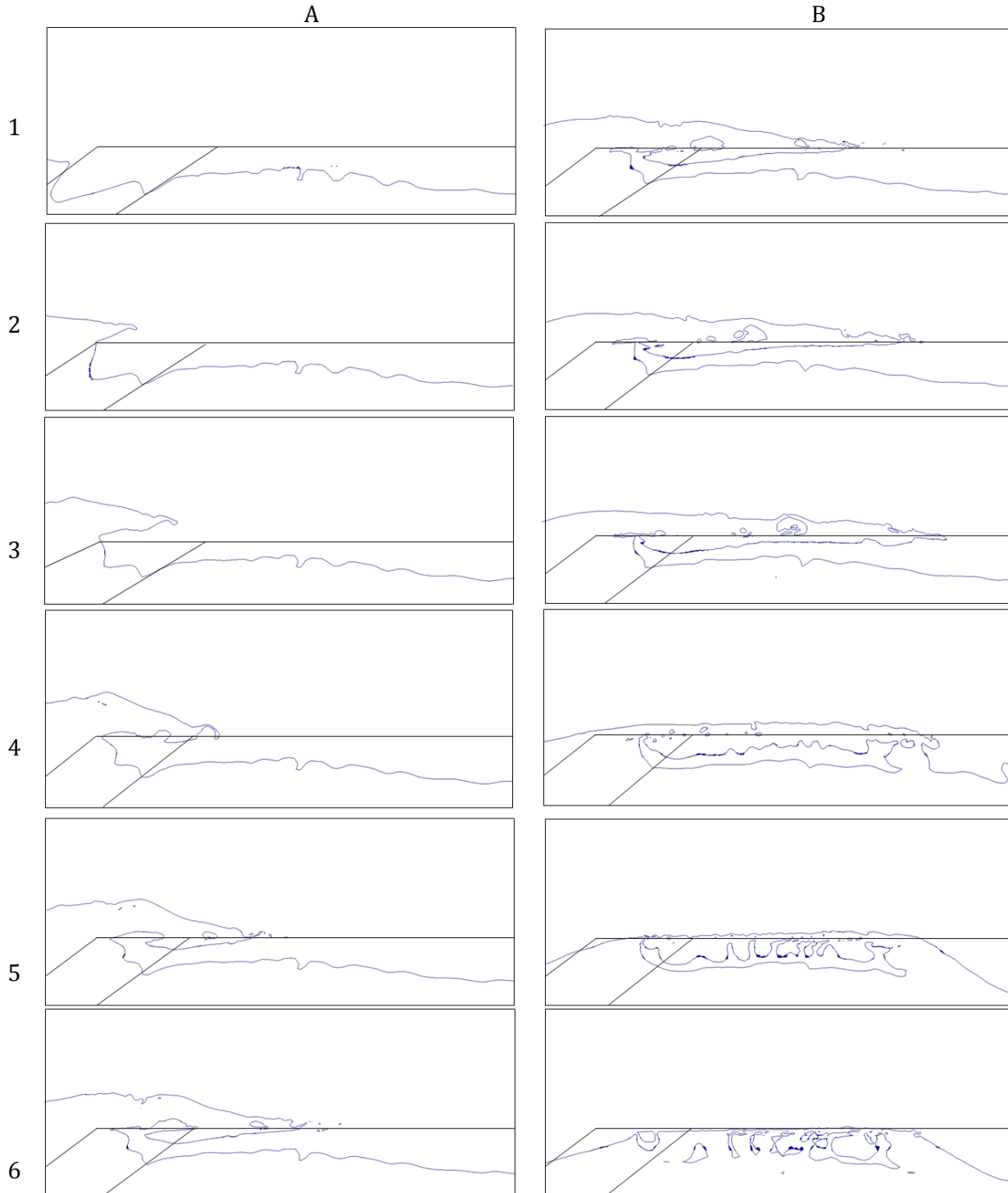
Appendix Figure K.1: α contour 0.5, swell run

Appendix Figure K.2 shows contour plots of an overtopping sea wave. The time order of occurrence of these images is: A1, A2, A3, A4, A5, A6, B1, B2, B3, B4, B5, B6. The seaward filter layer is indicated.

Appendix Figure K.2: α contour 0.5, sea run